THÈSE PRÉSENTÉE À

L'UNIVERSITÉ DU QUÉBEC À CHICOUTIMI

COMME EXIGENCE PARTIELLE

DU DOCTORAT EN SCIENCES DE LA TERRE ET DE L'ATMOSPHÈRE

PAR

JÉRÔME AUGUSTIN

ÉTUDE DES MINÉRALISATIONS AURIFÈRES DU DISTRICT DE MANA, BURKINA FASO. ÉVOLUTION HYDROTHERMALE D'UN SYSTÈME AURIFÈRE ET CONTRAINTES TECTONO-MÉTAMORPHIQUES

DÉCEMBRE 2017

RÉSUMÉ

L'Afrique de l'Ouest est désormais un acteur majeur dans la production d'or mondial avec de nombreux gisements d'or encaissés dans les ceintures de roches vertes du Paléoprotérozoïque. Cependant, ces ceintures ne sont encore que peu explorées et leur formation ainsi que leur évolution durant l'orogénèse Éburnéenne restent incertaines. Le district de Mana est situé dans la partie nord de la ceinture de roches vertes de Houndé d'âge Birimien (2,2-2,0 Ga), dans la partie ouest du Burkina Faso. C'est un district de classe mondiale qui contient 5 gisements aurifères orogéniques pour un total de ~8 Moz. Plusieurs typologies de minéralisation ont été identifiées dans différentes roches hôtes en lien avec des déformations polyphasées.

Ce projet de recherche visait à déterminer l'évolution structurale, hydrothermale et l'origine de la source de l'or du district de Mana dans le but de guider les travaux d'exploration à l'échelle locale et régionale et potentiellement dans le reste de l'Afrique de l'Ouest. Pour mener à bien ce projet, les caractéristiques stratigraphiques et structurales ainsi que les minéralisations ont été étudiées aux échelles locale et régionale.

L'étude de la colonne lithostratigraphique couplée aux données de géophysiques et de géochronologies ont permis d'identifier trois groupes stratigraphiques distincts (le Birimien inférieur, le Birimien supérieur et le type Tarkwaïen) sous des conditions métamorphiques du faciès des schistes verts. Le Birimien inférieur (< 2172 Ma) est composé de roches basaltiques en alternance avec des roches volcano-sédimentaires qui contiennent des niveaux de shales noirs riches en pyrites diagénétiques et d'une séquence calco-alcaline andésitique dans sa partie sommitale. Les études lithogéochimiques sur les basaltes ont permis de définir une affinité tholéiitique avec une mise en place en contexte de plateau océanique en lien avec une plume mantellique. Ce type de basaltes a le potentiel d'être pré-enrichi en or, tout comme les pyrites diagénétiques dans les niveaux de shales noirs. Ces unités sont interprétées comme la source principale de l'or à l'échelle du district. Les groupes du Birimien supérieur (2172-2113 Ma) et du type Tarkwaïen (~2113 Ma) sont associés à des bassins sédimentaires et leur contribution comme source primaire de l'or est considérée comme très limitée.

L'histoire structurale du district de Mana a enregistré des déformations polyphasées. La première déformation $D1_{MD}$ opère durant l'évènement Éoéburnéen (~2172 Ma) et développe des plis isoclinaux F_{1MD} et des failles inverses qui affectent le Birimien inférieur durant la mise en place pré- à syn-tectonique des granodiorites de bordures. La sédimentation du Birimien supérieur (2172-2113 Ma) suit une période d'extension ($D2_{MD}$)

avec la formation du bassin de Mana et à la fin, des bassins clastiques de type Tarkwaïen. La déformation $D3_{MD}$ marque l'évolution vers un régime transpressif de direction E-W à WNW-ESE durant l'évènement Éburnéen (~2113-2090 Ma). Cette déformation replisse les plis F_{1MD} pour former des plis F_{3MD} et développe des zones cisaillement dextre. La déformation majeure $D4_{MD}$ réactive les failles majeures et forme des plis F_{4MD} suivant un régime transpressif de direction NNW-SSE en lien avec la mise en place du pluton dioritique de Kokoï. La déformation tardive $D5_{MD}$ est liée à une compression N-S qui forme des clivages de crénulation, des failles inverses et des fractures. Cette déformation pourrait être aussi jeune que ~2022 Ma.

L'étude des minéralisations aurifères révèle que l'activité hydrothermale du district de Mana était polyphasée et caractérisée par 4 pulses en lien avec deux systèmes hydrothermaux ayant des sources distinctes. Le premier pulse hydrothermal est généré pendant la déformation $D1_{MD}$ et est enregistré dans les gisements de Fofina et Siou en lien avec des minéralisations sous forme de veines de quartz et de pyrites disséminés. L'étude au LA-ICP-MS des éléments traces dans les pyrites permet de déduire la présence d'un fluide métamorphique (As, Ni, Cu, Ag, Sb, W, Au et Pb) à Fofina et d'un fluide magmatique (Au, Ag, Bi, Te, W ± Sb) à Siou. Le deuxième pulse hydrothermal est documenté dans le gisement de Nyafé durant la déformation $D3_{MD}$ et se manifeste par des veinules à sulfures formant des stockwerks. Les pyrites de Nyafé se caractérisent par la présence de couronnes riches en Au-As formées durant la précipitation des arsénopyrites. Le troisième pulse hydrothermal s'est produit pendant la déformation $D4_{MD}$, et correspond à la formation d'une silicification massive et de sulfures (pyrite et arsénopyrite) dans les gisements de Wona-Kona et Yaho. Tout comme à Nyafé, les couronnes en Au-As sont présentes sur les pyrites dans les deux gisements. Ces pyrites zonées (Nyafé, Wona-Kona, Yaho) sont interprétées comme étant les produits d'un même système hydrothermal, dont la source des fluides et de l'or provient du métamorphisme du Birimien inférieur et plus particulièrement des shales noirs (pyrite diagénétique) et possiblement des basaltes tholéiitiques. Le dernier épisode hydrothermal se déroule durant la fin de la déformation $D4_{MD}$ ou durant $D5_{MD}$ en lien avec la formation d'or libre dans des fractures tardives aux gisements de Wona-Kona et Siou.

L'étude du district de Mana démontre une histoire métallogénique et tectonique polyphasée qui a permis de produire des gisements aurifères économiques. De nouveaux outils d'exploration pour les gisements aurifères orogéniques, incluant en outre des diagrammes binaires (chimie des basaltes et des pyrites), ont été développés afin d'estimer rapidement la fertilité aurifère d'une ceinture de roches vertes.

REMERCIEMENTS

Je tiens à montrer toute ma gratitude envers mon directeur Damien Gaboury pour m'avoir proposé le projet de thèse. Il a su me donner la chance d'étudier les gisements d'or orogéniques en Afrique de l'Ouest et me guider depuis ma maîtrise jusqu'à la fin de ce doctorat. Je lui suis reconnaissant de m'avoir inculqué sa passion pour la géologie économique ainsi que la rigueur nécessaire à la recherche scientifique.

Je tiens également à remercier la compagnie SEMAFO Inc. pour avoir rendu possible ce projet de recherche par sa contribution financière, son appui logistique et l'accès à l'ensemble des données non-publiées. Je remercie plus particulièrement Michel Crevier, Vice-Président Exploration et Géologie minière qui a su me donner ma chance dans cette longue aventure au pays des hommes intègres et qui m'a permis de développer mes talents professionnels. Je remercie également les vieux routards de l'exploration Richard Roy, David Lalonde, Denis Boisvert (maintenant à Endeavour Mining), Donald Trudel (maintenant à IAMGOLD), Dofinta Bondé et Faustin Yameogo pour les longues journées de terrain et de discussions géologiques autour d'une bonne Beaufort.

Mes sincères remerciements à tous les membres de l'équipe d'exploration de Mana Minéral S.A. pour leur accueil et pour avoir partagé leur expérience avec moi. Plus particulièrement, je remercie Apollinaire Sawadogo, Moussa Semdé, Sayouba Kaboré, Issa Zoungrana, Idrissa Kaboré, Tall Mamoudou et bien sur la géomatique Fatima Hassani, Colette Kongobo, Abdelhak Nouaseri, Sylvestre Ilboudo. Un merci supplémentaire pour mes acolytes de terrain et de bureau de Burkina Géoservices SARL., Lucas Brião Koth et Sliman Machroh avec qui j'ai partagé des moments épiques et philosophiques. Je remercie également mes collègues de la mine de Mana Frédéric Paré, Nicolas Boucher, Alexandre Aubin et Olivier Fusco.

Je tiens à remercier chacun des membres de mon jury Réal Daigneault, Benoit Dubé et Pierre A. Cousineau qui ont accepté de réviser mon manuscrit.

Un grand merci à Dany Savard du Labmater de l'UQAC, Olivier Bruguier de l'Université de Montpellier ainsi que Natacha Fournier de IOS Géoservices pour les traitements et les analyses géochimiques. Je remercie l'ensemble du personnel de l'unité d'enseignement en Sciences de la Terre de l'UQAC ainsi que les étudiants du bac et du REDIST. On a bien rigolé durant ces années.

J'ai bien sur une pensée pour mes amis Lucas, Charley, Dominique, Édouard, Rémi, Ossman, Renato, Bruna et Arnaud et les autres que je n'oublie pas. Merci pour le soutien et les soirées.

Je voudrais remercier ma famille qui m'a soutenu tout au long de ma thèse, et plus particulièrement mes parents et ma sœur qui m'ont donné le goût de l'effort et de m'avoir inculqué qu'il faut se battre dans la vie pour réussir.

Ma plus belle découverte reste ma fiancée Laurie qui m'a soutenu tout au long de mon doctorat et avec qui je vais pouvoir réaliser mes rêves.

TABLE DES MATIÈRES

LISTE DES FIGURES

CHAPITRE 1

CHAPITRE 2

CHAPITRE 3

CHAPITRE 4

CHAPITRE 5

LISTE DES TABLEAUX

CHAPITRE 1

CHAPITRE 2

CHAPITRE 3

CHAPITRE 4

LISTE DES ANNEXES

CHAPITRE 1

1. INTRODUCTION

1.1. PROBLEMATIQUE GÉNÉRALE

1.1.1. FORMATION DES GISEMENTS AURIFÈRES OROGÉNIQUES

Les gisements de type orogénique ont une importance économique majeure puisqu'ils représentent plus de 75% de l'or extrait dans le monde (Tomkins, 2013a). Les gisements aurifères orogéniques sont associés à des contextes tectoniques en compression et en transpression, syn- à post-pic métamorphique (Kerrich and Wyman, 1990; Goldfard et al., 2005; Bierlein et al., 2009). Le terme "orogénique" implique des processus liés à la formation d'orogène. Les gisements d'or orogéniques ne sont pas formés de façon uniforme au cours des temps géologiques et il existe des périodes d'accrétions favorables pour leur formation incluant la seconde moitié de l'Archéen tardif (2,8-2,55 Ga), la seconde moitié du Paléoprotérozoïque (2,15-1,75 Ga) et le Phanérozoïque (540-0 Ma) (Goldfarb et al., 2001; Tomkins et al., 2013b; Groves et al., 2016 - Fig. 1.1). L'Afrique de l'Ouest est actuellement la plus grosse province aurifère d'âge Paléoprotérozoïque avec une production et des ressources cumulées de plus de 10 000 t d'or (~321 Moz - Goldfarb et al., 2017) marquée par la présence de nombreux gisements aurifères de classe mondiale (Fig. 1.1). On peut citer l'exemple du gisement aurifère orogénique d'Obuasi (~62 Moz) dans la partie sud du Ghana (Fig. 1.1 - Fougerouse et al., 2017).

La formation de ces gisements est en lien direct avec des processus d'accrétion crustale ou de collision en contexte de subduction et peut se développer dans des environnements d'arc, d'arrière arc ou de prisme d'accrétion (Groves et al., 2003). De plus, une importante activité

magmatique permet la formation et la circulation des fluides hydrothermaux à partir de la dévolatisation de l'empilement volcano-sédimentaire durant le métamorphisme prograde, le plus souvent au faciès métamorphique des schistes verts. À ces conditions, le comportement ductile-fragile facilite le transfert des fluides aurifères des niveaux sous-jacents (Goldfarb et al., 2005; Groves et al., 1998; Phillips and Powell, 2009). Les terrains ont généralement enregistré des déformations polyphasées en lien avec de grands accidents lithosphériques majeurs souvent cisaillant qui permettent la canalisation des fluides hydrothermaux et la précipitation de l'or (Groves et al., 2016).

Les études récentes sur les gisements orogéniques montrent des caractéristiques communes sur l'ensemble du globe et de tous âges (Groves et al., 1998; Large et al., 2009; Thomas et al., 2011; Lawrence et al., 2013; Goldfarb et al., 2015; Groves et Santosh, 2015). Ainsi les minéralisations sont spatialement associées avec des corridors de déformation (failles de $2^{ème}$ et $3^{ème}$ ordre) au sein de ceintures de roches vertes dans des conditions métamorphiques aux faciès des schistes verts et localement au faciès inférieur des amphibolites. L'or est associé avec des enrichissements en métaux tels que S, Cu, Mo, Sb, Bi, W, Pb, Zn, Te, Hg, As et Ag avec des apports variables en CO_2, K, S, As et Sb (Goldfarb et al., 2005; Richards, 2009). Les compostions en volatiles des fluides sont caractérisées par une faible salinité avec des assemblages en H_2O-CO_2 ± N_2 et des hydrocarbures CH_4-C_2H_6 (Gaboury, 2013; Lawrence et al., 2013).

D'un point de vue des typologies, les minéralisations aurifères orogéniques se présentent préférentiellement sous forme de veines et veinules de quartz-carbonate contenant une

quantité variable de sulfures (pyrite, arsénopyrite, chalcopyrite et autres), en compatibilité structurale avec le régime de déformation dissipé le long des failles en cisaillement fragiles-ductiles (Gaboury et al., 2001; Meffre et al., 2016). Pour les failles en domaine ductile, les minéralisations aurifères sont généralement sous forme de sulfures disséminés car les comportements rhéologiques plastiques atténuent la rupture cassante des failles et fractures limitant ainsi la formation des veines (Witt and Vanderhor, 1998; Vielreicher et al., 2002).

1.1.2. LES GRANDS PROBLÈMES DES GISEMENTS AURIFÈRES OROGÉNIQUES

Les gisements aurifères orogéniques en comparaison avec d'autres types de gisements aurifères, restent les moins bien compris, car ils se forment à des profondeurs de 5-15 km, rendant ainsi l'étude des systèmes hydrothermaux actifs impossibles. En conséquence, plusieurs paramètres fondamentaux sur les processus de formation demeurent à préciser. L'article de Tomkins (2013a), fait une revue des connaissances et des principales questions concernant la source de l'or des gisements orogéniques. Ces questions sont synthétisées dans la figure 1.2. Deux questions majeures sont introduites, il s'agit : 1) de l'origine de la formation des fluides hydrothermaux, et 2) de la source de l'or. Les recherches récentes sur les grandes provinces métallogéniques orogéniques s'accordent sur deux sources possibles pour les fluides minéralisateurs et trois sources pour l’or: 1) les fluides métamorphiques provenant de la déshydratation de roches lors d'un métamorphisme prograde (Fyfe et

al.,1978; Kerrich and Fyfe, 1981; Colvin, 1989; Kerrich, 1999; Beaudoin and Pitre, 2005; Goldfarb et al., 2005; Pitcairn et al., 2006, 2010, 2015; Large et al., 2012; Bierlein and Pisarevsky, 2008; Phillips and Powell, 2010; Tomkins, 2010; Thomas et al., 2011; Gaboury, 2013, Hu et al., 2016); et 2) les fluides magmatiques associés aux intrusions alcalines felsiques à intermédiaires (Lang and Baker, 2001; Bierlein et McKnight, 2005; Mair et al., 2011; McFarlane et al., 2011; Xue et al., 2013; Helt et al., 2014; Bigot and Jébrak, 2015). La source de l'or peut être 1) magmatique (Helt et al., 2014), 2) dérivée des pyrites primaires par transformation métamorphique en pyrrhotite dans les roches métasédimentaires (Thomas et al., 2011), et 3) lessivée des métabasaltes (Velásquez et al., 2011; Pitcairn et al., 2015).

1.1.2.1. LA SOURCE MÉTAMORPHIQUE

Pour la génération des fluides métamorphiques, les travaux de Phillips and Powell (2009, 2010) ont introduit le modèle de dévolatisation métamorphique. Ce modèle implique une formation des fluides et de l'or en profondeur lors des processus métamorphiques liés au passage du faciès métamorphique des schistes verts vers le faciès des amphibolites (T = 440-520°C). Ce passage implique une dévolatisation des unités mafiques en profondeur et génère des fluides de faible salinité riches en H_2O, CO_2 et H_2S, et qui transportent l'or sous forme de complexes sulfurés. Le modèle de dévolatisation implique que les gisements aurifères ne peuvent se former au-delà du faciès des schistes verts. Les fluides

métamorphiques les plus fertiles sont libérés sous les 500-550°C avec une faible proportion au-delà de 550°C (Tomkins, 2010). Ces résultats sont en accord avec le fait que la plupart des gisements aurifères orogéniques sont encaissés dans des roches aux faciès des schistes verts à amphibolite inférieur (Groves et al., 2003). Les gisements aurifères orogéniques sont spatialement associés à des roches métamorphiques qui sont généralement associées à la source de l'or. Le problème est de déterminer l'échelle de la mobilité de l'or et de définir les lithologies susceptibles d'être à l'origine de la source de l'or. Pour la source métamorphique, 2 groupes de roches métamorphiques, présentes en grandes quantités dans les ceintures de roches vertes sont proposés : 1) Les roches métasédimentaires et 2) les roches métavolcaniques mafiques à ultramafiques. Le tableau 1.1 illustre les différentes sources d'or possibles en lien avec les gisements orogéniques.

Les roches métasédimentaires représentent le plus gros volume de roches sujet à la dévolatisation lors de la formation des gisements d'or orogéniques (Rauchenstein-Martinek et al., 2014). Le meilleur cas d'étude concerne la ceinture des Schistes d'Otago en Nouvelle-Zélande (Fig. 1.3). Cette ceinture est constituée de roches métasédimentaires (turbidite) et métavolcaniques d'âge mésozoïque et contient des gisements d'or orogéniques de classe mondiale (exemple Macraes, 7 Moz - Tableau 1.1). Afin de déterminer l'origine de la source de l'or, Pitcairn et al. (2006) ont démontré un appauvrissement systématique en métaux tels que Au, As, Bi, Sb, Te et W dans les unités métamorphiques (roches métasédimentaires) comparativement aux roches non-métamorphiques (Fig. 1.3). Cette suite d'éléments appauvris est identique à celle des éléments enrichis dans les gisements aurifères orogéniques d'Otago. Il propose alors que ces gisements sont formés par un fluide

métamorphique régional qui mobilise les métaux durant le métamorphisme prograde. Cet argument est supporté par l'absence d'intrusions susceptibles de générer des fluides magmatiques. Pour déterminer les quantités de métaux susceptibles d'être produits par la dévolatisation des roches métasédimentaires des Schistes d'Otago, Pitcairn et al. (2014) proposent que pour un volume de 50 km^3 de roches métasédimentaires, 11,27 t Au, 10,1 Mt As, 47 000 t Hg, 560 000 t Sb et 14 000 Mt H_2O peuvent être mobilisés en 1 million d'années lors du métamorphisme de haut grade (~ 500°C). Les travaux récents dans cette région montrent que les pyrites diagénétiques contenues dans les roches métasédimentaires ont perdu de l'Ag, As, Hg, Sb dans des conditions de hautes températures (Pitcairn et al., 2010; Large et al., 2012).

Une autre suggestion de source concerne les roches métasédimentaires carbonées qui sont une source devenue idéale depuis le développement des cartes par ablation laser au LA-ICP-MS. Cette méthode a permis de reconnaître la présence de pyrites biogéniques et diagénétiques ayant des contenus élevés en Au, As, Ag, Bi, Ni, Cu, Mo, V et Pb dans les gisements de Sukhoi Log (Sibérie) et Bendigo (Australie) (Large et al., 2007, 2009; Thomas et al., 2011 - Tableau 1.1). Ces mêmes éléments se retrouvent dans les gisements orogéniques. Thomas et al. (2011) ont démontré que la transition métamorphique des schistes verts - amphibolite des roches métasédimentaires de Bendigo permet la conversion de la pyrite en pyrrhotite avec la libération d'or accumulé dans les pyrites diagénétiques et forme une zonation autour des pyrites diagénétiques en Au et As. Gaboury (2013) confirme ces observations à travers l'étude des gisements d'or orogénique de Detour Lake (Canada) et du district de Mana (Burkina Faso). En analysant la composition en gaz des inclusions

fluides, la présence d'éthane a été détectée. L'éthane (C_2H_6) est un hydrocarbure léger qui provient de la dégradation thermogénique de la matière organique. Cela souligne l'importance des shales en profondeur, pour la génération des fluides métamorphiques et l'importance en tant que source de l'or des pyrites primaires. De plus, Gaboury (2013) explique aussi l'apparition des fluides riches en CO_2 et pauvre en H_2O dans de nombreux gisements d'or par le biais de la réaction du C_2H_6 avec H_2O pour former du CO_2 ce qui implique que les roches mères métasédimentaires carbonées sont importantes à l'échelle mondiale.

Les roches métabasaltiques ont été suggérées comme une source d'or pour les gisements orogéniques (Bierlein and Pisarevsky, 2008; Bierlein and Craw, 2009; Velásquez et al., 2011; Perrouty et al., 2014; Pitcairn et al., 2015). Plus particulièrement, il s'agit des basaltes de plateau océanique qui se forment en contexte océanique intra-plaque en lien avec la formation d'un panache mantellique en association avec des komatiites. Ce panache génère un pré-enrichissement en or dix fois supérieur par rapport aux basaltes de rides océaniques (MORB) (Bierlein and Pisarevsky 2008; Webber et al., 2013). Deux explications sont proposées (Bierlein and Pisarevsky, 2008; Bierlein and Craw, 2009): 1) les panaches mantelliques proviennent de la frontière noyau-manteau et transportent l'or ainsi que d'autres éléments sidérophiles qui viennent enrichir la croûte supérieure (Hawkesworth and Scherstén, 2007) et 2) au cours de l'accrétion du plateau océanique sur le continent, le manteau chaud est mis en contact avec du matériel crustal ce qui déclenche un dégazage de la croûte ainsi que sa fusion. Des plateaux océaniques d'âge Birimien ont été proposés pour le craton Ouest Africain (Abouchami et al., 1990; Boher et al., 1992) et

pour le bouclier Guyanais (Velásquez et al., 2011) lors des processus d'accrétion qui se corrèlent avec la mise en place des plus gros gisements orogéniques au Paléoprotérozoïque (Goldfarb et al., 2017). La formation de métabasaltes du Paléoprotérozoïque El Callao au Venezuela est un bel exemple de l'influence d'un panache mantellique en contexte de plateau océanique qui montre un enrichissement primaire en or (Velásquez et al., 2011) avec la formation de la Mine Colombia (24 Moz - Tableau 1.1). Cependant, les derniers travaux de Pitcairn et al. (2015), montrent que le lessivage des MORB (Mid Ocean Ridge Basalt) et WPB (Within Plate Basalt) présent dans les Schistes d'Otago peut libérer de l'or mais dans une quantité moindre que celle des roches métasédimentaires. D'autre part, les basaltes ne fournissent pas suffisamment d'As et S pour expliquer leur enrichissement dans les gisements, ce qui est considéré comme une validation indirecte que les métabasaltes ne sont pas la source principale de l'or.

1.1.2.2. LA SOURCE MAGMATIQUE

Dans les ceintures de roches vertes archéennes, de nombreux gisements aurifères de classe mondiale (Wallaby, Victory, Bellerophon, Malartic) se retrouvent en contact avec des intrusions intermédiaires à felsiques recoupant la séquence stratigraphique (Mason and Melnik, 1986; Spooner, 1991; Palin and Xu, 2000; Salier et al., 2004; Mcfarlane et al., 2011; Helt et al., 2014; Bigot and Jébrak, 2015; Xue and Campbell, 2015). La plupart des travaux dans le domaine de l'or orogénique ont démontré que les magmas constituent une

source négligeable d'or dans les systèmes orogéniques (Groves et al., 1998; Boiron et al., 2003). Cependant, Lang and Baker (2001) suggèrent que dans des conditions orogéniques singulières, bien qu'encore mal contraintes (accrétion à collision), les intrusions magmatiques peuvent constituer les sources principales de l'or. Il en résulte un modèle, non encore définitif, dénommé "Intrusion-related gold system" (filiation intrusive). Ce modèle implique une zonalité verticale qui se manifeste par des styles structuraux et des variations spatiales de la composition des fluides. La zonalité latérale se caractérise par la variation en métaux de base (As, Sb, Hg, W, Sn) vers la périphérie, alors que la minéralisation plus riche en or (Bi- Te ±W) est dans l'intrusion en lien avec une altération potassique (feldspath K), riche en carbonates et siliceuse (Fig. 1.4). Les fluides minéralisateurs sont à salinité faible avec un assemblage en volatiles à CO_2-CH_4-N_2-H_2S (Sillitoe and Thompson, 1998). La faiblesse de ce modèle réside dans le fait que les observations ont été faites dans un nombre limité de gisements. Helt et al. (2014) montrent la présence d'une source magmatique primaire pour le gisement de Canadian Malartic (Québec) à travers l'étude de la composition des inclusions fluides, des isotopes $\delta^{18}O_{(fluide)}$ (5-9 wt. %) et $\delta^{34}S$ des pyrites comme traceur de la source des fluides (Tableau 1.1). La source magmatique est génétiquement liée à des intrusions monzodioritique à syénitique avec un enrichissement en Au, Ag, Te, Mo, W, Pb, et Bi (Bigot and Jébrak, 2015; Mériaud and Jébrak, 2017). Il faut noter qu'il est possible d'avoir des mélanges entre les fluides métamorphiques et magmatiques qui viennent complexifier l'interprétation des données (Fig. 1.2). Cet exemple est documenté par Zang et al. (2014) sur le gisement d'or Chang'an (Chine). Son étude sur la chimie en éléments traces des pyrites démontre une signature faible en Au, As, Cu et Zn

pour le fluide magmatique en lien avec une syénite. Le fluide métamorphique tardif est caractérisé par un cortège métallique en Au, Ag, Ni, Pb et Cu. Le mélange des fluides magmatiques et métamorphiques est caractérisé par des valeurs élevées en Au, As, Pb et Co.

1.2. PROBLÉMATIQUE SPÉCIFIQUE

1.2.1. GÉOLOGIE RÉGIONALE

Le Burkina Faso se situe dans la partie sud du craton ouest-africain dans le domaine Baoulé-Mossi d'âge Paléoprotérozoïque qui est séparé du domaine archéen de Kenema-Man à l'ouest par la faille transcurrente de Sassandra (SF) (Fig. 1.5a). Les terrains paléoprotérozoïques, aussi appelés terrains birimiens, sont constitués d'une multitude de ceintures de roches vertes et de bassins volcano-sédimentaires, intrudés par différentes générations de granitoïdes et affectés par des déformations polyphasées (Hirdes et al., 1996; Doumbia et al., 1998; Gasquet et al., 2003; Le Métour et al., 2003; Feybesse et al., 2006).

Tout comme en Afrique de l'Ouest, le Burkina Faso contient de nombreuses ceintures de roches vertes birimiennes (~2,25 - 2,0 Ga) qui renferment l'ensemble des gisements aurifères orogéniques incluant ceux de Mana (Fig. 1.5b). Ainsi en 2015, le Burkina Faso s'est classé comme le troisième plus gros producteur d'or d'Afrique de l'Ouest (1,1 Moz produit) et quatrième à l'échelle du continent africain (Robertson and Peters, 2016).

La partie ouest du Burkina Faso est particulièrement prolifique pour l'or, plus particulièrement, la ceinture birimienne de roches vertes de Houndé (Figs. 1.5b, 1.6) compte des ressources totales estimées à 11 Moz (Augustin et al., 2016). Cette ceinture de direction NS à NNE est constituée à sa base d'une séquence de basaltes tholéiitiques et de gabbro suivie par une séquence intermédiaire calco-alcaline andésitique (Fig. 1.6). Cette transition entre un volcanisme tholéiitique à calco-alcalin marque l'évolution d'une croûte océanique ou d'un plateau océanique vers la formation d'îles en arc juvéniles entre ~2200 et 2160 Ma (Baratoux et al., 2011).

Cette période correspond au début de la phase de raccourcissement E-W Éburnéen (D1) avec la mise en place de granitoïdes de la série des TTG (Tonalite-Trondhjémite-Granodiorite - groupe ME1) et le dépôt de roches volcano-sédimentaires et sédimentaires du Birimien datée à ~2160-2124 Ma (Hirdes et al., 1996; Lüdtke et al., 1999; Castaing et al., 2003; Baratoux et al., 2011; Metelka et al., 2011). La déformation D1 est marquée par la formation de grands plis régionaux en lien avec un métamorphisme aux faciès des schistes verts à localement amphibolite. La fin de la déformation D1 est caractérisée localement par un régime transtensif en lien avec le dépôt des roches sédimentaires détritiques discordantes de type Tarkwaïen (~2120-2110 Ma) (Bossière et al., 1996; Koffi et al., 2016). Cette unité forme une bande étroite de 400 km de long dans la partie ouest de la ceinture de Houndé (Fig. 1.6). Certains plutons de composition granodioritique à granitique (groupe ME2) se mettent également en place pendant cette période. La déformation D2 évolue vers un régime transpressif orienté NNW-SSE avec le

développement de zones en cisaillement de direction NNE à NE contenant la majeure partie des minéralisations aurifères orogéniques (~2110-2090 Ma, Baratoux et al., 2011; Metelka et al., 2011; Augustin et al., 2016; Hein, 2016). Les derniers plutons granitiques potassiques se mettent en place durant cette période (épisodes ME3 - ME4). La dernière phase de déformation D3 forme des clivages de crénulation et des failles en chevauchement E-W durant une compression N-S (Baratoux et al., 2011; Metelka et al., 2011). Cette déformation n'est pas datée et pourrait correspondre à la fin de l'épisode éburnéen ou au Pan-Africain (Nikiéma et al., 1993).

Dans la partie ouest de la ceinture, les roches sédimentaires d'âge néoprotérozoïque de Taoudéni se retrouvent en discordance sur les roches du Birimien (Bronner et al., 1980; Bertrand-Sarfati et al., 1990 - Fig. 1.6).

1.2.2. GÉOLOGIE LOCALE

Le district de Mana est situé au nord de la ceinture birimienne de Houndé à ~300 km de Ouagadougou, la capitale (Figs. 1.6, 1.7). Dans ce projet, l'étude s'est concentrée sur la partie sud du district de Mana où se situe l'ensemble des gisements économiques (Fig. 1.7). La séquence stratigraphique est composée d'une série volcanique de basalte tholéiitique à la base, suivie d'une série volcanique calco-alcaline constituée d'andésites, de pyroclastites et de tufs au sommet (Fig. 1.7). Des roches volcano-sédimentaires sont intercalées dans les unités volcaniques en associations avec des niveaux de cherts et localement des shales

noirs. Dans la partie centrale du district, les roches sédimentaires fines à localement grossières dominent. Ces sédiments consistent en des wackes et des pélites qui sont affectés par des plissements. À l'est, la bande de roches sédimentaires détritiques de type Tarkwaïen définit un contact avec le granite de Siou (Fig. 1.7). Cette bande constituée de grès siliceux à galets centimétriques à métriques de quartz est en discordance sur l'ensemble stratigraphique avec un âge de dépôt maximal de 2113 ± 23 Ma (Bossière et al., 1996). Le même type de séquence est observé dans la partie NW du district (Fig. 1.7).

Sur les bordures du district de Mana, des intrusions granitiques de la série des TTG sont injectées et limitées par des failles crustales en cisaillement de direction NNE-SSW À N-S. C'est dans ces structures que l'on retrouve les deux plus gros gisements aurifères, incluant Wona-Kona de classe mondiale (4,0 Moz Au - Augustin et al., 2016), Siou (1,0 Moz Au) ainsi que le gisement de Yaho (1,0 Moz Au) (Fig. 1.7 - Tableau 1.2). Des failles de second ordre de direction NE-SW et ENE-WSW se retrouvent dans le cœur du district en lien avec les gisements aurifères satellites de Fofina (0,42 Moz) et Nyafé (0,37 Moz) (Fig. 1.7 - Tableau 1.2). Des failles en chevauchement de direction E-W sont également présentes dans le secteur nord de Bouna (Fig. 1.7). Le métamorphisme est aux faciès des schistes verts à amphibolite inférieur proche des auréoles de contact des plutons. Les assemblages métamorphiques consistent en des proportions variables de chlorite, trémolite, albite, épidote et micas blancs (muscovite).

La couverture sédimentaire du Néoprotérozoïque du bassin de Taoudéni, discordante sur le socle structuré Éburnéen, est essentiellement composée de formations gréseuses, marines et

fluviatiles (Bertrand-Sarfati et al., 1990). Elle est présente dans la partie ouest du district (Fig. 1.7). Plusieurs générations de dykes doléritiques post-Éburnéen recoupent l'ensemble du district suivant des directions NE-SW et NW-SE (Fig. 1.7) (Jessell et al., 2015).

1.2.3. INTÉRÊTS DE LA ZONE D'ÉTUDE

Le district de Mana encaisse sur moins de 15 km de rayon, 5 gisements aurifères orogéniques (total ~ 230 t Au) le long de corridors de déformation en cisaillements (Fig. 1.7). La géologie de ce district a été documentée par 2 projets de maîtrise (Augustin, 2011; Sinaré, 2013), 5 projets de fin d'étude (PFE) (Béland, 2009; Paulin-Bissonnette, 2012; Mercier, 2013; Dupuis, 2013; Gilbert, 2014) et 2 articles scientifiques (Gaboury, 2013; Augustin et al., 2016). Ces études ont permis d'avoir une meilleure compréhension des gisements aurifères de Mana et sont synthétisées dans le tableau 1.2.

La particularité du district de Mana est qu'il renferme l'ensemble des unités stratigraphiques (basaltes, roches sédimentaires incluant des shales noirs) susceptibles de contenir de l'or primaire et donc d'être la source de l'or orogénique. Ces unités ont le potentiel de générer des fluides métamorphiques sur l'ensemble du district durant l'histoire tectonique polyphasée de Mana. De plus, les granitoïdes de bordures sont spatialement associés aux deux plus gros gisements (Wona-Kona et Siou) et seraient de bons candidats pour la mise en place de fluides magmatiques (Fig. 1.7). La fertilité du secteur de Mana permet donc de poser plusieurs questions. Par exemple, y a-t-il une contribution de

plusieurs sources d'or ? Y a-t-il un système hydrothermal ou plusieurs et si oui quelle est la composition de ces fluides ? Quelles sont les liens entre l'évolution géodynamique du district de Mana et les minéralisations ?

Les travaux de PFE sur le gisement de Siou (Fig. 1.7) donnent quelques éléments de réponses concernant la source des fluides hydrothermaux (Dupuis, 2013). Ces résultats montrent que le cœur des pyrites est défini par un assemblage métallique à Au, Ag, Bi, Te, qui pourrait être interprété comme une signature magmatique. De plus, une zonation en As Ni, Co, et Se est observée avec un appauvrissement des concentrations en Au que l'on retrouve sous forme libre dans des microfractures tardives. Ces zonations à As, Ni, Co sont récurrentes dans la littérature (Large et al., 2007, 2009; Thomas et al., 2011) et elles sont imputable à une source de roches métasédimentaires (shales noirs) en profondeur d'où l'origine les fluides métamorphiques. Cette zonation a également été observée dans les pyrites des gisements de Wona, Yaho et Fofina (Augustin, 2011; Paulin-Bissonnette, 2012; Sinaré, 2013). La présence de CH_4 et C_2H_6 dans les inclusions fluides des filons de quartz de Siou (Gaboury, 2013) confirme aussi cette hypothèse. L'ensemble de ces résultats suggère qu'à l'échelle du district de Mana, deux signatures de fluides coexistent. Ces premières conclusions permettent de justifier ce sujet de doctorat qui implique une étude détaillée de la géochimie des roches encaissantes et des sulfures, pour une meilleure compréhension du ou des systèmes hydrothermaux en lien avec les épisodes de déformation. Afin de déterminer les liens génétiques entre les granitoïdes et les minéralisations aurifères et de définir un cadre géochronologique, des datations ont été faites sur des schistes à muscovite du gisement de Wona-Kona (Ar-Ar sur muscovite) et sur

les granitoïdes de bordure (U/Pb sur zircon). Ces datations ont été couplées avec les relations de recoupement des déformations. L'ensemble de ces données a permis de générer des guides d'exploration pertinents afin de cibler des secteurs ayant un potentiel aurifère.

En résumé, la problématique concernant le district de Mana est comparable à celle de tout autre district aurifère. On cherche dans un premier temps à déterminer la source de l'or à travers des études sectorielles par lithogéochimies sur les roches encaissantes, sur la composition des minéralisations et des fluides, de les contraindre dans un cadre temporel en lien avec les épisodes de déformation. En outre, l'étude des minéralisations vise à quantifier leurs âges respectifs, leur(s) origine(s) (magma, fluide et métal), la part de chacun et le rôle de la déformation. Ces questions s'inscrivent dans la problématique du modèle géodynamique pour ce terrain (ceinture et granitoïdes), en particulier il est nécessaire de cerner comment le district de Mana et sa minéralisation se rattachent à cette histoire.

1.3. OBJECTIFS

Ce projet avait pour objectif de déterminer les signatures géochimiques qui traduisent l'évolution d'un système hydrothermal, afin d'élaborer un modèle métallogénique et structural dans le but de proposer des guider d'exploration à l'échelle régionale.

Afin d'atteindre ce but, 5 objectifs ont été définis :

- Identifier la nature des roches encaissantes susceptibles d'être la source de l'or.

- Caractériser la chronologie relative des épisodes de déformation en lien avec les minéralisations.
- Déterminer la source des fluides hydrothermaux à travers l'étude des minéralisations.
- Déterminer le rôle génétique des granitoïdes afin d'expliquer leur rôle spatio-temporel avec les minéralisations.
- Formuler des guides d'exploration applicables aux gisements aurifères orogéniques.

1.4. MÉTHODOLOGIE

Dans cette section, l'approche méthodologique utilisée pour accomplir l'ensemble des objectifs fixés précédemment est détaillée (Tableau 1.3). Le détail des procédures analytiques est fourni dans les chapitres spécifiques suivants. La méthodologie proposée vise à déterminer les facteurs de contrôle des minéralisations, tels que la lithologie, la minéralogie, les relations entre les structures et la chronologie de mise en place et l'origine des fluides hydrothermaux. Les travaux nécessaires à l'aboutissement de ce projet sont divisés en deux parties : les travaux de terrain au Burkina Faso et les travaux de laboratoire à l'Université du Québec à Chicoutimi (UQAC).

1.4.1. TRAVAUX DE TERRAIN ET ÉCHANTILLONNAGE

Les travaux de terrain ont consisté en une cartographie régionale du district de Mana dans le but de déterminer le contexte géologique et structural afin d'identifier les différents faciès géologiques et les relations de chronologie relative. Une emphase particulière a été portée sur les diverses relations entre les éléments structuraux (schistosité, linéation, plissement, etc.) ainsi que sur la distribution des granitoïdes et leurs rôles avec les minéralisations aurifères. Très peu d'échantillons de roches fraîches ont été prélevés sur le terrain du fait de l'altération météoritique de surface. Cette approche a permis de produire une carte géologique de la partie sud du district de Mana et de définir la chronologie des épisodes de déformations régionales.

Les cartographies détaillées à l'échelle des dépôts (Fofina, Nyafé, Siou, Wona-Kona et Yaho) ont permis de caractériser et de mieux identifier la distribution des unités lithologiques, les styles de minéralisations et les éléments structuraux. Les carottes de forages ont été utilisées pour définir les relations de recoupement entre les roches encaissantes et les minéralisations ainsi que leur minéralogie. Ces derniers ont permis d'établir la chronologie relative des différents épisodes hydrothermaux à l'échelle des gisements et du district. La majorité des échantillons pour analyses géochimiques et pour la confection des lames-minces a été recueillie dans les forages carottés. Suivant le protocole de Semafo Inc., au moins un quart de carotte a été laissé comme témoin dans les boites.

1.4.2. TRAITEMENT ET PRÉPARATION DES ÉCHANTILLONS

Seuls les échantillons les moins altérés ont été utilisés pour la confection des lames minces et des analyses géochimiques. Deux lames minces ont été confectionnées pour chacun des échantillons (Labo Québec). Une lame de 30 µm pour les observations pétrographiques et une lame mince de 100 µm pour les analyses au LA-ICP-MS sur les sulfures à l'UQAC. Les analyses lithogéochimiques ont été envoyées à un laboratoire commercial (ALS CHEMEX à Vancouver). Les échantillons pour analyses isotopiques Sm-Nd et Rb-Sr ont été envoyés à l'Isotope Geochemistry and Geochronology Research Centre (IGGRC) de l'Université de Carleton d'Ottawa. Les datations U-Pb sur zircons ont été préparées chez IOS Géoservices à Chicoutimi et analysées à l'Université de Montpellier. Les datations Ar-Ar sur muscovite ont été analysées à l'Université de Melbourne en Australie.

1.4.3. ANALYSES PÉTROGRAPHIQUES ET MINÉRALOGIQUES

En premier lieu, l'étude pétrographique a été effectuée macroscopiquement lors de la cueillette des échantillons. Par la suite une étude des lames minces au microscope optique de l'UQAC a permis de déterminer la minéralogie, la texture, les altérations et les microstructures des différents échantillons. De plus, des plages minérales de sulfures (pyrite et arsénopyrite) ont été sélectionnées puis analysées au LA-ICP-MS afin de produire des cartes en éléments traces.

1.4.4. ANALYSES LITHOGÉOCHIMIQUES

Les analyses lithogéochimiques par Inductively Coupled Plasma-Mass Spectrometry (ICP-MS) et Atomic Emission Spectrometry (ICP-AES) ont permis d'obtenir les teneurs en éléments majeurs, traces et les éléments des terres rares. Plus de 300 échantillons provenant de l'ensemble du district de Mana ont été analysés incluant des unités basaltiques, des dykes de QFP et des plutons granitiques. Les résultats permettent de générer des diagrammes de discrimination binaires pour les roches volcano-plutoniques (exemple de $Na_2O + K_2O$ vs. SiO_2 - Cox et al. (1979)) et des diagrammes ternaires (Al_2O_3, MgO, Fe_2O_3+TiO_2 - Jensen (1976)) afin de discriminer le type de lithologie et le contexte tectonique (Ce/Nb vs. Th/Nb - Polat et al. (1999)). Des diagrammes multiéléments normalisés au manteau primitif (Sun et McDonough, 1989) permettent de comparer les spectres de terres rares avec les études précédentes (Augustin, 2011; Sinaré, 2013) et ceux de la littérature. Par exemple, la présence d'une signature de basalte tholéiitique de plateau océanique permet d'émettre l'hypothèse d'un pré-enrichissement en or favorable pour la source de l'or. Les diagrammes Zr/Nb sur Nb/Th de Condie (2003, 2005), permettront d'appuyer cette hypothèse et de discriminer la présence ou non d'un panache mantellique.

1.4.5. ANALYSES MINÉRALOGIQUES ET EN ÉLÉMENTS TRACES

Les analyses minéralogiques ont pour but de caractériser les zones minéralisées à travers l'étude des paragénèses minérales, des types de sulfures (texture) et les relations de

recoupement. Cette première étape a permis de sélectionner des familles de sulfures (pyrite et arsénopyrite) basées sur leur texture afin de faire des analyses quantitatives des éléments traces au LA-ICP-MS (Laser Ablation-Inductively Coupled Plasma-Mass Spectrometry) de l'UQAC. Des cartes semi-quantitatives de la distribution des éléments traces suivant le type de texture, ont permis de déterminer les sulfures primaires à secondaires (syn-minéralisation). Ces cartes ont été générées par le logiciel IOLITE.

Les travaux récents sur l'étude des cortèges métalliques des pyrites de gisements aurifères orogéniques (Large et al., 2007, 2009; Thomas et al., 2011) permettront une comparaison avec nos résultats. En outre, cette étude de pointe permettra de répondre à plusieurs questions sur : 1) la signature des fluides hydrothermaux à travers l'étude des cortèges métalliques des sulfures, 2) l'existence des relations génétiques entre les gisements à travers une étude comparative des signatures de sulfures, 3) l'existence d'un ou plusieurs systèmes hydrothermaux et 4) la chronologie relative des différentes pulses aurifères sur une base comparative.

1.4.6. DATATIONS U/Pb ET Ar/Ar

Différentes méthodes géochronologiques ont été utilisées dans le cadre de ce projet. La géochronologie isotopique U/Pb sur zircons a été conduite sur les granites de Wona-Kona, Siou et Kokoï afin d'obtenir les âges de cristallisation. Pour chaque échantillon, 5 kg de phase granitique ont été traités par IOS Géoservices afin d'extraire les zircons. Des lames

minces ont également été produites ainsi que des analyses au microscope électronique à balayage (MEB), permettant l'acquisition d'images en mode électrons rétrodiffusés (BSE, Backscattered Electron Images) afin de déterminer les zonations des zircons. Les analyses au LA-ICP-MS sur zircons ont été faites à l'Université de Montpellier suivant le protocole de Bruguier et al. (2001). Les dates permettent de caler la chronologie relative de la ceinture de Houndé en lien avec les différents épisodes de déformations et de minéralisations.

La géochronologie isotopique Ar-Ar sur muscovite a été utilisée sur les schistes à muscovite du gisement de Wona-Kona afin de dater l'épisode minéralisateur. Les échantillons provenant des carottes de forages ont été envoyés à l'Université de Melbourne et analysés par un spectromètre de masse de type ARGUSVI selon la méthode de Phillips et al. (2007). Les dates obtenues donnent l'âge des altérations hydrothermales associées à l'or et peuvent être confrontées avec celles des granitoïdes de Mana.

1.4.7. ANALYSES DES ISOTOPES RADIOGÉNIQUES Sm-Nd ET Rb-Sr

Les analyses isotopiques ont été effectuées sur 8 échantillons de basaltes provenant de carottes de forages à l'échelle du district et viennent compléter les analyses lithogéochimiques. Les analyses ont été confiées au l'IGGRC de l'Université de Carleton afin de déterminer les ratios $^{87}Sr/^{86}Sr$, $^{87}Rb/^{86}Sr$, $^{147}Sm/^{144}Nd$, $^{143}Nd/^{144}Nd$ qui ont été recalculés à 2,25 Ga pour déterminer le $\varepsilon Nd_{(2.25\ Ga)}$ et $^{87}Sr/^{86}Sr_{(2.25\ Ga)}$. Les analyses ont été

faites par un spectromètre de masse de type TIMS (Thermal Ionization Mass Spectrometer) suivant la méthode de Richard et al. (1976). Les résultats permettront d'évaluer la contamination crustale et l'évolution mantellique du système conduisant à la mise en place des basaltes afin de déterminer leur potentiel primaire pour la source de l'or.

1.5. FORMAT DE LA THÈSE

La présente thèse de doctorat en Sciences de la Terre et de l'Atmosphère est présentée sous la forme d'un recueil de trois manuscrits d'articles scientifiques et s'organise en six chapitres. Le premier chapitre est une introduction qui place cette étude dans un contexte scientifique général. Les trois chapitres suivants correspondent à des articles rédigés en anglais, soumis et publiés dans des revues spécialisées internationales dont le premier auteur est l'auteur de la thèse. Le premier article (chapitre 2) a été publié dans le journal « *Journal of African Earth Sciences* » en mai 2017 et a pour titre : « *Paleoproterozoic plume-related basaltic rocks in the Mana gold district in western Burkina Faso, West Africa: Implications for exploration and the source of gold in orogenic deposits* ». Cet article traite de la mise en place des basaltes du district de Mana qui représentent la base de la stratigraphie et plus particulièrement leur rôle possible comme source d'or des gisements d'or orogéniques de Mana. Un diagramme binaire a été développé afin de guider les travaux d'exploration. Dans cet article, le premier auteur a fait les observations sur le terrain et est responsable de l'analyse des résultats et de la rédaction de l'article. Les

analyses ICP-MS/AES et isotopiques ont été réalisées par des laboratoires indépendants. Damien Gaboury a contribué aux discussions scientifiques, à la rédaction de certaines sections de la discussion et aux corrections.

Les deux articles suivants (chapitres 3 et 4) ont eu pour objectifs de définir l'évolution structurale et hydrothermale du district de Mana. Le deuxième article (chapitre 3) intitulé « *Structural and gold mineralizing evolution of the world-class orogenic Mana District, Burkina Faso: multiple mineralizing events over 150 million years* », a été publié en août 2017 dans la revue « *Ore Geology Reviews* ». Cet article traite de l'évolution structurale du district de Mana en lien avec la mise en place des minéralisations d'or orogéniques observées dans les différents gisements. Dans cet article, le premier auteur a fait les observations sur le terrain et est responsable de l'analyse des résultats et de la rédaction de l'article. Les analyses ICP-MS/AES et de datation isotopique ont été réalisées par des laboratoires indépendants. Damien Gaboury a contribué aux discussions scientifiques, à la rédaction et aux corrections. Michel Crevier a contribué au processus de discussion et de corrections.

Le troisième article intitulé « *Multi-stage and multi-sourced fluid and gold for the formation of orogenic gold deposits in the World-Class Mana district - Burkina Faso - reveled by LA-ICP-MS study of pyrites and arsenopyrites* », a été soumis en septembre 2017 dans la revue « *Economic Geology* ». Cet article visait à déchiffrer l'évolution hydrothermale du/ou des système(s) minéralisateur(s) à travers l'étude des sulfures, principalement la pyrite et l'arsénopyrite et de déterminer les sources de l'or. Dans cet

article, le premier auteur a fait les observations macro et microscopiques, a réalisé en partie les analyses au LA-ICP-MS et est responsable de l'analyse et de l'interprétation des résultats et de la rédaction.

Enfin les chapitres 5 et 6 sont respectivement une discussion et conclusion de cette étude, ainsi que les retombées académiques et économiques. Chaque manuscrit a été soumis accompagné de matériel électronique supplémentaire. Ces données sont présentées dans les annexes.

1.6. RÉFÉRENCES

Abouchami, W., Boher. M., Michard, A., Albarède, F., 1990. A major 2.1 Ga event of mafic magmatism in Western Africa: An early stage of crustal accretion. Journal of Geophysical Research 95, 17605-17629.

Augustin, J., 2011. Facteurs de contrôle et processus métallogéniques des minéralisations aurifères du gisement de Wona, mine Mana, Burkina Faso. Mémoire de maîtrise en sciences de la terre. Université du Québec à Chicoutimi, p. 1-220.

Augustin, J., Gaboury, D., Crevier, M., 2016. The world-class Wona-Kona gold deposit, Burkina Faso. Ore Geology Reviews 78, 667-672.

Baratoux, L., Metelka, V., Naba, S., Jessell, M.W., Grégoire, M., Ganne, J., 2011. Juvenile Paleoproterozoic crust evolution during the Eburnean orogeny (~2.2-2.0 Ga), western Burkina Faso. Precambrian Research 191, 18-45.

Beaudoin, G., Pitre, D., 2005. Stable isotope geochemistry of the Archean Val-d'Or (Canada) orogenic gold vein field. Mineralium Deposita 40, 59-75.

Béland, J., 2009. Caractérisation gîtologique du gisement aurifère Nyafé, Burkina Faso. Projet de fin d'études. Université du Québec à Chicoutimi, p. 1-21.

Bertrand-Sarfati, J., Moussine-Pouchkine, A., Affaton, P., Trompette, R., Bellion, Y. 1990. Cover sequences of the West African craton. In: Dallmeyer, R.D., Lecorche, J.P. (Eds.), The West African Orogens and Circum-Atlantic Correlatives. Springer-Verlag, p. 65-82.

Bierlein, F.P., McKnight, S., 2005. Possible intrusion-related gold systems in the western Lachlan Orogen, southeast Australia. Economic Geology 100, 385-398.

Bierlein, F.P., Pisarevsky, S., 2008. Plume-related oceanic plateaus as a potential source of gold mineralization. Economic Geology 103, 425-430.

Bierlein, F.P., Craw, D., Petrogenetic character and provenance of metabasalts in the aspiring and Torless Terranes, South Island, New Zealand: Implications for the gold endowment of the Otago Schist? Chemical Geology 260, 301-315.

Bierlein, F.P., Groves, D.I., Cawood, P.A., 2009. Metallogeny of accretionary orogens-the connection between lithospheric processes and endowment. Ore Geology Reviews 36, 282-292.

Bigot, L., Jébrak, M., 2015. Gold mineralization at the syenite-hosted Beattie gold deposit, Duparquet, Neoarchean Abitibi Belt, Canada. Economic Geology 110, 315-335.

Boher, M., Abouchami, W., Michard, A., Albarède, F., Arndt, N., 1992. Crustal growth in West Africa at 2.1 Ga. Journal of Geophysical Research 97, 345-369.

Boiron, M.C., Cathelineau M., Banks D.A., Fourcade S., Vallance J., 2003. Mixing of metamorphic and surficial fluids during the uplift of the Hercynian upper crust: Consequences for gold deposition. Chemical Geology 194, 119-141.

Bossière, G., Bonkoungou, I., Peucat, J.J., Pupin, J.P., 1996. Origin and age of Paleoproterozoic conglomerates and sandstones of the Tarkwaian Group in Burkina Faso, West Africa. Precambrian Research 80, 153-172.

Bronner, G., Roussel, J., Trompette, R., 1980. Genesis and geodynamic evolution of the Taoudeni cratonic basin (Upper Precambrian and Paleozoic), Western Africa. Geodynamics 1, 81-87.

Bruguier, O., Télouk, P., Cocherie, A., Fouillac, A. M., Albarède, F., 2001. Evaluation of Pb-Pb and U-Pb Laser Ablation ICP-MS Zircon Dating using Matrix-Matched Calibration Samples with a Frequency Quadrupled (266 nm) Nd-YAG Laser. Geostandards and Geoanalytical Research 25, 361-373.

Castaing, C., Billa, M., Milési, J.P., Thiéblemont, D., Le Métour, J., Egal, E., Donzeau, M., Guerrot, C., Cocherie, A., Chèvremont, P., Tegyey, M., Itard, Y., Zida, B., Ouedraogo, I., Koté, S., Kaboré, B.E., Ouedraogo, C., Ki, J.C., Zunino, C., 2003. Notice explicative de la carte géologique et minière du Burkina Faso à 1/1 000 000. BRGM BUMIGEB, p. 1-147.

Colvine, A.C., 1989. An empirical model for the formation of Archean gold deposits-products of final cratonization of the Superior province, Canada. Economic Geology Monograph 6, 37–53.

Condie, K.C., 2003. Incompatible element ratios in oceanic basalts and komatiites: Tracking deep mantle sources and continental growth rates with time. Geochemistry, Geophysics, Geosystems 4, 1-28.

Condie, K.C., 2005. High field strength element ratios in Archean basalts: A window to evolving sources of mantle plumes? Lithos 79. 491-504.

Cox, K.G., Bell, J.D., Pankhurst, R.J., 1979. The interpretation of igneous rocks. Allen & Unwin, p. 1-464.

Craw, D., 2002. Geochemistry of late metamorphic hydrothermal alteration and graphitisation of host rock, Macraes gold mine, Otago Schist, New Zealand. Chemical Geology 191, 257-275.

Doumbia, S., Pouclet, A., Kouemelan, A., Peucat, J.J., Vidal, M., Delor, C., 1998. Petrogenesis of juvenile-type Birimian (Paleoproterozoic) granitoids in central Côte d'Ivoire, West Africa: Geochemistry and geochronology. Precambrian Research 87, 33-63.

Dupuis, J.F., 2013. Caractérisation de la distribution des éléments dans les grains de pyrite, projet Siou, Burkina Faso. Projet de fin d'études. Université du Québec à Chicoutimi, p. 1-35.

Feybesse, J.L., Billa, M., Guerrot, C., Duguey, E., Lescuyer, J.L., Milési, J.P., Bouchot, V., 2006. The paleoproterozoic Ghanaian province: Geodynamic model and ore controls, including regional stress modeling. Precambrian Research 149, 149-196.

Gaboury, D., Carrier, A., Crevier, M., Pelletier, C., 2001. Predictive distribution of fault-fill and extensional veins: Example from Sigma gold mine, Abitibi Subprovince, Canada. Economic Geology 96, 1397-1405.

Gaboury, D., 2013. Does gold in orogenic deposits come from pyrite in deeply buried carbon-rich sediments?: Insight from volatiles in fluid inclusions. Geology 42, 1207-1210.

Gasquet, D., Barbey, P., Adou, M., Paquette, J.L., 2003. Structure, Sr-Nd isotope geochemistry and zircon U-Pb geochronology of the granitoids of the Dabakala area (Côte d'Ivoire): Evidence for a 2.3 Ga crustal growth event in the Paleoproterozoic of West Africa? Precambrian Research 127, 329-354.

Gilbert, M., 2014. Signatures en éléments traces des séricites provenant des gisements du - district aurifère de Mana, Burkina Faso. Projet de fin d'études. Université du Québec à Chicoutimi, p. 1-51.

Goldfarb, R.J., Groves, D.I., Gardoll, S., 2001. Orogenic gold and geologic time: A global synthesis. Ore Geology Reviews 18, 1-75.

Goldfarb, R.J., Baker, T., Dubé, B., Groves, D.I., Hart, C.J.R., Gosselin, P., 2005. Distribution, character, and genesis of gold deposits in metamorphic terranes. Economic Geology One Hundredth Anniversary Volume 1905-2005. In Hedenquist, J. W., Thompson, J. F. H., Goldfarb, R. J., and Richards, J. P., eds., Economic Geology. 100th Anniversary Volume 1905-2005: Littleton, Colorado, Society of Economic Geologists, 407-450.

Goldfarb, R.J., André-Mayer, A.S., Jowitt, S., Mudd, G.M., 2017. West Africa: The world's premier Paleoproterozoic gold province. Economic Geology 112, 123-143.

Groves, D.I., Goldfarb, R.J., Gebre-Marriam, M., Hagemann, S.G., Robert, F., 1998. Orogenic gold deposits: A proposed classification in the context of their crustal distribution and relationship to other deposit types. Ore Geology Reviews 13, 7-27.

Groves, D.I., Goldfarb, R.J., Hart, C.J.R., 2003. Gold deposits in metamorphic belts: Overview of current understanding, outstanding problems, future research, and exploration significance. Economic Geology 98, 1-29.

Groves, D.I., Santosh, M., 2015. Province-scale commonalities of some world-class gold deposits: Implications for mineral exploration. Geoscience Frontiers 6, 389-399.

Groves, D.I., Goldfarb, R.J., Santosh, M., 2016. The conjunction of factors that lead the formation of giant gold provinces and deposits in non-arc settings. Geoscience Frontiers 7, 303-314.

Fougerouse, D., Micklethwaite, S., Ulrich, S., Miller, J., Godel, B., Adams, D.T., McCuaig, T.C., 2017. Evidence for two stages of mineralization in West Africa largest gold deposit: Obuasi, Ghana. Economic Geology 112, 3-22.

Fyfe, W.S., Price, N.J., Thompson A.B., 1978. Fluids in the earth's crust. Their significance in metamorphic, tectonic and chemical transport processes. Developments in geochemistry 1. Amsterdam, Elsevier, p. 383

Hart, C.J.R., McCoy, D., Goldfarb, R.J., Smith, M., Roberts, P., Hulstein, R., Bakke, A.A., Bundtzen, T.K., 2002. Geology, exploration and discovery in the Tintina gold province, Alaska and Yukon. Society of Economic Geologists Special Publication 9, 241-274.

Hawkesworth C., Scherstén A., 2007. Mantle plumes and geochemistry. Chemical Geology 241, 319-331.

Hein, K.A.A., 2016. The Bagassi gold deposits on the eastern margin of the Houndé greenstone belt, Burkina Faso. Ore Geology Reviews.

Helt, K.M., Williams-Jones, A.E., Clark, J.R., Wing, B.A., Wares, R.P., 2014. Constraints on the genesis of the Archean oxidized, intrusion-related Canadian Malartic gold deposit, Québec, Canada. Economic Geology 109, 713-735.

Hirdes, W., Davis, D.W., Lüdtke, G., Konan, G., 1996. Two generations of Birimian (Paleoproterozoic) volcanic belts in northeastern Côte d'Ivoire (West Africa): Consequences for the "Birimian controversy". Precambrian Research 80, 173-191.

Hu, S.Y., Evans, K., Fisher, L., Rempel, K., Craw, D., Evans, N.J., Cumberland, S., Robert, A., Grice, K., 2016. Associations between sulfides, carbonaceous material, gold and other trace elements in polyframboids: Implications for the source of orogenic gold deposits, Otago Schist, New Zealand. Geochimica et Cosmochimica Acta 180, 197-213.

Jensen, L.S., 1976. A new cation plot for classifying sub-alkaline volcanic rocks. In: Ontario Division Mines Miscellaneous, p. 1-66.

Jessell, M., Santoul, J., Baratoux, L., Youbi, N., Ernst, R.E., Metelka, V., Miller, J., Perrouty, S., 2015. An updated map of West African mafic dykes. Journal of African Earth Sciences 112, 440-450.

Kerrich, R., Fyfe, W.S., 1981. The gold-carbonate association: Source of CO_2, and CO_2 fixation reactions in Archaean lode deposits: Chemical Geology 33, 265-294.

Kerrich, R., Wyman, D.A., 1990. Geodynamic setting of mesothermal gold deposits: An association with accretionary tectonic regimes. Geology 18, 882-885.

Kerrich, R., 1999. Nature's gold factory. Science 284, 2101-2102.

Koffi, Y.H.., Wenmenga, U., Djro, S.G., 2016. Tarkwaian deposits of the Birimian belt of Houndé: Petrological, structural and geochemical study (Burkina-Faso, West Africa). International Journal of Geosciences 7, 685-700.

Lang, J.R., Baker, T., 2001. Intrusion-related gold systems: The present level of understanding. Mineralium Deposita 36, 477-489.

Large, R.R., Maslennikov, V., Robert, F., Danyushevsky, L.V., Chang, Z.S., 2007. Multistage sedimentary and metamorphic origin of pyrite and gold in the giant Sukhoi Log deposit, Lena Gold Province, Russia. Economic Geology 102, 1232-1267.

Large, R.R., Danyushevsky, L., Hollit, C., Maslennikov, V., Meffre, S., Gilbert, S., Bull, S., Scott, R., Emsbo, P., Thomas, H., 2009. Gold and trace element zonation in pyrite using a laser imaging technique: Implications for the timing of gold in orogenic and Carlin-style sediment-hosted deposits. Economic Geology 104, 635-668.

Large, R., Thomas, H., Craw, D., Henne, A., Henderson, S., 2012. Diagenetic pyrite as a source for metals in orogenic gold deposits, Otago Schist, New Zealand. New Zealand Journal of Geology and Geophysics 55, 137-149.

Lawrence, D.M., Treloar, P.J., Rankin, A.H., Boyce, A., Harbidge, P., 2013. A fluid inclusion and stable isotope study at the Loulo mining district, Mali, West Africa: Implications for multifluids sources in the generation of orogenic gold deposits. Economic Geology 108, 229-257.

Le Métour, J., Chèvremont, P., Donzeau, M.E., Thiéblemont, E., Tegey, D., Guerrot, M.C.M., Itard, B., Castaing, Y., Delpont, C., Ki, G., Zunino, J.C.C., 2003. Notice explicative de la carte géologique du Burkina Faso au 1/200,000. Feuille Houndé, p. 1-82.

Lüdtke, G., Hirdes, W., Konan, G., Koné, Y., N'da, D., Traoré, Y., Zamblé, Z., 1999. Géologie de la région Haute Comoé Sud-feuilles Dabakala (2b, d et 4b, d). Direction de la Géologie Abidjan Bulletin, p. 1-176.

Mair, J.L., Farmer, G.L., Groves, D.I., Hart, C.J., Goldfarb, R.J., 2011. Petrogenesis of postcollisional magmatism at Scheelite Dome, Yukon, Canada: Evidence for a lithospheric mantle source for magmas associated with intrusion-related gold systems. Economic Geology 106, 451-480.

Mason, R., and Melnik, N., 1986. The anatomy of an Archean gold system-the McIntyre-Hollinger complex at Timmins, Canada. In Gold 86, 45-55.

McFarlane, C.R.M., Mavrogenes, J., Lentz, D., King, K., Allibone, A., Holcombe, R., 2011. Geology and intrusion-related affinity of the Morila gold mine, southeast Mali. Economic Geology 106, 727-750.

Meffre, S., Large, R.R., Steadman, J.A., Gregory, D.D., Stepanov, A.S., Kamenetsky, V.S., Ehrig, K., Scott, R.J., 2016. Multi-stage enrichment processes for large gold-bearing ore deposit. Ore Geology Reviews 76, 268-279.

Mercier, M.A., 2013. Caractérisation de la distribution des éléments traces dans les sulfures de la zone Yaho, Burkina Faso. Projet de fin d'études. Université du Québec à Chicoutimi, p. 1-54.

Mériaud, N., Jébrak, M., 2017. From intrusion-related to orogenic mineralization: The Wasamac deposit, Abitibi Greestone Belt, Canada. Ore Geology Reviews 84, 289-308.

Metelka, V., Baratoux, L., Naba, S., Jessell, M.W., 2011. A geophysically constrained litho-structural analysis of the Eburnean greenstone belts and associated granitoid domains, Burkina Faso, West Africa. Precambrian Research 190, 48-69.

Milési, J.P., Feybesse, J.L., Pinna, P., Deschamps, Y., Kampunzu, H., Muhongo, S., Lescuyer, J.L., Le Goff, E., Delor, C., Billa, M., Ralay, F., Heinry, C., 2004. Geological map of Africa 1/10,000,000, SIGAfrique project. In: 20th Conference of African Geology, BRGM, Orléans, France, 2-7 June, http://www.sigafrique.net (last accessed 14/12/2010).

Nikiéma, S., Benkhelil, J., Corsini, M., Bourges, F., Abdoulaye, D., Maurin, J.-C., 1993. Tectonique transcurrente Éburnéenne au sein du Craton Ouest-Africain, exemple du sillon de Djibo (Burkina Faso). Comptes Rendus de l'Académie des Sciences 316, 661-668.

Palin, J.M., Xu, Y., 2000. Gilt by association? Origins of pyritic gold ores in the Victory mesothermal gold deposit, Western Australia. Economic Geology 95, 1627-1634.

Paulin-Bissonnette, A., 2012. Caractérisation de l'habitus de l'or dans les sulfures provenant des zones de Fobiri et Fofina au Burkina Faso. Projet de fin d'études. Université du Québec à Chicoutimi, p. 1-49.

Perrouty, S., Lindsay, M.D., Jessell, M.W., Aillères, L., Martin, R., Bourassa, Y., 2014. 3D modeling of the Ashanti belt, southwest Ghana: Evidence for a litho-stratigraphic control on gold occurrences within the Birimian Sefwi Group. Ore Geology Reviews 63, 252-264.

Perrouty, S., Gaillard, N., Piette-Lauzière, N., Mir, R., Bardoux, M., Olivo, G.R., Linnen, R.L., Bérubé, C.L., Lypaczewski, P., Guilmette, C., Feltrin, L., Morris. W.A., 2017. Structural setting for Canadian Malartic style of gold mineralization in the Pontiac Subprovince, south of the Cadillac Larder Lake Deformation Zone, Québec, Canada. Ore Geology Reviews 84, 185-201.

Petrie, B.S., Craw, D., 2005. Lithological controls on structural evolution of mineralized schist, Macraes gold mine, Otago, New Zealand. New Zealand Journal of Geology and Geophysics 48, 435-446.

Phillips, G.N., Powell, R., 2009. Formation of gold deposits: Review and evaluation of the continuum model. Earth-Science Reviews 94, 1-21.

Phillips, G.N., Powell, R., 2010. Formation of gold deposits: A metamorphic devolatization model. Journal of Metamorphic Geology 28, 689-718.

Pitcairn, I.K., Teagle, D.A.H., Craw, D., Olivo, G.R., Kerrich, R., Brewer, T.S., 2006. Sources of metals and fluids in orogenic gold deposits: Insight from the Otago and Alpine Schists, New Zealand. Economic Geology 101, 1525-1546.

Pitcairn, I.K., Olivo, G.R., Teagle, D.A.H., Craw, D., 2010. Sulfide evolution during prograde metamorphism of the Otago and Alpine Schists, New Zealand. Canadian Mineralogist 48, 1267-1296.

Pitcairn I.K., Craw, D., Teagle, D.A.H., 2014. The gold conveyor belt: Large-scale gold mobility in an active orogeny. Ore Geology Reviews 62, 129-142.

Pitcairn, I.K., Craw, D., Teagle, D.A.H., 2015. Metabasalts as sources of metals in orogenic gold deposits. Mineralium Deposita 50, 373-390.

Polat, A., Kerrich, R., Wyman, D.A., 1999. Geochemical diversity in oceanic komatiites and basalts from the late Archean Wawa greenstone belts, Superior Province, Canada: Trace element and Nd isotope evidence for a heterogeneous mantle. Precambrian Research 94, 139-173.

Rauchenstein-Martinek, K., Wagner, T., Wälle, M., Heinrich, C.A., 2014. Gold concentrations in metamorphic fluids: A LA-ICPMS study of fluid inclusions from the Alpine orogenic belt. Chemical Geology 385, 70-83.

Richard, P., Shimizu, N., Allègre, C.J., 1976. 143Nd/146Nd, a natural tracer: An application to oceanic basalts. Earth and Planetary Science letters 31, 269-278.

Richards, J.P., 2009. Postsubduction porphyry Cu-Au and epithermal Au deposits: Products of remelting of subduction-modified lithosphere. Geology 37, 247-250.

Robertson, M., Peters, L., 2016. West African Goldfields. Episodes 39, 155-176.

Salier, B.P., Groves, D.I., McNaughton, N.J., Fletcher, I.R., 2004. The world-class Wallaby gold deposit, Laverton, Western Australia: An orogenic-style overprint on a magmatic-hydrothermal magnetite-calcite alteration pipe? Mineralium Deposita 39, 473-494.

Sillitoe, R.H., Thompson, J.F., 1998. Intrusion-related vein gold deposits: Types, tectono-magmatic settings and difficulties of distinction from orogenic gold deposits. Resource Geology 48, 237-250.

Sinaré, M., 2013. Métallogénie du gisement aurifère de Yaho, ceinture birimienne de Houndé, Burkina Faso. Mémoire de maîtrise en sciences de la terre. Université du Québec à Chicoutimi, p. 1-266.

Spooner, E.T.C., 1991. The magmatic model for the origin of Archean Au-quartz vein ore systems: An Assessment of the evidence. Brazil Gold 91, 313-318.

Sun, S.S., McDonough, W.F., 1989. Chemical and isotopic systematics of oceanic basalts: Implications for mantle composition and processes. Geological Society, Special Publication, p. 313-345.

Thomas, H.V., Large, R.R., Bull, S.W., Maslennikov, V., Berry, R.F., Fraser, R., Froud, S., Moye, R., 2011. Pyrite and pyrrhotite textures and composition in sediments, laminated quartz veins, and reef at Bendigo golf mine, Australia: Insights for ore genesis. Economic Geologists 106, 1-31.

Tomkins, A.G., 2010. Window of metamorphic sulfur liberation in the crust: Implications for gold deposits genesis. Geochimica et Cosmochimica Acta 74, 3246-3259.

Tomkins, A.G., 2013a. On the source of orogenic gold. Geology 41, 1255-1256.

Tomkins, A.G., 2013b. A biochemical influence on the secular distribution of orogenic gold. Economic Geology 108, 193-197.

Vielreicher, N.M., Ridley, J.R., Groves, D.I., 2002. Marymia: An Archean, amphibolite facies-hosted, orogenic lode-gold deposit overprinted by Palaeoproterozoic orogenesis and base metal mineralization, Western Australia. Mineralium Deposita 37, 737-764.

Velásquez, G., Béziat, D., Salvi, S., Tosiani, T., Debat, P., 2011. First occurrence of Paleoproterozoic oceanic plateau in the Guiana Shield: The gold-bearing El Callao formation, Venezuela. Precambrian Research 186, 181-192.

Velásquez, G., Béziat, D., Salvi, S., Siebenaller, L., Borisova, A.Y., Porkrovski, G.S., De Parseval, P., 2014. Formation and deformation of pyrite and implications for gold mineralization in the El Callao district, Venezuela. Economic Geology 109, 457-486.

Webber, A.P., Roberts, S., Taylor, R.N., Pitcairn, I.K., 2013. Golden plumes: Substantial golf enrichment of oceanic crust during ridge-plume interaction. Geology 41, 87-90.

Wilson, C.J.L., Schaubs, P.M., Leader, L.D., 2013. Mineral precipitation in the quartz reefs of the Bendigo gold deposit, Victoria, Australia. Economic Geology 108, 259-278.

Witt, W.K., Vanderhor, F., 1998. Diversity within a unified model for Archean gold mineralization in the Yilgarn Craton of Western Australia: An overview of the late-orogenic, structurally-controlled gold deposits. Ore Geology Reviews 13, 26-64.

Xue, Y., Campbell, I., Ireland, T.R., Holden, P., Armstrong, R., 2013. No mass-independent sulfur isotope fractionation in auriferous fluids supports a magmatic origin for Archean gold deposits. Geology 41, 791-794.

Xue, Y., Campbell, I., 2015. The mineralogy of the Bellerophon-Nelson telluride-bearing gold deposit, St-Ives camp, Yilgarn Craton, western Australia. The Canadian Mineralogist, canmin-4352.

Yudovskaya, M.A., Distler, V.V., Prokofiev, V.Y., Akinfiev, N., 2016. Gold mineralisation and orogenic metamorphism in the Lena province of Siberia as assessed from Chertovo Koryto and Sukhoi Log deposits. Geoscience Frontiers 7, 453-481.

Zang, J., Deng, J., Chen, H.Y., Yang, L.Q., Cooke, D., Danyushevsky, L., Gong, Q.J., 2014. LA-ICP-MS trace element analysis of pyrite from the Chang'an gold deposit, Sanjiang region, China: Implication for ore-forming process. Gondwana Research 26, 557-575.

FIGURES DU CHAPITRE 1

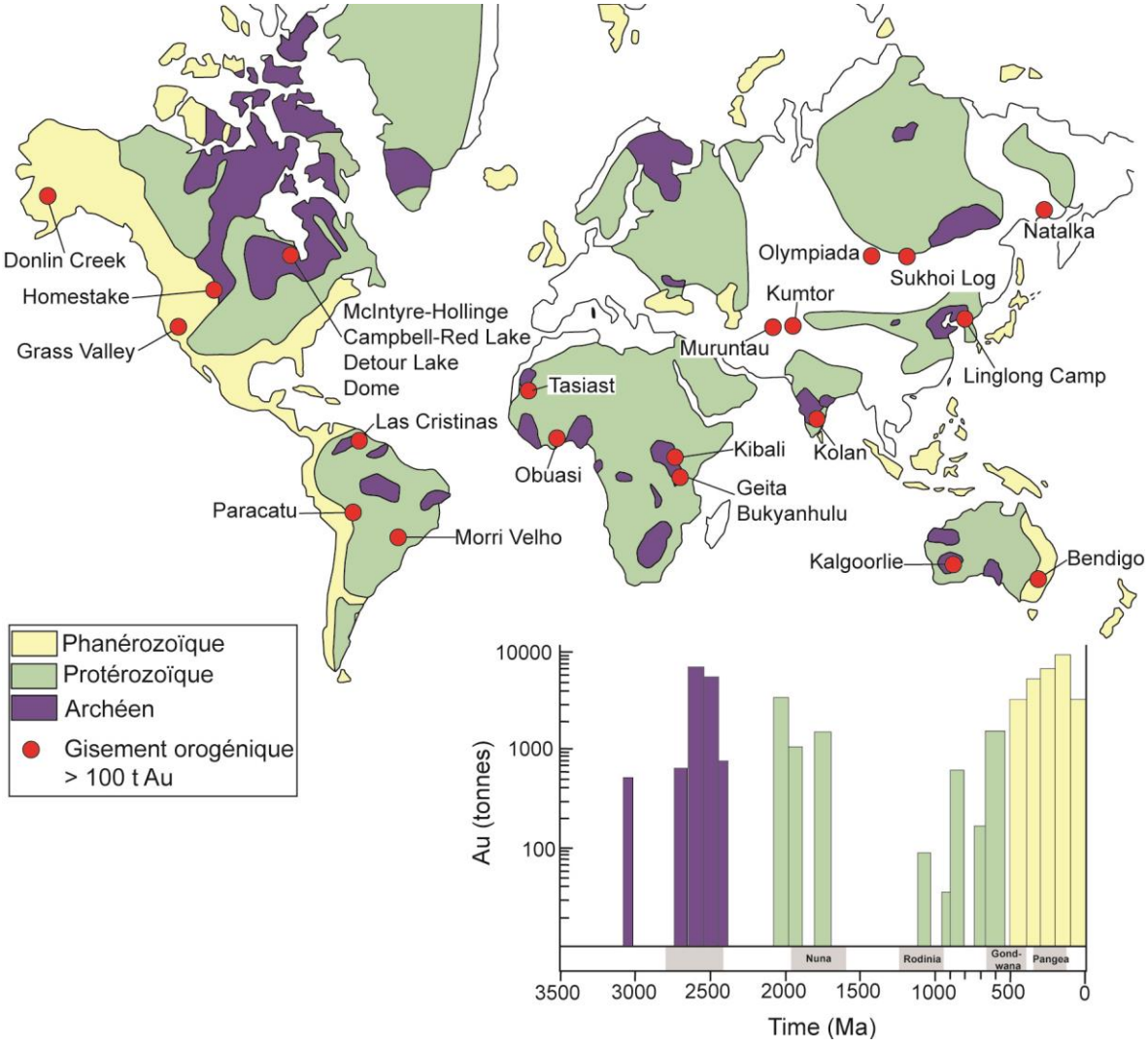

Figure 1.1 Distribution mondiale des terrains archéen, protérozoïque et phanérozoïque avec la distribution des 24 plus gros gisements ou district aurifères orogéniques, modifiées de Groves et al. (2016) et Tomkins (2013b).

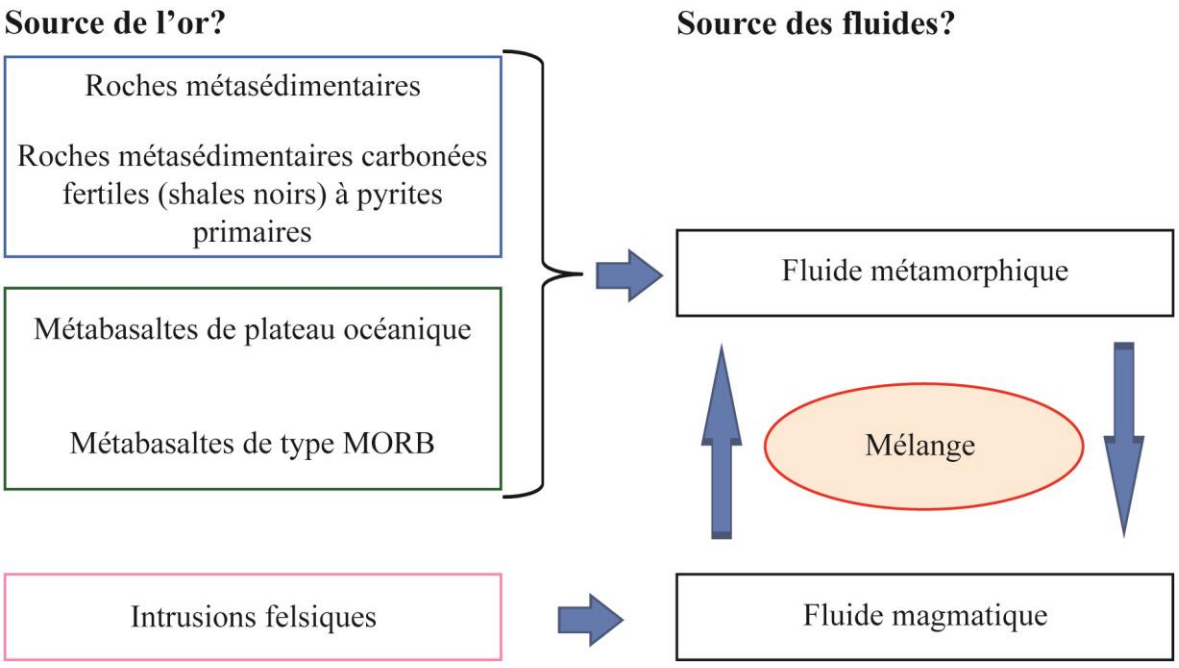

Figure 1.2 Problématique reliée à l'origine de la source de l'or et des fluides hydrothermaux conduisant à la formation des gisements aurifères orogéniques.

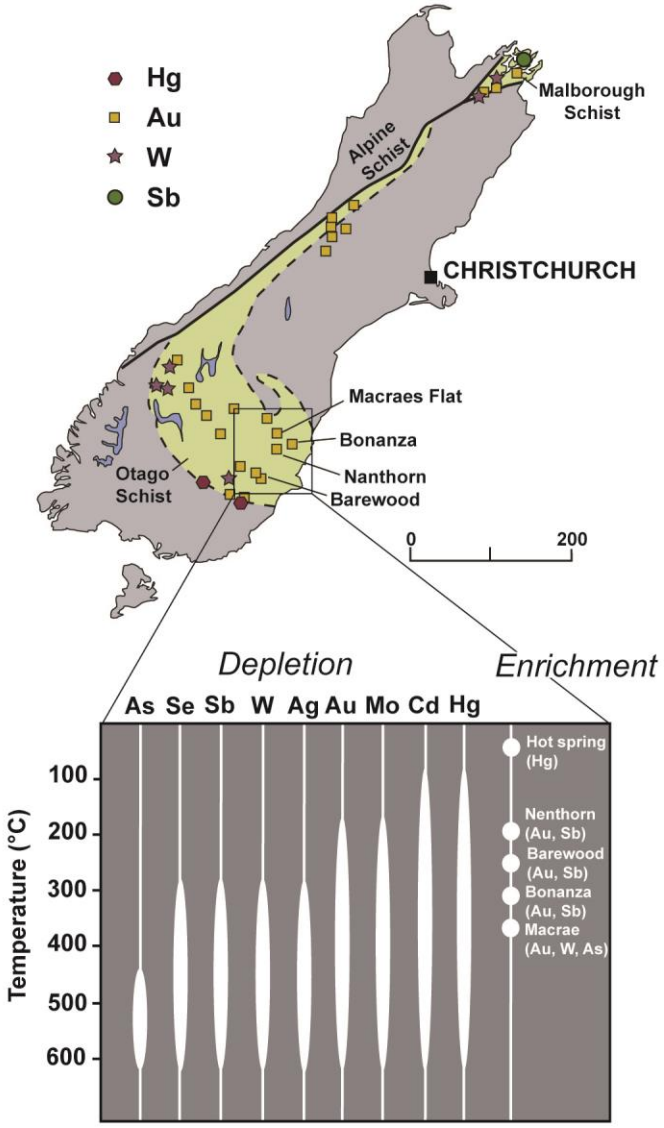

Figure 1.3 Distribution des gisements aurifères orogéniques dans la ceinture de schiste de l'île du sud de la Nouvelle Zélande et bilan métallique des Schistes d'Otago, d'après Pitcairn et al. (2006).

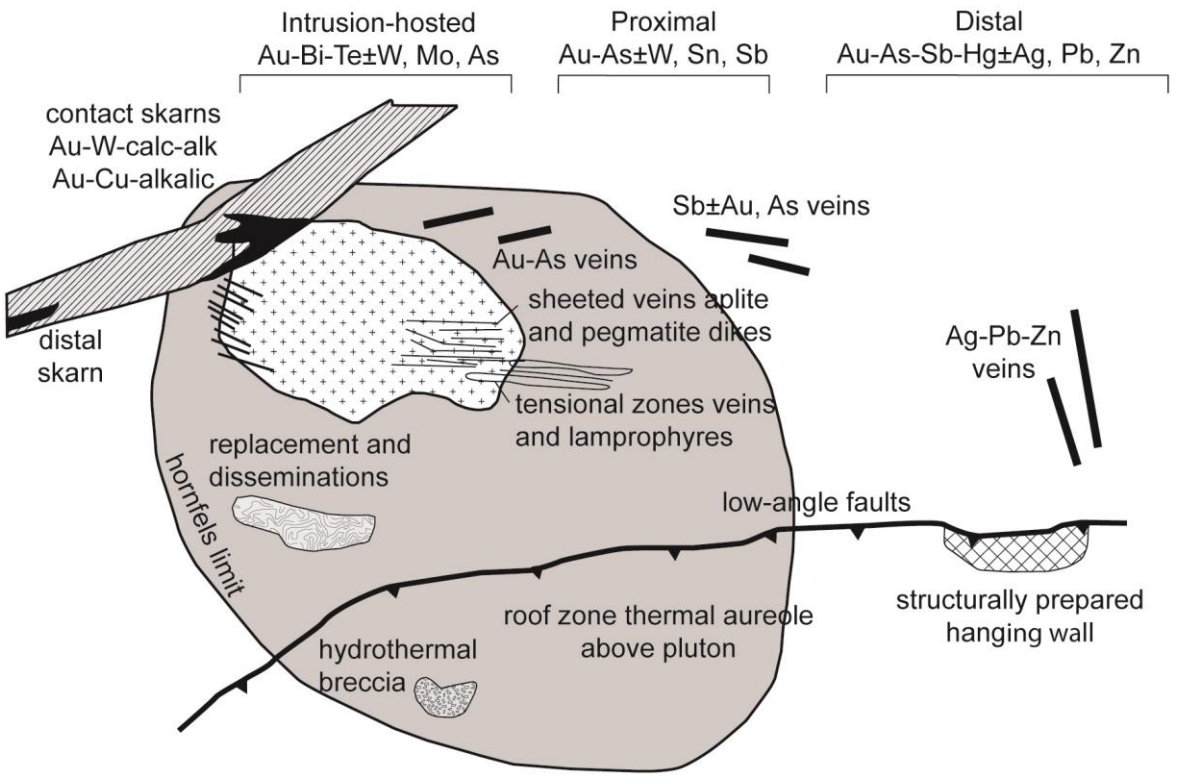

Figure 1.4 Modèle « Intrusion-Related Gold System (IRGS) » selon Hart et al. (2002) avec la zonalité des cortèges métalliques.

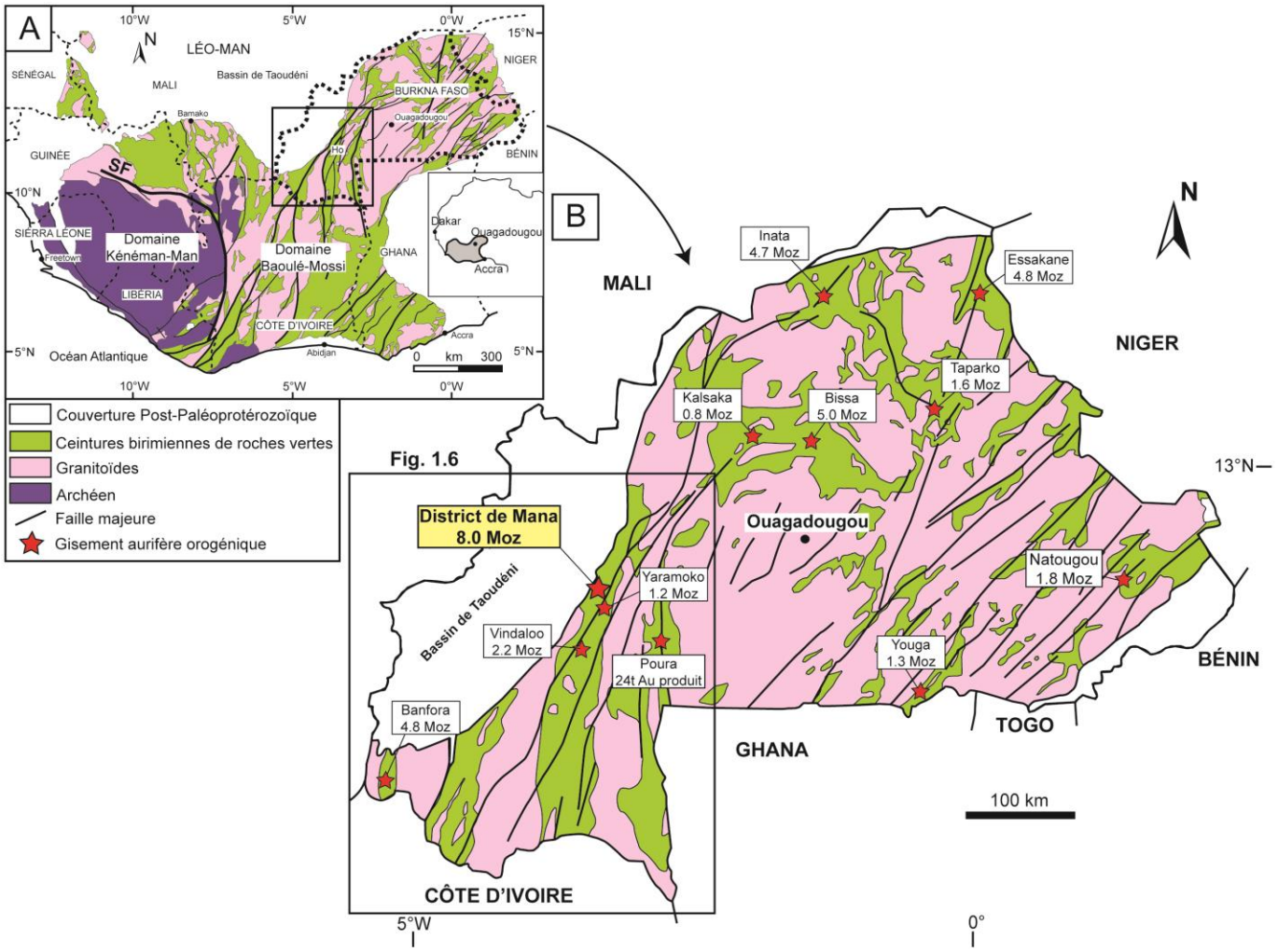

Figure 1.5 (a) Carte géologique simplifiée du craton ouest-africain, modifiée d'après Milési et al. (2004). (b) Carte géologique simplifiée du Burkina Faso avec la distribution des gisements d'or, modifiée d'après Castaing et al. (2003).

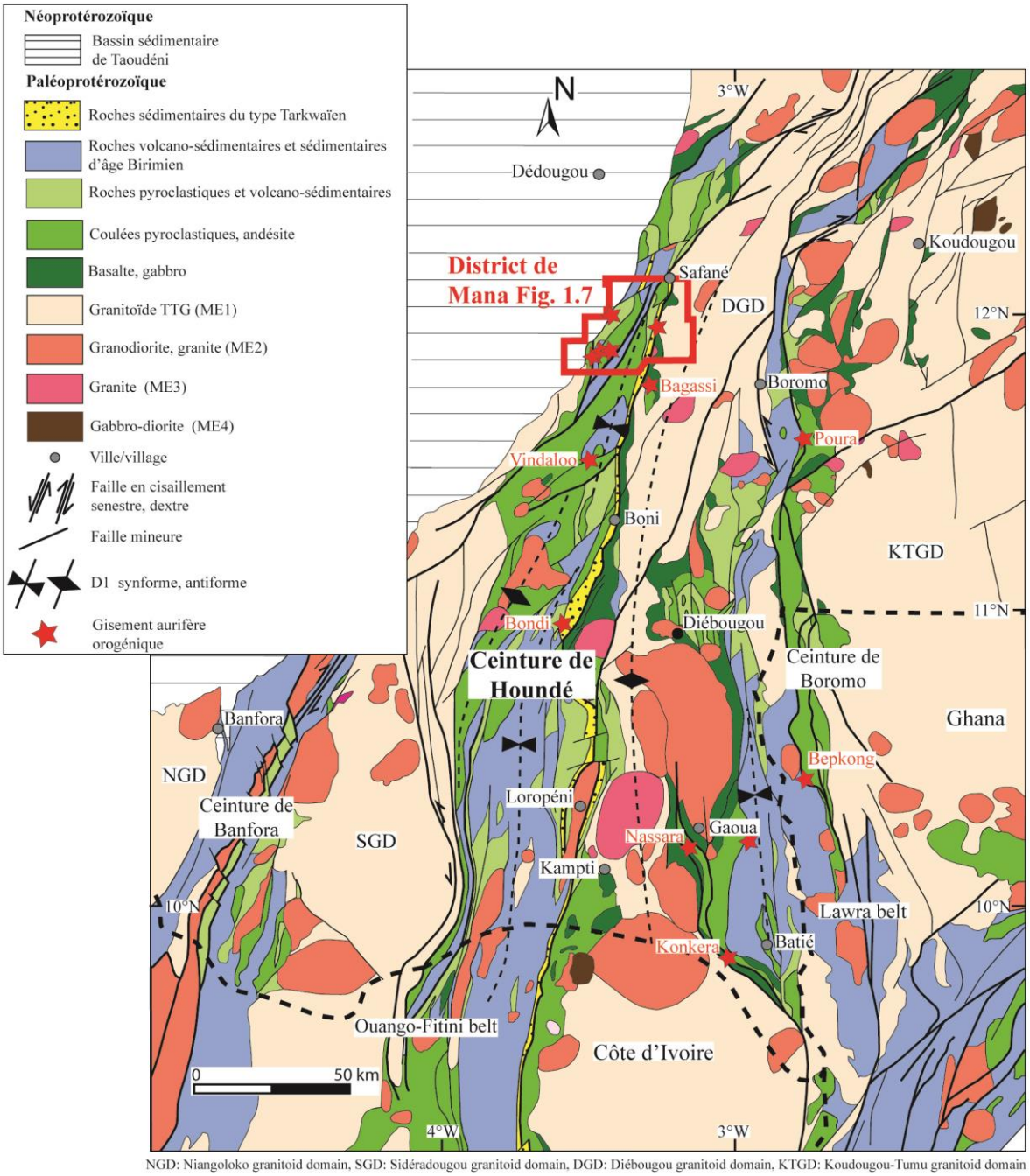

Figure 1.6 Carte géologique de la partie ouest du Burkina Faso, modifiée de Baratoux et al. (2011).

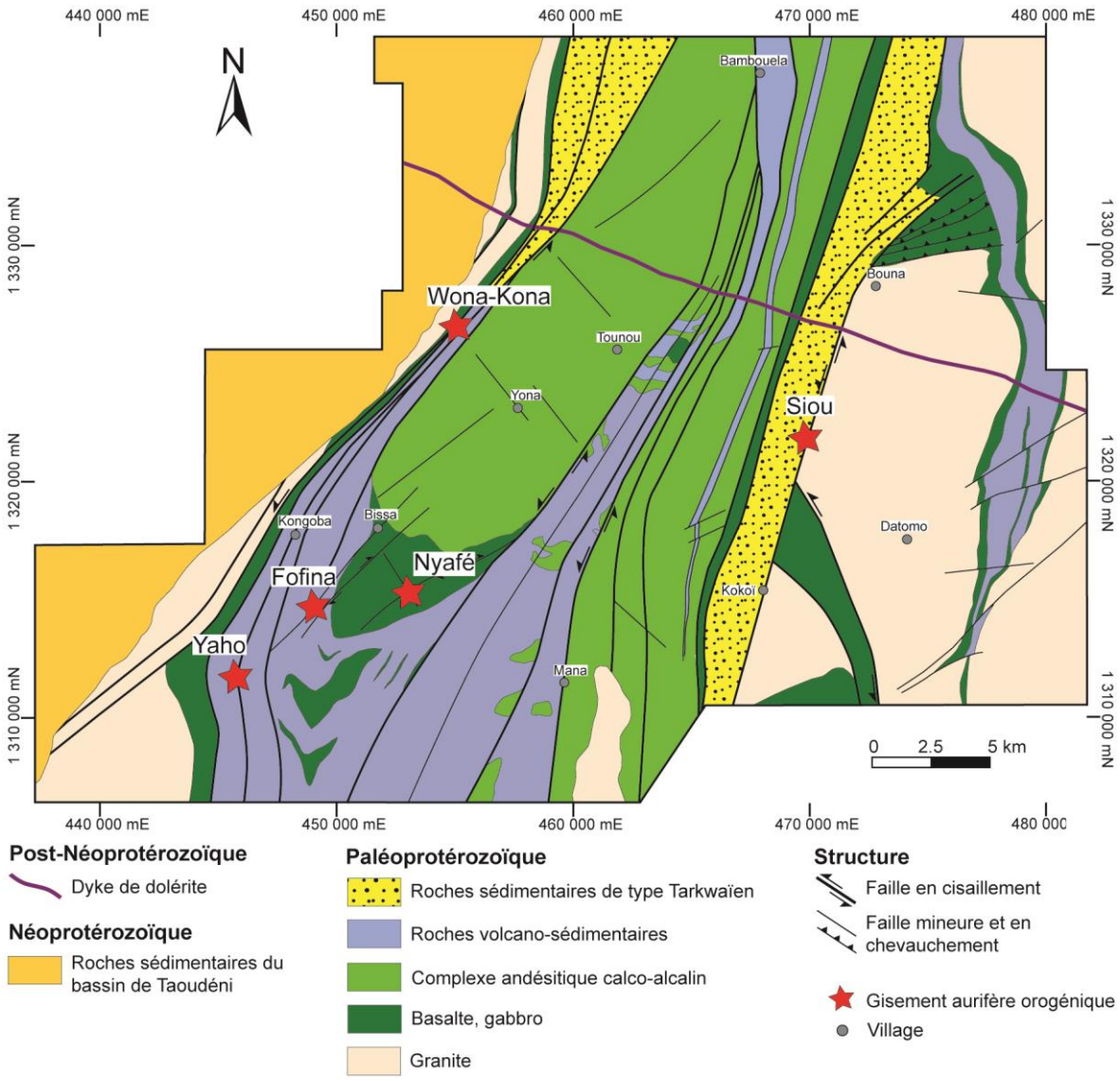

Figure 1.7 Carte géologique du district de Mana avec la répartition spatiale des 5 gisements aurifères orogéniques, d'après SEMAFO Inc.

TABLEAUX DU CHAPITRE 1

Tableau 1.1 Synthèses des différentes sources de l'or en lien avec les gisements d'or orogéniques.

Type de fluide	Source	Secteur district	Gisement	Âge	Structure	Style de minéralisation	Sulfures	Enrichissement en métaux	Composition des fluides	Altération hydrothermale	Références
Fluide métamorphique	Roches sédimentaires	Schistes d'Otago (Nouvelle Zélande)	Macraes > 7,0 Moz	Mésozoïque	Faille en cisaillement	Sulfures disséminés Veines de quartz	Pyrite Arsénopyrite	Au, As, Sb, W	H_2O-CO_2-CH_4 $\delta^{18}O$ = 8-11 300-350°C	Quartz Albite Muscovite Chlorite Épidote	Craw (2002) Petrie et Craw (2005) Large et al. (2012)
	Roches sédimentaires carbonées (shales noirs) à pyrite diagénétique	Lena (Sibérie)	Sukhoi Log 30 Moz	Néoprotérozoïque (Vendien)	Anticlinal Faille en chevauchement	Sulfures disséminés Veines de quartz-carbonates	Pyrite	Au, As, Ni	H_2O-CO_2-NaCl 450°C	Chlorite Carbonates	Large et al. (2007, 2009) Yudovskaya et al. (2016)
		Victoria (Australie)	Bendigo 22 Moz	Paléozoïque (Ordovicien)	Anticlinal Faille inverse	Sulfures disséminés Veines de quartz	Pyrite Arsénopyrite Sphalérite Chalcopyrite	Au, As	H_2O-CO_2 ± NaCl 300°C $\delta^{18}O$ = 15,9-19	Carbonates	Thomas et al. (2011) Wilson et al. (2013)
	Basalte de plateau océanique	Guasipati-El Callao (Venezuela)	El Callao 24 Moz	Paléoprotérozoïque (Birimien)	Faille en cisaillement	Veines de quartz	Pyrite Chalcopyrite Sphalérite	Au, As, Cu	H_2O-CO_2 ± NaCl 250°C	Séricite Chlorite Carbonates Albite	Velásquez et al. (2014)
Fluide magmatique	Intrusion felsique à intermédiaire	Province supérieure Abitibi (Québec)	Malartic 13,4 Moz	Archéen	Faille en cisaillement	Sulfures disséminés Veines de quartz	Pyrite Chalcopyrite Sphalérite Galène	Au, Ag, Te ± W, Sb, Bi, Pb	CO_2-SO_2 $\delta^{18}O$ = 5,2-9,8 450°C	Séricite Chlorite Carbonates Hématite	Helt et al. (2014) Perrouty et al. (2017)

Tableau 1.2 Synthèse des caractéristiques générales des 5 gisements aurifères orogéniques du district de Mana.

Gisement	Or*	Lithologie	Faciès métamorphique	Structure	Style de minéralisation	Sulfures	Enrichissement en métal	Altération	Références
Fofina	0,42 Moz à 3,6 g/t	Volcanoclastite Shales noirs Basalte tholéiitique Dyke felsique de QFP	Schistes verts	Anticlinal Faille en cisaillement de 2ème ordre	Sulfures disséminés Veines de quartz-carbonates	Pyrite Arsénopyrite	Au, Cu, Zn Pb, Sb	Chlorite Séricite Carbonates de fer Faible silicification	Paulin-Bissonnette (2012)
Nyafé	0,37 Moz à 6,0 g/t	Basalte tholéiitique Dyke felsique de QFP	Schistes verts	Faille en cisaillement de 2ème ordre	Stockwerks à sulfures	Arsénopyrite Pyrite Chalcopyrite	-	Chlorite Séricite Épidote Carbonates de fer	Béland (2009) Gilbert (2014)
Siou	1,0 Moz à 6,0 g/t	Roches sédimentaires du type Tarkwaïen Basalte tholéiitique Granodiorite	Schistes verts	Faille en cisaillement de 1er ordre	Veines de quartz à or libre	Pyrite Arsénopyrite	Au, As, Ni, Co, Bi, Pb, Cu, Se	Séricite Chlorite Carbonates Hématite	Dupuis (2013) Gibert (2014)
Wona-Kona	4,0 Moz à 2,3 g/t	Roches volcano-sédimentaires Shales noirs Basalte tholéiitique Dyke felsique de QFP Granodiorite	Schistes verts	Faille en cisaillement de 1er ordre	Veines de quartz-carbonates Silicification à sulfures et or libre	Pyrite Arsénopyrite Chalcopyrite Sphalérite	Au, As	Quartz Séricite Chlorite Carbonates de fer Épidote	Augustin (2011) Gilbert (2014) Augustin et al. (2016)
Yaho	1,0 Moz à 1,0 g/t	Roches sédimentaires détritiques Dyke felsique de QFP	Schistes verts	Faille en cisaillement de 2ème ordre	Sulfures disséminés Veines de quartz-carbonates Silicification	Pyrite Arsénopyrite	Au, As, Co, Ni	Séricite Quartz Carbonates de fer	Sinaré (2013) Mercier (2013) Gilbert (2014)

* = somme de la production + réserves + ressources (données SEMAFO Inc.).

Tableau 1.3 Objectifs versus méthodologie et appareillage.

Objectif principal	Objectifs spécifiques	Méthodes	Appareillage
Études des minéralisations aurifères du district de Mana, Burkina Faso. Évolution hydrothermal d'un système aurifère et contraintes tectono-métamorphique	Déterminer la nature des roches encaissantes et la source de l'or	Compilation des données des gisements	Banque de données de SEMAFO Inc.
		Cartographie régionale et détaillée des fosses Description de forages et échantillonnage	Terrain
		Analyses pétrographiques et minéralogiques	Microscope optique (UQAC)
		Analyses lithogéochimiques	ICP-MS/AES (ALS)
		Analyses isotopiques Sm-Nd, Rb-Sr	TIMS (IGGRC)
	Chronologie relative des épisodes de déformation associée à la minéralisation et leur cinématique	Cartographie détaillée, relation de recoupement des structures	Terrain
		Détermination des paragenèses minérales	Microscope optique (UQAC)
	Origine des fluides hydrothermaux et nature des minéralisations	Cartographie détaillée des fosses, des forages et échantillonnage	Terrain
		Analyses pétrographiques et minéralogiques	Microscope optique (UQAC)
		Distribution des éléments traces dans les sulfures	LA-ICP-MS (UQAC)
	Rôle génétique et chronologie des intrusions granitiques	Analyses pétrographiques et minéralogiques	Microscope optique (UQAC)
		Analyses lithogéochimiques	ICP-MS/AES (ALS)
		Datation Ar-Ar muscovite	ARGUSVI (U. Melbourne)
		Datation U-Pb	LA-ICP-MS (U. Montpellier) MEB (IOS)
	Guides d'exploration à l'échelle du district	Fusion des données	UQAC

CHAPITRE 2

2. Paleoproterozoic plume-related basaltic rocks in the Mana gold district in western Burkina Faso, West Africa: Implications for exploration and the source of gold in orogenic deposits

Jérôme Augustin, Damien Gaboury

Journal of African Earth Sciences, 2017, vol. 129, p. 17-30

2.1. RÉSUMÉ

Les roches volcaniques birimiennes du district de Mana sont situées dans un important segment minéralisé en or de la ceinture paléoprotérozoïque de roches vertes de Houndé, à l'ouest du Burkina Faso, qui contient des ressources cumulées de ~11 Moz. Cinq gisements d'or orogéniques (~8 Moz) sont encaissés dans, ou à proximité de roches basaltiques. Ces roches ont été étudiées pour investiguer leur possible rôle comme source de l'or des gisements orogéniques plus jeunes. Ces roches correspondent à des basaltes tholéiitiques enrichis en Fe avec des spectres REE plats, $(La/Yb)_N$ = 0,96-1,3 et sans anomalie négative en Eu (Eu/Eu*= 0,92-1,26). Les basaltes ont également des rapports isotopiques initiaux en Sr faibles (0,693612 à 0,702190) et des valeurs positives εNd (+2,25 à +3,14). En utilisant un diagramme Ce/Nb vs. Th/Nb et diverses analyses de basaltes liés à des panaches du monde entier, les basaltes de Mana se révèlent être liés à un panache. De plus, en utilisant les diagrammes binaires Zr/Nb vs. Nb/Th et Nb/Y vs. Zr/Y et les champs de référence, les roches basaltiques de Mana semblent avoir été formées directement au-dessus de la tête du panache. Étant donné que les basaltes liés à un panache ont tendance à être enrichis en or par rapport au MORB, nous proposons que le contenu en or du district de Mana soit principalement lié à la présence de roches basaltiques liées à un panache. Ainsi ces roches peuvent avoir servi comme un réservoir de métal important lors de la remobilisation subséquente pour la formation des gisements d'or orogéniques. Nous proposons également que lors d'un projet d'exploration aurifère, deux diagrammes géochimiques simples impliquant Zr, Y, Nb et Th puissent être utilisés à un stade précoce pour tester l'origine des

roches basaltiques et donc établir indirectement la fertilité d'une ceinture spécifique contenant des gisements d'or orogéniques.

2.2. ABSTRACT

Birimian volcanic rocks of the Mana district are located in the an important gold-mineralized segment of the Paleoproterozoic Houndé greenstone belt, western Burkina Faso, which contains cumulative resources of ~11 Moz. Five orogenic gold deposits (~8 Moz) are hosted in or close to basaltic rocks. Theses rocks were studied to investigate their possible role as a gold source in younger orogenic gold deposits. They are Fe-rich tholeiitic basalts with flat REE patterns, with $(La/Yb)_N$ = 0.96-1.3 and without negative Eu anomaly (Eu/Eu* = 0.92-1.26). The basalts also have low initial Sr isotopic ratios (0.693612 to 0.702190) and positive εNd values (+2.25 to +3.14). Using a Ce/Nb vs. Th/Nb diagram and various plume-related basalts worldwide for comparison, the basalts are shown to be plume-related. In addition to using Zr/Nb vs. Nb/Th and Nb/Y vs. Zr/Y binary diagrams and reference fields, the Mana basaltic rocks appear to have formed directly above the plume-head. Because plume-related basalts tend to be enriched in gold relative to MORB, we propose that the gold endowment of the Mana district is mostly related to the occurrence of plume-related basaltic rocks, which may have served as an important metal stock during subsequent remobilization of the orogenic gold deposits. We also propose that during an early stage gold exploration project, two simple geochemical diagrams involving

Zr, Y, Nb and Th could be used at an early stage to test the origin of the basaltic rocks and hence indirectly establish the fertility of a specific belt in terms of hosting orogenic gold deposits.

2.3. INTRODUCTION

Orogenic gold deposits contribute over 75% of the world's total gold production (Phillips, 2013), but the primary sources of gold remain controversial (Tomkins, 2013a). Numerous workers have tried to address this problem (e.g., Pitcairn et al., 2006; Large et al., 2012; Tomkins, 2013a; Pitcairn et al., 2015) which also have fundamental implications for selecting potential gold exploration terrains. Recent works have highlighted three main sources of gold: 1) intrusion-related sources (e.g., Lang and Baker, 2001; Helt et al., 2014); 2) carbonaceous, pyrite-rich sedimentary rocks (Pitcairn et al., 2006; Large et al., 2007; 2009, 2012; Thomas et al., 2011; Gaboury, 2013); and 3) basaltic rocks (Bierlein and Pisarevsky, 2008; Bierlein and Craw, 2009; Willman et al., 2010; Pitcairn et al., 2015). Among basaltic rocks, plume-related rocks have the highest primary gold endowment and exhibit enrichment up to 13 times greater than that of mid-ocean ridge basalts (MORB) (Webber et al., 2013). Such plume-related rocks thus have greater potential to constitute important primary gold source (Bierlein and Pisarevsky, 2008; Webber et al., 2013) in the remobilization process during the metamorphogenic formation of orogenic gold deposits (Phillips and Powell, 2010).

Among the three main periods of orogenic gold mineralization recognized worldwide (Goldfarb et al., 2001; Tomkins, 2013b), including the Late Archean (2.7-2.5 Ga), Early Proterozoic (2.1-1.8 Ga), and Phanerozoic (<1 Ga), the Early Proterozoic is of special interest due to the recent high rate of gold deposit discoveries relating to this period (Nyame, 2013). This period roughly coincides with the formation of the Birimian greenstone belts that occur mostly in Western Africa, with a few additional examples in South America (Fig. 2.1). Most of the recent discoveries were in Burkina Faso, a country that is covered approximately 20% by greenstone belts (~70,000 km^2) (Béziat et al., 2008). In the last decade, seven mines were put into production, and numerous deposits are at advanced stage (Fig. 2.2a). Between 2007 and 2015, ~6.1 Moz were produced from total resources of ~30 Moz of gold (Avocet, 2015; Endeavour Mining, 2015; ITIE, 2014, 2016; IAMGOLD, 2015; Nordgold, 2015; Semafo Inc, 2015). Currently, Burkina Faso is the fourth highest gold-producing country in Africa, after South Africa, Ghana and Mali (Markwitz et al., 2016; Robertson and Peters, 2016). Among the various greenstone belts in Burkina Faso (Fig. 2.2a), the Houndé belt is currently known to be the richest in gold, with a cumulative production, reserves and resources of ~11 Moz (Roxgold, 2013; Endeavour Mining, 2015; Semafo Inc, 2015; Sarama Resources, 2016) (Fig. 2.2a). The Mana district is the richest segment within the Houndé belt and hosts five orogenic gold deposits containing a total of ~8 Moz (Semafo Inc., 2015), including the world class Wona-Kona gold deposit (>4 Moz: Augustin et al., 2016) (Fig. 2.2a).

The lithological succession of the Birimian terranes is made up of basaltic to andesitic rocks, interbedded with clastic sedimentary sequences including the late Tarkwaian group

and intruded by several generations of granitoids (Leube et al., 1990; Milési et al., 1992; Sylvester and Attoh, 1992; Béziat et al., 2000; Roddaz et al., 2007; Lompo, 2009). In the West African Craton (WAC), the origin of the basaltic rocks, constituting the base of the Birimian greenstone belts, is still debated. Three geodynamic contexts for the formation of these rocks have been proposed including 1) a plume-related setting (Abouchami et al., 1990; Boher et al., 1992); 2) island arc setting (Dia, 1988; Sylvester and Attoh, 1992; Ama Salah et al., 1996; Baratoux et al., 2011; Béziat et al., 2000; Soumalia et al., 2004; Dampare et al., 2008; de Kock et al., 2012; Senyah et al., 2016); and 3) MORB (Lompo, 2010). The Mana district is thus a unique terrain in the western Burkina Faso to test the origin of these basaltic rocks and to address their potential role as the source of gold in orogenic deposits.

In this paper, we present new geochemical data for major and trace elements, and Sr and Nd isotopic data of the basaltic tholeiitic rocks in the Mana district. This dataset is compared with published data from the WAC and modern plume setting. The basaltic rocks of the Mana district are shown to be related to oceanic plume volcanism and interpreted to have been formed directly above the plume head. Even though other factors are likely involved in the formation of economic orogenic gold deposits (Goldfarb et al., 2001; Bierlein et al., 2006), we argue that gold endowment in Mana district is mostly related to the occurrence of plume-related basaltic rocks presumably enriched in primary gold. The rapid identification of the source of basaltic rocks based on trace elements and their position relative to the plume head can serve as a direct criterion for selecting more favorable belts during early exploration stages.

2.4. CRATON SCALE GEOLOGY

The Man-Leo Shield, in the WAC comprises a Paleoproterozoic domain (Baoulé-Mossi domain) to the east and an Archean domain (the Kénéma-Man domain) to the west. These two domains are separated by the Sassandra fault (Bessoles, 1977; Feybesse et al., 1989; Feybesse and Milési, 1994; Kouamelan et al., 1997; Egal et al., 2002) (Fig. 2.1). The Paleoproterozoic domain comprises the Birimian terrains (2.2-2.0 Ga) (Abouchami et al., 1990; Boher et al., 1992; Taylor et al., 1992; Hirdes et al., 1996) and forms linear to arcuate greenstone belts of volcanic and volcano-sedimentary sequences, granitic batholiths and narrow sedimentary basins (Alric, 1990; Leube et al., 1990; Hirdes et al., 1996; Doumbia et al., 1998; Feybesse et al., 2006; Pawling et al., 2006) (Fig. 2.1). The volcanic pile is characterized by bimodal tholeiitic and/or calc-alkaline rocks and younger sedimentary sequences (Junner, 1935; Ledru et al., 1991; Milési et al., 1989, 1991). These formations were affected by polyphased deformation and metamorphism during the Eburnean orogeny (Bonhomme, 1962) between ~2150 Ma and 1980 Ma (Baratoux et al., 2011; Block et al., 2015).

The geodynamic evolution of the WAC remains the subject of considerable debate, and two main models exist. One model involves horizontal accretion and crustal thickening along orogenic parallel thrust faults similar to the modern tectonic plate setting (Milési et al., 1989; Ledru et al., 1991; Allibone et al., 2002; Feybesse et al., 2006). The other involves sagduction-like vertical movements that are related to differential densities of late intrusive

rocks during the cratonization phase which may have induced dome and basin geometry (Pons et al., 1995; Vidal et al., 1996, 2009; Lompo, 2009, 2010).

Numerous geodynamic settings have been proposed to account for the formation of the basaltic volcanic rocks. Several authors have argued that the basaltic rocks were formed in an oceanic plateau by mantle plume-derived magmatic activity at the craton scale, which accounts for the massive accumulation of tholeiitic basalts at ~2250-2200 Ma subsequently followed by arc-related volcanism at the top of the sequence (Abouchami et al., 1990; Boher et al., 1992; Pouclet et al., 1996; Albarède, 1998; Lompo, 2009). Leube et al. (1990) suggested that continental rifting in Ghana might account for the formation of the voluminous basaltic rocks. Arc- or subduction-related contexts in Mali, Ivory Coast, Burkina Faso, Senegal and Guinea have also been suggested (Liégeois et al., 1991; Vidal and Alric, 1994; Ama Salah et al., 1996; Ndiaye et al., 1997; Béziat et al., 2000; Egal et al., 2002; Soumalia et al., 2004; Ganne et al., 2011). In relation to the western Burkina Faso greenstone belts (Houndé, Banfora and Boromo), Baratoux et al. (2011) documented evolution from tholeiitic oceanic crust or an oceanic plateau to a juvenile volcanic island arc during the period from approximately 2200 to 2160 Ma. Other workers suggested that the Paleoproterozoic crust of the WAC was heterogeneous (Béziat et al., 2000). In addition, isotopic data appear to indicate a juvenile source for the Paleoproterozoic volcanic rocks (Abouchami et al., 1990; Liégeois et al., 1991; Boher et al., 1992; Taylor et al., 1992; Cheilletz et al., 1994; Hirdes et al., 1996; Ama Salah et al., 1996; Ndiaye et al., 1997; Dia et al., 1997; Doumbia et al., 1998; Gasquet et al., 2003).

2.5. BIRIMIAN BELT GEOLOGY

The lithostratigraphy of western Burkina Faso is characterized by Birimian meta-volcanic and meta-sedimentary sequences occurring as greenstone belts (e.g., Boromo, Houndé, and Banfora) that are generally oriented NNE-SSW to N-S (Fig. 2.2a) (Castaing et al., 2003; Baratoux et al., 2011; Metelka et al., 2011). Polycyclic deformations, which are referred to as the Eburnean orogeny (2200-2000 Ma) (Bonhomme, 1962; Liégeois et al., 1991; Milési et al., 1992; Ledru et al., 1994; Egal et al., 2002), overprinted the volcano-sedimentary rocks and induced folding, shearing and greenschist to amphibolite facies metamorphism. The greenstone belts are separated by granitoid domains with ages between 2153 and 2097 ± 7 Ma (Hirdes et al., 1996; Chèvremont et al., 2003; Koté et al., 2003; Le Métour et al., 2003). Multiple episodes of granitoid intrusions have been distinguished, such as the tonalite-trondhjemite-granodiorite suite (TTG) and granitic intrusions (Baratoux et al., 2011). The greenstone belts comprise mafic tholeiitic volcanic rocks (Lower Birimian) together with intermediate and acid calc-alkaline effusive suites that are typical of volcanic-arc environments (Béziat et al., 2008; Baratoux et al., 2011). Volcano-sedimentary units are interbedded with volcanic assemblages (Hirdes et al., 1996; Castaing et al., 2003). In the Houndé belt, shallow water detrital sedimentary rocks, which are considered genetically similar to the Tarkwaian meta-sediments in Ghana, occur as an approximately 400-km-long by 1-2-km-wide unit (Bossière et al., 1996). Later doleritic dykes crosscut all of the greenstone-related rocks (Jessell et al., 2015).

The NS trending Houndé greenstone belt comprises tholeiitic basalts and gabbros at the base (Fig. 2.2a). On the top, andesitic volcanic rocks occur in the central and southern part of the belt (Baratoux et al., 2011). The unit of mafic rocks is bounded to the east by the Boni shear zone, which defines the contact with late Tarkwaian-type sedimentary rocks (Baratoux et al., 2011; Koffi et al., 2016) with a maximum deposition age of between 2171 ± 7 Ma and 2113 ± 23 Ma (Bonkoungou, 1994; Bossière et al., 1996). To the west, sedimentary rocks of the Neoproterozoic Taoudeni basin overlay the Paleoproterozoic basement (Bronner et al., 1980; Bertrand-Sarfati et al., 1990).

2.6. THE MANA DISTRICT

The Mana district is located in the northern part of the Houndé greenstone belt. Based on current knowledge (Augustin, 2011; Sinaré, 2013; Augustin et al., 2016), it is the most gold-endowed portion of the belt and contains five gold deposits hosted in different rock types (Fig. 2.2a; Table 2.1). The lithostratigraphic succession is typical of greenstone belts and is characterized at the base by a major tholeiitic basaltic suite with some intercalations of argillic sedimentary rocks that are overlain by predominant pelagic and detrital sedimentary rocks (shale, sandstones, greywacke and volcanoclastics). The Mana district basalt (MDB) unit has undergone submarine hydrothermal alterations with epidote, chlorite, localized albite and shows zones of strong silicification, some of which are anomalous in gold (Augustin, 2011; Augustin et al., 2016). Accessory minerals include

rutile and disseminated pyrite. South of the district, the basalts exhibit distinctive volcanic pristine textures such as amygdules, pillow lavas, pillow breccias and hyaloclastite deposits (Nyafé and Fofina deposits). Most of the basaltic rocks are aphyric and aphanitic. The maximum thickness of the basaltic pile is estimated to be ~6 km (Baratoux et al., 2011). Calc-alkaline volcanic series, including andesitic pillowed lavas, volcanoclastic flows and tuffaceous facies occur at the top of the basaltic rocks. The Paleoproterozoic formations are affected by polyphased deformation and greenschist-facies metamorphism with amphibolite facies that locally occur as metamorphic aureoles around some later-formed granitoids.

2.7. SAMPLE SELECTION AND ANALYTIC METHODS

For this study, thirty-seven representative samples of the Mana district were selected based on the following criteria: 1) drill hole samples were taken from cores at depths below about 120 m to avoid superficial alteration; 2) samples located proximal (<200 m) from known gold deposits were not collected to limit possible overprinting by hydrothermal alteration; 3) samples distributed spatially to cover the district (Fig. 2.2b); 4) the least deformed samples (less schistose); and 5) samples with the lowest loss on ignition (LOI) values (<3%). The samples were pulverized at the ALS Geochemical Laboratory of Vancouver, Canada. The major elements were analyzed using inductively coupled plasma-atomic emission spectroscopy (ICP-AES). Trace elements were determined by inductively coupled

plasma-mass spectrometry (ICP-MS) using an Agilent 7500a instrument. Standard and duplicate samples were routinely added to monitor analytical precision and accuracy.

Eight samples were subjected to Sr-Nd isotopic analysis using a Thermal Ionization Mass Spectrometer (TIMS) at the Isotope Geochemistry and Geochronology Research Center of Carleton University (IGGRC), Ottawa. The samples were selected from the group of 37 samples based on their flat REE-HFSE patterns, very low LOI values and representative spatial distribution. Silicate rock powders were spiked with a mixed ^{148}Nd-^{149}Sm before dissolution in an acid mixture of approximately 29 M HF and 16 M HNO_3. The samples were then dried on a hotplate before being re-dissolved in 8 M HNO_3 and 6 M HCl sequentially. The dried sample residues were then dissolved in 2.5 M HCl and loaded into 14-ml Bio-Rad borosilicate glass chromatography columns containing 3.0 ml of Dowex AG50W-X8 cation resin. The columns were subsequently washed with 23 ml of 2.5 M of HCl before eluting the rare earth elements using 9 ml of 6 M HCl. The REE fractions were dissolved in 0.26 M HCl and then loaded onto Eichrom Ln Resin chromatographic columns containing Teflon powder coated with HDEHP [di(2-ethylhexyl) orthophosphoric acid (Richard et al., 1976). Nd was eluted using 0.26 M HCl after which Sm was eluted using 0.5 M HCl. Isotope ratios measured using a ThermoFinnigan Trion TIMS. The samples were loaded with H_3PO_4 on one side of the Re double filaments, and the isotope ratios measured at temperatures of 1700-1800 °C. Isotope ratios were normalized to ^{146}Nd/^{144}Nd = 0.72190. The International La Jolla standard (O'Neil et al., 2008) was measured at ^{143}Nd/^{144}Nd = 0.511847 ± 7, n = 26 (Feb 2005-June 2007), and the internal laboratory Nd standard was measured at 0.511826 ± 14, n = 114 (Oct 2010-Oct 23, 2014). Sm and Nd

concentrations were measured precisely within 1%, and $^{147}Sm/^{144}Nd$ ratios were reproducible to 0.5%. Analyses of the USGS standard BCR-2 (Wilson, 1997) yielded Nd = 29.02 ppm, Sm = 6.68 ppm, and $^{143}Nd/^{144}Nd$ = 0.512668 ± 20 (n = 4). Total procedural blanks for Nd (Sm) were measured at <50 pg.

2.8. RESULTS

2.8.1. MAJOR ELEMENT CHEMISTRY

Major element compositions for 37 samples of the MDB are listed in Table 2.2 and in Annexe 1. Geochemical data for volcanic rocks from the Boromo and Houndé belts and the Paleoproterozoic tholeiitic series of the WAC were also used for comparison (Lompo, 2009; Baratoux et al., 2011). The rocks contain 46.7 to 52.6 wt. % of SiO_2, 10.7 to 14.6 wt. % of Fe_2O_3, 5.96 to 8 wt. % of MgO and 0.77 to 1.32 wt. % of TiO_2. The magnesium numbers (Mg# (Mg/Mg + Fe)) for the MDB ranges from 45.82 to 59.68. These rocks exhibit sub-alkali basaltic affinity when plotted on a Nb/Y vs. Zr/TiO_2*0.0001 graph (Fig. 2.3). In the Miyashiro (1974) diagram discriminating boundaries (Fig. 2.4) confirm a tholeiitic affinity that is consistent with the Paleoproterozoic tholeiitic series of WAC (Lompo, 2009). The AFM diagram of Jensen (1976) shows a Fe-rich tholeiitic tendency for MDB (Fig. 2.5), similar to the tholeiitic basalts of western Burkina Faso (Baratoux et al., 2011).

2.8.2. TRACE ELEMENT GEOCHEMISTRY

Trace element data are presented in Table 2.2. Chondrite-normalized REE patterns of the MDB are shown in Fig. 2.6a. All MDB samples display rather flat REE patterns $(La/Yb)_N$ = 0.96-1.31 (Fig. 2.6a). No negative Eu anomaly is present (Eu/Eu* = 0.92-1.26), suggesting that plagioclase is not one of the main phases involved in fractional crystallization (Rudnick, 1992). On a comparative basis, the basaltic rocks of the WAC (Lompo, 2009) and the Pacific Plateau (Storey et al., 1991) have very similar REE patterns to that of the MDB (Fig. 2.6b). On the primitive mantle normalized spider diagram (Fig. 2.6c), the MDB samples present a relatively flat HFSE pattern without any Nb anomaly, suggesting a lack of crustal contamination (Weaver and Tarney, 1981). Positive Sr anomaly indicates the accumulation or removal of plagioclase and magnetite (Amortegui et al., 2011), whereas negative Rb and K anomalies could be related to some very weak hydrothermal alteration.

2.8.3. Sr AND Nd ISOTOPE GEOCHEMISTRY

Sr-Nd isotopic data for 8 whole-rock samples are listed in Table 2.3. For the MDB, the initial $^{87}Sr/^{86}Sr$ ratios and Nd values were calculated at an age of 2.2 Ga relative to the present-day chondritic values of $^{143}Nd/^{144}Nd$ = 0.512640 and $^{147}Sm/^{144}Nd$ = 0.1967 (Abouchami et al., 1990; Boher et al., 1992). Rb and Sr contents range from 0.2 to 7.5 ppm and 76 to 149 ppm, respectively. Nd and Sm concentrations range from 6.7 to 9.2 ppm and 2.14 to 3.05 ppm, respectively. The MDB is characterized by an initial $^{87}Sr/^{86}Sr$ ratio

ranging from 0.693612 to 0.702190. Initial Nd isotopic ratios range from 0.512631 to 0.512803 and exhibit positive εNd values, ranging between 2.25 and 3.14 at 2.2 Ga (Table 2.3).

2.9. DISCUSSION

Lompo (2009) described three types of Paleoproterozoic tholeiitic series (PTH1 to PTH3: Fig. 2.4) in the WAC and proposed a mantle plume evolution of the ocean basin floor for the first group (PTH1) which is characterized by flat REE patterns. Geodynamically, Lompo (2009) proposed that the PTH1 was formed in a subsiding seafloor basin. Conversely, the juvenile island arc concept (Liégeois et al., 1991; Vidal and Alric, 1994; Ama Salah et al., 1996; Ndiaye et al., 1997; Béziat et al., 2000; Egal et al., 2002; Soumalia et al., 2004; Ganne et al., 2011) implies that basalts having mid-oceanic ridge (MORB) affinities (flat REE patterns) were likely assembled within oceanic island arcs during subduction processes. In the following discussion, we compare the geodynamic setting of modern island arc and oceanic plateau with our dataset, assuming that the same or similar processes were active during Paleoproterozoic times, and discuss their role as a gold source for orogenic gold deposits.

2.9.1. PLUME RELATED GEODYNAMIC CONTEXT

Using a Ce/Nb vs. Th/Nb diagram (Fig. 2.7: Polat et al., 1999) and reference samples of oceanic basalts of the Wawa province and the oceanic basalt of El Callao (Venezuela) in the Guyana shield (Polat et al., 1999; Kerrich et al., 2008; Velásquez et al., 2011), the MDB samples plot in the modern oceanic plateau field that is defined by the Ontong Java and Broken Ridge samples (Mahoney et al., 1995; Polat et al., 1999; Kerr et al., 2000) (Fig. 2.7). Moreover, the MDB samples lie in the same field as the Wawa and El Callao formation samples (ECB), which have been interpreted as originating from an oceanic plateau that is derived from a heterogeneous multi-component plume (Polat et al., 1999; Velásquez et al., 2011). Furthermore, the flat REE patterns with low fractionated $(La/Yb)_N$ values suggest that the tholeiitic basalts were formed by mantle plume processes that are similar to those that formed modern oceanic plateau basalts (Abouchami et al., 1990; Boher et al., 1992; Pouclet et al., 1996; Lompo, 2009). Thus, the MDB may likely represent a new example of accreted Paleoproterozoic oceanic plateau crust in the Birimian terranes of the WAC, an observation which may appear to corroborate the interpretations of some previous studies (Abouchami et al., 1990; Boher et al., 1992; Pouclet et al., 1996; Albarède, 1998; Lompo, 2009).

2.9.2. MANTLE SOURCE

Some element ratios, such as Zr/Nb, Nb/Th, Nb/Y and Zr/Y, can be used to discriminate a mantle source because they have similar incompatibilities in the mantle (Condie, 2005). Fig. 2.8a and b confirm that the MDB samples lie in the oceanic plateau setting defined by Condie (2005) and the data plot near primitive mantle source (PM). The primitive mantle source origin can be constrained by εNd (Zhu, 2007). Abouchami et al. (1990) and Boher et al. (1992) have established the composition of depleted mantle for Birimian basalts with εNd values from 1.1 to 4.2. In this study, εNd values range from 2.25 to 3.14, suggesting that the MDB magma was derived from a primitive mantle (PM) source. A plume-related origin is also supported by the Zr-Y-Nb-Th diagrams (Fig. 2.8a, b), where the plume head (OPB) and tail sources (OIB) can be distinguished using classification fields obtained from Condie (2005). The MDB samples lie in the plume head field (Fig. 2.8a, b), suggesting that the basaltic rocks are derived directly from a mantle plume in the oceanic plateau.

2.9.3. CRUSTAL CONTAMINATION

Most isotopic studies on the WAC show no evidence of crustal contamination by an Archean crust (Abouchami et al., 1990; Boher et al., 1992; Doumbia et al., 1998; Gasquet et al., 2003; Feybesse et al., 2006; Pawling et al., 2006). Geochemical and isotopic data obtained for the MDB show a similar composition to other Birimian basalts of the WAC and the Guyana Shield in South America (Abouchami et al., 1990; Boher et al., 1992;

Pawling et al., 2006; Velásquez et al., 2011). All MDB samples are characterized by positive εNd values with $^{87}Sr/^{86}Sr_{(i)}$ ratios between 0.693612 and 0.702190. The composition of the MDB samples is isotopically close to that of the contemporaneously depleted mantle of DePaolo (1988), and lies within the Birimian basalt and granitoid field (Fig. 2.9) proposed by Abouchami et al. (1990), Boher et al. (1992), Pawling et al. (2006), and Velásquez et al. (2011).

2.9.4. GOLD SOURCE IN THE WEST AFRICAN CRATON

In the WAC, most orogenic gold deposits are spatially associated with volcanic mafic rocks in the Birimian greenstone belts (Fig. 2.1), suggesting a genetic link (Nyame, 2013; Perrouty et al., 2014). These rocks recorded the most extensive and rapid episode of continental crust formation which occurred in the early part of the Paleoproterozoic (2.2-2.1 Ga: Boher et al., 1992; Hirdes et al., 1996; Attoh and Ekwueme, 1997). In the gold endowed Paleoproterozoic Ashanti belt (Ghana), Perrouty et al. (2014) showed that 85% of gold occurrences are proximal to a specific Fe-rich tholeiitic basaltic unit (BV1) and suggested that this unit played a significant role in gold deposit formation, either 1) as a chemical and structural traps for gold or 2) as a direct source of gold. They concluded that both hypotheses can explain the distribution of the gold occurrences. However, for the gold source hypothesis, comparison with the MDB samples is impossible, as no trace and isotopic data were provided in their study.

According to Goldfarb et al. (2001) and Groves et al. (2005), a major period of mantle plume activity yields important lithospheric growth at active continental margins. The mantle plume process transports siderophile elements from the core-mantle boundary layer (Hawkesworth and Scherstén, 2007; Bierlein and Pisarevsky, 2008). If mantle plumes were responsible for the rapid tholeiitic basalt growth, these should have a primary genetic implication for the gold mineralization event in the WAC. Several authors (e.g., Oppliger et al., 1997; Kerrich et al., 2000; Bierlein et al., 2006; Bierlein and Pisarevsky, 2008) have proposed that Au enrichment might be supplied by a mantle plume carrying Au into the upper mantle, for geological periods ranging from Archean to modern time. Webber et al. (2013) demonstrated that influence of the modern Iceland plume on the Mid-Atlantic Ridge progressively enriched the oceanic crust with gold by as much as 13 times the normal background of a MORB. This enrichment can produce a large volume of metal-enriched oceanic crust, thus forming a major stock of metal for later metamorphogenic formation of gold deposits, as proposed by Bierlein and Pisarevsky (2008) and Webber et al. (2013). Phillips et al. (1987) estimated the volume of leached rocks needed to generate the giant Kalgoorlie gold deposit to be around 19 km^3 of tholeiitic basalts per 1 Moz Au assuming a concentration of 2 ppb Au in the mafic source. In addition to gold, basaltic rocks can be enriched in siderophile elements (As, Sb, and Te) due to their entrainment in the ascending mantle plume from the mantle-core boundary (Bierlein and Pisarevsky, 2008), and these elements are common in many WAC gold deposits (Lawrence et al., 2013; Markwitz et al., 2016).

Recent work by Pitcairn et al. (2015), using samples from the Otago Schist and Alpine fault area (New Zealand), directly addressed gold extraction from the leaching of MORB and WPB (with-in plate basalts) by metamorphic devolatization (Phillips and Powell, 2009, 2010). The authors (Phillips and Powell, 2009, 2010; Pitcairn et al., 2015) concluded that basaltic rocks have the potential to provide gold in similar amounts to those found in pyritic carbonaceous sedimentary rocks as proposed by Pitcairn et al. (2010). However, Pitcairn et al. (2015) discarded this gold source, suggesting instead that basaltic rocks do not provide sufficient As and S to account for their enrichment in orogenic gold deposits.

In the Mana district, Gaboury (2013) documented C_2H_6 in fluid inclusions from the major gold deposits (Wona, Nyafé, Fobiri, Yaho and Siou) and argued that gold was extracted during the metamorphism of primary gold-enriched pyrite that occurs in black shales at various levels in the volcanic pile. This finding might appear to contradict the proposed role of gold-enriched plume-related basaltic rocks as the direct source of gold in orogenic deposits. However, primary pyrite is formed by bacterial sulfate reduction from seawater, and the low level of gold in seawater is scavenged by growing primary pyrite (Tomkins, 2013b; Steadman et al., 2015). Considering that a large proportion of gold in seawater is extracted from basaltic lavas by low- to high-temperature seafloor hydrothermal venting activities (Patten et al., 2016), it should be assumed that if the level of primary gold in plume related basaltic rocks is higher than that in normal MORB, then the resulting gold concentration in seawater would be higher and consequently higher also in pyrite-bearing shales. In short, plume-related basalts, with their documented higher primary magmatic gold endowment (Webber et al., 2013), have the potential to provide a more fertile gold

source for the formation of orogenic gold deposits. Gold from the basaltic rocks may be released after subsequent metamorphism and deformation of the volcanic belts through direct hydrothermal leaching of the basaltic rocks. Nevertheless, early seafloor hydrothermal activity overprinting the plume-related basalts also have the potential for upgrading the gold background of the basaltic rocks as suggested by Pitcairn et al. (2015) and related sedimentary rocks (e.g., carbonaceous-pyritic shales).

2.9.5. IMPLICATIONS FOR GOLD EXPLORATION

We assume that plume-related rocks are enriched in gold, even if no direct analysis for gold is provided that supports this assumption in this study. Such an analysis would be of no interest, as basaltic rocks have been subjected to metamorphism and weak seafloor alteration. Furthermore, as the MDB samples were from an important gold district, the rigorous demonstration that gold was primary enriched in basaltic rocks stand as an almost impossible goal.

Interpretations from our dataset imply that the basaltic rocks were formed directly above the plume head and are consequently more enriched in primary gold according to Webber et al. (2013). Spatially, the Houndé belt is located close to the middle of the all known greenstone belts in the WAC (Fig. 2.1). This implies that other belts may have been formed by more distal plume-related magmatism or combined MORB and plume-related processes. As a mantellic plume is a large geological feature, belts could have been either formed as a

single coherent belt that has since been dismembered by cratonization-related intrusions (Baratoux et al., 2011) or as smaller, individual and isolated belts. Nevertheless, for early stage exploration, the proposed concept implies that the geochemistry of basaltic rocks, even those analyzed in commercial laboratories, should provide information about the potential fertility of a belt in hosting gold deposits, assuming that subsequent deformation and metamorphism were favorable for extracting gold from the basaltic and related sources (e.g., pyritic shales). Using simple diagrams of Zr/Nb vs. Nb/Th and Nb/Y vs. Zr/Y with the specific fields of Condie (2003), it is proposed that the gold favorability of a belt can be established by considering whether the basalts are related or unrelated to a plume, and if related, by considering their relative position to the plume head.

2.10. CONCLUSION

The Paleoproterozoic Birimian meta-volcanic rocks of the Mana district are Fe-rich tholeiitic basalts with flat chondrite-normalized REE and primitive mantle normalized HFSE multi-element patterns. Positive values of εNd (+2.25 to +3.14) and low fractionated $(La/Yb)_N$ values (0.96-1.31) suggest the basalts formed by mantle plume processes, similar to those that formed modern oceanic plateaus from a primitive mantle source with little or no crustal contamination. Thus, the MDB represents an example of accreted Paleoproterozoic oceanic plateau crust in the Birimian terranes of the WAC, thereby

confirming some earlier studies in Burkina Faso, Niger, Mauritania, Senegal and the Ivory Coast.

The identification of plume-related basalts may be very important in the formation of orogenic gold deposits because such basalts could be primarily enriched in gold. The Mana basalts were likely produced directly above the plume head, suggesting that they may have been enriched in primary gold at higher crustal levels than more distal, tail-related basalts. We further suggest that two geochemical diagrams relating Zr, Y, Nb and Th could be used during early stage exploration to decipher the origin of basaltic rocks. According to the proposed concept, plume-related basaltic rocks and particularly those formed above plume head should be considered more prospective for the formation of orogenic gold deposits.

2.11. ACKNOWLEDGEMENTS

This PhD-related research by the first author is a part of a larger research program in the Mana district that receives financial support from SEMAFO Inc. We thank SEMAFO Inc. for granting access to their technical data, permitting field work and for authorizing the publication of these results. Special thanks go to senior geologists at SEMAFO Inc., particularly M.A. Crevier, R. Roy, D. Boisvert, D. Lalonde, D. Bonde, and F. Yameogo. We are grateful to S. Zhang from IGGRC for his help with the isotopic determinations and interpretation. Finally, Dre Lenka Baratoux and an anonymous reviewer are gratefully acknowledged for thorough revision and improvement of this manuscript.

2.12. REFERENCES

Abouchami, W., Boher, M., Michard, A., Albarède, F., 1990. A major 2.1 Ga event of mafic magmatism in Western Africa: An early stage of crustal accretion. Journal of Geophysical Research 95, 17605-17629.

Albarède, F., 1998. The growth of continental crust. Tectonophysics 296, 1-14.

Allibone, A., Teasdale, J., Cameron, G., Etheridge, M., Uttley, P., Soboh, A., Appiahkubi, J., Adanu, A., Arthur, R., Mamphey, J., Odoom, B., Zuta, J., Tsikata, A., Pataye, F., Famiyeh, S., Lamb, E., 2002. Timing and structural controls on gold mineralization at the Bogoso gold mine, Ghana, West Africa. Economic Geology 97, 949-969.

Ama Salah, I., Liégeois, J.P., Pouclet, A., 1996. Évolution d'un arc insulaire océanique Birimien précoce au Liptako nigérien (Sirba): Géologie, géochronologie et géochimie. Journal of African Earth Sciences 22, 235-254.

Amortegui, A., Jaillard, E., Lapierre, H., Martelat, J.E., Bosch, D., Bussy, F., 2011. Petrography and geochemistry of accreted oceanic fragments below the Western Cordillera of Ecuador. Geochimical Journal 45, 57-78.

Alric, G., 1990. Géochimie du volcanisme birimien (Protérozoïque inférieur) de l'Unité de Haute-Comoé, NE de la Côte d'Ivoire: Premiers résultats. Journal of African Earth Sciences 10, 669-681.

Attoh, K., Ekwueme, B.N., 1997. The West African shield. Oxford Monograph on Geology and Geophysics 35, 517-528.

Augustin, J., 2011. Facteurs de contrôle et processus métallogéniques des minéralisations aurifères du gisement de Wona, mine Mana, Burkina Faso. Unpublished M.Sc. thesis. Université du Québec à Chicoutimi, 1-220.

Augustin, J., Gaboury, D., Crevier, M., 2016. The world-class Wona-Kona gold deposit, Burkina Faso. Ore Geology Reviews 78, 667-672.

Avocet, 2015. Annual Report and Accounts, News Release April 26, 2016, p. 104. London, England.

Baratoux, L., Metelka, V., Naba, S., Jessell, M.W., Grégoire, M., Ganne, J., 2011. Juvenile Paleoproterozoic crust evolution during the Eburnean orogeny (~2.2-2.0 Ga), western Burkina Faso. Precambrian Research 191, 18-45.

Bertrand-Sarfati, J., Moussine-Pouchkine, A., Affaton, P., Trompette, R., Bellion, Y., 1990. Cover sequences of the west African craton. In: Dallmeyer, R.D., Lecorche, J.P. (Eds.), The West African Orogens and Circum-Atlantic Correlatives. Springer-Verlag, p. 65-82.

Bessoles, B., 1977. Géologie de l'Afrique. Le craton ouest-africain. Mémoire BRGM, Paris, p. 1-88.

Béziat, D., Bourges, F., Debat, P., Lompo, M., Martin, F., Tollon, F., 2000. A Paleoproterozoic ultramafic-mafic assemblage and associated volcanic rocks of the Boromo greenstone belt: Fractionates and associated from island-arc volcanic activity in the West African Craton. Precambrian Research 101, 25-47.

Béziat, D., Dubois, M., Debat, P., Nikiéma, S., Salvi, S., Tollon, F., 2008. Gold metallogeny in the Birimian craton of Burkina Faso (West Africa). Journal of African Earth Sciences 50, 215-233.

Bierlein, F.P., Craw, D., 2009. Petrogenetic character and provenance of metabasalts in the aspiring and Torlesse Terranes, South Island, New Zealand: Implications for the gold endowment of the Otago Schist? Chemical Geology 260, 301-315.

Bierlein, F.P., Pisarevsky, S., 2008. Plume-related oceanic plateaus as a potential source of gold mineralization. Economic Geology 103, 425-430.

Bierlein, F.P., Stein, H.J., Coira, B., Reynolds, P., 2006. Timing of gold and crustal evolution of the Paleozoic south central Andes, NW Argentina-implications for the endowment of orogenic belts. Earth and Planetary Science Letters 245, 702-721.

Block, S., Ganne, J., Baratoux, L., Zeh, A., Parra-Avila, L.A., Jessell, M.W., Aillères, L., Siebenaller, L., 2015. Petrological and geochronological constraints on lower crust exhumation during Paleoproterozoic (Eburnean) orogeny, NW Ghana, West African Craton. Journal of Metamorphic Geology 33, 463-494.

Boher, M., Abouchami, W., Michard, A., Albarède, F., Arndt, N., 1992. Crustal growth in West Africa at 2.1 Ga. Journal of Geophysical Research 97, 345-369.

Bonhomme, M., 1962. Contribution à l'étude géochronologique de la plate-forme de l'Ouest Africain. Annals de la Faculté, des Sciences de l'Université, de Clermont-Ferrand. Géologie et Minéralogie 5, p. 1-62.

Bonkoungou, I., 1994. Le Tarkwaïen du sillon de Houndé (Burkina-Faso): Un ensemble volcano-détritique acide calco-alcalin à 2.15 Ga. Unpublished Ph.D. thesis. In: Étude pétrologique, métamorphique et structurale. The University of Nantes, France, p. 1-419.

Bossière, G., Bonkoungou, I., Peucat, J.J., Pupin, J.P., 1996. Origin and age of Paleoproterozoic conglomerates and sandstones of the Tarkwaian group in Burkina Faso, West Africa. Precambrian Research 80, 153-172.

Bronner, G., Roussel, J., Trompette, R., 1980. Genesis and geodynamic evolution of the Taoudeni cratonic basin (Upper Precambrian and Paleozoic), Western Africa. Geodynamics 1, 81-87.

Castaing, C., Billa, M., Milési, J.P., Thiéblemont, D., Le Métour, J., Egal, E., Donzeau, M., Guerrot, C., Cocherie, A., Chèvremont, P., Tegyey, M., Itard, Y., Zida, B., Ouedraogo, I., Koté, S., Kabore, B.E., Ouedraogo, C., Ki, J.C., Zunino, C., 2003. Notice explicative de la carte géologique et minière du Burkina Faso à 1/1,000,000. BRGM BUMIGEB, p. 147.

Cheilletz, A., Barbey, P., Lama, C., Pons, J.L., Zimmermann, D., 1994. Âge de refroidissement de la croûte juvénile birimienne d'Afrique de l'Ouest, Données U/Pb et K-Ar sur les formations à 2.1 Ga du SW du Niger. Comptes Rendus de l'Académie des Sciences de Paris, Série II 319, 435-442.

Chèvremont, P., Donzeau, M., Le Métour, J., Egal, E., Castaing, C., Thiéblemont, D., Tegyey, M., Guerrot, C., Billa, M., Itard, Y., Delpont, G., Ki, J.C., 2003. Notice explicative de la carte géologique du Burkina Faso à 1/200,000. Feuille Koudougou, p. 85.

Condie, K.C., 2003. Incompatible element ratios in oceanic basalts and komatiites: Tracking deep mantle sources and continental growth rates with time. Geochemistry, Geophysics, Geosystems 4, 1-28.

Condie, K.C., 2005. High field strength element ratios in Archean basalts: A window to evolving sources of mantle plumes? Lithos 79, 491-504.

Dampare, S.B., Shibata, T., Asiedu, D.K., Osae, S., Banoeng-Yakubo, B., 2008. Geochemistry of Paleoproterozoic metavolcanic rocks from the southern Ashanti volcanic belt Ghana: Petrogenic and tectonic setting implications. Precambrian Research 162, 403-423.

de Kock, G.S., Théveniaut, H., Botha, P.M.W., Gyapong, W., 2012. Timing the structural events in the Paleoproterozoic Bole-Nangodi belt terrane and adjacent Maluwe basin, West African Craton, in central-west Ghana. Journal of African Earth Sciences 65, 1-24.

DePaolo, D.J., 1988. Nd Isotope Geochemistry. An Introduction. Springer, Berlin, p. 1-187.

Dia, A., 1988. Caractères et significations des complexes magmatiques et métamorphiques du secteur de Sandikounda-Laminia (Nord de la boutonnière de Kédougou, Est du Sénégal). Un modèle géodynamique du Birimien de l'Afrique de l'Ouest. Unpublised Ph.D Thesis, Sénégal. The Universty of Dakar, p. 1-350.

Dia, A., Vans Schmus, W.R., Kröner, A., 1997. Isotopic constraints on the age and formation of a Paleoproterozoic volcanic arc complex in the Kedougou Inlier, eastern Senegal, West Africa. Journal of African Earth Sciences 24, 197-213.

Doumbia, S., Pouclet, A., Koumelan, A., Peucat, J.J., Vidal, M., Delor, C., 1998. Petrogenesis of juvenile-type Birimian (Paleoproterozoic) granitoids in central Côte d'Ivoire, West Africa: Geochemistry and geochronology. Precambrian Research 87, 33-63.

Egal, E., Thiéblemont, D., Lahondere, D., Guerrot, C., Costea, C.A., Iliescu, D., Delor, C., Goujou, J.C., Lafon, J.M., Teygey, M., Diaby, S., Kolié, P., 2002. Late eburnean granitization and tectonics along the northwestern margin of the Archean Kénéma-man domain (Guinea, West African Craton). Precambrian Research 117, 57-84.

Endeavour Mining, 2015. Mineral Reserves and Mineral Resources (31 December 2015). https://www.endeavourmining.com/operations/reserves-and-resources-nov-2015.

Feybesse, J.L., Milési, J.P., 1994. The Archaean/Proterozoic contact zone in West Africa: A mountain belt of decollement, thrusting and folding on a continental margin related to 2.1 Ga convergence of Archaean cratons? Precambrian Research 69, 199-227.

Feybesse, J.L., Milési, J.P., Joahn, V., Dommanget, A., Calvez, J.H., Boher, M., Abouchami, W., 1989. La limite Archéen-Protérozoïque inférieur d'Afrique de l'Ouest: Une zone de chevauchement majeur antérieure à l'accident de Sassandra, l'exemple des régions d'Odiénne, et de Touva (Côte d'Ivoire). Comptes rendus de l'Académie des Sciences de Paris II 309, 1874-1853.

Feybesse, J.L., Billa, M., Guerrot, C., Duguey, E., Lescuyer, J.L., Milési, J.P., Bouchot, V., 2006. The Paleoproterozoic Ghanaian province: Geodynamic model and ore control, including regional stress modeling. Precambrian Research 149, 149-196.

Gaboury, D., 2013. Does gold in orogenic deposits come from pyrite in deeply buried carbon-rich sediments?: Insight from volatiles in fluid inclusions. Geology 41, 1207-1210.

Ganne, J., De Andrade, V., Weinberg, R.F., Vidal, O., Dubacq, B., Kagambega, N., Naba, S., Baratoux, L., Jessell, M., Allibone, J., 2011. Modern-style plate subduction preserved in the Paleoproterozoic West African craton. Nature Geoscience 5, 60-65.

Gasquet, D., Barbey, P., Adu, M., Paquette, J.L., 2003. Structure, Sr-Nd isotope geochemistry and zircon U-Pb geochronology of the granitoids of the Dabakala area (Côte d'Ivoire): Evidence for a 2.3 Ga crustal growth event in the Paleoproterozoic of West Africa? Precambrian Research 127, 329-354.

Goldfarb, R.J., Groves, D.I., Gardoll, S., 2001. Orogenic gold and geologic time: A global synthesis. Ore Geology Reviews 18, 1-75.

Groves, D.I., Condie, K.C., Goldfarb, R.J., Hronsky, J.M.A., Vielreicher, R.M., 2005. Secular changes in global tectonic processes and their influence on the temporal distribution of gold-bearing mineral deposits. Economic Geology 100, 203-224.

Hawkesworth, C., Scherstén, A., 2007. Mantle plumes and geochemistry. Chemical Geology 241, 319-331.

Helt, K.M., Williams-Jones, A.E., Clark, J.R., Wing, B.A., Wares, R.P., 2014. Constraints on the genesis of the Archean oxidized, intrusions-related Canadian Malartic gold deposit, Québec, Canada. Economic Geology 109, 713-735.

Hirdes, D., Davies, D., Lüdkte, G., Konan, G., 1996. Two generations of Birimian (Paleoproterozoic) volcanic belts in northeastern Côte d'Ivoire (West Africa): Consequences for the Birimian controversy. Precambrian Research 80, 173-191.

IAMGOLD, 2015. Technical Report on the Essakane Gold Mine, Sahel Region, Burkina Faso, p. 1-248.

ITIE, 2014. Rapport de conciliation des paiements des sociétés minières à l'état et des recettes perçues par l'état des dites sociétés pour l'exercice 2012, p. 1-173.

ITIE, 2016. Rapport ITIE Burkina Faso, p. 1-168.

Jensen, L.S., 1976. A new cation plot for classifying sub-alkaline volcanic rocks. In: Ontario Division Mines Miscellaneous Paper, p. 1-66.

Jessell, M., Santoul, J., Baratoux, L., Youbi, N., Ernst, R.E., Metelka, V., Miller, J., Perrouty, S., 2015. An updated map of West African mafic dykes. Journal of African Earth Sciences 112, 440-450.

Junner, N.R., 1935. Gold in the Gold Coast. Unpublished M.Sc. thesis. In: Gold Coast Geological Survey Memoire, vol. 4, p. 1-67.

Kerr, A.C., White, R.V., Saunders, A.D., 2000. LIP reading: Recognizing oceanic plateaux in the geological record. Journal of Petrology 41, 1041-1056.

Kerrich, R., Goldfarb, R.J., Groves, D.I., Garwin, S., 2000. The geodynamics of world-class gold deposits: Characteristics, space-time distribution, and origins. Economic Geology 13, 501-551.

Kerrich, R., Polat, A., Xie, Q., 2008. Geochemical systematics of 2.7 Ga Kinojevis group (Abitibi), and Manitouwadge and Winston lake (Wawa) Fe-rich basalt-rhyolite associations: Backarc rift oceanic crust? Lithos 101, 1-23.

Koffi, Y.H., Wenmenga, U., Djro, S.C., 2016. Tarkwaian deposits of the Birimian belt of Houndé: Petrological, structural and geochemical study (Burkina-Faso, West Africa). International Journal of Geosciences 7, 685-700.

Koté, S., Ouedraogo, I., Donzeau, M., Le Métour, J., Egal, E., Thiéblemont, D., Tegyey, M., Guerrot, C., Chèvremont, P., Milési, J.P., Billa, M., Itard, Y., Ki, J.C., 2003. Notice explicative de la carte géologique du Burkina Faso à 1/200,000. Feuille Léo, p. 1-70.

Kouamelan, A.N., Delor, C., Peucat, J.J., 1997. Geochronological evidence for reworking of Archean terrains during the early Proterozoic (2.1 Ga) in the western Côte d'Ivoire (Man Rise-West African craton). Precambrian Research 86, 177-199.

Lang, J.R., Baker, T., 2001. Intrusion-related gold systems: The present level of understanding. Mineralium Deposita 36, 477-489.

Large, R.R., Maslennikov, V., Robert, F., Danyushevsky, L.V., Chang, Z.S., 2007. Multistage sedimentary and metamorphic origin of pyrite and gold in the giant Sukhoi Log deposit, Lena Gold Province, Russia. Economic Geology 102, 1232-1267.

Large, R.R., Danyushevsky, L., Hollit, C., Maslennikov, V., Meffre, S., Gilbert, S., Bull, S., Scott, R., Emsbo, P., Thomas, H., 2009. Gold and trace element zonation in pyrite using a laser imaging technique: Implications for the timing of gold in orogenic and Carlin-style sediment-hosted deposits. Economic Geology 104, 635-668.

Large, R.R., Thomas, H., Craw, D., Henne, A., Henderson, S., 2012. Diagenetic pyrite as a source for metals in orogenic gold deposits, Otago Schist, New Zealand. New Zealand Journal of Geology and Geophysics 55, 137-149.

Lawrence, D.M., Treloar, P.J., Rankin, A.H., Harbridge, P., Holliday, J., 2013. The geology and mineralogy of the Loulo mining district, Mali, West Africa: Evidence for two distinct styles of orogenic gold mineralization. Economic Geology 108, 199-227.

Le Métour, J., Chèvremont, P., Donzeau, M.E., Thiéblemont, E., Tegey, D., Guerrot, M.C.M., Itard, B., Castaing, Y., Delpont, C., Ki, G., Zunino, J.C.C., 2003. Notice explicative de la Carte géologique du Burkina Faso a 1/200,000. Feuille Houndé, p. 1-82.

Ledru, P., Pons, J., Milési, J.P., Feybesse, J.L., Johan, V., 1991. Transcurrent tectonics and polycyclic evolution in the lower Proterozoic of Senegal-Mali. Precambrian Research 50, 337-354.

Ledru, P., Johan, V., Milési, J.P., Tegyey, M., 1994. Markers of the last stages of the Paleoproterozoic collision: Evidence for a 2 Ga continent involving circum-South Atlantic provinces. Precambrian Research 69, 169-191.

Leube, A., Hirdes, W., Mauer, R., Kesse, G., 1990. The early Proterozoic Birimian supergroup of Ghana and some aspect of its associated gold mineralization. Precambrian Research 46, 139-165.

Liégeois, J.P., Claessens, W., Camara, D., Klerkx, J., 1991. Short-lived Eburnian orogeny in southern Mali. Geology tectonics, U-Pb and Rb-Sr geochronology. Precambrian Research 50, 111-136.

Lompo, M., 2009. Geodynamic evolution of the 2.25-2.0 Ga Paleoproterozoic magmatic rocks in the Man-Leo Shield of the West African Craton. A model of subsidence of an oceanic plateau, vol. 323. Geological Society, London, p. 231-254.

Lompo, M., 2010. Paleoproterozoic structural evolution of the Man-Leo Shield (West Africa). Key structures for vertical to transcurrent tectonics. Journal of African Earth Sciences 58, 19-36.

Mahoney, J.J., Jones, W.B., Frey, F.A., Salters, V.J.M., Pyle, D.G., Davies, H.L., 1995. Geochemical characteristics of lavas from Broken Ridge, the Naturaliste Plateau and southernmost Kerguelen Plateau: Cretaceous plateau volcanism in the southeast Indian Ocean. Chemical Geology 120, 315-345.

Markwitz, V., Hein, K.A.A., Miller, J., 2016. Compilation of West African minerals deposits: Spatial distribution and mineral endowment. Precambrian Research 274, 61-81.

Metelka, V., Baratoux, L., Naba, S., Jessell, M.W., 2011. A geophysically constrained litho-structural analysis of the Eburnean greenstone belts and associated granitoid domains, Burkina Faso, West Africa. Precambrian Research 190, 48-69.

Milési, J.P., Feybesse, J.L., Ledru, P., Dommanget, A., Ouedraogo, M.F., Marcoux, E., Prost, A., Vinchon, C., Sylvain, J.P., Johan, V., Tegyey, M., Calvez, J.Y., Lagny, P., 1989. Minéralisations aurifères de l'Afrique de l'Ouest, leurs relations avec l'évolution litho-structurale au Protérozoïque inférieur Carte géologique au 1/ 2,000,000. Chronique de Recherche Minière 497, 3-98.

Milési, J.P., Ledru, P., Ankrah, P., Johan, V., Marcoux, E., Vinchon, C., 1991. The metallogenic relationship between Birimian and Tarkwaian gold deposits in Ghana. Mineralium Deposita 26, 228-238.

Milési, J.-P., Ledru, P., Feybesse, J.-L., Dommanget, A., Marcoux, E., 1992. Early Proterozoic ore deposits and tectonics of the Birimian orogenic belt West Africa. Precambrian Research 58, 305-344.

Milési, J.P., Feybesse, J.L., Pinna, P., Deschamps, Y., Kampunzu, H., Muhongo, S., Lescuyer, J.L., Le Goff, E., Delor, C., Billa, M., Ralay, F., Heinry, C., 2004. Geological map of Africa 1:10,000,000, SIGAfrique project. In: 20th Conference of African Geology. BRGM, Orléans, France, 2-7 June. http://www.sigafrique.net (last accessed 14/12/2010).

Miyashiro, A., 1974. Volcanic rock series in island arcs and active continental margins. American Journal of Science 274, 321-355.

Ndiaye, P.M., Dia, A., Vialette, Y., Diallo, D.P., Ngom, P.M., Sylla, M., Wade, S., Dioh, E., 1997. Données pétrographiques, géochimiques et géochronologiques nouvelles sur les granitoïdes du Paléoprotérozoïque du Super-groupe de Dialé-Daléma (Sénégal Oriental): Implications pétrogénétiques et géodynamiques. Journal of African Earth Sciences 25, 193-208.

Nordgold, 2015. Mineral Resources and Ore Reserves Update, News Release April 14, 2016, p. 1-26. Amsterdam, the Netherlands.

Nyame, F.K., 2013. Origins of Birimian (ca 2.2 Ga) mafic magmatism and the Paleoproterozoic 'greenstone belt' metallogeny: A review. Island Arc 22, 538-548.

Oppliger, G.L., Murphy, J.B., Brimhall Jr., G.H., 1997. Is the ancestral Yellowstone hotspot responsible for the Tertiary "Carlin" mineralization in the Great Basin of Nevada? Geology 25, 627-630.

O'Neil, J., Carlson, R.W., Francis, D., Stevenson, R.K., 2008. Neodymium-142 evidence for hadean mafic crust. Science 321, 1828-1831.

Patten, C.G.C., Pitcairn, I.K., Teagle, D.A.H., Harris, M., 2016. Mobility of Au and related elements during hydrothermal alteration of the oceanic crust: Implication for the sources of metals in VMS deposits. Mineralium Deposita 51, 179-200.

Pawling, S., Gueye, M., Klischies, R., Schwarz, S., Wemmer, K., Siegesmund, S., 2006. Geochemical and Sr-Nd isotopic data on the birimian of the Kedougou-Kenieba inlier (eastern Senegal): Implications on the Paleoproterozoic evolution of the West African Craton. South African Journal of Geology 109, 411-427.

Perrouty, S., Lindsay, M.D., Jessell, M.W., Aillères, L., Martin, R., Bourassa, Y., 2014. 3D Modeling of the Ashanti belt, southwest Ghana: Evidence for an lithostratigraphic control on gold occurrences within the Birimian Sefwi Group. Ore Geology Reviews 63, 252-264.

Phillips, G.N., 26-29 September, 2013. Australian and global setting for gold in 2013. In: Proceedings World Gold 2013. The Australian Institute of Mining and Metallurgy, Brisbane, Australia, p. 15-21.

Phillips, G.N., Powell, R., 2009. Formation of gold deposits: Review and evaluation of the continuum model. Earth-Science Reviews 94, 1-21.

Phillips, G.N., Powell, R., 2010. Formation of gold deposits: A metamorphic devolatilization model. Journal of Metamorphic Geology 28, 689-718.

Phillips, G.N., Groves, D.I., Brown, I.J., 1987. Source requirements for the Golden Mile, Kalgoorlie: Significance to the metamorphic replacement model of Archean gold deposits. Canadian Journal of Earth Sciences 24, 1643-1651.

Pitcairn, I.K., Teagle, D.A.H., Craw, D., Olivo, G.R., Kerrich, R., Brewer, T.S., 2006. Sources of metals and fluids in orogenic gold deposits: Insight from the Otago and Alpine Schists, New Zealand. Economic Geology 101, 1525-1546.

Pitcairn, I.K., Olivo, G.R., Teagle, D.A.H., Craw, D., 2010. Sulfide evolution during prograde metamorphism of the Otago and alpine schists, New Zealand. The Canadian Mineralogist 48, 1267-1295.

Pitcairn, K.I., Craw, D., Teagle, D.A.H., 2015. Metabasalts as sources of metals in orogenic gold deposits. Mineralium Deposita 50, 373-390.

Polat, A., Kerrich, R., Wyman, D.A., 1999. Geochemical diversity in oceanic komatiites and basalts from the late Archean Wawa greenstone belts, Superior Province, Canada: Trace element and Nd Isotope evidence for a heterogeneous mantle. Precambrian Research 94, 139-173.

Pons, J., Barbey, P., Dupuis, D., Leger, J.M., 1995. Mechanisms of pluton emplacement and structural evolution of 2.1 Ga juvenile continental crust: The Birimian of southwestern Niger. Precambrian Research 70, 281-301.

Pouclet, A., Vidal, M., Delor, C., Simeon, Y., Alric, G., 1996. Le volcanisme Birimien du nord-est de la Côte-d'Ivoire, mise en évidence de deux phases volcano-tectoniques distinctes dans l'évolution géodynamique du Paléoprotérozoïque. Bulletin de la Société Géologique de France 167, 529-541.

Richard, P., Shimizu, N., Allègre, C.J., 1976. $^{143}Nd/^{146}Nd$, a natural tracer: An application to oceanic basalts. Earth and Planetary Science Letters 31, 269-278.

Robertson, M., Peters, L., 2016. West African Goldfields. Episodes 39 (2), 155-176.

Roddaz, M., Debat, P., Nikiéma, S., 2007. Geochemistry of Upper Birimian sediments (major and trace elements and Nd-Sr isotopes) and implications for weathering and tectonic setting of the Late Paleoproterozoic crust. Precambrian Research 159, 197-211.

Roxgold, 2013. Roxgold Announces an Updated Mineral Resource Estimate for the 55 Zone. Ahead of Upcoming PEA Study, News Release August 27, 2013, Toronto, Ontario, p. 1-6.

Rudnick, R.L., 1992. Restites, Eu anomalies and the lower continental crust. Geochimica et Cosmochimica Acta 56, 963-970.

Sarama Resources, 2016. Sarama Resources Acquires the Bondi Gold Deposit in Burkina Faso from Orezone Gold, News Release May 24, 2016. http://www. saramaresources.com/getattachment/a46fa0f6-b4f4-46fd-abbde53461daf368/Sarama Resources-Acquires-The-Bondi-Gold-Deposit-I.aspx.

Semafo Inc, 2015. Mana, Burkina Faso; 2015 Mineral Reserves and Resources. http:// www.semafo.com/English/operations-and-exploration/reserves-and resources/default.aspx.

Senyah, G.A., Dampare, S.B., Asiedu, D.K., 2016. Geochemistry and tectonic setting of the Paleoproterozoic metavolcanic rocks from the Chirano gold district, Sefwi belt, Ghana. Journal of African Earth Sciences 122, 32-46.

Sinaré, M., 2013. Métallogénie du gisement aurifère de Yaho, ceinture birimienne de Houndé, Burkina Faso. Unpublished M.Sc. thesis. Université du Québec à Chicoutimi, p. 1-266.

Soumalia, A., Henry, P., Rossy, M., 2004. Contexte de mise en place des roches basiques de la ceinture de roches vertes birimiennes de Diagorou-Darbani (Liptako, Niger, Afrique de l'Ouest): Plateau océanique ou environnement d'arc/bassin arrière-arc océanique. Comptes rendus Géoscience 336, 1137-1147.

Steadman, J.A., Large, R.R., Meffre, S., Olin, P., Danyushevsky, L.V., Gregory, D.D., Belousov, I., Lounejeva, E., Ireland, T.R., Holden, P., 2015. Synsedimentary to early diagenetic gold in black shale-hosted pyrite nodules at the Golden Mile deposit, Kalgoorlie, Western Australia. Economic Geology 110, 1157-1191.

Storey, M., Mahoney, J.J., Kroenke, L.W., Saunders, A.D., 1991. Are oceanic plateaus sites of komatiite formation? Geology 19, 376-379.

Sun, S.S., McDonough, W.F., 1989. Chemical and isotopic systematics of oceanic basalts: Implications for mantle composition and processes. In: Sanders, A.D., Norry, M.J. (Eds.), Magmatism in the Ocean Basins, vol. 42. Geological Society Special Publication, p. 313-345.

Sylvester, P.J., Attoh, K., 1992. Lithostratigraphy and composition of 2.1 Ga greenstone belts of the West African Craton and their bearing on crustal evolution and the Archean-Proterozoic boundary. The Journal of Geology 100, 377-393.

Taylor, P.N., Moorbath, S., Leube, A., Hirdes, W., 1992. Early Proterozoic crustal evolution in the Birimian Ghana: Constraints from geochronology and isotope geochemistry. Precambrian Research 56, 97-111.

Thomas, H.V., Large, R.R., Bull, S.W., Maslennikov, V., Berry, R.F., Fraser, R., Froud, S., Moye, R., 2011. Pyrite and pyrrhotite textures and composition in sediments, laminated quartz veins, and reef at Bendigo gold mine, Australia: Insights for ore genesis. Economic Geology 106, 1-31.

Tomkins, A.G., 2013a. On the source of orogenic gold. Geology 41, 1255-1256.

Tomkins, A.G., 2013b. A biochemical influence on the secular distribution of orogenic gold. Economic Geology 108, 193-197.

Velásquez, G., Béziat, D., Salvi, S., Tosiani, T., Debat, P., 2011. First occurrence of Paleoproterozoic oceanic plateau in the Guiana Shield: The gold-bearing el Callao Formation, Venezuela. Precambrian Research 186, 181-192.

Vidal, M., Alric, G., 1994. The Paleoproterozoic (Birimian) of Haute-Comoé in the West African Craton Ivory Coast: A transtensional back-arc basin. Precambrian Research 65, 207-229.

Vidal, M., Delor, C., Pouclet, A., Siméon, Y., Alric, G., 1996. Évolution géodynamique de l'Afrique de l'Ouest entre 2,2 Ga et 2 Ga, Le style "archéen" des ceintures vertes et des ensembles sédimentaires Birimiens du nord-est de la Côte d'Ivoire. Bulletin de la Société Géologique de France 167, 307-319.

Vidal, M., Gumiaux, C., Cagnard, F., Pouclet, A., Ouattara, G., Pichon, M., 2009. Evolution of a Paleoproterozoic "weak type" orogeny in the west African craton (Ivory Coast). Tectonophysics 477, 145-159.

Weaver, B.L., Tarney, J., 1981. The Scourie dyke suite: Petrogenesis and geochemical nature of the Proterozoic sub-continental mantle. Contributions to Mineralogy and Petrology 78, 175-188.

Webber, A.P., Roberts, S., Taylor, R.N., Pitcairn, I.K., 2013. Golden plumes: Substantial golf enrichment of oceanic crust during ridge-plume interaction. Geology 41, 87-90.

Willman, C.E., Korsch, R.J., Moore, D.H., Cayley, R.A., Lisitsin, V.A., Rawling, T.J., Morand, V.J., O'Shea, P.J., 2010. Crustal-scale fluid pathways and source rocks in the Victorian Gold Province, Australia: Insights from deep seismic reflection profiles. Economic Geology 105, 895-915.

Wilson, S.A., 1997. The Collection, Preparation, and Testing of USGS Reference Material BCR-2. Columbia River, Basalt: U.S. Geological Survey Open-File Report 98.

Winchester, J.A., Floyd, P.A., 1977. Geochemical discrimination of different magma series and their differentiation products using immobile elements. Chemical Geology 20, 325-343.

Zhu, B., 2007. Pb-Sr-Nd isotopic systematics of mantle-derived rocks in the world. Earth Science Frontiers 14, 24-36.

FIGURES DU CHAPITRE 2

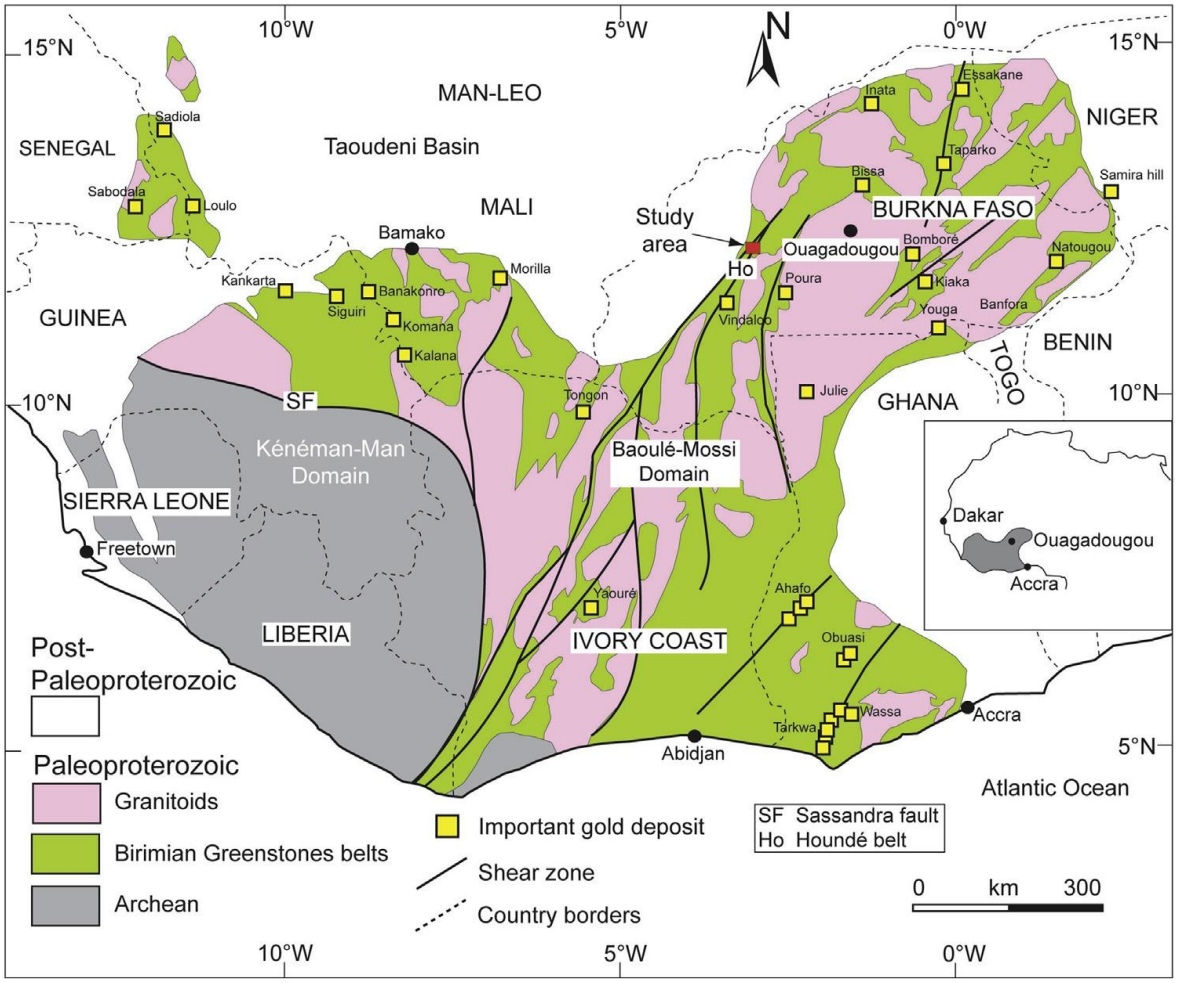

Figure 2.1 Geological map of the Leo-Man Craton showing the location of the study area and the most important gold deposits across the WAC (Modified from Milési et al. (2004); Baratoux et al. (2011)).

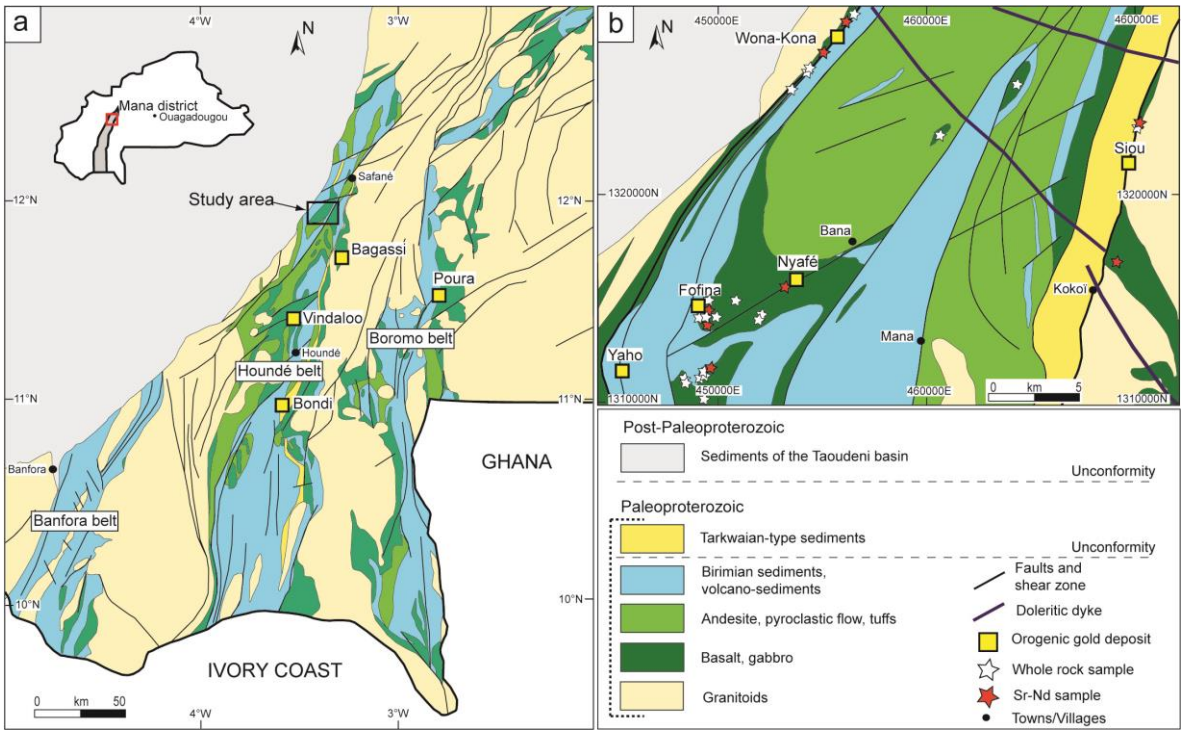

Figure 2.2 (a) Simplified regional map of western Burkina Faso (modified from Metelka et al. (2011)). (b) Geology map of the Mana district showing the sampling locations, which are represented by stars. Yellow squares represent the major orogenic gold deposits.

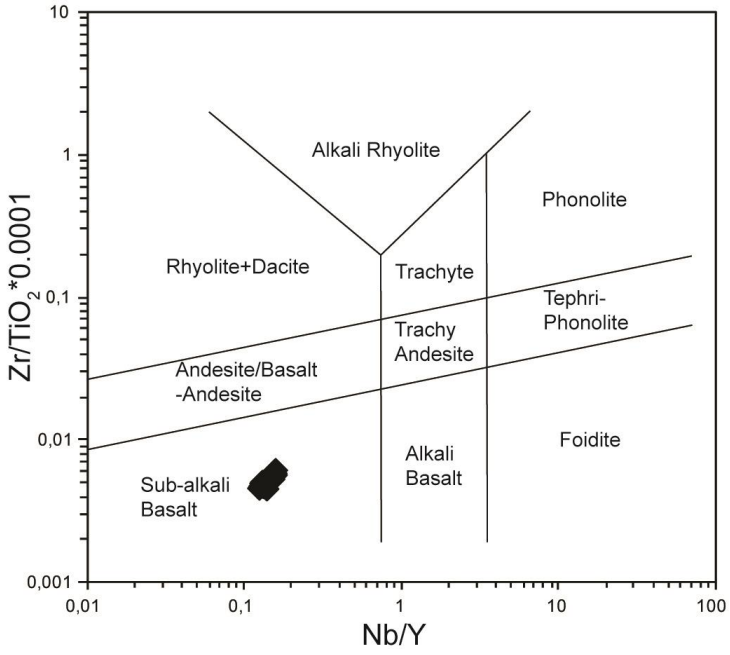

Figure 2.3 A plot of the basaltic samples within the Nb/Y vs. $Zr/TiO_2*0.0001$ classification diagram of Winchester and Floyd (1977).

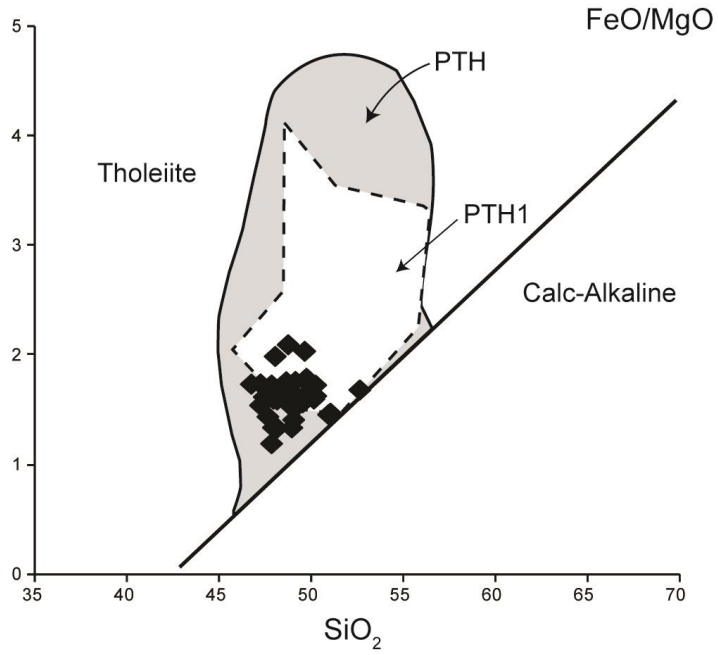

Figure 2.4 The FeO/MgO vs. SiO_2 diagram of Miyashiro (1974). The compilation of Paleoproterozoic tholeiitic PTH and PTH1 series from Lompo (2009) of the West African Craton (WAC) are shown for comparison.

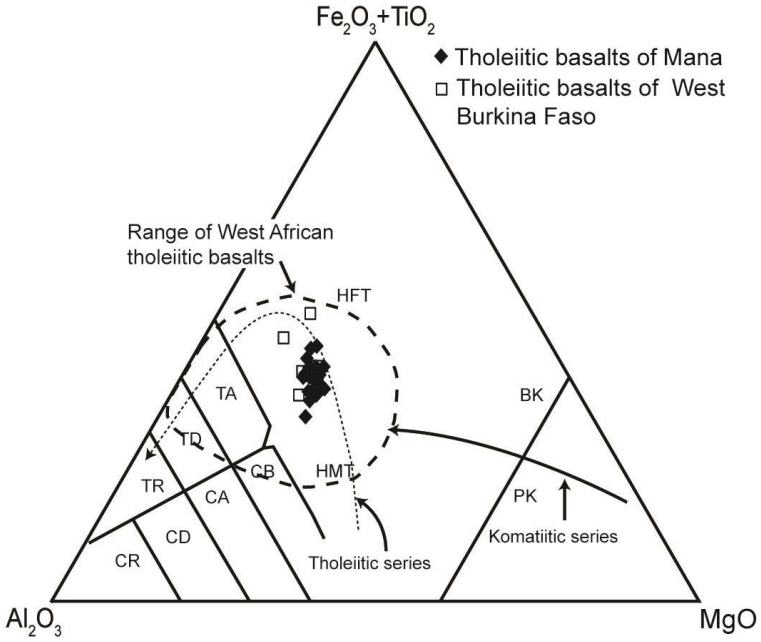

Figure 2.5 Jensen's cationic plot (after Jensen (1976)) showing the compositional range of the ECB. Compositions are compared with those of western Burkina Faso (Baratoux et al., 2011) and West African tholeiitic basalts (Abouchami et al., 1990).

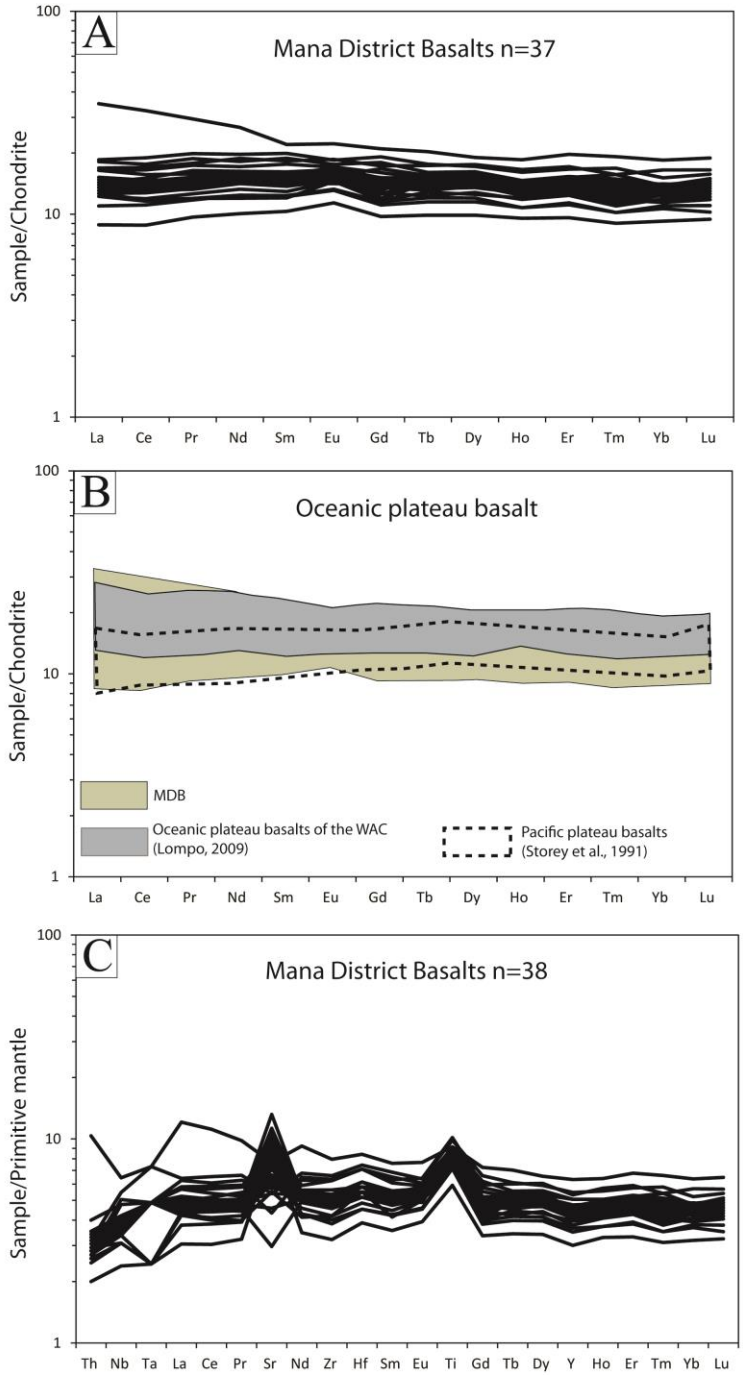

Figure 2.6 (a) Chondrite normalized rare-earth elements patterns (Sun and McDonough, 1989) for the MDB. (b) Comparison with oceanic plateau basalts of the WAC (Lompo, 2009) and modern Pacific Plateau basalt fields (Storey et al., 1991). (c) Primitive mantle normalized trace element spidergram for the MDB (Sun and McDonough, 1989).

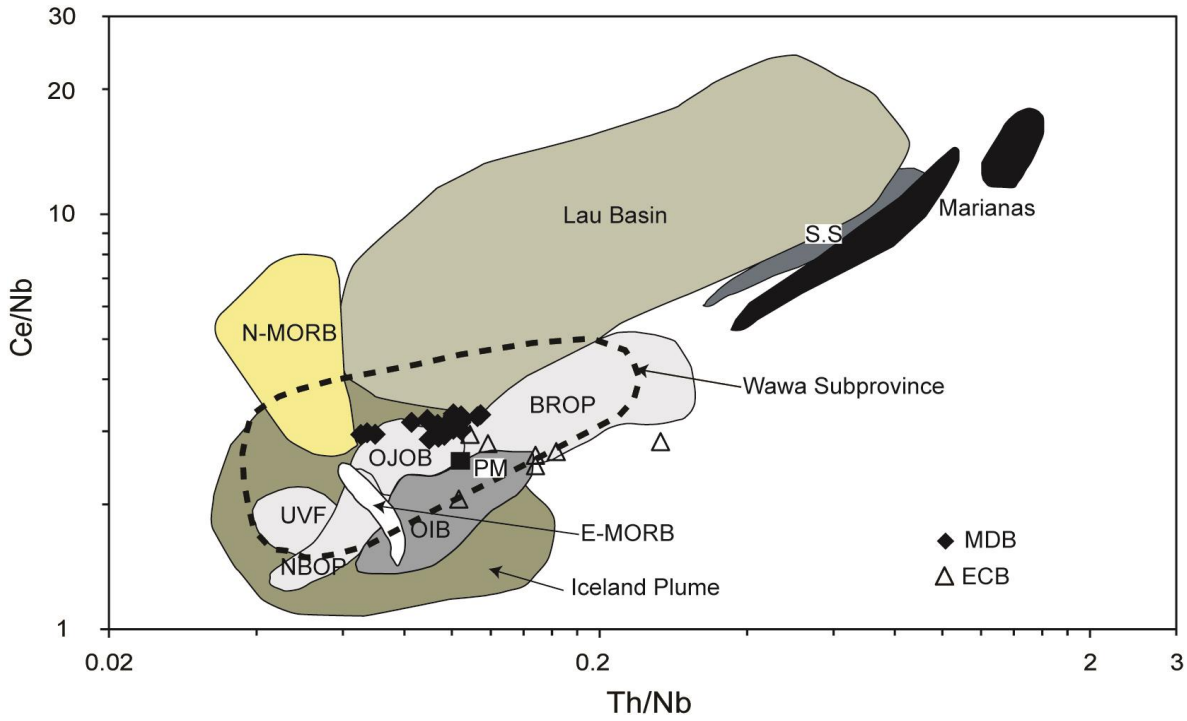

Figure 2.7 Ce/Nb vs. Th/Nb variation diagram, modified from Polat et al. (1999). The dashed line indicates the compositional domain of komatiites and basalts from the Schreiber- Hemlo and White River-Dayohessarah greenstone belts in the Wawa subprovince (Canada). El Callao Basalts (ECB: Venezuela) were taken from Velásquez et al. (2011). Fields for the Umu Volcanic Field (UVF), Nauru Basin (NB), Broken Ridge Oceanic Plateau (BROP), Ontong Java Oceanic Plateau (OJOP) and Iceland Plume are shown.

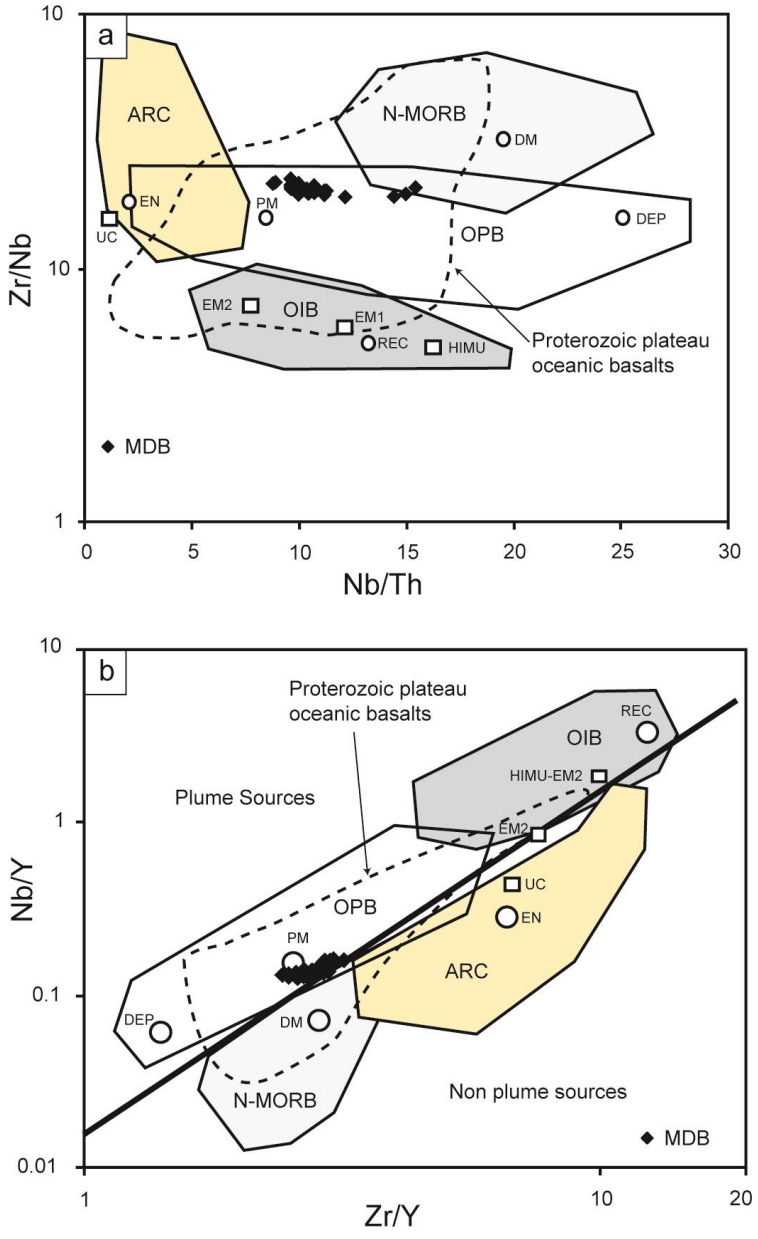

Figure 2.8 Diagrams showing mantle compositional components and fields for basalts. (a) Zr/Nb vs. Nb/Th diagram for the MDB. (b) Nb/Y vs. Zr/Y diagram. ARC: Arc-Related Basalts, OPB: Oceanic Plateau Basalts, N-MORB: Normal-Middle Oceanic Ridge Basalt, OIB: Oceanic Island Basalt, EN: Enriched Component, PM: Primitive Mantle, UC: Upper Continental Crust, DM: Shallow Depleted Mantle, REC: Recycling Component, DEP: Depleted Plume Component, HIMU: High μ(U/Pb) source. EM1 and EM2: Enriched Mantle Sources (Modified after Condie (2003), (2005)). The Proterozoic plateau oceanic basalts were obtained from Condie (2003).

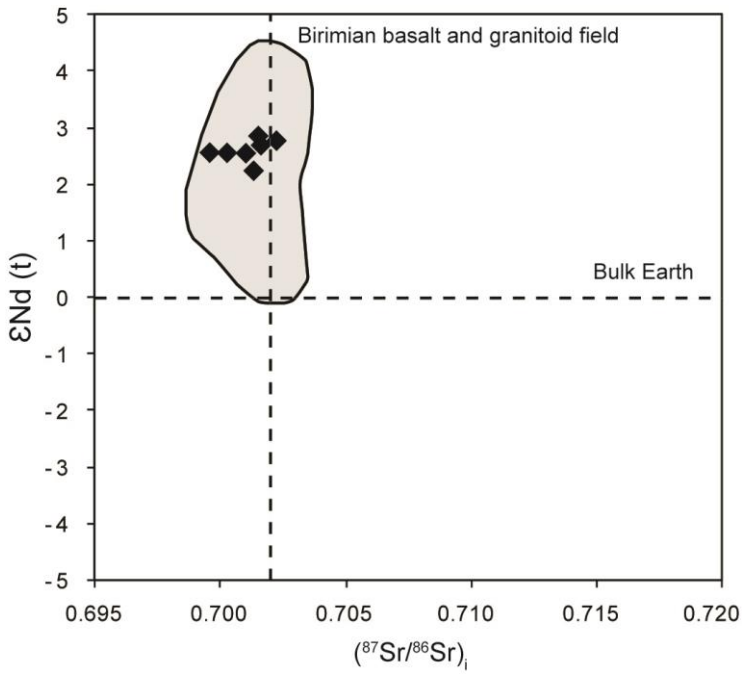

Figure 2.9 ($^{87}Sr/^{86}Sr)_i$ vs. εNd(t) plot for the MDB. Birimian basalt and granitoid fields from Pawling et al. (2006).

TABLEAUX CHAPITRE 2

Table 2.1 General characteristics of the Mana gold deposits.

Deposit Name	Gold (Moz)	Host rock	Structural Characteristics	Mineralization Style	Hydrothermal Alteration
Wona-Kona	4.0	Tholeiitic meta-basalts Meta-sediments Granodiorite	Regional structure Wona-Kona sinistral Shear zone	Quartz-sulfide veins. silicification and free gold	Quartz-sericite-chlorite-carbonates-epidote
Siou	1.7	Granodiorite Tholeiitic meta-basalts Tarkwaian-type sediments	Regional structure Boni sinistral Shear zone	Quartz-sulfide veins and free gold	Sericite-hematite-carbonates
Yaho	0.49	Meta-sediments	Sinistral shear zone	Disseminated and quartz-sulfide veins	Sericite-carbonates
Fofina	0.38	Tholeiitic meta-basalts Meta-sediments	Anticlinal fold	Quartz-sulfide veins	Chlorite-sericite-carbonates
Nyafé	0.37	Tholeiitic meta-basalts	Small scale structure dextral shear zone	Quartz-sulfide veinlets	Chlorite-epidote-carbonates

Table 2.2 Representative geochemical analyses of the Mana district basalts.

Sample	215284	215285	215286	245992	245996	245997	245998	245999	246000	246992	246995
Major elements (wt. %)											
SiO_2	48	48.7	46.7	48.8	47.2	47.9	48.9	48.7	47.9	48.6	49.6
Al_2O_3	13.4	12.75	13.7	14.2	14.55	14	14.3	13.9	14	13.8	13.95
Fe_2O_3	13.6	13.95	13.1	12.95	13.25	12.75	12.9	12.7	13.4	12.6	13.2
FeO	12.24	12.55	11.79	11.65	11.92	11.47	11.61	11.43	12.06	11.34	11.88
CaO	9.69	9.42	8.75	11.8	11.35	11	9.38	10.05	9.1	11.55	11.3
MgO	6.12	5.96	6.75	6.89	6.82	6.92	7.55	7.1	7.49	6.41	7.22
Na_2O	2.07	2.12	2.16	1.45	2.35	1.83	2.21	1.51	2.41	1.11	1.35
K_2O	0.08	0.08	0.06	0.03	0.07	0.17	0.14	0.08	0.08	0.02	0.05
TiO_2	1.18	1.28	1.12	1.11	1.11	1.1	1.12	1.1	1.17	1.09	1.12
MnO	0.2	0.2	0.2	0.2	0.21	0.21	0.19	0.2	0.21	0.19	0.2
LOI	2.77	2.16	2.83	2.68	2.5	2.45	2.88	2.87	2.95	2.9	2.4
Mg#	47.12	45.83	50.50	51.30	50.48	51.80	53.68	52.54	52.53	50.18	51.99
TOTAL	97.3	96.8	95.5	100.5	99.5	98.5	99.7	98.4	98.9	98.4	100.5
Trace elements (ppm)											
Ba	12.3	12.6	14.8	9	14.8	27.2	24.4	11.9	17.8	8.5	15.8
Rb	0.6	0.8	0.5	0.4	0.8	2.4	2.1	0.9	0.9	0.4	0.8
Sr	120.5	114	195	140.5	62.7	96.5	149	185.5	157	230	173.5
Cr	200	170	180	250	250	240	260	250	260	250	270
V	370	391	333	295	283	287	303	295	304	293	318
Cu	97	81	93	103	108	104	114	105	116	109	116
Co	59.1	56	58.6	50.4	51.8	50.7	51.5	49.8	52	50.7	53.7
Ni	88	68	109	116	123	118	116	111	111	111	134
Zn	102	102	101	98	102	88	95	93	91	96	112
Th	0.24	0.27	0.22	0.29	0.27	0.25	0.26	0.27	0.28	0.29	0.3
Nb	3.6	3.9	3.4	2.8	2.6	2.7	2.8	2.7	2.7	2.8	3
Zr	70	74	70	57	58	55	58	57	60	58	58
Hf	2.2	2.3	2.2	1.8	1.8	1.7	1.8	1.8	1.9	1.8	1.9
Y	23	24.9	21.6	19.7	19.2	19.6	20.6	19.9	20.3	20.1	23
La	4.3	4.4	3.9	3.5	3	3.2	3.4	3.5	3.4	3.4	3.9
Ce	10.8	11.6	10.1	8.9	7.9	8.3	8.8	8.7	8.9	8.9	9.6
Pr	1.73	1.83	1.6	1.39	1.25	1.31	1.38	1.39	1.4	1.4	1.45
Nd	8.5	9.2	8	7.3	6.7	6.9	7.3	7.3	7.5	7.4	7.4
Sm	2.89	3.05	2.7	2.3	2.17	2.29	2.41	2.34	2.39	2.42	2.47
Eu	1.02	1.07	0.99	0.88	0.82	0.89	0.98	0.9	0.88	0.94	0.96
Gd	3.7	3.94	3.29	2.94	2.86	2.85	3.1	3.02	3.11	3	2.88
Tb	0.6	0.66	0.56	0.53	0.5	0.52	0.55	0.54	0.56	0.52	0.57
Dy	4.11	4.36	3.79	3.63	3.53	3.53	3.83	3.62	3.88	3.75	3.93
Ho	0.83	0.91	0.79	0.79	0.74	0.74	0.79	0.77	0.8	0.79	0.83
Er	2.51	2.76	2.36	2.29	2.24	2.21	2.46	2.31	2.45	2.34	2.54
Yb	2.35	2.57	2.21	2.25	2.16	2.25	2.38	2.28	2.4	2.34	2.38
Lu	0.38	0.4	0.34	0.34	0.34	0.33	0.37	0.34	0.35	0.36	0.35
Ce/Nb	3	2.97	2.97	3.18	3.04	3.07	3.14	3.22	3.30	3.18	3.2
Th/Nb	0.06	0.07	0.06	0.10	0.10	0.09	0.09	0.1	0.10	0.10	0.1
Zr/Nb	19.44	18.97	20.59	20.36	22.31	20.37	20.71	21.11	22.22	20.71	19.33
Nb/Th	15.00	14.44	15.45	9.65	9.63	10.80	10.77	10	9.64	9.65	10
Nb/Y	0.16	0.16	0.16	0.14	0.13	0.14	0.14	0.14	0.13	0.14	0.13
Zr/Y	3.04	2.97	3.24	2.89	3.02	2.81	2.81	2.86	2.96	2.89	2.52
$(La/Nb)_N$	1.31	1.23	1.27	1.12	1	1.02	1.02	1.10	1.02	1.04	1.18
Eu/Eu*	0.95	0.94	1.01	1.03	1.01	1.06	1.10	1.03	0.99	1.07	1.10

Table 2.3 Rb-Sr and Sm-Nd isotopic compositions for selected basalts of the Mana district.

Sample	Rb (ppm)	Sr (ppm)	Sm (ppm)	Nd (ppm)	$^{87}Rb/^{86}Sr$	$^{87}Sr/^{86}Sr$	± 2σ	$^{147}Sm/^{144}Nd$	$^{143}Nd/^{144}Nd$	εNd (2.2 Ga)	$^{87}Sr/^{86}Sr$ (2.2 Ga)
V3ISO1	7.5	132	2.81	8.4	0.164	0.705433	0.000019	0.1948	0.512742	2.57	0.700217
V3ISO2	0.4	122.5	2.14	6.7	0.009	0.701868	0.000013	0.1964	0.512772	2.71	0.701568
V3ISO3	3.3	124.5	2.47	7.6	0.077	0.701954	0.000032	0.1966	0.512767	2.58	0.699522
V3ISO4	1	114.5	2.07	7	0.025	0.701788	0.000017	0.1990	0.512803	2.57	0.700967
V3ISO5	0.6	126.5	2.23	6.9	0.014	0.701901	0.000037	0.1964	0.512780	2.87	0.701466
V3ISO6	13	76.4	3.04	9.1	0.495	0.709320	0.000031	0.1852	0.512631	3.14	0.693612
V3ISO7	0.2	149	2.18	6.8	0.004	0.702313	0.000028	0.1972	0.512787	2.79	0.702190
V3ISO8	0.8	114	3.05	9.2	0.020	0.701923	0.000012	0.1924	0.512691	2.25	0.701279

CHAPITRE 3

3. Structural and gold mineralizing evolution of the world-class orogenic Mana District, Burkina Faso: Multiple mineralizing events over 150 million years

Jérôme Augustin, Damien Gaboury, Michel Crevier

Accepté pour publication le 2 août 2017 dans Ore Geology Reviews

3.1. RÉSUMÉ

Le district de Mana, situé dans la partie nord de la ceinture birimienne de roches vertes de Houndé à l'ouest du Burkina Faso, est un district d'or orogénique de classe mondiale (~8 Moz) comprenant cinq gisements d'or (Fofina, Nyafé, Siou, Wona-Kona et Yaho). Ces gisements sont localisés dans des domaines lithostratigraphiques spécifiques et l'or est contrôlé par divers éléments structuraux. La cartographie à l'échelle régionale et à l'échelle des gisements, l'âge des intrusions et la géochimie, ainsi que les données de géophysiques aériennes et de résistivités électriques, ont été utilisées pour déchiffrer l'évolution tectonique de chaque gisement aurifère et du district. Cinq évènements de déformation et quatre évènements de minéralisation aurifère ont été mis en évidence.

Le premier évènement de déformation ($D1_{MD}$: raccourcissement orienté E-W) a affecté les roches volcaniques et sédimentaires métamorphisées du groupe inférieur du Birimien. Cet épisode de déformation précoce a été corrélé avec la formation de plis (F_{1MD}) à plongement N et de failles chevauchantes de direction N-S contemporaines avec la mise en place des plutons pré- à syn-cinématiques de Wona-Kona et Siou datés à ~2172 Ma, en lien avec un métamorphisme aux faciès des schistes verts. Les veines de quartz-carbonates (V_{1MD}) de Fofina et Siou se sont formées durant la période éoéburnéenne $D1_{MD}$, manifestant le premier évènement aurifère autour de ~2172 Ma.

L'évènement de déformation suivant ($D2_{MD}$: extension orientée E-W) est associé avec la sédimentation du groupe Birimien supérieur (bassin de Mana) recouvrant le groupe

Birimien inférieur. La géométrie du bassin de Mana est contrôlée par les failles en cisaillement de Mana et Maoula. La formation des roches de type Tarkwaïenne recouvrant le groupe Birimien supérieur, contrôlée par les failles en cisaillement de Wona-Kona et de Siou, s'est formée à la fin de l'évènement $D2_{MD}$ ou au début de l'évènement $D3_{MD}$ avec un âge maximal de sédimentation de ~2113 Ma.

Le troisième évènement de déformation ($D3_{MD}$: transpression E-W à WNW-ESE) a affecté l'ensemble des roche supracrustales. Il est caractérisé par la formation de plis F_{3MD} à l'échelle de la carte et de failles en cisaillement dextres pendant l'orogénèse éburnéenne (~2113-2090 Ma). Un deuxième évènement minéralisateur s'est produit pendant la $D3_{MD}$ et se manifeste par des veines de quartz-carbonates (V_{3MD}) et des sulfures disséminés dans les gisements de Yaho, Fofina, Nyafé et de Wona-Kona.

Le quatrième évènement de déformation ($D4_{MD}$: transpression NNW-SSE) est corrélé avec du cisaillement sénestre le long des failles majeures transcurrentes et le développement de plis asymétriques (F_{4MD}) de direction NNE associés avec des axes de plis verticaux. La minéralisation Syn- $D4_{MD}$ est caractérisée principalement par une forte silicification (Si_{4MD}) avec de la pyrite disséminée et de l'arsénopyrite le long de la zone en cisaillement de Wona-Kona et par de petites veinules de quartz-carbonates (V_{4MD}). Cet évènement est considéré comme le principal épisode aurifère dans la partie ouest du district de Mana.

Le cinquième et dernier évènement de déformation ($D5_{MD}$) a un caractère cassant et a été responsable de la formation de clivages de crénulation E-W subverticaux et de failles

inverses sous un raccourcissement général N-S. Ce dernier évènement de déformation est potentiellement associé avec le dernier évènement aurifère enregistré comme de l'or libre en association avec de la muscovite dans des fractures cassantes développées dans les corps minéralisées des gisements de Wona-Kona et Siou. Cet évènement pourrait-être aussi jeune que ~2022 Ma, soit l'âge obtenu à partir de la datation Ar-Ar des schistes à muscovite du gisement de Wona-Kona.

Notre contribution principale est de mettre en évidence de multiples évènements de minéralisation aurifère à l'échelle du district basés sur la cartographie à l'échelle régionale et celle détaillée à l'échelle des gisements. Il a été interprété que l'or a été introduit dès ~2172 Ma et peut-être aussi tard que ~2022 Ma pendant au moins 3 à 4 évènements de raccourcissement tectonique durant une plage de temps qui n'avait pas encore été reconnue à l'échelle du district pour toutes les ceintures Birimiennes.

3.2. ABSTRACT

The Mana district, located in the northern part of the Birimian Houndé greenstone belt in western Burkina Faso, is a world-class Paleoproterozoic orogenic gold district (~8 Moz) including five gold deposits (Fofina, Nyafé, Siou, Wona-Kona and Yaho). These deposits are located in specific lithostratigraphic domains, and gold is controlled by various structural features. Deposit- and regional-scale mapping, intrusion age and geochemistry, as well as airborne aeromagnetic and electrical resistivity geophysical data, were used to

decipher the tectonic evolution of each gold deposit and the district. Five deformational and four gold mineralizing events were recognized.

The first deformation event ($D1_{MD}$: E-W oriented shortening) affected the metamorphosed volcanic and sedimentary rocks of the Lower Birimian group. This early deformation episode was correlated with the formation of gently N-plunging folds (F_{1MD}) and N-S-striking thrusts faults coeval with emplacement of the pre- to synkinematic Wona-Kona and Siou plutons dated at ~2172 Ma, under greenschist facies metamorphism. The quartz-carbonate veins (V_{1MD}) at Fofina and Siou formed during $D1_{MD}$ at Eoeburnean time, manifesting the first gold event at approximately ~2172 Ma.

The following deformation event ($D2_{MD}$: E-W oriented extension) is associated with the deposition of the Upper Birimian group (Mana basin) overlying the Lower Birimian group. The geometry of the Mana basin is controlled by the Mana and Maoula shear zones. The Tarkwaian-type rock formation overlying the Upper Birimian group, controlled by the Wona-Kona and Siou shear zones, is constrained at the end of $D2_{MD}$ or at the beginning of the $D3_{MD}$ event with a maximum deposition age at ~2113 Ma.

The third deformation event ($D3_{MD}$: E-W to WNW-ESE transpression) affected the entire supracrustal rock. Such event is correlated with the formation of map-scale F_{3MD} folds and dextral shear zones during the Eburnean orogeny (~2113-2090 Ma). A second gold mineralizing event occurred during $D3_{MD}$ and is manifested by quartz-carbonate veins

(V_{3MD}) and disseminated sulfides at the Yaho, Fofina and Nyafé and possibly Wona-Kona deposits.

The fourth deformation event ($D4_{MD}$: NNW-SSE transpression) is correlated with sinistral shearing along the major transcurrent faults and the development of asymmetric NNE-striking folds (F_{4MD}) associated with vertical fold axes. Syn-$D4_{MD}$ mineralization is characterized mainly by a strong silicification (Si_{4MD}) with disseminated pyrite and arsenopyrite along the Wona-Kona shear zone and by tiny quartz-carbonate veinlets (V_{4MD}). This event is considered the main gold-bearing event in the western margin of the Mana district.

The fifth and last deformation event ($D5_{MD}$) is brittle in character and was responsible for the formation of E-W subvertical crenulation cleavages and reverse faults under overall N-S shortening. This late deformation event is tentatively associated with a last gold event recorded as free gold associated with muscovite in brittle fractures developed in competent orebodies at the Wona-Kona and Siou deposits. This event could be as young as ~2022 Ma, the age obtained from Ar-Ar datation of muscovite-schists at the Wona-Kona deposit.

Our main contribution is that we decipher multiple gold mineralizing events at the district scale based on deposit- and regional-scale mapping. It is interpreted that gold was introduced as early as ~2172 Ma and possibly as late as ~2022 Ma during at least 3 or even 4 shortening tectonic events in a timeframe not yet recognized at the district scale for all the Birimian belts.

3.3. INTRODUCTION

Precambrian greenstone belts of the West African Craton (WAC) (Fig. 3.1a) host many orogenic gold deposits, especially in Ghana, Mali and Burkina Faso, with the latter being the third leading gold producing country in West Africa (Feybesse et al., 2006; Béziat et al., 2008; Markwitz et al., 2016; Robertson and Peters, 2016). Recent studies in the WAC based on structural, geochronological and geochemical data have documented some aspects of the genetic model for the formation of orogenic gold deposits related to the Eburnean orogeny between 2115 and 2000 Ma (e.g., Lawrence et al., 2013a and b; Masurel et al., 2017a and b for Mali; Oberthür et al., 1994; Allibone et al., 2002a and b; Feybesse et al., 2006; Perrouty et al., 2012; Block et al., 2016; Fougerouse et al., 2017 for Ghana; Béziat et al., 2008; Baratoux et al., 2015; Tshibubudze and Hein, 2016 for Burkina Faso; Lebrun et al., 2017a and b for Guinea). Gold-endowed granite-greenstone belts depend mainly on their structural architecture and the timing between polyphase deformation and hydrothermal events (Lawrence et al., 2013a; Tshibubudze and Hein, 2013; Lebrun et al., 2017b). Most gold deposits are hosted along or proximal to major first-order structures linked to a late stage of orogenic crustal growth (Allibone et al., 2002b; Lawrence et al., 2013a; Perrouty et al., 2014; Amponsah et al., 2016; Markwitz et al., 2016). However, multiple mineralization events are poorly constrained in time. The recent studies in the WAC showed two major gold mineralization events, which occurred during the Eburnean orogeny (Robertson and Peters, 2016). The first hydrothermal gold event is described in Ghana by Perrouty et al. (2012, 2015) in the Wassa gold deposit during the first D1 Eoeburnean event (2190-2160 Ma) in association with TTG granitoid emplacement (Parra-

Avila et al., 2015). The second gold-bearing hydrothermal event is associated with the Eburnean event (2130-2070 Ma) and is mostly controlled by regional-scale transcurrent faults (Baratoux et al., 2015; Perrouty et al., 2015; Le Mignot et al., 2017). Gold mineralization is concentrated along these regional-scale shear zones in association with gold-bearing quartz-sulfide veins or strongly silicified bodies (Augustin et al., 2016, Lawrence et al., 2013a; Tshibubudze and Hein, 2016). For the latter cases, most world-class deposits in the WAC also recorded a late remobilization of the early mineralization expressed as free gold in cracks, and this hydrothermal event accounts for higher-grade gold mineralization (Augustin et al., 2016; Hein, 2016; Salvi et al., 2016; Fougerouse et al., 2017). The Giant Obuasi gold deposit (62 Moz) is a good example of multiple mineralization events (Allibone et al., 2002a). The early mineralization is associated with disseminated gold-bearing arsenopyrite, whereas the visible gold is controlled by late fracturing and folding of quartz veins (Fougerouse et al., 2017).

In Burkina Faso, the Paleoproterozoic Birimian Houndé greenstone belt (HGB) is currently known as the richest gold-bearing belt (Fig. 3.1b), with historical production and cumulative resources of ~11 Moz, and it represents one of the largest orogenic gold districts in West Africa (Roxgold, 2013; Endeavour Mining, 2015; Semafo Inc., 2015; Sarama Resources, 2016; Augustin and Gaboury, 2017). The world-class Mana district (MD) is hosted in the northern part of the HGB, approximately 260 km SW of Ouagadougou. The MD is the richest segment, hosting five orogenic gold deposits within a 1000 km^2 area, including Fofina, Nyafé, Yaho, Siou and the world-class Wona-Kona (Augustin et al., 2016), for combined reserves, resources including inferred and production

of more than 8 Moz (Semafo Inc., 2015). All 5 orogenic gold deposits are characterized by different host rocks, structural features and mineralization styles (Augustin, 2011; Sinaré, 2013; Augustin et al., 2016) (Table 3.1; Fig. 3.2).

Such a variation in characteristics raises the question whether or not this related to local geological features or multiphase gold events. This question has major academic and exploration implications. For academic proposes, the MD is an ideal terrain for deciphering the link between the tectono-structural evolution of a belt and gold influx at a district scale. For mineral exploration, such a study will yield new exploration targets, regardless of whether there is only one major or numerous mineralizing events.

This paper presents new structural, geochronological, geochemical and geophysical data integrated with field mapping at deposit to regional scales. A structural analysis was carried out coupled with geochronological constraints to decipher the local structural evolution of the MD in conjunction with gold mineralization. It is demonstrated that gold deposits were formed by at least 3 to 4 different mineralizing events, with one very early event not previously recognized in the HGB, and that some deposits recorded multiple events. A very young age of ~2022 Ma yields a possible time frame of 150 Ma from the first to the last gold events. Moreover, deposit formation can be individualized relative to local or region-scale structural features, hence providing exploration guides.

3.4. GEOLOGY SETTING

3.4.1. THE BAOULÉ-MOSSI PALEOPROTEROZOIC DOMAIN

The Baoulé-Mossi Paleoproterozoic domain is flanked to the east by the Archean nucleus of the southern WAC (Fig. 3.1a). The Paleoproterozoic domain comprises the Birimian terrains (2.2-2.0 Ga) (Abouchami et al., 1990; Boher et al., 1992; Taylor et al., 1992; Hirdes et al., 1996) and form elongate linear to arcuate greenstone belts of metamorphosed volcanic, volcano-sedimentary and sedimentary rocks, separated by either extensive tonalite-trondhjemite-granodiorite (TTG) and granitoid provinces or by slightly younger sedimentary basins (Milési et al., 1989; Leube et al., 1990; Hirdes et al., 1996; Feybesse et al., 2006; Baratoux et al., 2011; Metelka et al., 2011) (Fig. 3.1a). The lithostratigraphic succession of the greenstone belt is composed from bottom to top of a mafic tholeiitic volcanic sequence overlain by calc-alkaline andesitic to felsic volcanic rocks and topped by volcano-sedimentary and sedimentary rocks (Milési et al., 1992; Hirdes et al., 1996; Pouclet et al., 1996; Feybesse et al., 2006; Baratoux et al., 2011). Numerous studies of the formation of the tholeiitic and calc-alkaline volcanic series have invoked a geotectonic setting of oceanic plateaus related to the mantle plume (Abouchami et al., 1990; Boher et al., 1992; Pouclet et al., 1996; Arndt et al., 1997; Albarède, 1998; Lompo, 2009; Baratoux et al., 2011; Augustin and Gaboury, 2017) and/or volcanic island arcs (Dia, 1988; Liégeois et al., 1991; Vidal and Arlic, 1994; Ama Salah et al., 1996; Béziat et al., 2000; Soumalia et al., 2004; Dampare et al., 2008; Baratoux et al., 2011; de Kock et al., 2012; Ganne et al., 2012) constrained by U-Pb ages between 2200 and 2160 Ma (Davis et al., 1994; Loh and

Hirdes, 1996; Lüdtke et al., 1999). The Birimian volcano-sedimentary units yield maximum deposition ages as young as 2130 to 2107 Ma (U-Pb detrital zircon age; Doumbia et al., 1998; Lüdtke et al., 1999) and are unconformably overlain by Tarkwaian syn-orogenic sedimentary sequences (conglomerates, phyllites and quartzites) with a maximum age of deposition varying between 2110 Ma and 2095 Ma (Davis et al., 1994; Pigeois et al., 2003; Perrouty et al., 2012).

Intense plutonic activity generated juvenile TTG suites between 2250 and 2060 Ma, which gradually evolved towards more-differentiated intrusions (potassic granites and alkaline syenites) until 2070 Ma (Milési et al., 1989; Ledru et al., 1991; Hirdes et al., 1996; Castaing et al., 2003; Gasquet et al., 2003; Naba et al., 2004; Feybesse et al., 2006; Pouclet et al., 2006; Agyei Duodu et al., 2009; de Kock et al., 2011; Tshibududze et al., 2015).

The Eburnean orogeny (Bonhomme, 1962) between ~2150 and 1980 Ma induced the structural features of the polydeformed Baoulé-Mossi domain, such as the NNE-SSW trending subvertical architecture of litho-tectonic units (Davis et al., 1994; Feybesse et al., 2006; Baratoux et al., 2011; Block et al., 2015). Recent studies have divided the Eburnean orogeny into 6 major deformation phases (Milési et al., 1989; Ledru et al., 1991; Allibone et al., 2002a and b; Feybesse et al., 2006; Tshibududze et al., 2009; Metelka et al., 2011; Perrouty et al., 2012; Lawrence et al., 2013a; Block et al., 2016). The first phase D1 (NE-SW to N-S shortening), is associated with a major crustal thickening related to the Eoeburnean, alternatively named the Tangaean (~2170-2140 Ma) (Tshibubudze et al., 2009; Hein, 2010; de Kock et al., 2011; Perrouty et al., 2012; Block et al., 2015). During

this first phase, a local extensional deformation phase, D2 (E-W extension), associated with exhumation of higher-grade lower crustal rocks and deposition of the Kumasi Group sedimentary rocks has been reported from northern and southern Ghana (Perrouty et al., 2012; Block et al., 2015). The second major Eburnean phase is related to E-W compression between ~2130 and ~2110 Ma D3 (NW-SE transpression) developing kilometer-scale folds and thrusts faults. The fourth phase, D4 (NNW-SSE transpression) is expressed by sinistral shear zones that reactivated syn-D3 thrust faults, and local D5 (WNW-ESE shortening) defined by small-scale recumbent folds after 2100 or 2070 Ma (Hirdes et al., 1992; Metelka et al., 2011; Jessell et al., 2012; Perrouty et al., 2012). The last phase, D6, is mainly documented in Burkina Faso and consisted of a N-S shortening referred as the Wabo-Tampelse event, which formed thrust faults and a spaced crenulation cleavage (Debat et al., 2003; Hein et al., 2004; Hein, 2010; Baratoux et al., 2011 and 2015; Augustin et al., 2016).

The Eburnean orogeny caused craton-wide metamorphism dominated by lower to upper greenschist facies in most of the volcanic and volcano-sedimentary rocks, with the formation of chlorite-muscovite-dominant mineral assemblages (Feybesse et al., 2006; Ganne et al., 2012; Jessell et al., 2012; Block et al., 2015). Ganne et al. (2012) have documented blueschist metamorphic facies in the eastern part of Burkina Faso. Local hornblende hornfels facies are developed as aureoles surrounding Eburnean granitoids (Debat et al., 2003; Pawling et al., 2006; Block et al., 2015) or along crustal-scale structures (Block et al., 2015).

The Birimian basement is unconformably overlain by the Neoproterozoic and younger sedimentary rocks of the Taoudeni basin (Deynoux, 1983; Bertrand-Sarfati et al., 1991) (Fig. 3.1) and is intruded by at least six generations of post-Eburnean doleritic dykes recorded craton wide (Jessell et al., 2015).

3.4.2. THE HOUNDÉ GREENSTONE BELT

The HGB is characterized by mafic to intermediary volcanic rocks occurring mostly in the central portion, whereas volcano-sedimentary and sedimentary units are distributed essentially along the belt flanks, following a NNE-SSW to N-S trend (Castaing et al., 2003; Baratoux et al., 2011; Metelka et al., 2011) (Fig. 3.1b). The MD is located in the northern portion of the HGB (Fig. 3.1b). According to Baratoux et al. (2011), the HGB's stratigraphy is characterized at the bottom by a thick sequence (4 - 6 km) of tholeiitic basalts and gabbro intercalated by an intermediary (mostly andesite) calc-alkaline sequence, including massive to pillowed lavas, tuffs, pyroclastic flows and, locally, diorites. Some of the volcanoclastic rocks and rhyolites were dated at 2212 ± 31 Ma and 2176 ± 4 Ma (U-Pb ages: Le Métour et al., 2003). This succession from tholeiitic to calc-alkaline volcanism manifests an evolution from an extensive oceanic plateau setting to volcanic arcs that formed between ~2200 and ~2160 Ma (Baratoux et al., 2011; Augustin and Gaboury, 2017) (Fig. 3.1b) and are known as the Lower Birimian group. The uppermost unit (Upper Birimian) consists of volcano-sedimentary and fine-grained

sedimentary rocks (volcanoclastics, argillites and wackes). Theses sedimentary units are interpreted to be younger than the main volcanic activity, as suggested by a minimum radiometric age of deposition of ~2160 Ma to ~2124 Ma (Hirdes et al., 1996; Lüdtke et al., 1999; Castaing et al., 2003; Baratoux et al., 2011). In the eastern margin of the HGB, shallow water detrital sedimentary rocks (Figs. 3.1b, 3.2), considered genetically similar to the Tarkwaian sedimentary rocks in Ghana (Feybesse et al., 2006), occur as an extensive ~400 km long by 1-2 km wide linear band along the Boni shear zone (BSZ) (Bossière et al., 1996; Koffi et al., 2016). These Tarkwaian-type sedimentary rocks overlie the Birimian supergroup (Lower and Upper Birimian groups), with maximum deposit ages of 2113 ± 23 Ma at Safané village along the BSZ (detrital zircon U-Pb: Bossière et al., 1996) to 2115 ± 2 Ma in the Ouango-Fitini belt, in northern Ivory Coast (detrital zircon U-Pb: Lüdtke et al., 1999) (Fig. 3.1b). Another, more restricted NE-trending Tarkwaian-type basin is also documented in the western margin of the northern part of the HGB (Baratoux et al., 2011), specifically in the MD (Figs. 3.1b, 3.2). All the volcanic and sedimentary rocks recorded mostly greenschist metamorphism and locally amphibolite facies. To the east and west, the HGB is bounded by granitoid domains, named Diébougou (DGD) and Sidéradougou (SGD) (Fig. 3.1b), with ages between ~2152 ± 2 Ma and 2097 ± 10 Ma (zircon U-Pb and Pb-Pb: Lüdtke et al., 1999; Chèvremont et al., 2003; Le Métour et al., 2003). Multiple episodes of granitoid injections have been distinguished (Fig. 3.1b) by Baratoux et al. (2011), such as the calc-alkaline tonalite-trondhjemite-granodiorite suite (TTG equivalent ME1), potassic granitic intrusions (ME2 and ME3) and small calc-alkaline gabbro-diorite bodies (ME4).

Baratoux et al. (2011) described three deformation events in the HGB during the Eburnean orogeny (~2160 and 1980 Ma) associated with the regional greenschist facies metamorphism. The Eburnean deformation phase $D1_{HGB}$ (~2160-2120 Ma) corresponds to an E-W to WNW shortening and is characterized by a penetrative metamorphic foliation (S_{1HGB}) in association with N to NNE shear zones and overturned folds (F_{1HGB}). Shallow-water detrital Tarkwaian-type sedimentary rocks were deposited during the late $D1_{HGB}$ event (~2120-2110 Ma). The second phase of the Eburnean orogeny, $D2_{HGB}$, affected both the Birimian supergroup and the Tarkwaian-type group. $D2_{HGB}$ is characterized by an E-W to WNW transpressional regime and is manifested by anastomosing steeply dipping NE to NNE transcurrent shear zones, which induced the elongate aspect of the belt (Fig. 3.1b). The S_{2HGB} fabric overprinted the $D1_{HGB}$ structures and the Tarkwaian-type sedimentary rocks in the BSZ under lower greenschist facies between ~2113 and ~2097 Ma. The last stage of deformation, $D3_{HGB}$, developed E-W crenulation cleavages, chevrons and kink folds, NE-SW normal faults and E-W thrust faults during N-S shortening. The timing of the $D3_{HGB}$ event is not well constrained and could be late Eburnean or even Pan-African (Nikiéma et al., 1993).

In the western margin, Neoproterozoic sedimentary rocks of the Taoudeni unconformably overlie the Birimian Supergroup basement (Deynoux, 1983; Bertrand-Sarfati et al., 1991).

At the HGB scale, most of the gold deposits are associated with ductile-brittle $D2_{HGB}$ shear zones and faults, such as the Vindaloo and Madras (resources of 2.5 Moz at an average grade of 2.1 g/t: Endeavour Mining, 2015), Bondi (resources of 0.4 Moz at an average

grade of 2 g/t.: Sarama Resources, 2016) and Bagassi (resources of 0.85 Moz at an average grade of 15 g/t: Roxgold, 2013) (Fig. 3.1b) deposits. These orogenic gold deposits are associated with disseminated gold-sulfide mineralization and quartz-carbonate veins. The Bagassi deposit is the highest-grade gold mineralization in the HGB, where a quartz vein system hosts visible free gold (Hein, 2016). The other gold deposits, such as Fofina, Nyafé, Yaho, Siou and Wona-Kona, are described in section 5.

3.5. METHODOLOGY

3.5.1. FIELD DATA

Fieldwork consisted of lithological and structural drill core logging and geological mapping of the MD. More than 3,500 outcrops were mapped with a dense array of lithological and structural observations (Fig. 3.3). The presence of a thick lateritic blanket (3-20 m) restricted the use of traditional mapping technique in some places. When possible, data from reverse circulation (RC) drill holes and diamond drill cores were used to determine the local stratigraphic succession. The stratigraphic sequence was thus established using field lithological, structural and interpretations of regional geophysical data. For each open pit mine (Fofina, Nyafé, Siou and Wona-Kona), a detailed map was produced with emphasis on the structural crosscutting relationships and gold mineralization styles and distribution. The geological setting and characteristics of the unmined Yaho deposit were established only from drill core data.

A major issue related to such an approach of linking local and regional structural features lies in the significance of the various structural fabrics in conjunction with specific tectonic events. To overcome this issue, each deposit was mapped following their own structural features. Planar features were reported in strike/dip quadrant and linear data as azimuth and plunge. At the regional scale, the main fabric was identified by S_p whereas at the deposit scale, the most primitive fabric was referenced as S_1, and others were incrementally numerated according to their chronological relationships. As such, local structural features are ascribed to local deformation events, but the link with regional events is established based on arguments (in the discussion section).

3.5.2. GEOPHYSICAL DATA

Geophysical data, including airborne aeromagnetic (first vertical and tilt derivatives, analytical signal) and electrical resistivity ground IP data provided by Semafo Inc., served to delineate large-scale structures such as shear zones, large-scale folds and dykes, and hence for refining the geological mapping. The magnetic data were acquired during 2009 and 2010 by SAGAX in the MD, with NW-SE oriented flight lines spaced at 100 m, 25 m from the ground, and 1,000 m NE-SW tie lines. The data were gridded using a 50 m pixel size. The total magnetic field data were reduced to the pole (MacLeod et al., 1993), used for the first vertical derivative (Fig. 3.3), were used to interpret structural and lithological boundaries. The electric resistivity data were acquired in 2010 by SAGAX in the MD's

central domain along lines striking NE-SW and separated by 200 m. The resistivity difference between the volcanic rocks (high resistivity ~85 to 1018 ohm-m) and volcanoclastic and sedimentary rocks (low resistivity ~8 to 48 ohm-m) was used to interpret the distribution of the strata.

3.5.3. WHOLE ROCK ANALYSIS

A total of 43 representative samples of intrusive rocks were used for this study (Fig. 3.2). They include 22 samples from the Siou pluton, 4 from the Wona-Kona pluton, 4 from the Kokoï pluton and 13 from felsic porphyry dykes (QFP) from the Fofina (n = 4), Nyafé (n = 2), Wona-Kona (n = 6) and Yaho (n = 1) deposits. Only fresh rocks (least-altered rocks) from drill cores located below 100 m were selected to avoid weathered rocks. The samples were analyzed by ALS Geochemical Laboratory of Vancouver in Canada. Analytical methods are described in Annexe 2.

3.5.4. ZIRCON U-Pb

Laser ablation age determinations on zircons from plutonic rocks were performed at the University of Montpellier (Géosciences Montpellier). U-Pb geochronology was undertaken to establish the ages of emplacement of the Siou, Wona-Kona, and Kokoï plutons and to

constrain the timing of the tectonic events (Fig. 3.2). Analytical methods are described in the Annexe 2.

3.5.5. Ar-Ar DATING

The $^{39}Ar/^{40}Ar$ method was used to date hydrothermal muscovite in close spatial association with the gold mineralization. Three samples taken from drill cores of the muscovite-schist unit at the Wona-Kona gold deposit (Fig. 3.2) were sent to the Noble Gas laboratory of the School of Earth Sciences at the University of Melbourne for dating following the method of Phillips and Miller (2006). Analytical methods are described in the annexe 2.

3.6. THE MANA DISTRICT

3.6.1. GEOLOGY OF THE MANA DISTRICT

The MD (Fig. 3.1a) contains 5 known gold deposits hosted in different rocks and structural features (Augustin, 2011; Sinaré, 2013; Augustin et al., 2016; Augustin and Gaboury, 2017) (Fig. 3.2, Table 3.1). According to field mapping, the lithostratigraphic sequence of the MD was divided informally into 3 groups (Fig. 3.4).

The first group is associated with the Lower Birimian volcanic and volcano-sedimentary rocks exposed as a window in the central and eastern domains. These rocks are intruded in

the eastern domain by the Siou pluton and the Diébougou granitoid domain (DGD) (Fig. 3.2). At the base, the MD is composed of tholeiitic volcanic series exhibiting distinctive volcanic pristine textures such as amygdules, pillow lavas, pillow breccias and hyaloclastite (Fig. 3.4). Local coarser-grained gabbroic sills and dykes are observed in drill cores from the Fofina and Nyafé open pits. These units are moderately to strongly magnetic (Fig. 3.3). Volcanoclastic and pelagic sedimentary rocks (black shale) with very thin beds define a 50-300-m-thick rock package intercalated within the tholeiitic suite and locally crosscut by mafic to intermediate sills (Fig. 3.4). The black shales are carbonaceous and locally pyritic. Abundant metric layers of cherts (ferruginous and manganiferous) are associated with the volcano-sedimentary rocks. The calc-alkaline volcanic series, including massive andesite, pillow lavas, pyroclastic flows and tuffaceous facies, occur at the top, associated with N- to NE-trending metric magnetic dioritic dykes that crosscut the entire Lower Birimian sequence, as evidenced by the magnetic map (Fig. 3.3). The NE- to SE-trending felsic QFP dykes intrude the base of the Lower Birimian sequence but are not observed in the calc-alkaline volcanic rocks (Figs. 3.2, 3.4). All the volcanic rocks underwent the greenschist metamorphism facies defined by the chlorite and epidote assemblage. These rocks were also affected by hydrothermal alterations with chlorite, muscovite, iron carbonates and local silicification with disseminated pyrite. Local amphibolite metamorphism facies is restricted to the contact aureole of intrusive rocks (Augustin and Gaboury, 2017). The Fofina and Nyafé gold deposits are hosted in this group (Fig. 3.2).

The second group corresponds to the Upper Birimian volcano-sedimentary rocks and is composed of thick to thin beds of wackes, siltstones and locally feldspathic sandstones with

some intercalations of flysch-related rocks (Figs. 3.2, 3.4). These rocks overlie the Lower Birimian and occur within a kilometric-scale basin referred to here as the Mana basin (Fig. 3.2), delimited by two NNE- to NE-trending faults: the Mana shear zone (MSZ) and the Maoula shear zone (MLSZ). The thickness of this group is not well constrained due to complex stacking and folding of the strata during the Eburnean orogeny. Muscovite and iron carbonates mineral assemblages suggest that the rocks are metamorphosed at greenschist facies conditions.

The third group of rocks is composed of shallow-water detrital Tarkwaian-type sedimentary rocks. These rocks occur in the eastern margin (Fig. 3.2), where they form a narrow NNE-trending basin controlled by the BSZ hosting the Siou gold deposit. Polygenic conglomerates, feldspathic sandstones with cross-beds defined by hematite and siltstones compose this third group (Fig. 3.4). The same type of detrital sedimentary sequence occurs in the western margin of the MD, controlled by the NE-trending Wona-Kona shear zone (WKSZ), which hosts the Yaho deposit (Fig. 3.2). Rocks of this group recorded hydrothermal alteration manifested by silicification, potassic and carbonate alterations. Chlorite-muscovite mineral assemblages are compatible with greenschist metamorphism facies. The origin of these sedimentary rocks is addressed in the discussion.

The MD is bounded by elongate plutons at its external western and eastern limits, named the Siou and Wona-Kona granodioritic plutons. These plutons are related to the TTG series (Fig. 3.2) and are considered representative of the first magmatic pulse (ME1) of Baratoux et al. (2011). These plutons are composed of plagioclase, K-feldspar (microcline), quartz

and biotite. The Siou pluton intrudes the Lower Birimian group and is affected by the BSZ. It is bounded to the east by the Diébougou granitoid domain (DGD) (Fig. 3.2). The Wona-Kona pluton is affected by the WKSZ, which is part of the Sidéradougou granitoid domain (SGD). Two smaller intermediate dioritic plutons (Kokoï and Mana, Fig. 3.2), controlled by the BSZ, crosscut the whole stratigraphic sequence and are interpreted to be younger than the TTG plutons. These plutons are considered representative of the third or fourth magmatic pulse (ME3/ME4) of Baratoux et al. (2011). The Kokoï pluton is outcropping locally, with an assemblage of plagioclase, amphibole, biotite and quartz. The Mana pluton has been delineated based on its magnetic signature (Fig. 3.3) and the bordering amphibolite facies in the adjacent country rocks.

A late SE-trending dioritic dyke crosscuts all the Birimian sequences but is affected by offset along the major shear zones (BSZ and WKSZ), probably related to late shear zone reactivation (Fig. 3.3).

In the western part of the MD, the Birimian basement is unconformably overlain by flat-lying sandstones of the Neoproterozoic Taoudeni basin and is intruded by a SE-trending high magnetic post-Eburnean doleritic dyke dated at 250 ± 13 Ma (Hottin and Ouedraogo, 1992) (Fig. 3.2).

3.6.2. STRUCTURAL FEATURES

Based on field mapping and interpretation of airborne data, 3 major shortening events can be deciphered associated with the 3 lithostratigraphic groups (Figs. 3.2, 3.3). These deformation events are only valid for the MD and will be addressed in the discussion regarding their regional signification.

The rocks of the Lower Birimian group have recorded all deformation events. In the central domain, the structural architecture is controlled by multiple kilometric isoclinal NS to NE axial F_p folds that are defined by the magnetic contrast between the volcanic and the volcano-sedimentary rocks highlighting the S_0 surface (Fig. 3.3). In the Lower Birimian, the stratification defines two large-scale synforms, which are separated by the Mana basin (Upper Birimian) (Figs. 3.2, 3.3). Two planar fabrics are observed: 1) a N to NNE steeply dipping S_p schistosity marked by the alignment of chlorite and 2) an overprinting NE steeply dipping S_{p+1} chlorite-muscovite schistosity associated with first and second-order shear zones (Fig. 3.3). The S_p fabric is well developed in the southern part of the central domain and is axial planar to Fp folds (Fig. 3.3).

In the eastern part, rocks of Lower Birimian group are affected by F_p folds with gently to steeply-plunging fold axes (i.e. 5 to 90°) (Fig. 3.3). The Siou pluton is also affected by a N to NNE, S_p schistosity, thus suggesting an early to syn-tectonic emplacement (Fig. 3.3). The S_{p+1} shear zones refolded F_p folds to form F_{p+1} folds with subvertical plunging axes in the central domain. The S_{p+1} shear zones host the Nyafé and Filon 67 deposits (Fig. 3.3).

Regionally, these parallel shear zones merge with the first-order NNE-trending MLSZ (Fig. 3.3), hence suggesting a genetic link. In the western part of the MD, tholeiitic basalts and the Wona-Kona granodioritic pluton are affected by the NE-trending WKSZ. Some SE-trending late fractures, faults and crenulation cleavages (S_{p+2}) are identified and crosscut the S_p and S_{p+1} fabric, representing a later deformation event (Fig. 3.3).

The Upper Birimian rocks are exposed as a block (Mana basin) bounded by the N- to NNE-trending MLSZ and MSZ, which lies oblique to the region-wide trend of the Lower Birimian group (Figs. 3.2, 3.3). The S_0 surfaces show significant variability in orientation with the development of isoclinal F_p folds with steeply plunging fold axes and axial-planar cleavage S_p (Fig. 3.3). S_p fabric is marked by the alignment of the muscovite. A second planar fabric, S_{p+1}, associated with ENE crenulation cleavage and steeply dipping brittle faults, is observed locally (Fig. 3.3).

The Tarkwaian-type group is associated and overprinted by two first-order N- to NE-trending shear zones characterized by a penetrative S_p schistosity defined by alignment of muscovite and iron carbonates. These shear zones are developed along the contacts between the greenstone belt and the granitoids (BSZ and WKSZ shear zones, Fig. 3.3).

In the western domain, the NE-trending WKSZ is delimited to the north and south by N-trending second-order horsetail structures (Fig. 3.2). An ENE-WSW S_{p+1} crenulation cleavage is observed in the Wona-Kona and Yaho deposits and in the southwestern part of the Wona-Kona pluton (Fig. 3.3).

In the eastern part, the Tarkwaian-type sedimentary rocks form a narrow (< 2 km) NNE elongate (> 100 km) basin bounded on both east and west sides by the BSZ, which also affected the Siou and Kokoï plutons (Figs. 3.1b, 3.3). Some of the NNE isoclinal F_p folds are developed with gently to steeply-plunging fold axes toward the north (i.e. 15 to 90°). The contact between the Kokoï pluton and the Siou pluton is affected by N- to NW-trending shear zones hosted in the tholeiitic basalts. The Siou pluton and the DGD are transected by NE-trending brittle-ductile shear zones (Fig. 3.3). At the northern apex of the Siou pluton, EW- to ENE-WSW trending thrust faults are developed. Finally, E-W steeply dipping S_{p+1} crenulation cleavages affect the Lower Birimian and Tarkwaian-type groups (Fig. 3.3). The ENE-WSW magnetic lineaments in the core of the Siou and Kokoï plutons are interpreted to be S_{p+1} (Fig. 3.3).

3.6.3. LITHOGEOCHEMISTRY

3.6.3.1. PLUTONS

The major and trace element compositions of the Wona-Kona, Siou and Kokoï plutons are presented in Table 3.2 and the Annexe 3. They cover a wide range of silica contents: from 58 to 62 wt.% SiO_2 for the Kokoï pluton and from 68 to 76 wt.% SiO_2 for the Wona-Kona and Siou plutons. In the QAP classification diagram of Streckeisen (1976), the modal compositions of the samples plot in the fields of granodiorite for the Wona-Kona-Siou and granodiorite to tonalite for the Kokoï plutons (Fig. 3.5a). Most plutonic samples plot

between the calc-alkaline-trondhjemitic and calc-alkaline-granodioritic trends of Lameyre and Bowden (1982). On the SiO_2 vs. $Na_2O + K_2O$ binary diagram of Cox et al. (1979), the Kokoï pluton plots in the field of diorite, whereas the Wona-Kona-Siou granodiorites plot in the field of granite (Fig. 3.5b). The Kokoï pluton shows elevated Mg# (56-62) with respect to granodiorites (Mg# = 15-46) and felsic QFP dykes (Mg# = 8-68).

The trace element geochemistry of these plutons are presented in chondrite-normalized rare earth element (REE) spectra and in primitive mantle-normalized multi-element diagrams (Fig. 3.6). These plutons exhibit fractionated multi-element patterns with negative HFSE (Nb-Ta-Ti), P anomalies and positive Pb anomalies, typical of crustal material (Martin, 1994). All the samples have similar fractionated REE patterns suggesting that they share a common origin but with variable differentiation rates.

The Wona-Kona and Siou plutons have similar chondrite-normalized REE patterns (Fig. 3.6a, b). They exhibit light rare earth element (LREE) enrichment with $(La/Yb)_N$ ratios of 16.9-42 and heavy rare earth element (HREE) depletion with $(Gd/Yb)_N$ ratios of 2.5-4.2. No negative Eu anomaly is present (Eu/Eu* = 0.93-1.31), suggesting that plagioclase was not a main phase in the residual source region (Martin et al., 2005). On primitive mantle spidergrams (Fig. 3.6a, b), the samples are enriched in LILEs such as Rb, Ba, Th, U and Pb and are depleted in HFSEs such as Nb, Ta, Ti and P. Negative anomalies in Nb, Ta and Ti are typical of magma generated in an arc-tectonic context (Jahn et al., 2008). The negative P anomaly may be explained by apatite fractionation during magmatic differentiation (Jahn

et al., 2008). Niobium, Ta and Ti negative anomalies are linked to the presence of a titaniferous phase or amphibole in the residue (Martin, 1994 and 1999).

The Kokoï dioritic samples have similar REE patterns (Fig. 3.6c) with slightly fractionated ($(La/Yb)_N$ = 15.6-17.5) and no Eu anomaly (Eu/Eu* = 0.96-1.07). The HREEs show a depletion, with $(Gd/Yb)_N$ ratios of 2.4-2.5. On primitive mantle spidergrams (Fig. 3.6c), the samples are enriched in LILEs such as Rb, Ba, Th, U and Pb and are depleted in HFSEs such as Nb, Ta, Ti and P.

3.6.3.2. FELSIC QFP DYKES

The major and trace element compositions of the Fofina, Nyafé, Wona-Kona and Yaho felsic QFP dykes are presented in Table 3.3 and the Annexe 4. They contain 68.3 to 76.6 wt.% of SiO_2, 1.02 to 2.38 wt.% of Fe_2O_3 with low MgO (0.16 to 1.28 wt.%) and high concentrations of Na_2O (1.03 to 4.60 wt.%) and K_2O (1.74 to 4.37 wt.%). Their magnesium numbers (Mg#: (Mg/Mg+Fe)) range from 8.09 to 68.67, suggesting different pulses. These samples plot in the fields of monzogranite to granodiorite (Fig. 3.5a). Based on REEs (Fig. 3.6d), the felsic QFP dykes show two different patterns, implying two groups: QFP1 and QFP2. The QFP1 rocks have fractionated REE patterns, with $(La/Yb)_N$ ratios of 15.8-25.8, and HREE depletion, with $(Gd/Yb)_N$ ratios of 1.6-2.6 and a discrete negative Eu anomaly (Eu/Eu* = 0.71-0.88) (Fig. 3.6d). On primitive mantle spidergrams, they are enriched in LILEs such as Rb, Ba, Th and Pb and are depleted in HFSEs such as Nb, Ta, Ti and P. The

QFP1 characteristics are very similar to the Wona-Kona and Siou plutons (Fig. 3.6d). The QFP2 samples are characterized by LREE enrichment ($(La/Yb)_N$ = 3.7-16) relative to HREEs ($(Gd/Yb)_N$ = 1.3-1.8), with an obvious negative Eu anomaly (Eu/Eu* = 0.48-0.73). On primitive mantle spidergrams, these samples are clearly different from the QFP1 group (Fig. 3.6d), implying a different origin compared to the Wona-Kona and Siou plutons. Spatially, the QFP1 dykes occur at the Fofina, Nyafé and Wona-Kona mines, whereas the QFP2 dykes were encountered at the Yaho deposit and the Wona-Kona mine.

3.6.4. GEOCHRONOLOGY

3.6.4.1. LA-ICP-MS U-Pb ZIRCON AGES FROM SELECTED PLUTONS

Three major plutons (Wona-Kona, Siou and Kokoï) were dated according to their spatial relationship with gold deposits. The analytical data are presented in Table 3.4.

Sample I1C24B from drill hole was obtained from the eastern part of the Wona-Kona pluton and represents a coarse-grained granodiorite (Fig. 3.2). A total of 26 analyses were performed on 22 zircon grains (Table 3.4). The zircon crystals are characterized by elongate shapes with variable sizes and some fractured, ranging from 100 to 300 µm long (Fig. 3.7a, b). Numerous grains show an oscillatory zoning concordant with the external shape and suggesting a magmatic growth (Vavra, 1990). All the spots define a discordia line (MSWD = 0.14) giving a well-defined upper intercept of 2173 ± 7 Ma and a lower

intercept of 117 ± 540 Ma (Fig. 3.7c). Twenty-five central oscillatory zoned domains are concordant within errors and provide a $^{207}Pb/^{206}Pb$ weighed mean age of 2172 ± 6 Ma (MSWD = 0.15), which is interpreted as the age of crystallization of the Wona-Kona granodiorite.

Sample I1C25B was collected from the western part of the Siou pluton from a coarse-grained granodiorite body with the same texture as the Wona-Kona granodiorite (Fig. 3.2). A total of 26 spots were performed on 21 zircon grains (Table 3.4). The grains are euhedral to subhedral with elongate shapes and size ranging from 100 to 300 µm. Growth zones highlighted by cathodoluminescence are visible only in some grains (Fig. 3.7d, e). It is noteworthy that where the grains preserved euhedral to subhedral shapes, the central oscillatory zoned domain is, in some grains, transgressed by a featureless zircon domain (Fig. 3.7d). A close examination of the data (see Table 3.4) indicates that the central oscillatory-zoned domains have Th/U ratios ranging from 0.18 to 0.61, whereas transgressive featureless domains tend to have lower Th/U ratios, ranging from 0.04 to 0.25. This suggests that the featureless outer domain corresponds to the replacement of the oscillatory-zoned domain, probably through recrystallization processes (Pidgeon, 1992; Pidgeon et al., 1998). The preservation of the euhedral external morphology is consistent with a pseudomorphic replacement and a static recrystallization process of pre-existing zircons. When both domains are present within one single grain (r1g1, r3g4; Table 3.4), the Th/U ratios in both domains are almost identical, suggesting that recrystallization may not have been sufficient to expel Th outside the zircon lattice. However, the younger calculated ages (see below) are systematically associated with the unzoned domains, indicating that

the U-Pb system has been reset, which is in agreement with the highest retention of Th compared to Pb in the zircon lattice. Following this, analytical results were subdivided into three populations (Fig. 3.7f, g).

The first population corresponds to zoned central parts of the grains. These results provide a $^{207}Pb/^{206}Pb$ weight mean age of 2176 ± 8 Ma (MSWD = 0.1; n = 10) (Fig. 3.7f), which is interpreted as the age of emplacement and crystallization of the Siou granodiorite. This age is similar to the Wona-Kona granodiorite age (2172 ± 6 Ma) (Fig. 3.7c).

The second population corresponds to featureless external domains and yields a younger $^{207}Pb/^{206}Pb$ weight mean age of 2135 ± 11 Ma (Fig. 3.7f). This age is interpreted as resulting from recrystallization of the pre-existing magmatic zircons and is similar to the second magmatic pulse identified by Baratoux et al. (2011) in the Houndé greenstone belt and corresponds to the main metamorphic peak in the Lawra belt in northern Ghana (Block et al., 2015).

In addition to the two main populations, two zircon grains r1g3-2c and r2g12 provided ages as old as 2219 ± 24 Ma and 2308 ± 24 Ma (Fig. 3.7f). These ages are interpreted as inheritance in the source of the granodiorite or as older material assimilated during ascent and emplacement of the pluton.

Sample I1C20B, from the Kokoï pluton to the south of the Siou deposit, is a coarse-grained diorite (Fig. 3.2). A total of 9 grains were analyzed (9 spots in total, Table 3.4). The grains are subhedral and fine-grained (<150 µm), with no visible zonation (Fig. 3.7h). All 9 spots

define a discordia line (MSWD = 1.13) with an upper intercept of 2090 ± 7 Ma and a lower intercept at -104 ± 110 Ma (Fig. 3.7i). The 2090 ± 7 Ma age is interpreted as the age of crystallization of the Kokoï pluton.

3.6.4.2. $^{39}Ar/^{40}Ar$ DATATION

Three samples of muscovite-schists hosted by tholeiitic basalts along the WKSZ (Figs. 3.2, 3.8a) were dated. Hydrothermal muscovite occurs as a major phase in the main gold mineralization of the Wona-Kona deposit formed along the main S_{p+1} schistosity (Fig. 3.8a, b) (Augustin et al., 2016). Late S_{p+2} crenulation cleavages crosscut the S_{p+1} (Fig. 3.8b) which could be associated with the late gold remobilization event described by Augustin et al. (2016). Consequently, the Ar-Ar geochronology has the potential to constrain a minimum age of the muscovite crystallization during the main gold event or a later gold remobilization event.

The $^{39}Ar/^{40}Ar$ analytical results for muscovite from the Wona-Kona gold deposit (sample SE2, SE4, SE7) are presented in Fig. 3.8, and the analytical results are presented in Table 3.5. The term “integrated age” is used there, as it is common usage for an apparent age obtained from the summed argon released from step heating and their associated uncertainties. The three muscovite samples yielded plateau ages ranging from 2017 ± 11 to 2032 ± 11 Ma (2σ), with MSWD and P values ranging from 0.62 to 1.3 and 0.29 to 0.54 (Fig. 3.8c, d, e). They also show a range of apparent ages from 1790 ± 14 to 2329 ± 21 Ma.

Overall, the plateaus, including an ^{39}Ar release of less than 62.6 %, suggest that the samples registered post-crystallization disturbances. Sample SE2 (Fig. 3.8c) shows dips in pseudoplateaus that are probably related to a younger event (or events) in which fluid percolated and disturbed the K-Ar systematics (Villa, 2010). The pattern of decreasing apparent ages with increasing temperatures (Sample SE4) suggests that the muscovite may have been partially altered by a younger event related to a partial loss of radiogenic argon (Fig. 3.8d). Finally, sample SE7 also has disturbed spectra, showing an irregular pattern with 5 pseudoplateaus giving an identical integrated age of 2022 ± 11 Ma (Fig. 3.8e).

3.7. MANA GOLD DEPOSITS

For descriptive purposes and synthesis, the deposits are divided into central, eastern and western domains according to their position relative to the belt geometry. The lithostratigraphy, structures, mineralization styles, and alteration assemblages are presented for each deposit (Table 3.1).

3.7.1. THE CENTRAL DOMAIN

The central domain includes deposits (Fofina and Nyafé) hosted in the Lower Birimian sequence (Figs. 3.2, 3.4). After their description, a tentative correlation of the mineralization phases and structural features is proposed.

3.7.1.1. FOFINA DEPOSIT

The Fofina gold deposit (Fig. 3.9) is located in the central southern part of the MD (Figs. 3.2, 3.3) and is mined by two open pits (the Fofina main zone and the V1-V7 zone). These 2 orebodies occur over a strike length of 1 km and with current reserves and resources of 0.42 Moz at a grade of 3.6 g/t Au (Semafo Inc., 2015) (Table 3.1). The mineralization is refractory and mostly exploited in the weathered profile.

The Fofina lithostratigraphy consists of an assemblage of metamorphosed tholeiitic basalts in the eastern part (V1-V7) and sedimentary and volcanoclastic rocks in the western part (Fig. 3.9). The tholeiitic basalts contain plagioclase and pyroxene overprinted by secondary alteration phases such as chlorite, epidote and albite. These expose a volcanic facies that changes toward massive flow, pillow-lavas and volcanic-breccia, indicating normal polarity. The volcano-sedimentary rocks overlie the tholeiitic basalts in the Fofina main zone and are composed of interbedded volcanoclastites (Fig. 3.10a), siltstone and graphitic black shales rich in nodular pyrite (Fig. 3.10b). Based on the drill hole data, all the units are crosscut by a SE-trending felsic QFP1 dyke with quartz and plagioclase feldspar phenocrysts in a quartz-muscovite matrix. This dyke is affected by dextral displacement and is overprinted by a planar fabric (Figs. 3.9, 3.10c).

The earliest structural component, $D1_F$, consists of N-trending steeply E-dipping axial planar schistosity (S_{1F}) crosscutting the bedding (S_0) in the open pit (Figs. 3.9, 3.10d). Anticlinal F_{1F} folds associated with S_{1F} schistosity have fold axis plunging gently to

moderately (20-40°) toward the north (Fig. 3.9). In the sedimentary rocks, the mineralization is stratoid, with disseminated, porous and fine-grained nodular pyrite forming a 30-45-m-thick band with quartz-carbonate veins (V_{1F}) along the contact between black shale and tholeiitic basalts within the anticlinal hinge (F_{1F}) (Fig. 3.10b, d). The hydrothermal alteration is characterized by carbonates (ankerite-calcite) and weak silicification aligned with the S_{1F} schistosity. In the basaltic rocks, boudinaged and folded quartz-carbonate veins (10 - 100 cm: V_{1F}) associated with chlorite and a local pervasive silicification (Fig. 3.10e) are developed in the eastern part following the W-dipping stratification defined by breccia and pillow basalts and locally along the E-dipping hinge of F_{1F} folds (Figs. 3.9, 3.10e). Gold occurs with euhedral pyrite and arsenopyrite (Fig. 3.10e). Gold grades in the Fofina main zone are commonly > 4.0 g/t.

The second deformation, $D2_F$, is manifested by NNE-trending shear zones (S_{2F} = N030/75) developed in anisotropic rocks such as black shale but also in basaltic rocks (Fig. 3.9). Kinematic indicators such as C-S_{2F} fabric relationship, slickenfibres on fault wall and felsic QFP dykes offset indicate dextral displacement (Figs. 3.9, 3.10f, g). Locally, in the volcano-sedimentary units, the S_{1F} fabric and V_{1F} quartz-carbonate veins are refolded to form NNE-trending F_{2F} folds in association with the S_{2F} axial planar schistosity (Fig. 3.9). The second phase of mineralization is associated with the S_{2F} shear zones, occurring as V_{2F} fault-fill and related extensional quartz- veins and veinlets (Fig. 3.9). The grey-white quartz veinlets (V_{2F}) and quartz veins are concentrated in Fofina V1-V7 pit (Fig. 3.10h). The veins are 10 to 300 m long and 5 to 30 cm wide. This vein generation is undeformed and crosscuts the V_{1F} quartz vein, with an oblique N020-N035 trend and 75° to 90° E-dipping

(Fig. 3.9). Chlorite and muscovite define the hydrothermal alteration enveloping the V_{2F} veins with local iron carbonate (ankerite) along the S_{2F} schistosity (Fig. 3.10h). Gold is associated with sulfide phases, including pyrite and traces of arsenopyrite and chalcopyrite with an average grade of 3 g/t (Fig. 3.10h).

3.7.1.2. NYAFÉ DEPOSIT

The Nyafé gold deposit is located 2 km to the northeast of the Fofina deposit and was mined with four open pits (Figs. 3.2, 3.11). The mine produced 0.37 Moz at an average grade of 6 g/t Au (SGS, 2009) (Table 3.1). The Nyafé mineralization is split into two tabular orebodies, referred to as Nyafé main and Filon 67 (Fig. 3.11). Nyafé main was mined along 2.4 km, whereas Filon 67, which is a satellite lode, was followed for 500 m (Fig. 3.11). The mineralization is refractory, like the Fofina deposit, and was only exploited in the oxidized superficial part.

The Nyafé and Filon 67 deposits are hosted in a sequence of metamorphosed tholeiitic basalts exhibiting distinctive pristine volcanic textures, such as amygdules, pillow lavas, pillow breccias, gabbro sills and hyaloclastic with submarine hydrothermal alterations composed of epidote, chlorite, and localized albite (Figs. 3.11, 3.12a, b). All units are crosscut by SE-trending metric felsic QFP1 dykes similar to the one at Fofina and are affected by muscovite alteration (Figs. 3.11, 3.12c). All of the Nyafé and Filon 67 pits have good pillow-lava exposures defining a NE-trending S_0 stratification (Fig. 3.12b). The

pillows are up to 1 m in size and show typical features such as convex shapes, peduncles and amygdule concentrations, indicating a systematic reversed polarity plunging moderately (40-50°) to the SE, hence indicating an early reverse folding or thrusting (Figs. 3.11b, 3.12b).

The structural architecture of Nyafé and Filon 67 are controlled by three deformation events. The early structural component, $D1_N$, consists of a discrete N- to NNE-trending steeply E-dipping schistosity (S_{1N} = N030/80 - Fig. 3.11) affecting the tholeiitic but not the QFP1 dykes (Fig. 3.12c). This event may be associated with the reverse folding or thrusting towards the NW.

The second deformation, $D2_N$, is manifested by two brittle-ductile NE-trending second-order shear zones, with a S_{2N} chlorite-muscovite schistosity mapped in the Nyafé and Filon 67 open pits (Figs. 3.11, 3.12d). These shear zones are 2-10 m wide, are traced across a 2.5 km length and are developed in tholeiitic basalts and the felsic QFP1 dykes (Figs. 3.11, 3.12a). The S_{2N} shear zones are associated with C-S_{2N} subvertical fabric (N045 to N060) with a subhorizontal striation lineation L_{2N} (N045/05), compatible with a dextral displacement (Fig. 3.12d, e). However, in the southern part of the Nyafé main pit, two felsic QFP1 dykes show a sinistral displacement with a 5 m offset (Fig. 3.11), suggesting a late reactivation of the shear zones.

The same type of mineralization is observed in the Nyafé and Filon 67 pits and is characterized by quartz veinlets (V_{1N}) forming a stockwork that is crosscut by late quartz-

carbonate veins (V_{2N}) (Fig. 3.12d). The quartz veinlets (V_{1N}) are folded by the S_{2N} fabric and are associated with arsenopyrite, minor pyrite and, locally, chalcopyrite with no free gold (Fig. 3.12f). High grade is mostly associated with the V_{1N} (> 7.0 g/t). The alteration assemblage consists mainly of muscovite with lesser chlorite and iron carbonates (siderite/ankerite) (Figs. 3.12d, f). They are hosted along the shear zones, and gold mineralization cuts across the felsic QFP1 dykes (Figs. 3.11, 3.12f). The quartz-carbonate veins (V_{2N}) are boudinated along the C-S_{2N} fabric and contain calcite with rare sulfides, no free gold and low grade gold (< 1.0 g/t) (Fig. 3.12d). The alteration assemblage consists mainly of minor muscovite and chlorite (Fig. 3.12d).

The late event, $D3_N$, is characterized by N100 to N130 steeply dipping brittle fractures and faults filled by weathering minerals without mineralization (Figs. 3.11, 3.12g).

3.7.1.3. CORRELATION BETWEEN THE FOFINA AND THE NYAFÉ DEPOSITS

Based on 700 structural measurements coupled with the electric resistivity map, where major stratification trends can be mapped, two major deformation events (Fig. 3.13) can be individualized. The local structural framework is mainly controlled by a major E-W shortening phase, $D1_{F\text{-}N}$, that produced N-trending kilometric-scale isoclinal folds ($F_{1F\text{-}N}$) associated with the V_{1F} quartz-carbonates veining in the Fofina deposit (Figs. 3.9, 3.13b, c). The second deformation, $D2_{F\text{-}N}$, is associated with an E-W shortening phase that formed a

series of NE-trending isoclinal folds (F_{2F-N}) that refolded F_{1F-N} with fold axes plunging (20-90°) to the NE and SW (Fig. 3.13b, c). Although spaced, the S_{2F-N} planar fabric axial to F_{2F-N} is mostly manifested by well-defined second-order NNE- to NE-trending dextral shear zones (Fig. 3.13). These shears zones contain the V_{2F} veins of the Fofina (Fig. 3.9) and the V_{1N}-V_{2N} veins of the Nyafé and Filon 67 deposits (Fig. 3.11). The late $D3_{F-N}$ deformation is recognized only in the Nyafé deposit and is manifested by minor N100 to N130 faults and fractures associated with NS to NNE-SSW shortening (Figs. 3.11, 3.12g).

3.7.2. THE EASTERN DOMAIN - SIOU DEPOSIT

The Siou deposit is located in the eastern domain 15 km from the Wona-Kona gold deposit (Fig. 3.2). The Siou mineralization has been defined over a strike length of approximately 2 km and is spatially associated with the first-order BSZ (Fig. 3.3). Gold mineralization is located close to the faulted contact between the Tarkwaian-type group to the west and the Siou pluton to the east (Fig. 3.14), but essentially within the pluton. With current gold reserves of 1 Moz at 6 g/t Au (Semafo Inc., 2015), it is the second-largest gold deposit in the MD (Table 3.1).

The host rocks comprise the Tarkwaian-type sedimentary rocks on the western side of the mineralized zone and the Siou granodiorite pluton to the east (Figs. 3.4, 3.14). The Tarkwaian-type is composed of polygenic sandstone conglomerate intercalated with pelitic feldspathic sandstone and siltstone (Fig. 3.15a, b). In the open pit, the S_0 bedding is not

visible close to the contact, because the sedimentary rocks are strongly deformed and schistose. However, Gaboury (2014) mapped open folds with subhorizontal NNE-trending axes affecting the S_0 in the upper benches of the pit.

Some lenticular bodies of massive tholeiitic basalts are intercalated along the contact between the granodiorite pluton and the detrital sedimentary rocks in the northern portion of the open pit (Fig. 3.14). These enclaves have an assemblage of calcite, chlorite and magnetite (Fig. 3.14) and are interpreted to represent the relic of the Lower Birimian rocks (Fig. 3.4).

In the open pit, three main structural events can be recognized (Fig. 3.14). The first event, $D1_S$, is expressed by approximately 40-m-wide N-trending reverse brittle faults (N010/50) developed within the Siou pluton associated with a S_{1S} schistosity marked by alignment of muscovite (Fig. 3.15a, b, c). The mineralization is characterized by two boudinated white quartz veins (V_{1S}) with some interconnected veins and veinlets (Fig. 3.15b). They are 1.5 to 2 km long and 50 cm to 5 m wide, with an assemblage of quartz and rare sulfides (minor pyrite, arsenopyrite and chalcopyrite) (Fig. 3.15c, d). These veins are confined along the N010/40-50 shear zone (Fig. 3.15b). The geometric arrangement between fault-fill and shallow-dipping tension veins indicates reverse displacement along the shear zone during gold mineralization (Fig. 3.15b, c).

The mineralization is surrounded by a proximal muscovite halo in the granodiorite, with minor iron carbonates and a distal hematite halo to the east (Figs. 3.14, 3.15b). The

muscovite flakes form millimetric seams parallel to the thrust zone and crosscut the V_{1S} (Fig. 3.15c).

The second event, $D2_S$, is manifested by a S_{2S} schistosity (N040/75) that is only developed in the Tarkwaian-type sedimentary rocks associated with barren white quartz veinlets (Figs. 3.14, 3.15e). The hydrothermal alteration assemblage is characterized by chlorite, calcite and lesser muscovite aligned with the S_{2S} schistosity (Fig. 3.15e).

The third event, $D3_S$, is expressed by the brittle-ductile N-trending steeply dipping BSZ (S_{3S}), which is traced at the regional scale by the magnetic image (Fig. 3.3). In the pit, the BSZ is manifested by N010-trending S_{3S} to C-S_{3S} muscovite fabric with a steeply (80°) to moderate (55°) dip to the east (Fig. 3.15a, e) and associated stretching lineation (L_{3S} = N010/05) (Fig. 3.15f). The C-S_{3S} fabric overprints the Tarkwaian-type sedimentary rocks. The geometrical relationships are compatible with a sinistral displacement (Fig. 3.15e). The BSZ shows an oblique E-dipping of 20° to 25° cutting the main gold-bearing veins (V_{1S}) (Fig. 3.15a). However, in the SW portion of the magnetic map (Fig. 3.3), a N135 dioritic dyke, crosscutting all stratigraphic units, is cut by the BSZ and is displaced dextrally for 1 km. Such dextral offset is interpreted as a late reactivation of the BSZ. The $D3_S$ shear zone also overprints the Siou pluton, where some fractures crosscut the main gold-bearing veins (V_{1S}) (Fig. 3.15c). Some free visible gold grains with muscovite and galena are hosted in the late factures in the V_{1S} quartz veins and are interpreted as a late higher economic gold grade (> 6 g/t) (Fig. 3.15d).

3.7.3. THE WESTERN DOMAIN

3.7.3.1. THE WONA-KONA DEPOSIT

The world-class orogenic Wona-Kona deposit is the largest gold deposit in the MD. This orebody is hosted along the major NE-trending regional-scale WKSZ, defined along 5 km (Fig. 3.3), and was exploited in two open pits (Wona and Kona) (Fig. 3.16). The gold production was 1.2 Moz, with reserves of approximately 0.9 Moz at the end of 2014 at an average grade of 2.3 g/t Au (Semafo Inc., 2015) (Table 3.1).

Augustin et al. (2016) described the structural and mineralization characteristics of the Wona-Kona deposit. The orebody is hosted along the contact between an assemblage of tholeiitic basalt and volcano-sedimentary rocks (Fig. 3.16). The volcano-sedimentary rocks are formed by interbedded mafic magnetic volcanoclastic rocks and graphite-rich black shale with disseminated primary pyrites associated with the Lower Birimian group (Figs. 3.4, 3.17a). The tholeiitic basalts have an aphanitic texture with various proportions of epidote, chlorite, actinolite and albite associated with metric NE-trending muscovite-schists in the Kona pit (Figs. 3.8a, 3.16). NE-trending felsic QFP1-QFP2 and intermediate dykes crosscut all the units and are overprinted by the mineralization (Figs. 3.16, 3.17b, c). Wona-Kona pluton is overprinted by a hematite hydrothermal alteration (Fig. 3.17d).

The structural evolution of the Wona-Kona deposit is characterized by three deformation events (Augustin et al., 2016). The first deformation ($D1_{WK}$) is manifested by N to NNE vertical S_{1WK} chlorite schistosity and S_{1WK} foliation in the Wona-Kona pluton marked by

alignment of hematite (Figs. 3.16, 3.17d). The second deformation ($D2_{WK}$) is correlated with the formation of NE-trending ductile-brittle shear zones associated with S_{2WK} muscovite-iron carbonates schistosity (N045/80), and it occurs only in highly strained rocks (Figs. 3.16, 3.17a). The C-S_{2WK} relationships, with a shallow plunging striation lineation (L_{2WK} = N045/20), indicate a dextral displacement (Fig. 3.17b, c, e). The first and main gold mineralization event corresponds to a strong silicification (Si_{2WK}) with disseminated pyrite and arsenopyrite, crosscut by tiny quartz-carbonate veinlets (V_{2WK}) surrounded by a large hydrothermal alteration halo of muscovite and iron carbonates (ankerite/siderite) (Augustin et al., 2016) (Fig. 3.17a). This mineralization is hosted along S_{2WK} shear zone with average gold grade of 2.3 g/t (Figs. 3.16, 3.17a).

In the northwestern part of the Kona pit, muscovite schists hosted in volcanic rocks as well as felsic QFP dykes are present but are not gold-bearing (Figs. 3.8a, 3.16). The last deformation, $D3_{WK}$, is characterized by an E-W-trending subvertical S_{3WK} crenulation cleavage (N070/85) developed in highly strained rocks, especially in volcanoclastic rocks and muscovite-schists (Figs. 3.8b, 3.16, 3.17f). Some kinematic indicators suggest a possible reactivation of the silicified mineralized zone during a brittle-like deformation associated with the remobilization and precipitation of free gold in late microfractures (Fig. 3.17g) (Augustin et al., 2016). This later mineralizing event is the richest of the Wona-Kona deposit.

3.7.3.2. THE YAHO DEPOSIT

The Yaho deposit is a low-grade gold system located in the southeastern part of the MD and is associated with second-order horsetail faults of the WKSZ (Figs. 3.2, 3.3). The main body is traced along 2 km (Fig. 3.18) and has current indicated resources of approximately 1 Moz (average grade of 1.0 g/t Au, Semafo Inc., 2013) (Table 3.1). Because the Yaho deposit is not mined, geological information was mostly extracted from drill cores and from a few outcrops (Sinaré, 2013).

The Yaho deposit is interpreted to be hosted within a steeply-inclined fold with a vergence towards the east and associated with a subhorizontal N-trending axis. In detail, the lithostratigraphic succession is divided into three distinct sedimentary units: 1) polygenic conglomerates, 2) feldspathic sandstones, and 3) siltstones. The polygenic conglomerates are the oldest occurring in the core of the anticlinal fold. These are composed of several types of centimetric to metric pebbles (rhyolite, felsic QFP, siltstone, quartz, chert and wacke) (Fig. 3.19a). Some of the rhyolitic pebbles are affected by a schistosity that must have been formed at an earlier stage before erosion and sedimentation (Fig. 3.19b). The polygenic conglomerates are surrounded by a feldspathic sandstone layer showing cross-bedding structures (Fig. 3.19c). The siltstones are locally interbedded with thin beds of wackes (Fig. 3.19d). The sedimentary rocks are intruded by metric felsic QFP2 dykes with quartz and plagioclase feldspar porphyroblasts in a quartz-muscovite groundmass, but their trend is not identified (Figs. 3.18, 3.19e). In the western margin, the sedimentary units are bounded by tholeiitic basalt of the Lower Birimian group (Fig. 3.18).

Three deformation events are recognized in the Yaho deposit. The first deformation, $D1_Y$, is manifested by a NNW- to N-trending S_0-S_{1Y} muscovite fabric axial planar to the F_{1Y} anticlinal fold, with dipping at approximately 70° to the W (Fig. 3.18). The D_{1Y} event is associated with an E-W shortening. Related to $D1_Y$, bedding-parallel smoked quartz veins (V_{1Y}) and carbonate-veinlets (1-15 cm) with minor pyrite and arsenopyrite are folded by an anticlinal F_{1Y} fold (Fig. 3.19f). Primary disseminated pyrite grains follow the bedding in the detrital sedimentary rocks, suggesting some primary mineralization or an early syn-$D1_Y$ hydrothermal event (Fig. 3.19c). These two mineralization styles are not economic with an average grade at 0.4 g/t.

The second deformation, $D2_Y$, is related to the formation of a NNW- to N-trending W-dipping ductile-brittle shear zone associated with the S_{2Y} muscovite-iron carbonate schistosity (N342/80) developed in the core of the Yaho anticlinal F_{1Y} (Fig. 3.18). The rare outcrops expose elongate pebbles parallel to the S_{2Y} and local sigma-shaped clasts, indicating an apparent sinistral displacement along the shear zones (Fig. 3.19h). However, no clear stretching lineation was observed. The second and main mineralization type related to $D2_Y$ corresponds to a metric subvertical silicification (Si_{2Y}) surrounded by a hydrothermal alteration halo of muscovite and iron carbonates hosted in the polygenic conglomerates (Fig. 3.18). Pyrite and arsenopyrite occur with the silicified zone and contain the highest gold grade mineralization (> 2 g/t), but without free gold (Fig. 3.19g) (Sinaré, 2013).

The late deformation, $D3_Y$, forms E-W-trending subvertical S_{3Y} crenulation cleavages (N260/70) developed only in strongly foliated polygenic conglomerate and sandstone (Figs. 3.18, 3.19i).

3.7.3.3. CORRELATION BETWEEN THE WONA-KONA AND YAHO DEPOSITS

The Wona-Kona and Yaho deposits are hosted along the WKSZ, a major structural feature delimiting the western limit of the MD. In the airborne magnetic map (Fig. 3.3), the WKSZ defines a major NE-trending discontinuity with N-trending horsetail structures at both of its extremities, where Tarkwaian-type sedimentary rocks appear to have accumulated.

One of the main difficulties in correlating deformation events is that both deposits are hosted in different rocks formed at different times but along the same interpreted structural feature. Major faults record all the tectonic events, commonly at a point where is it difficult to totally decipher their evolution. In the present case, however, $D1_{WK}$ is recorded by Lower Birimian rocks, whereas $D1_Y$ is recorded in Tarkwaian-type sedimentary rocks. Clearly, a direct and simple correlation of fabrics is not possible at this stage, but it is discussed below.

3.8. DISCUSSION

The MD recorded complex interrelationships among stratigraphic sequence, several phases of pluton emplacement, felsic QFP1-2 dyke injections, and multiple tectonic and mineralizing events. The applied methodology of integrating field, geophysical data and the datation of granitoids and the geochemistry of intrusive rocks allow us to subdivide the tectonic evolution into 5 sequential deformation events, termed $D1_{MD}$ to $D5_{MD}$, associated with 4 gold mineralizing events. These events are summarized in Fig. 3.20 and are discussed below. Finally, the proposed evolution of the MD is compared to the documented deformational and mineralizing events from other greenstone belts in the WAC (Fig. 3.21).

3.8.1. STRUCTURAL EVOLUTION OF THE MANA DISTRICT

The MD records a long tectonic history, including phases of shortening and extension, manifested by structural fabric development and sedimentary basin filling, respectively. Furthermore, the major deformation corridors bordering the belt, have recorded a complex history of reactivation, commonly dissipated by fabric reworking, hence limiting our total characterization and understanding of all tectonic events. The tectonic evolution proposed below is based on an integration of regional and deposit-scale field data including airborne magnetic data, radiometric ages and relationship between the lithostratigraphic sequence and the structural fabric.

3.8.1.1. COMPRESSIONAL $D1_{MD}$

The first deformation event, $D1_{MD}$, is clearly recognized in the Lower Birimian basement units (Fig. 3.4) and corresponds to large-scale N- to NNE-trending F_{1MD} folds with fold axes plunging moderately to the north (Figs. 3.2, 3.13). This deformation is also related to the formation of the bordering faults, such as the WKSZ and BSZ, where rocks were verticalized and strongly foliated. In the F_{1MD} folds, V_{1MD} quartz-carbonate veins in the Fofina deposit (equivalent to V_{1F}) were developed parallel to S_0 bedding and overprinted by subsequent deformation (Fig. 3.10d). These F_{1MD} folds are associated with an axial plane S_{1MD} schistosity that trends NS to NNE, with a vertical dip documented in the Fofina and Nyafé pits (S_{1F}-S_{1N}, Figs. 3.9, 3.11). In the Nyafé pit, the reversed polarity of the pillow lavas (Fig. 3.12b) indicates a tectonically overturned fold induced by at least two structures: 1) a reverse fold or 2) a thrust fault during the $D1_{MD}$, but our understanding of this deformation remains unclear. The $D1_{MD}$ is recorded only by rocks of the Lower Birimian group (Figs. 3.2, 3.3). Furthermore, the NE- to SE-trending felsic QFP1 dyke swarm observed in the Lower Birimian sequence (Fofina and Nyafé deposits) crosscuts the F_{1MD} folds, hence constraining the $D1_{MD}$ deformation to an event before the felsic QFP1 dyke injection. These felsic QFP1 dykes show similar trace and rare earth elements as the Wona and Siou plutons, suggesting a possible co-genetic link with these plutons (Fig. 3.6d). However, the QFP1 dykes are apparently devoid of S_{1MD} schistosity and are absent in the calc-alkaline volcanic series affected by $D1_{MD}$. All these factors imply that the QFP1 dykes were likely injected at the end of the $D1_{MD}$ deformation but without having reached the

upper part of the stratigraphic succession (calc-alkaline supracrustal rocks of the Lower Birimian group and rocks of the Upper Birimian group).

In the eastern margin, the Siou pluton and the Diébougou granitoid domain are affected by N-trending S_{1MD} schistosity (Fig. 3.3). In the western domain, the Wona-Kona deposit records a N- to NNE-trending vertical schistosity (S_{1WK}) affecting the Lower Birimian group and the Wona-Kona pluton (Figs. 3.16, 3.17b, d). Consequently, it is interpreted that the Siou (2176 ± 8 Ma: Fig. 3.7f) and Wona-Kona (2172 ± 6 Ma: Fig. 3.7c) plutons were emplaced during pre- to early-$D1_{MD}$.

In the Siou deposit, N-trending and E-dipping thrust faults ($D1_S$) associated with the development of V_{1S} quartz veins are hosted in the Siou pluton but are absent in the Tarkwaian-type rocks (Fig. 3.15). There is no evidence allowing the age of the $D1_S$ to be clearly constrained, but the N005/50 reverse fault with a moderate dip (50° to the east) is compatible with an E-W shortening phase during either the $D1_{MD}$ or $D3_{MD}$ event (Fig. 3.20).

The $D1_{MD}$ deformation is interpreted to be the result of an E-W shortening event during an early to syn-tectonic emplacement of the Wona-Kona and Siou plutons at ~2172 Ma (Fig. 3.20).

3.8.1.2. EXTENSIONAL $D2_{MD}$

The $D2_{MD}$ extensional deformation is proposed here to account for the sedimentary rocks occurring along the fault-bounded NNE-trending Mana basin and to be coherent with the literature. However, there is no structural evidence of extension on the field. The volcano-sedimentary rocks sit on the $D1_{MD}$ deformed calc-alkaline sequence of the Lower Birimian, implying a later deposition event (Figs. 3.2, 3.3). The absence of felsic QFP1 dykes cutting across the Upper Birimian rocks suggests a deposition after 2172 Ma (pluton ages). According to the stratigraphic sequence (Fig. 3.4), the Upper Birimian rocks were deposited after ~2170 and before ~2113 Ma. The Mana basin may be thus a dropped bloc of upper stratigraphic rocks delimited by regional faults (MSZ and MLSZ).

The Tarkwaian-type rocks form linear basins commonly exposed along the major faults (BSZ and WKSZ) (Fig. 3.2). Tarkwaian-type deposition was dated at the east margin of the Houndé belt (Safané), with a maximum age of 2113 ± 23 Ma controlled by the BSZ (Bossière et al., 1996). These rocks are thus younger than the Upper Birimian rocks, but no relationship is exposed (Fig. 3.2). In the western domain (Fig. 3.2), the detrital sedimentary rocks observed in the Yaho deposit are composed of polygenic conglomerates (rhyolite, quartz, chert, felsic QFP, wacke), feldspathic sandstones associated with cross-bedding structures and siltstone (Sinaré, 2013) (Fig. 3.19). These characteristics are similar to Tarkwaian-type sequence defined in the Siou deposit (Fig. 3.15) and by Bossière et al. (1996) and Baratoux et al. (2011). The rhyolitic and QFP pebbles must be part of the Lower Birimian, as described in the Houndé belt by Le Métour et al. (2003) and this study. The

large proportion of wacke pebbles is probably sourced from the Upper Birimian group, as recorded in the Mana basin. Although the Upper Birimian and Tarkwaian-type basins are known to be of different ages, they could have been linked: the Tarkwaian-type basin may have recorded more proximal and more temporally extended sedimentation along active major faults, whereas the Upper Birimian group may represent a more distal environment (Baratoux et al., 2011; Koffi et al., 2016). The tectonic context of sedimentation for both groups is far beyond the scope of this study.

3.8.1.3. TRANSPRESSIONAL $D3_{MD}$

The $D3_{MD}$ deformation marks the transition from an extensional to a shortening regime, manifested mostly by the formation of F_{3MD} folds and related S_{3MD} schistosity in the Birimian supergroup and the Tarkwaian-type group (Fig. 3.3). F_{3MD} is interpreted in the Yaho deposit (Fig. 3.18), defined by a slightly E-reversed isoclinal antiform fold (F_{1Y}), with a subhorizontal N-trending axis. Bedding-parallel smoked quartz veins (V_{1Y}) occur along F_{3MD} fold-layers but are overprinted by later events (Fig. 3.19f). The overall fold asymmetry (Figs. 3.3, 3.18) may be related to the shearing of the fold during late $D3_{MD}$ or related to the later $D4_{MD}$ deformation. Felsic QFP2 dykes are hosted in detrital sedimentary rocks of the Yaho deposit and are affected by the deformation events (Fig. 3.19e). The QFP2 dykes should have been injected after the Tarkwaian-type deposition (~2113 Ma).

Since QFP2 dykes also occur at the Wona-Kona deposits, this later dyking event is interpreted to be spatially related to the WKSZ.

In the Siou deposit, the NE S_{2S} schistosity is only developed in the Tarkwaian-type sedimentary rocks and, thus, must be related to the S_{3MD} schistosity and later reoriented by the C-S_{4MD} fabric during the $D4_{MD}$ (Figs. 3.14, 3.15e). In the upper part of the pit, now mined out, Gaboury (2014) reported open folds affecting the bedding in Tarkwaian-type sedimentary rocks with a subhorizontal NNE-trending axis (Fig. 3.3) and axial schistosity (S_{2S}) that are now ascribed to $F_{3MD.}$ These structural features observed in Tarkwaian-type rocks are likely related to activity within the BSZ.

In the Mana basin, some subhorizontal NNE-trending folds were observed in the volcano-sedimentary sequence, which are interpreted to be contemporaneous with the $D3_{MD}$ deformation event (Fig. 3.3).

Overall, $D3_{MD}$ results from an E-W to WNW-ESE shortening, developing subhorizontal folds and related schistosity in younger rocks (Fig. 3.20). However, such a shortening event should also have induced fault reactivation along already verticalized and strongly foliated rocks, such as along the WKSZ and BSZ corridors, as well as overprinting of rocks already folded (Fig. 3.3). The NE-trending WKSZ, especially in the Wona-Kona area, is well-oriented for dissipating dextral movement during $D3_{MD}$, accounting for the dextral displacement indicated by the fabric relationships (Fig. 3.16). Specifically, the C-S_{2WK} fabric relationships, with a shallow plunging striation lineation (L_{2WK} = N045/20), is

compatible with a dextral displacement (Fig. 3.17c, e). In the Nyafé and Fofina pits, the NE-trending gold-bearing structures are also compatible with the dextral displacement during $D3_{MD}$ (Figs. 3.10f, g, 3.12d, e). Such a $D3_{MD}$ shortening accounts for the reshaping of the initial N-oriented $F_{1F\text{-}N}$ to the more-NE-trending $F_{2F\text{-}N}$ (Fig. 3.13), with shearing development in their axial planes ($S_{2F\text{-}N}$).

It is interpreted that $D3_{MD}$ shortening event induced folds in younger rocks and dextral movement along NE-oriented major faults compatible with a transpressional regime. This event is time bracketed after the maximum deposition age of the Tarkwaian-type group (~2113 Ma) and before the $D4_{MD}$ (post ~2090 Ma) (Fig. 3.20).

3.8.1.4. TRANSPRESSIONAL $D4_{MD}$

The $D4_{MD}$ is mostly related to movement along the major faults, where structural features indicate a sinistral displacement related to a NNW-SSE shortening (Fig. 3.20). The Siou deposit records a NNE C-S_{3S} fabric with subhorizontal stretching lineation (L_{3S} = N010/05) (Figs. 3.14, 3.15e, f) that is compatible with a sinistral strike-slip reactivation of the BSZ corridor during $D4_{MD}$. At the regional scale, some discrete oblique NE-trending shear zones crosscut the Siou pluton and the Lower Birimian group with a sinistral kinematic, as interpreted by the magnetic lineament offset (Fig. 3.3). In the southeastern part, two NNW- to NW-trending shear zones border the Kokoï and Siou plutons (Fig. 3.3). The kinematic is unknown, but the same shear zones are defined out of the MD in the Bagassi region (Fig.

3.1b) with a $D1_{BAG}$ sinistral kinematic (Hein, 2016). The BSZ also dissipated a major apparent dextral offset, as recorded in the SW portion of the magnetic map (Fig. 3.3), where a dioritic dyke is displaced for 2 km. Because the age of this dyke is known, the dextral displacement may be related to $D3_{MD}$ or a late brittle movement.

In the western domain, the Yaho deposit is affected by a NNW- to N-trending W-dipping ductile-brittle shear zone associated with the S_{2Y} schistosity (N342/80) (Figs. 3.3, 3.18). The sigma-shaped clasts are compatible with a sinistral displacement temporally related to the weak pervasive silicification (Fig. 3.19g, h). Consequently, it is interpreted that the $D4_{MD}$ sinistral shearing overprinted the F_{3MD} anticlinal fold with weak silicification and muscovite alteration.

In the Mana basin, the development of vertical folds, especially along the bonding faults in the Upper Birimian group, is related to the reactivation of the MSZ and MLSZ (Fig. 3.3). The S-shaped asymmetry of the folds is compatible with a sinistral displacement along the MSZ and MLSZ (Figs. 3.2, 3.3).

The timing of the $D4_{MD}$ event is constrained by the Kokoï pluton emplacement dated at ~2090 Ma (Fig. 3.7i). In the western domain, the young Ar-Ar age of the muscovite schists at ~2022 Ma from Wona-Kona suggests that the muscovites were partially affected by a younger event (Fig. 3.8). This younger event could be related to late the $D4_{MD}$ or to $D5_{MD}$ deformations (see below). The $D4_{MD}$ deformation is interpreted to be related to a NNW-SSE shortening during a transpressional regime expressed by the reactivation of major

faults as a sinistral strike-slip movement bracketed between ~2090 Ma and ~2022 Ma (Fig. 3.20).

3.8.1.5. DEFORMATION $D5_{MD}$

The final deformation event, $D5_{MD}$, is characterized by a subvertical E-W trending (Fig. 3.20) crenulation cleavage (S_{5MD}) overprinting all earlier planar fabrics (Figs. 3.3, 3.20). The S_{5MD} cleavage is mostly developed in strongly schistose and anisotropic rocks (Wona-Kona = S_{3WK}, Yaho = S_{3Y} and Nyafé = fractures and faults: Figs. 3.8b, 3.11, 3.16, 3.18). The S_{5MD} is related to a N-S shortening event (Fig. 3.20). Finally, some E-W N-dipping thrust faults (north of Bouna village - Fig. 3.3) and late brittle NW-SE faults and fractures in the Nyafé deposit could have a genetic link with the $D5_{MD}$ deformation (Fig. 3.11).

3.8.2. GOLD MINERALIZATION EVENTS

The MD exposes three main styles of gold mineralization that could be related to the $D1_{MD}$, $D3_{MD}$, $D4_{MD}$ and/or $D5_{MD}$ shortening events (Figs. 3.10, 3.12, 3.15, 3.17, 3.19, 3.20).

The early gold mineralization event is clearly recognized in the Fofina deposit during the syn-$D1_{MD}$ deformation (~2172 Ma) associated with a N-trending F_{1MD} anticlinal fold (Fig. 3.9). The mineralization style is characterized by V_{1MD} quartz-carbonate veins accompanied

by a local pervasive silicification hosted along the contact between volcano-sedimentary rocks and tholeiitic basalts and within the tholeiitic basalt (Lower Birimian group) (Fig. 3.10d, e). Gold is associated with euhedral pyrite and traces of arsenopyrite (Fig. 3.10e).

In the Siou deposit, N-trending E-dipping thrust faults ($D1_S$) are associated with the development of V_{1S} quartz veins hosted in the Siou pluton (Fig. 3.14). These veins contain a minor pyrite-arsenopyrite assemblage and are cut by muscovite bands (Fig. 3.15c, d). The $D1_S$ faults are compatible with an E-W shortening from either the $D1_{MD}$ or $D3_{MD}$ events. Because no gold and no muscovite alteration are present in the Tarkwaian-type rocks (Fig. 3.15a), the mineralizing event is constrained during the $D1_{MD}$ event (~2172 Ma) (Fig. 3.20).

The Fofina and Siou deposits are thus examples of early gold mineralization related to $D1_{MD}$ during greenschist conditions (chlorite, silicification, carbonates and muscovite alterations). The heat generated by the synkinematic Siou and Wona-Kona plutonic bodies likely favored hydrothermal fluid circulation at ~2172 Ma (Fig. 3.20).

The second gold mineralizing event is related to the $D3_{MD}$ deformation, in association with the F_{3MD} folds and dextral shearing in all stratigraphic units (Fig. 3.20). In the western domain, the Yaho deposit is defined by V_{3MD} bedding-parallel smoked quartz veins and carbonate-veinlets (V_{1Y}) (1-15 cm), with minor gold-bearing pyrite and arsenopyrite (Fig. 3.19f). Primary disseminated pyrite grains in the detrital sedimentary rocks suggest an early formation during the Tarkwaian-type deposition or during syn-$D1_Y$ hydrothermal event (Fig. 3.19c).

In the central domain, the Fofina and Nyafé deposits expose the same type of quartz-carbonate veins and veinlets (V_{2F} and V_{1N}-V_{2N}) controlled by two NNE- to NE-trending second-order dextral shear zones (Fig. 3.13). These veins are commonly characterized by smoky to white quartz with ankerite-calcite-pyrite-arsenopyrite assemblages associated with chlorite and muscovite hydrothermal alteration (Figs. 3.10h, 3.12d). The gold is associated mainly with arsenopyrite and pyrite, hence explaining the more refractory character of the mineralization for both deposits. The timing of the second gold mineralizing event is constrained between the Tarkwaian-type group deposition (~2113 Ma, early $D3_{MD}$) and the $D4_{MD}$ deformation at ~2090 Ma (Fig. 3.20) under greenschist metamorphic facies.

The third gold mineralization event is restricted along the major bordering faults (WKSZ and BSZ) during the $D4_{MD}$ (~2090 Ma) sinistral shearing and is considered the main hydrothermal event of the MD (Fig. 3.20). In the western domain, the main gold mineralization is associated with a subvertical silicification alteration zone (Si_{4MD}) and quartz-carbonates veinlets (V_{4MD}) concentrated along the first-order WKSZ and observed in the Wona-Kona (Si_{2WK} and V_{2WK}) and Yaho deposits (Si_{2Y}) (Figs. 3.17a, 3.19g). The silicification is defined by a white to grey color, associated with ankerite, chlorite and surrounded by a large muscovite alteration halo. Gold is associated with pyrite and arsenopyrite (Augustin, 2011; Augustin et al., 2016). In the Yaho deposit, the silicification zone is controlled by $D4_{MD}$ sinistral shear zones surrounded by muscovite and iron carbonate alteration (Figs. 3.18, 3.19g).

The same alteration assemblage is documented for the Wona-Kona deposit (Augustin et al., 2016), hence suggesting a genetic link with $D4_{MD}$ sinistral deformation and silicification and gold mineralization. Because Wona-Kona is hosted within highly strained rocks having recorded a complex deformation history ($D1_{MD}$ to $D5_{MD}$), it is expected to be more difficult to decipher the main gold mineralizing event. However, the gold mineralization is related to a strong and large silicification zone that is very well defined (Augustin et al., 2016). This silicification zone displays an enlargement in the northern part of the Wona pit (Fig. 3.16) related to a flexure zone. This asymmetry related to the flexure is compatible with a sinistral event that induced dilatation and higher permeability for mineralizing fluid flow. Such a late $D4_{MD}$ mineralizing event is also compatible with the fact that the silicification totally overprints the strongly foliated host rocks. However, early-stage mineralization during dextral $D3_{MD}$ at Wona-Kona cannot be ruled out.

In short, the silicification observed in the Wona-Kona (Si_{2WK}) and Yaho (Si_{2Y}) deposits are related to the same $D4_{MD}$ sinistral event along the WKSZ corridor (Fig. 3.20). However, the physical conditions during mineralization are difficult to interpret because they correspond mainly to a silicification and, hence, could be at or below the greenschist facies.

The fourth mineralizing event corresponds to late high-grade free gold enrichment occurring in cracks, as observed in the Wona-Kona and Siou deposits (Figs. 3.15d, 3.17g). This mineralizing event is associated with some muscovite, hence implying a hydrothermal event. However, it is unclear whether this event introduced new gold from an external source or of it was just remobilization of gold for yielding higher grade. This event is

associated with a brittle reactivation of the major transcurrent faults (WKSZ and BSZ) during the late $D4_{MD}$ or $D5_{MD}$ events, and could have occurred as late as ~2022 Ma (Fig. 3.20). This interpretation is supported by the fact that the dated muscovite-schist samples are affected by crenulation cleavages related to $D5_{MD}$ (Fig. 3.8b).

In conclusion, 4 gold mineralizing events are recognized, and all the shortening events are associated with gold mineralization or gold remobilization.

3.8.3. THE MANA DISTRICT WITHIN THE CONTEXT OF THE WEST AFRICAN CRATON (WAC)

The deformation events and structural features described in the MD can be correlated with the deformation events documented for the WAC, especially for western Burkina Faso (Baratoux et al., 2011 and 2015; Metelka et al., 2011), southern Ghana (Perrouty et al., 2012) and northern Burkina Faso (Hein, 2010; Tshibubudze et al., 2015). These correlations are summarized in Fig. 3.21.

The oldest tectonic feature documented in the MD is associated with the $D1_{MD}$ E-W shortening event that affected the Lower Birimian group at the greenschist metamorphic facies. This event is characterized by N-S F_{1MD} folds with S_{1MD} axial planar schistosity and by N-S- and E-dipping thrust faults at the Siou deposit. It is temporally constrained by the early to syn-tectonic Siou and Wona-Kona plutons at ~2172 Ma (Fig. 3.20). In conjunction

with $D1_{MD}$, early gold mineralization was formed in the Fofina and Siou deposits as quartz-carbonate veins and early-disseminated sulfides. In the WAC, some early gold mineralization events are documented during the Eoeburnean orogeny (2190-2140 Ma) (Fig. 3.21). In southern Ghana, the D1 Eoeburnean event (2187-2158 Ma) corresponds to a N-S shortening affecting the Sefwi group and developing a series of isoclinal F_1 folds with a subvertical S_1 cleavage (Perrouty et al., 2012 and 2015). In the Wassa gold deposit, an early mineralization defined by quartz-carbonate veins and gold-bearing pyrites is dated at 2164 ± 22 Ma (Fig. 3.21) (Re-Os age; Le Mignot et al., 2017). In southwestern Burkina Faso, a $D1_{GA}$ Eburnean event (~2170-2140 Ma) related to a N-S shortening is recorded in the Gaoua area (Baratoux et al., 2015). The associated porphyry-type copper mineralization is dated at 2165 ± 24 and is also observed in the $D1_{NA}$ Nassara gold deposit (Baratoux et al., 2015; Ouiya et al., 2016; Le Mignot et al., 2017) (Fig. 3.1b). This early $D1_{GA}$ event is older than the regional D1 Eburnean event (~2160-2120 Ma) in western Burkina Faso, described as an E-W to WNW shortening at greenschist facies and manifested by the intense development of F_1 folding (Baratoux et al., 2011; Metelka et al., 2011). The syn-TTG granitoids (ME1) were emplaced during this event. In the Goren-Bouroum-Yalago and Oudalan-Gorouol belts in northeast Burkina Faso, a D1 Tangaean event (~2170-2130 Ma) is manifested by NW-trending dextral reverse shear zones and fold-thrusts formed during a period of NE-SW crustal shortening (Tshibubudze et al., 2009; Hein, 2010). In southern Burkina Faso, the Kiaka gold deposit records an early mineralization event associated with the late D1 Tangaean event, dated at 2157 ±32 Ma (Fontaine et al., 2017; Le Mignot et al., 2017). In short, the Eoeburnean/Tangaean events are subsets of a wider tectonic event

sharing similar structural characteristics and ages, and they are consistent with the proposed $D1_{MD}$ during the Eoeburnean event (Fig. 3.21).

The $D2_{MD}$ extension and basin-filling event documented in the MD is questionable at the regional scale. The origin and age of the Upper Birimian sedimentary sequence is unclear. Detrital zircons from one greywacke sample in the Bambéla volcano-sedimentary unit (south HGB, Ivory Coast - Fig. 3.1b) yield ages of 2180, 2150 and 2126 Ma (Lüdtke et al., 1999). In the Lawra belt (Northern Ghana), Block et al. (2016) obtained a maximum age of 2130 Ma based on the U-Pb monazite in the sedimentary rocks (Fig. 3.1b). These results suggest similar maximum deposition ages for the Upper Birimian and Tarkwaian-type sedimentary rocks. In Ghana, Perrouty et al. (2012) described a NW-SE extensional phase during the D2 event (2154-2125 Ma) with the formation of the Kumasi Basin that overlies the Sefwi group (Fig. 3.21). Accordingly, the origin of the Upper Birimian group is envisaged as the filling of a syntectonic foreland basin developed either during regional shortening and folding or during a tectonic quiescence/extension. The angular discordance of the Mana basin on the Lower Birimian group is more consistent with the second hypothesis and could be similar to the D2 of Perrouty et al. (2012) during 2154 to 2125 Ma (Fig. 3.21).

The $D3_{MD}$ E-W to WNW-ESE shortening is similar to the late D1 E-W shortening event of Baratoux et al. (2011) during a transtensional to transpressional regime (2120-2110 Ma) related to the formation of Tarkwaian-type sedimentary rocks in the eastern margin of the HGB (Fig. 3.21). The F_{3MD} folds and dextral faults developed during $D3_{MD}$ correlate with

the D3 Eburnean event defined by Perrouty et al. (2012) and dated between 2107 and 2097 Ma in southern Ghana (Fig. 3.21). This period constrains the reactivation of the WKSZ and BSZ with the Tarkwaian-type deposition and their shortening during $D3_{MD}$. The formation of the V_{3MD} quartz veins in conjunction with the F_{3MD} folds and dextral subsidiary faults in the central domain (Fofina, Nyafé) are also related to this period (Figs. 3.20, 3.21).

The $D4_{MD}$ is associated with a NNW-SSE shortening manifested by transcurrent sinistral shear zones and the formation of the main gold mineralization at ~2090 Ma, as constrained by the Kokoï pluton. Orogenic gold mineralizations related to the late shear zones are very common in West Africa (Milési et al., 1992; Allibone et al., 2002a and b; Béziat et al., 2008; Perrouty et al., 2012; Lawrence et al., 2013b; Tshibubudze et al., 2015; Markwitz et al., 2016; Masurel et al., 2017a). The $D4_{MD}$ is correlated to the following: 1) the D2 Eburnean event in western Burkina Faso, which took place between 2110 and 2090 Ma (Baratoux et al., 2011; Metelka et al., 2011); 2) the D2 event in northern Burkina Faso between 2130 to 1980 Ma associated with the Essakane gold deposit (Hein, 2010; Tshibubudze et al., 2015); and 3) the D4 and D5 events in southern Ghana, dated between 2110 and 2060 Ma (Perrouty et al., 2012) (Fig. 3.21). This period seems to have been the most prolific for gold deposition in the WAC. Recently, in Ghana and Burkina Faso, the Re-Os datation ages on pyrite constrained the late-orogenic gold deposit formation (Nassara in Burkina Faso; Wassa (second gold event), Obuasi, Damang in Ghana) between 2100 and 1980 Ma (White et al., 2014; Le Mignot et al., 2017) (Fig. 3.21). The late gold remobilization is documented in the Gaoua region during brittle to brittle-ductile $D3_{GA}$ between 2100 and 2080 Ma (Baratoux et al., 2015) (Fig. 3.21). The visible free gold

observed in the Wona-Kona and Siou deposits may be correlated with the $D3_{GA}$ during a late reactivation occurring after 2090 Ma and as young as 2022 Ma (this study).

The last deformation, $D5_{MD}$, is also recognized elsewhere in the WAC (Fig. 3.21). In western Burkina Faso, Baratoux et al. (2011) related this deformation to D3 and to $D4_{GA}$ in the Gaoua area (Baratoux et al., 2015). In northern Burkina Faso, Hein (2010) named it D3 for the Wabo-Tampelse shear zone in the Goren greenstone belt. In the Ashanti region (Ghana), Perrouty et al. (2012) used D6. The timing of this last deformation event is not clearly established but is either late-Eburnean or even Pan African. However, it cannot be excluded that the $D5_{MD}$ event may be responsible for the free gold remobilization at 2022 Ma.

3.9. CONCLUSION

In this paper, we presented new airborne geophysical and field data, integrated with deposit scale mapping, lithological and intrusion geochemistry and ages, in order to provide a coherent scenario of the evolution of the MD. This study distinguished at least 5 distinct deformational events ($D1_{MD}$ to $D5_{MD}$) associated with 4 gold mineralization events occurring in two phases (Eoeburnean and Eburnean) during the Paleoproterozoic.

The first deformation, $D1_{MD}$, affected the Lower Birimian group during an E-W shortening contemporaneous with the Siou and Wona-Kona granodioritic pluton emplacement (~2172

Ma). This group was overlain by the Upper Birimian group (Mana basin) during the $D2_{MD}$ extension and by the Tarkwaian-type group, which developed during late $D2_{MD}$ or the beginning of the $D3_{MD}$ E-W to WNW-ESE shortening controlled by the major faults (WKSZ and BSZ).

Gold mineralizing events occurred during the early and late stages of the Eoeburnean and Eburnean events. Quartz-carbonate veins (V_{1MD}) formed during the early phase ($D1_{MD}$) at the Fofina and Siou deposits. After the formation of the Upper Birimian and Tarkwaian-type rocks, a second mineralizing event is registered as V_{3MD} quartz-carbonate veins and disseminated pyrite grains. This hydrothermal event, bracketed between ~2113 and ~2090 Ma, is related to $D3_{MD}$ transpressional regime and dextral shearing, as recorded at Yaho, Fofina and Nyafé, and possibly at the Wona-Kona deposits. The main gold mineralization, manifested mainly by a strong silicification (Si_{4MD}) and lesser quartz-carbonate veinlets of V_{4MD} is concentrated along the WKSZ and is related to a sinistral reactivation displacement during the NNW-SSE $D4_{MD}$ transpression, dated at ~2090 Ma. Finally, free high-grade gold mineralization occurred during the late brittle reactivation of the WKSZ and BSZ. This event could be as young as ~2022 Ma. It is related either to the end of $D4_{MD}$ or the final $D5_{MD}$ shortening event. The $D5_{MD}$ event is manifested by E-W-trending crenulation cleavage mostly developed in highly strained rocks, and some brittle faults developed under overall N-S shortening. Our results highlighted the complex tectonic history recorded by the Birimian belts, a feature already recognized. However, our main contribution lies in the determination that gold was deposited during various events, all related to tectonic shortening, in a time frame that can be as long as 150 Ma, from ~2172 to ~2022 Ma.

3.10. ACKNOWLEDGEMENTS

The data presented in this paper are from a Ph.D. project by the first author, which is part of a larger research program on the Mana District supervised by Prof. D. Gaboury (UQAC) since 2007 in collaboration with SEMAFO Inc. We thank SEMAFO Inc. for granting access to their technical data, for permitting fieldwork and for authorizing the publication of these results. Special thanks must go to senior geologists at SEMAFO Inc, particularly R. Roy, D. Lalonde, D. Boisvert and F. Yameogo. We acknowledge N. Fournier and V. Lecomte from IOS Services Géoscientifiques for the zircon treatments. We are grateful to Dr. O. Bruguier from Géosciences Montpellier for his help with the U-Pb determinations and interpretations and to Prof. D. Philips for Ar-Ar datation. Constructive and detailed reviews by Stéphane Perrouty and Quentin Masurel greatly improved the manuscript.

3.11. REFERENCES

Abouchami, W., Boher. M., Michard, A., Albarède, F., 1990. A major 2.1 Ga event of mafic magmatism in Western Africa: An early stage of crustal accretion. Journal of Geophysical Research 95, 17605-17629.

Agyei Duodu, J., Loh, G.K., Hirdes, W., Boamah, K.O., Baba, M., Anokwa, Y.M., Asare, C., Brakohiapa, E., Mensah, R.B., Okla, R., Toloczyki, M., Davis, D.W., Glück, S., 2009. Geological Map of Ghana 1: 1,000,000. BGS, GCS, Accra (Ghana). Hannover (Germany).

Albarède, F., 1998. The growth of continental crust. Tectonophysics 296, 1-14.

Allibone, A., McCuaig, C.T., Harris, D., Etheridge, M, Munroe, S., Byrne, D., Amanor, J., Gyapong, W., 2002a. Structural controls on gold mineralization at the Ashanti gold deposit, Obuasi, Ghana. Society of Economic Geologists, Special Publication 9, 65-93.

Allibone, A., Teasdale, J., Cameron, G., Etheridge, M., Uttleu, P., Soboh, A., AppiahKubi, J., Adanu, A., Arthur, R., Mamphey, J., Odoom, B., Zuta, J., Tsikata, A., Pataye, F., Famiyeh, S., Lamb, E., 2002b. Timing and structural controls on gold mineralization at the Bogoso gold mine, Ghana, West Africa. Economic Geology 97, 949-969.

Ama Salah, I., Liégeois, J.P., Pouclet, A., 1996. Évolution d'un arc insulaire océanique birimien précoce au Liptako nigérien (Sirba) : géologie, géochronologie et géochimie. Journal of African Earth Sciences 22, 235-254.

Amponsah, P.O., Salvi, S., Béziat, D., Baratoux, L., Siebenaller, L., Jessell, M., Nude, P.M., Gyawu, E.A., 2016. Multistage gold mineralization in the Wa-Lawra greenstone belt, NW-Ghana: The Bepkong deposit. Journal of African Earth Sciences 120, 220-237.

Arndt, N.T., Albarède, E., Nisbet, E.G., 1997. Mafic and ultramafic magmatism. In: De Wit, M.J., Ashwaal, L.D., (Eds.), Greenstone belts. Clarendon Press, Oxford, p. 233-254.

Augustin. J., 2011. Facteurs de contrôle et processus métallogéniques des minéralisations aurifères du gisement de Wona, mine Mana, Burkina Faso. Unpublished M.Sc. thesis, Université du Québec à Chicoutimi, p. 1-220.

Augustin, J., Gaboury, D., Crevier, M., 2016. The world-class Wona-Kona gold deposit, Burkina Faso. Ore Geology Reviews 78, 667-672.

Augustin, J., Gaboury, D., 2017. Paleoproterozoic Plume-related basaltic rocks in the Mana gold district in Western Burkina Faso, West Africa: Implications for exploration and the source of gold in orogenic deposits. Journal of African Earth Sciences 129, 17-30.

Baratoux, L., Metelka, V., Naba, S., Jessell, M.W., Grégoire, M., Ganne, J., 2011. Juvenile Paleoproterozoic crust evolution during the Eburnean orogeny (~2.2-2.0 Ga), western Burkina Faso. Precambrian Research 191, 18-45.

Baratoux, L., Metelka, V., Naba, S., Ouiya, P., Siebenaller, L., Jessell, M.W., Naré, A., Salvi, S., Béziat, D., Franceschi, G., 2015. Tectonic evolution of the Gaoua region, Burkina Faso: Implications for mineralization. Journal of African Earth Sciences 112, 419-439.

Bertrand-Sarfati, J., Moussine-Pouchkine, A., Affaton, P., Trompette, R., Bellion, Y., 1991. Cover sequences of the West African craton. In: Dallmeyer, R.D., Lecorche, J.P. (Eds.), The West African Orogens and Circum-Atlantic Correlatives. Springer-Verlag, p. 65-82.

Béziat, D., Bourges, F., Debat, P., Lompo, M., Martin, F., Tollon, F., 2000. A Paleoproterozoic ultramafic-mafic assemblage and associated volcanic rocks of the Boromo greenstone belt: Fractionates and associated from island-arc volcanic activity in the West African Craton. Precambrian Research 101, 25-47.

Béziat, D., Dubois, M., Debat, P., Nikiéma, S., Salvi, S., Tollon, F., 2008. Gold metallogeny in the Birimian craton of Burkina Faso (West Africa). Journal of African Earth Sciences 50, 215-233.

Block, S., Ganne, J., Baratoux, L., Zeh, A., Parra, L.A., Jessell, M.W., Aillères, L., Siebenaller, L., 2015. Petrological and geochronological constraints on lower crust exhumation during Paleoproterozoic (Eburnean) orogeny, NW Ghana, West African Craton. Journal of Metamorphic Geology 33, 463-494.

Block, S., Jessell, M., Aillères, L., Baratoux, L., Bruguier, O., Zeh, A., Bosch, D., Caby, R., Mensah, E., 2016. Lower crust exhumation during Paleoproterozoic (Eburnean) orogeny, NW Ghana, West African Craton: Interplay of coeval contractional deformation and extensional gravitational collapse. Precambrian Research 274, 82-109.

Boher, M., Abouchami, W., Michard, A., Albarède, F., Arndt, N., 1992. Crustal growth in West Africa at 2.1 Ga. Journal of Geophysical Research 97, 345-369.

Bonhomme, M., 1962. Contribution à l'étude géochronologique de la plate-forme de l'Ouest Africain. Annals de la Faculté, des Sciences de l'Université, de Clermont-Ferrand. Géologie et Minéralogie 5, p. 1-62.

Bossière, G., Bonkoungou, I., Peucat, J.J., Pupin, J.P., 1996. Origin and age of Paleoproterozoic conglomerates and sandstones of the Tarkwaian Group in Burkina Faso, West Africa. Precambrian Research 80, 153-172.

Castaing, C., Billa, M., Milési, J.P., Thiéblemont, D., Le Métour, J., Egal, E., Donzeau, M., Guerrot, C., Cocherie, A., Chèvremont, P., Tegyey, M., Itard, Y., Zida, B., Ouedraogo, I., Koté, S., Kabore, B.E., Ouedraogo, C., Ki, J.C., Zunino, C., 2003. Notice explicative de la carte géologique et minière du Burkina Faso à 1/1,000,000. BRGM BUMIGEB, p. 1-147.

Chèvremont, P., Donzeau, M., Le Métour, J., Egal, E., Castaing, C., Thiéblemont, D., Tegyey, M., Guerrot, C., Billa, M., Itard, Y., Delpont, G., Ki, J.C., 2003. Notice explicative de la Carte géologique du Burkina Faso a 1/200,000. Feuille Koudougou, p. 1-85.

Cox, K.G., Bell, J.D., Pankhurst, R.J., 1979. The interpretation of igneous rocks. Allen & Unwin, p. 1-464.

Dampare, S.B., Shibata, T., Asiedu, D.K., Osae, S., Banoeng-Yakubo, B., 2008. Geochemistry of Paleoproterozoic metavolcanic rocks from the southern Ashanto volcanic belt, Ghana: Petrogenic and tectonic setting implications. Precambrian Research 162, 403-423.

Davis, D.W., Hirdes, W., Schaltegger, U., Nunoo, E.A., 1994. U-Pb constraints on deposition and provenance of Birimian and gold-bearing Tarkwaian sediments in Ghana, West Africa. Precambrian Research 67, 403-423.

Debat, P., Nikiéma, S., Mercier, A., Lompo, M., Béziat, D., Bourges, F., Roddaz, M., Salvi, S., Tollon, F., Wenmenga, U., 2003. A new metamorphic constraint for the Eburnean orogeny from Paleoproterozoic formations of the Man shield (Aribinda and Tampelga countries, Burkina Faso). Precambrian Research 123, 47-65.

Deynoux, M., 1983. Les formations de plate-forme d'âge Précambrien supérieur et Paléozoïque dans l'Ouest africain corrélation avec les zones mobiles. Pergamon Press, Oxford, United Kingdom, p. 46-74.

de Kock, G.S., Armstrong, R.A., Siegfried, H.P., Thomas, E., 2011. Geochronology of the Birim Supergroup of the West African Craton in the Wa-Bole region of west-central Ghana: Implications for the stratigraphic framework. Journal of African Earth Sciences 59, 1-40.

de Kock, G.S., Théveniaut, H., Botha, P.M.W., Gyapong, W., 2012. Timing the structural events in the Paleoproterozoic Bolé-Nangodi belt terrane and adjacent Maluwe basin, West African Craton, in central-west Ghana. Journal of African Earth Sciences 65, 1-24.

Dia, A., 1988. Caractères et significations des complexes magmatiques et métamorphiques du secteur de Sandikounda-Laminia (Nord de la boutonnière de Kédougou, Est Sénégal). Un modèle géodynamique du Birimien de l'Afrique de l'Ouest. UCAD, Dakar, p. 1-350.

Doumbia, S., Pouclet, A., Kouamelan, A., Peucat, J.J., Vidal, M., Delor, C., 1998. Petrogenesis of juvenile-type Birimian (Paleoproterozoic) granitoids in Central Côte-d'Ivoire, West Africa: Geochemistry and geochronology. Precambrian Research 87, 33-63.

Endeavour Mining, 2015. Mineral Reserves and Mineral Resources. 43.101 report.

Feybesse, J.L., Billa, M., Guerrot, C., Duguey, E., Lescuyer, J.L., Milési, J.P., Bouchot, V., 2006. The Paleoproterozoic Ghanaian province: Geodynamic model and ore control, including regional stress modeling. Precambrian Research 149, 149-196.

Fontaine, A., Eglinger, A., Ada, K., André-Mayer, A.S., Reisberg L., Siebenaller, L., Le Mignot, E., Ganne, J., Poujol, M., 2017. Geology of the world-class Kiaka polyphase gold deposit, West African Craton, Burkina Faso. Journal of African Earth Sciences 126, 96-122.

Fornelli, A., Piccarreta, G., Micheletti, F., 2014. In situ U-Pb dating combined with SEM imaging on zircon - A analytical bond for effective geological reconstructions. Geochrnology-Methods and Case studies, Edited by Nils-Axel Morner, chapter 5, p. 109-139.

Fougerouse, D., Micklethwaite, S., Ulrich, S., Miller, J., Godel, B., Adams, D.T., Campbell McCuaig, T., 2017. Evidence for two stages of mineralization in West Africa's largest gold deposit: Obuasi, Ghana. Economic Geology 112, 3-22.

Gaboury, D., 2014. Note de visite dans la fosse Siou. Internal report for Semafo Inc., p. 1-11.

Ganne, J., De Andrade, V., Weinberg, R.F., Vidal., O., Dubacq, B., Kagambega, N., Naba, S., Baratoux, L., Jessell, M., Allibon, J., 2012. Modern-style plate subduction preserved in the Paleoproterozoic West African Craton. Nature Geoscience 5, 60-65.

Gasquet, D., Barbey, P., Adou, M., Paquette, J.L., 2003. Structure Sr-Nd isotope geochemistry and zircon U-Pb geochronology of the granitoids of the Dabakala area (Côte d'Ivoire): Evidence for a 2.3 Ga crustal growth event in the Paleoproterozoic of West Africa? Precambrian Research 127, 329-354.

Hein, K.A.A, Morel, V., Kagoné, O., Kiemde, F., Mayes, K., 2004. Birimian lithogical succession and structural evolution in the Goren segment of the Boromo-Goren greenstone belt, Burkina Faso. Journal of African Earth Sciences 39, 1-23.

Hein, K.A.A., 2010. Succession of structural events in the Goren greenstone belt (Burkina Faso): Implications for West African tectonics. Journal of African Earth Sciences 56, 83-94.

Hein, K.A.A., 2016. The Bagassi gold deposits on the eastern margin of the Houndé greenstone belt, Burkina Faso. Ore Geology Reviews 78, 660-666.

Hirdes, W., Davis, D.W., Eisenlohr, B.N., 1992. Reassessment of Proterozoic granitoid ages in Ghana on the basis of U/Pb zircon and monazite dating. Precambrian Research 56, 89-96.

Hirdes, D., Davis, D., Lüdtke, G., and Konan, G., 1996. Two generations of Birimian (Paleoproterozoic) volcanic belts in northeastern Côte d'Ivoire (West Africa): Consequences for the Birimian controversy. Precambrian Research 80, 173-191.

Hottin, G., Ouedraogo, O.F., 1992. Carte géologique du Burkina Faso. Second Edition. Bureau de Recherches Géologiques et Minières, Burkina Faso.

Jahn, B.M., Liu, D., Wan, Y., Song, B., Wu, J., 2008. Archean crustal evolution of the Jiaodong peninsula, China, as revealed by zircon Shrimp geochronology, elemental and Nd-isotope geochemistry. American Journal of Science 308, 232-269.

Jessell, M.W., Amponsah, P.O., Baratoux, L., Asiedu, D.K., Loh, G.K., Ganne, J., 2012. Crustal-scale transcurrent shearing in the Paleoproterozoic Sefwi-Sunyani-Comoe region, West Africa. Precambrian Research 212, 155-168.

Jessell, M.W., Santoul, J., Baratoux, L., Youbi, N., Ernst, R.E., Metelka, V., Miller., J., Perrouty, S., 2015. An updated map of West African Mafic Dykes. Journal of African Earth Sciences 112, 440-450.

Koffi, Y.H.., Wenmenga, U., Djro, S.G., 2016. Tarkwaian deposits of the Birimian belt of Houndé: Petrological, structural and geochemical study (Burkina-Faso, West Africa). International Journal of Geosciences 7, 685-700.

Lameyre, J., Bowden, P., 1982. Plutonic rock type series: Discrimination of various granitoid series and related rocks. Journal of Volcanology and Geothermal Research 14, 169-186.

Lawrence, D.M., Treloar, P.J., Rankin, A.H., Harbidge, P., Holliday, J., 2013a. The geology and mineralogy of the Loulo mining district, West Africa: Evidence for two distinct styles of orogenic gold mineralization. Economic Geology 108, 199-227.

Lawrence, D.M., Treloar, P.J., Rankin, A.H., Boyce, A., Harbidge, P., 2013b. A fluid inclusion and stable isotope study at the Loulo mining district, Mali, West Africa: Implications for multifluids sources in the generation of orogenic gold deposits. Economic Geology 108, 229-257.

Le Métour, J., Chèvremont, P., Donzeau, M.E., Thiéblemont, E., Tegey, D., Guerrot, M.C.M., Itard, B., Castaing, Y., Delpont, C., Ki, G., Zunino, J.C.C., 2003. Notice explicative de la carte géologique du Burkina Faso au 1/200,000. Feuille Houndé, p. 1-82.

Le Mignot, E., Reisberg, L., André-Mayer, A.-S., Bourassa, Y., Fontaine, A., Miller, J., 2017. Re-Os geochronological evidence for multiple Paleoproterozoic gold events at the scale of the West African craton. Economic Geology 112, 145-168.

Lebrun, E., Thébaud, N., Miller, J., Roberts, M., Evans, N., 2017a. Mineralisation footprints and regional timing of the world-class Siguiri orogenic gold district (Guinea, West Africa). Mineralium Deposita 52, 539-564.

Lebrun, E., Miller, J., Thébaud, N; Ulrich, S., McCuaig, C., 2017b. Structural controls on an orogenic gold system: The world-class Siguiri gold district, Siguiri Basin, Guinea, West Africa. Economic Geology 112, 73-98.

Ledru, P., Pons, J., Milési, J.P., Feybesse, J.L., Johan, V., 1991. Transcurrent tectonics and polycyclic evolution in the lower Proterozoic of Senegal-Mali. Precambrian Research 50, 337-354.

Leube, A., Hirdes, W., Mauer, R., Kesse, G., 1990. The early Proterozoic Birimian supergroup of Ghana and some aspect of its associated gold mineralization. Precambrian Research 46, 139-165.

Liégeois, J.P., Claessens, W., Camara, D., Klerkx, J., 1991. Short-lived Eburnian orogeny in southern Mali. Geology tectonics, U-Pb and Rb-Sr geochronology. Precambrian Research 50, 111-136.

Loh, G., Hirdes, W., 1996. Explanatory notes for the geological map of southwest Ghana, 1/100,000-sheets Sekondi (0402A) and Axim (0403B). Ghana Geological Survey Bulletin 49, p. 1-63.

Lompo, M., 2009. A model of subsidence of an oceanic plateau magmatic rocks in the Man-Leo Shield of the West African Craton. Geodynamic evolution of the 2.25-2.0 Ga Paleoproterozoic. In: Reddy, S.M., Mazumder, R., Evans, D.A.D., Collins, A.S., (Eds.), Paleoproterozoic Supercontinents and Global Evolution. Geological Society, London, p. 231-254.

Lüdtke, G., Hirdes, W., Konan, G., Koné, Y., N'da, D., Traoré, Y., Zamblé, Z., 1999. Géologie de la région Haute Comoé Sud-feuilles Dabakala (2b, d et 4b, d). Direction de la Géologie Abidjan Bulletin, p. 1-176.

MacLeod, I.N., Jones, K., Dai, T.F., 1993. 3-D Analytic signal in the interpretation of total magnetic field data at low magnetic latitudes. Exploration Geophysics 24, 679-687.

Markwitz, V., Hein, K.A.A., Miller, J., 2016. Compilation of West African minerals deposits: Spatial distribution and mineral endowment. Precambrian Research 274, 61-81.

Martin, H., 1994. The Archean grey gneiss and the genesis of continental crust. In: Condie, K.C. (Ed.), The Archean Crustal Evolution. Elsevier, Amsterdam, p. 205-259.

Martin, H., 1999. The adakitic magmas: Modern analogues of Archean granitoids. Lithos 46, 411-429.

Martin, H., Smithies, R.H., Rapp, R., Moyen, J.F., Champion, D., 2005. An overview of adakite, tonalite-trondhjemite-granodiorite (TTG), and sanukitoid: Relationships and some implications for crustal evolution. Lithos 79, 1-24.

Masurel, Q., Thébaud, N., Miller, J., Ulrich, S., Hein, K.A.A., Cameron, G., Béziat, D., Bruguier, O., Davis, J.A., 2017a. Sadiola Hill: A world-class carbonate-hosted gold deposit in Mali, West Africa. Economic Geology 112, 23-47.

Masurel, Q., Thébaud, N., Miller, J., Ulrich, S., 2017b. The tectono-magmatic framework to gold mineralisation in the Sadiola-Yatela gold camp and implications for the paleotectonic setting of the Kédougou-Kénieba inlier, West Africa. Precambrian Research 292, 35-56.

Metelka, V., Baratoux, L., Naba, S., Jessell, M.W., 2011. A geophysically constrained litho-structural analysis of the Eburnean greenstone belts and associated granitoid domains, Burkina Faso, West Africa. Precambrian Research 190, 48-69.

Milési, J.P., Feybesse, J.L., Ledru, P., Dommanget, A., Ouedraogo, M.F., Marcoux, E., Prost, A., Vinchon, C., Sylvain, J.P., Johan, V., Tegyey, M., Calvez, J.Y., Lagny, P., 1989. Minéralisations aurifères de l'Afrique de l'Ouest, leurs relations avec l'évolution litho-structurale au Protérozoïque inférieur. Carte géologique ay 1/2,000,000. Chronique de la Recherche Minière 497, 3-98.

Milési, J.P., Ledur, P., Feybesse, J.L., Dommanget, A., Marcoux, E., 1992. Early Proterozoic ore deposits and tectonics of the Birimian orogenic belt, West Africa. Precambrian Research 58, 305-344.

Milési, J.P., Feybesse, J.L., Pinna, P., Deschamps, Y., Kampunzu, H., Muhongo, S., Lescuyer, J.L., Le Goff, E., Delor, C., Billa, M., Ralay, F., Heinry, C., 2004. Geological map of Africa 1/10,000,000. SIGAfrique Project. <http://www.sigafrique.net>.

Naba, S., Lompo, M., Debat, P., Bouchez, J.L., Béziat, D., 2004. Structure and emplacement model for late-orogenic Paleoproterozoic granitoids: The Tenkodogo-Yamba elongate pluton (eastern Burkina Faso). Journal of African Earth Sciences 38, 41-57.

Nikiéma, S., Benkhelil, J., Corsini, M., Bourges, F., Abdoulaye, D., Maurin, J.-C., 1993. Tectonique transcurrente Éburnéenne au sein du Craton Ouest-Africain, exemple du sillon de Djibo (Burkina Faso). Comptes Rendus de l'Académie des Sciences 316, 661-668.

Oberthür, T., Vetter, U., Schmidt Mumm, A., Weiser, T., Amanor, J.A., Gyapong, W.A., Kumi, R., Bleckinsop, T.G., 1994, The Ashanti gold mine at Obuasi in Ghana. Geologische Jahrbuch, v. D100, p. 31-129

Ouiya, P., Siebenaller, L., Salvi, L., Béziat, D., Naba, S., Baratoux, L., Naré, A., Franceschi, G., 2016. The Nassara gold prospect, Gaoua District, southwestern Burkina Faso. Ore Geology Reviews 78, 623-630.

Parra-Avila, L.A., Bourassa, Y., Miller, J., Perrouty, S., Fiorentini, M.L., McCuaig, T.C., 2015. Age constraints of the Wassa and Benso mesothermal gold deposits, Ashanti belt, Ghana, West Africa. Journal of African Earth Sciences 112, 524-535.

Pawling, S., Gueye, M., Klischies, R., Schwartz, S., Wemmer, K., Siegesmund, S., 2006. Geochemical and Sr-Nd isotopic data on the Birimian of the Kedougou-Kenieba inlier (eastern Senegal): Implications on the Paleoproterozoic evolution of the West African Craton. South African Journal of Geology 109, 411-427.

Perrouty, S., Aillères, L., Jessell, M.W., Baratoux, L., Bourassa, Y., Crawford, B., 2012. Revised Eburnean geodynamic evolution of the gold-rich southern Ashanti belt, Ghana, with the new field and geophysical evidence of pre-Tarkwaian deformations. Precambrian Research 204, 12-39.

Perrouty, S., Lindsay, M.D., Jessell, M.W., Aillères, L., Martin, R., Bourassa, Y., 2014. 3D modeling of the Ashanti belt, southwest Ghana: Evidence for a litho-stratigraphic control on gold occurrences within the Birimian Sefwi group. Ore Geology Reviews 63, 252-264.

Perrouty, S., Jessell, M.W., Bourassa, Y., Miller, J., Apau, D., Siebenaller, L., Velasquez, G., Baratoux, L., Aillères, L., Béziat, D., Salvi, S., 2015. The Wassa deposit: A polydeformed orogenic system in southwest Ghana - implications for regional exploration. Journal of African Earth Sciences 12, 536-547.

Phillips, D., Miller, J.M., 2006. $^{40}Ar/^{39}Ar$ dating of mica-bearing pyrite from thermally overprinted Archean gold deposits. Geology 34, 397-400.

Pidgeon, R.T., 1992. Recrystallization of oscillatory zoned zircon: Some geochronological and petrological implications. Contributions to Mineralogy and Petrology 110, 463-472.

Pidgeon, R.T., Nemchin, A.A., Hitchen, G.J., 1998. Internal structures of zircons from Archean granites from the Draling range batholith: Implications for zircons stability and the interpretation of zircon U-Pb ages. Contributions to Mineralogy and Petrology 132, 288-299.

Pigeois, J.P., Groves, D.I., Fletcher, I.R., McNaughton, N.J., Snee, L.W., 2003. Age constraints on Tarkwaian paleoplacer and lode-gold formation in the Tarkwa-Damang district, SW Ghana. Mineralium Deposita 38, 695-714.

Pouclet, A., Vidal, M., Delor, C., Simeon, Y., Alric, G., 1996. Le volcanisme birimien du nord-est de la Côte-d'Ivoire, mise en évidence de deux phases volcano-tectoniques distinctes dans l'évolution géodynamique du Paléoprotérozoïque. Bulletin de la Société Géologique de France 167, 529-541.

Pouclet, A., Doumbia, S., Vidal, M., 2006. Geodynamic setting of the Birimian volcanism in central Ivory Coast (western Africa) and its place in the Paleoproterozoic evolution of the Man Shield. Bulletin de la Société Géologique de France 177, 105-121.

Robertson, M., Peters, L., 2016. West African Goldfields. Episodes 39, 155-176.

Roxgold, 2013. Roxgold announces an updated mineral resource estimate for the 55 zone. Ahead of upcoming PEA study, news release august 27, 2013, Toronto, Ontario, p. 1-6.

Salvi, S., Sangaré, A., Driouch, Y., Siebenaller, L., Béziat, D., Debat, D., Femenias, O., 2016. The Kalana vein-hosted gold deposit, southern Mali. Ore Geology Reviews 78, 599-605.

Sarama Resources, 2016. Sarama Resources acquires the Bondi gold deposit in Burkina Faso from Orezone Gold, news release may 24, 2016.

Semafo Inc., 2013. Advanced Technical Report, Mana Property, Burkina Faso Reserve and Resource Update as at June 30, 2013, p. 1-157.

Semafo Inc., 2015. Mana, Burkina Faso; 2015 mineral reserves and resources. Recent 43.101 report.

SGS, 2009. Technical Report on the Resources and Reserves of the Mana gold deposits, Burkina Faso, p. 1-101.

Sinaré. M., 2013. Métallogénie du gisement aurifère de Yaho, ceinture birimienne de Houndé, Burkina Faso. Unpublished M.Sc. thesis, Université du Québec à Chicoutimi, p. 1-266.

Soumalia, A., Henry, P., Rossy, M., 2004. Contexte de mise en place des roches basiques de la ceinture de roches vertes de Diagorou-Darbani (Liptako, Niger, Afrique de l'Ouest): Plateau océanique ou environnement d'arc/bassin arrière-arc océanique. Comptes Rendus Geoscience 336, 1137-1147.

Streckeisen, A.L., 1976. To each plutonic rock its proper name. Earth Science Reviews 12, 1-33.

Sun, S.S., McDonough, W.F., 1989. Chemical and isotopic systematic of oceanic basalts: Implications for mantle composition and processes. In: Sanders, A.D., Norry, M.J. (Eds.), Magmatism in the Ocean Basins, vol. 42. Geological Society Special Publication, p. 313-345.

Taylor, P.N., Moorbath, S., Leube, A., Hirdes, W., 1992. Early Proterozoic crustal evolution in the Birimian Ghana: Constraints from geochronology and isotope geochemistry. Precambrian Research 56, 97-111.

Tshibubudze, A., Hein, K.A.A, Marquis, P., 2009. The Markoye shear zone in NE Burkina Faso. Journal of African Earth Sciences 55, 245-256.

Tshibubudze, A., Hein, K.A.A., 2013. Structural setting of gold deposits in the Oudalan-Gorouol volcano-sedimentary belt east of the Markoye Shear Zone, West African Craton. Journal of African Earth Sciences 80, 31-47.

Tshibubudze, A., Hein, K.A.A., McCuaig, T.C., 2015. The relative and absolute chronology of strato-tectonic events in the Gorom-Gorom granitoid terrane and Oudalan-Gorouol belt, northeast Burkina Faso. Journal of African Earth Sciences 112, 382-418.

Tshibubudze, A., Hein, K.A.A., 2016. Gold mineralisation in the Essakane goldfield in Burkina Faso, West African craton. Ore Geology Reviews 78, 652-659.

Vavra, G., 1990. On the kinematics of zircon growth and its petrogenetic significance: A cathodoluminescence study. Contributions to Mineralogy and Petrology 106, 90-99.

Vidal, M., Alric, G., 1994. The Paleoproterozoic (Birimian) of Haute-Comoe in the West African Craton Ivory Coast: A transtensional back-arc basin. Precambrian Research 65, 207-229.

Villa, I.M., 2010. Disequilibrium textures versus equilibrium modelling: Geochronology at the crossroads. In: Spalla, M., Marotta, A.M., Gosso, G. (Eds.), Advances in Interpretation of Geological Processes: Refinement of multi-scale data and integration in numerical modelling. Geological Society, Special Publications, 332, London, p. 1-15.

White, A., Burgess, R., Charnley, N., Selby, D., Whitehouse, M., Robb, L., Waters, D., 2014. Constraints on the timing of late-Eburnean metamorphism, gold mineralisation and regional exhumation at Damang mine, Ghana. Precambrian Research 243, 18-38.

FIGURES DU CHAPITRE 3

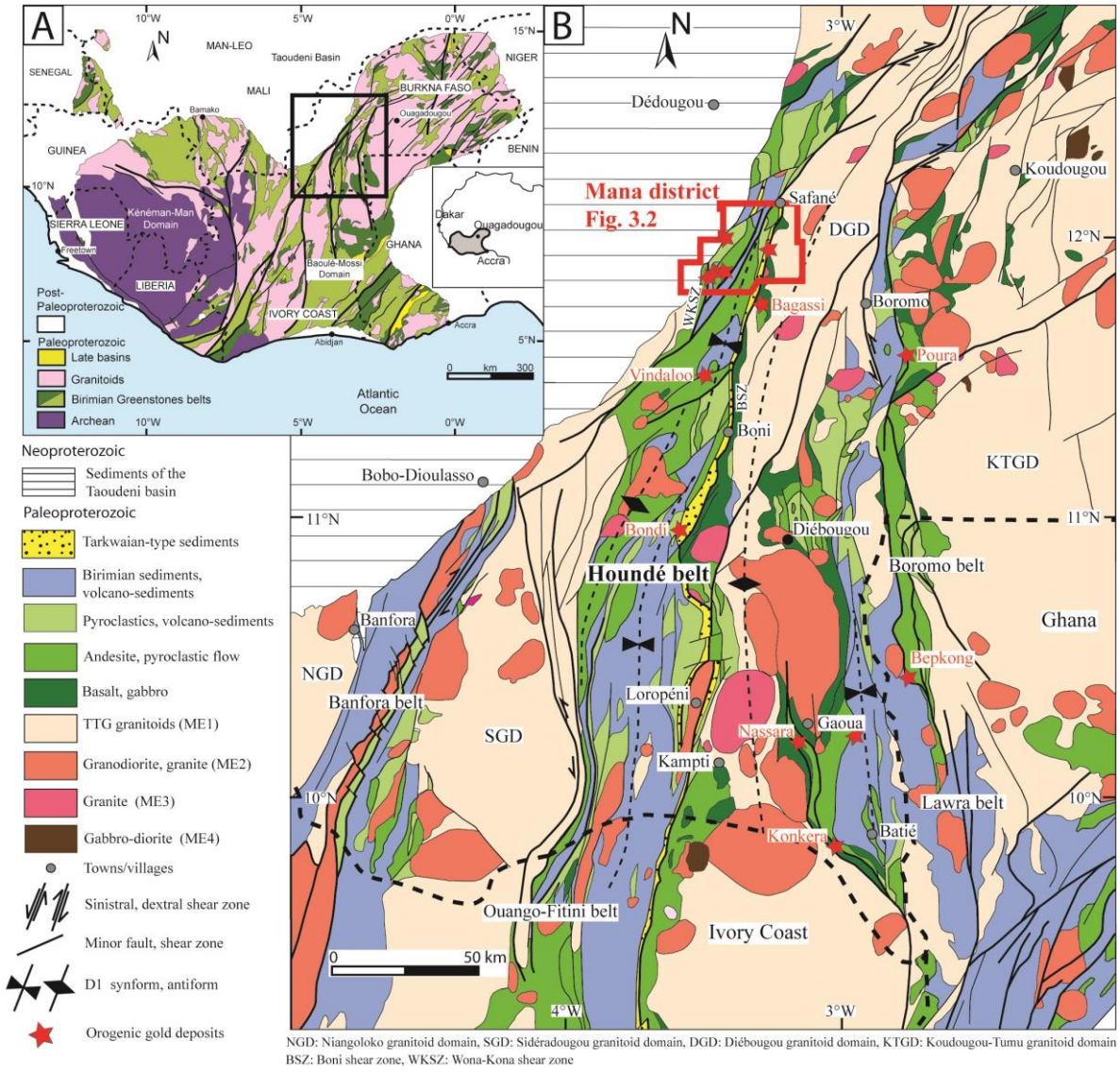

Figure 3.1 (a) Geologic map of the Leo-Man craton, modified after the BRGM SIGAfrique map, Milési et al. (2004). The dark grey areas are mafic to felsic lavas, and the light grey areas are metamorphosed volcanoclastic and sedimentary rocks. (b) Regional litho-structural map of western Burkina Faso, modified after Baratoux et al. (2011) and Metelka et al. (2011). The study area is indicated by the red polygon.

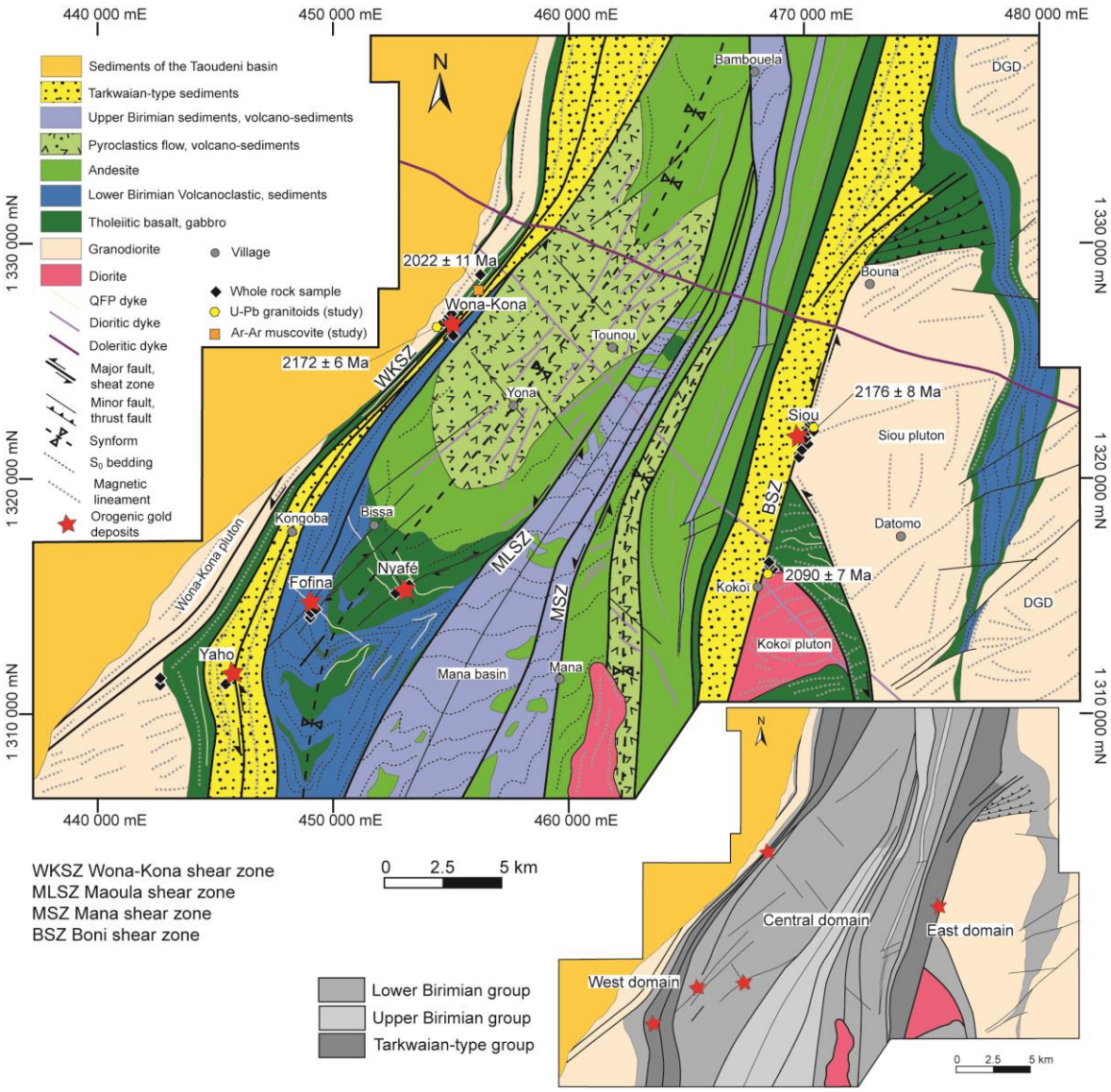

Figure 3.2 Simplified geological map of the Mana district, showing the 5 orogenic gold deposits studied (red stars). Radiometric ages presented on the map are from this study. The lower inset shows the three main domains established based on the lithostratigraphy and major structural features (Fig. 3.3).

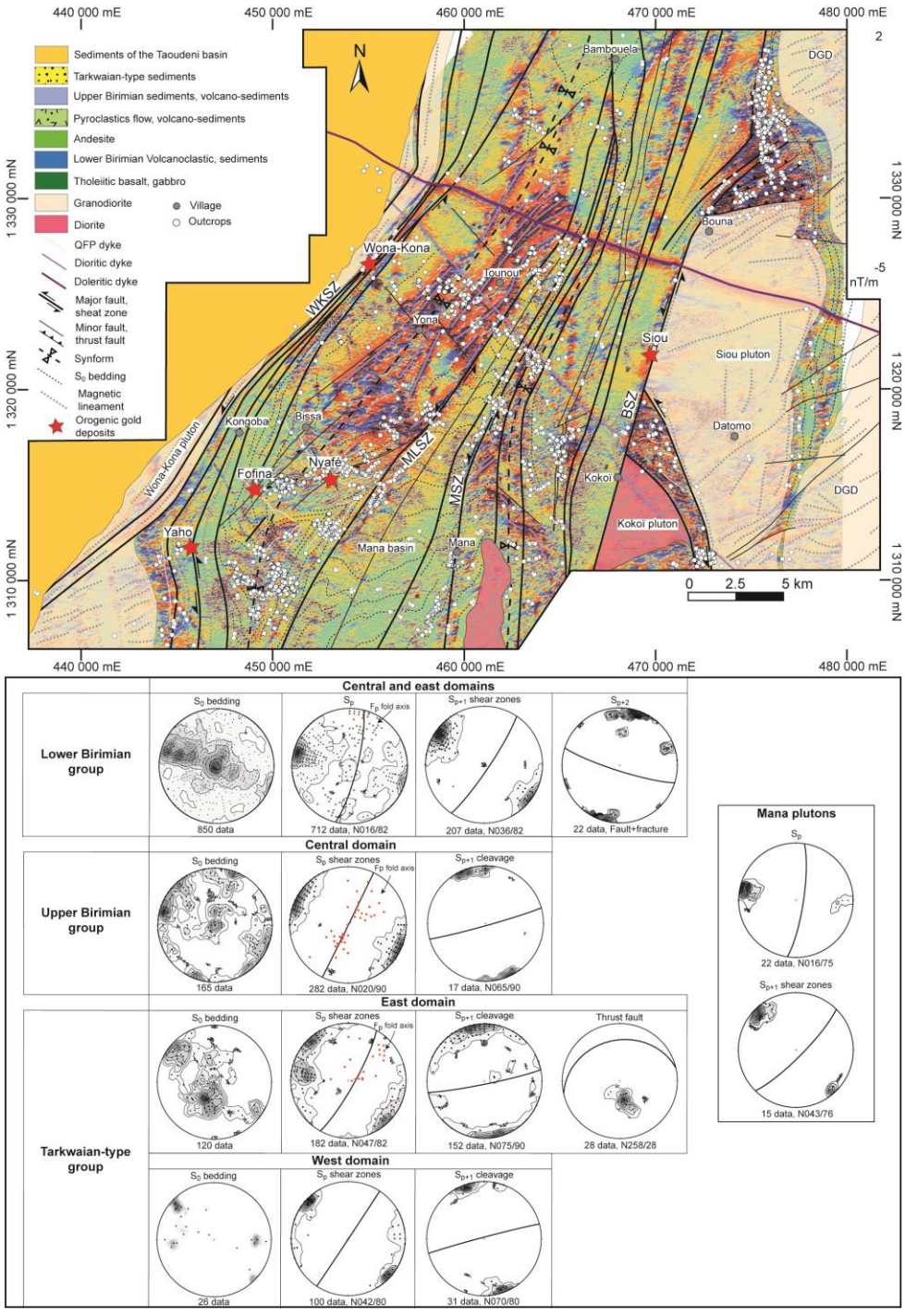

Figure 3.3 Interpretative geological map of plutons and shear zones in the Mana district based on field observations and airborne magnetic data (1st vertical derivative). Structural features for each lithostratigraphic group are presented as equal area lower hemisphere stereoplots.

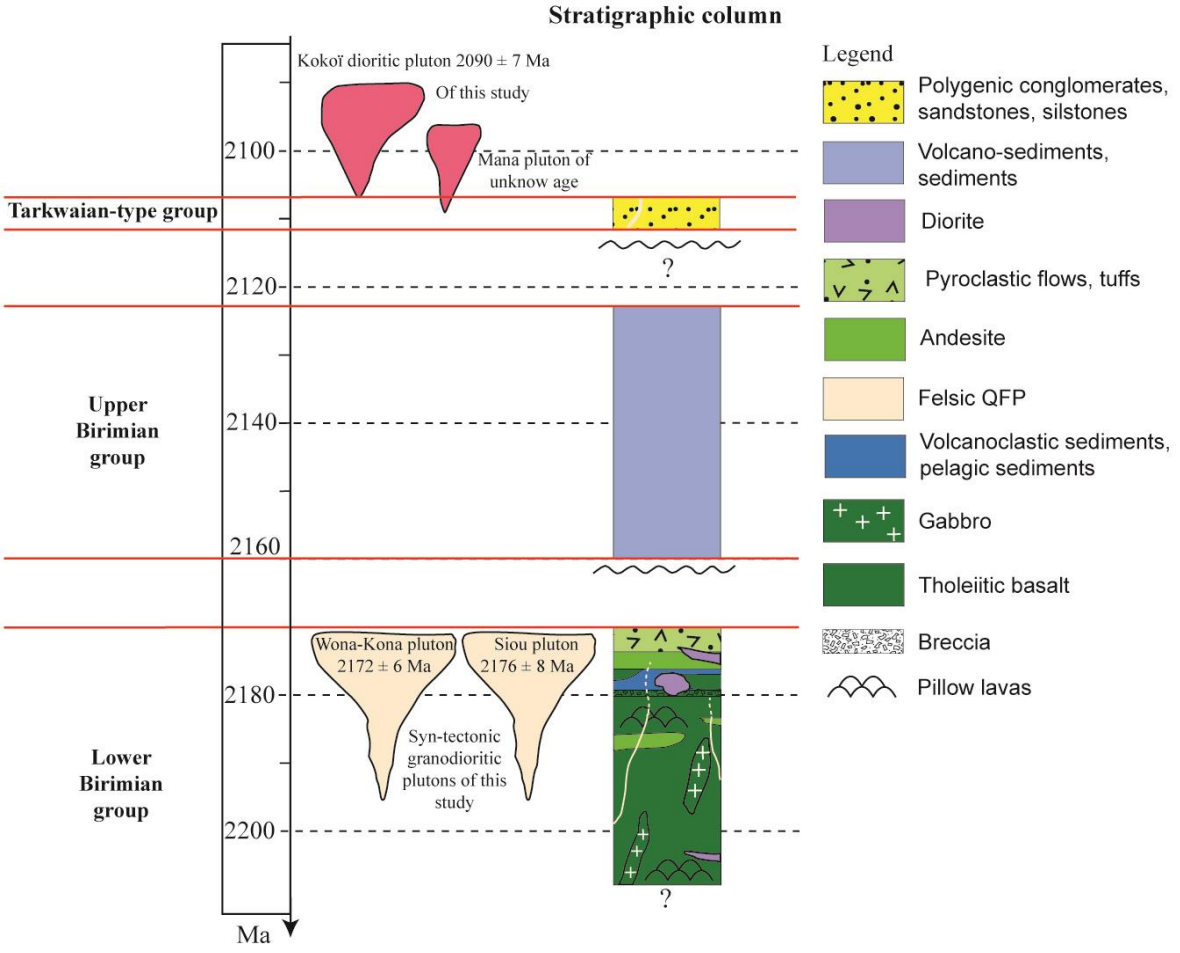

Figure 3.4 Simplified stratigraphic sequence for the Mana district, modified after Baratoux et al. (2011).

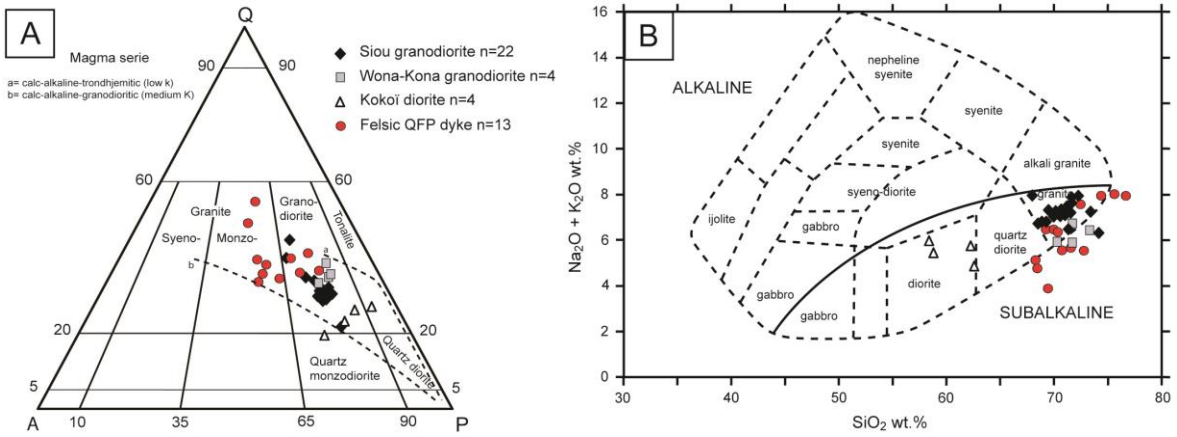

Figure 3.5 (a) QAP diagram (Streckeisen, 1976) for the plutons and felsic QFP dykes of the Mana district. Dashed lines represent chemical trends of Lameyre and Bowden (1982). (b) Total alkali vs. SiO_2 diagram from Cox et al. (1979).

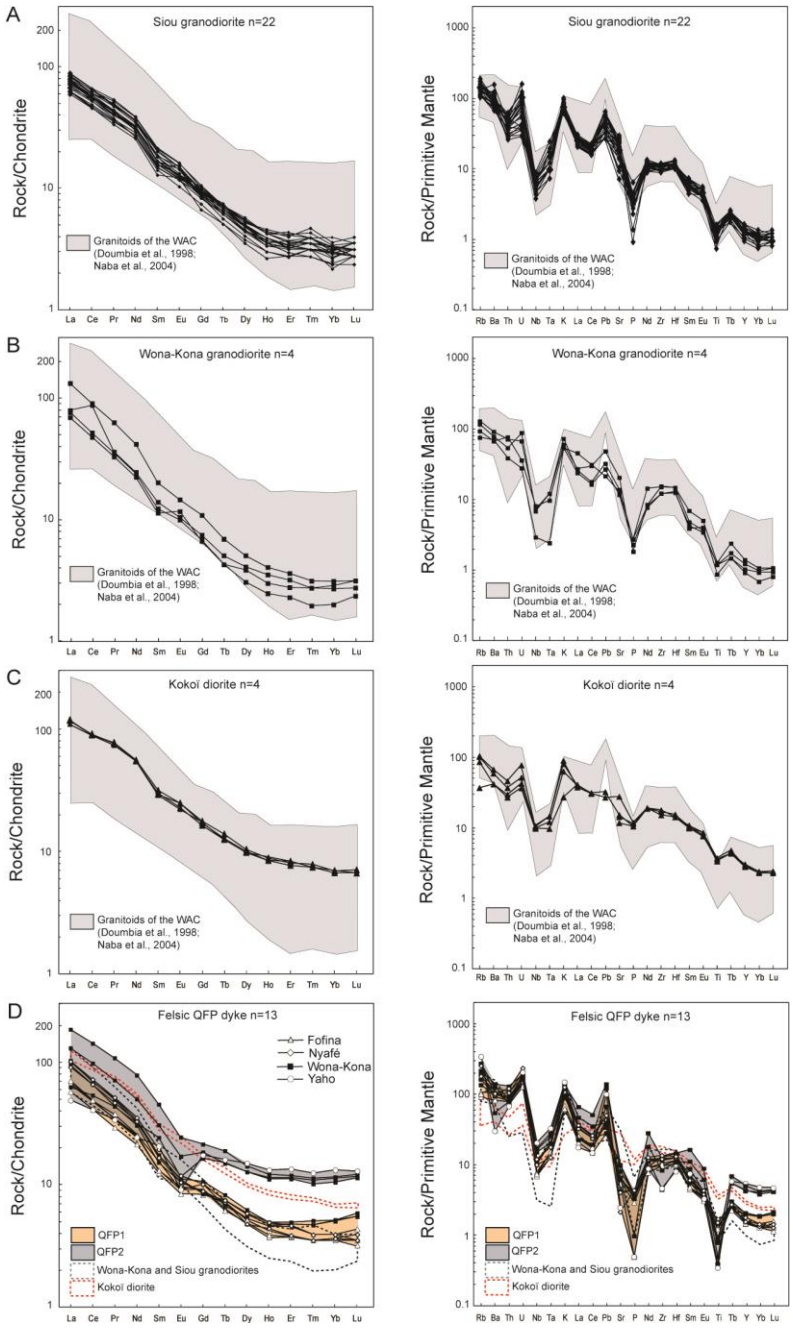

Figure 3.6 (a to d) Rare-earth element (REE) patterns and primitive mantle-normalized multi-element patterns of plutons and felsic QFP dykes of the Mana district. The normalizing values are those of Sun and McDonaugh (1989). The pluton samples are compared to granitoids from eastern Burkina Faso and the central Ivory Coast (Doumbia et al., 1998; Naba et al., 2004). The two types of felsic QFP dykes (QFP1 and QFP2) are compared with the plutons from the Mana district.

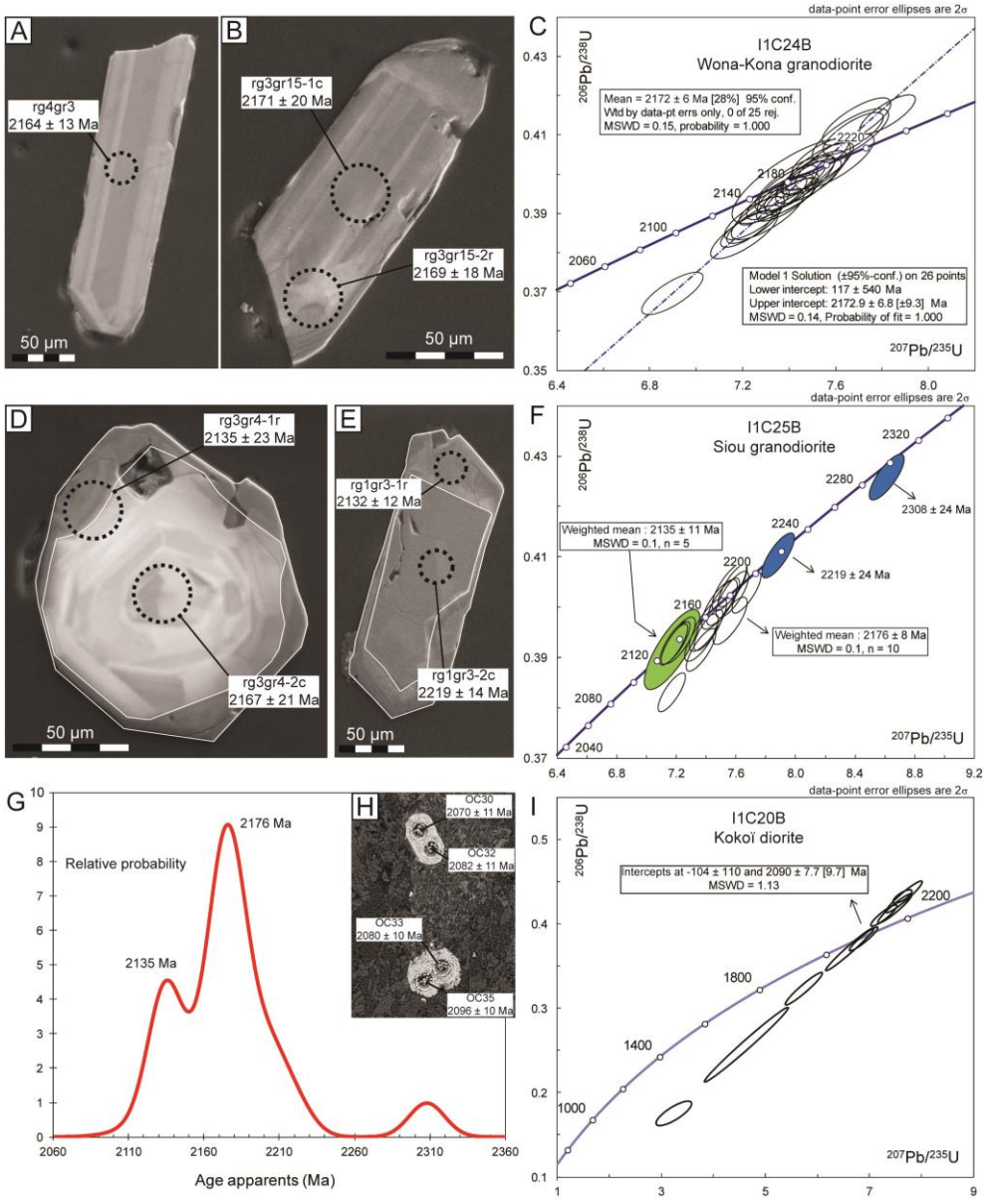

Figure 3.7 (a-b) Backscattered electron images of the representative zircon grains for the Wona-Kona granodiorite. (c) U-Pb concordia plots of zircons from the Wona-Kona granodiorite (sample I1C24B). (d-e) Backscattered electron images of the representative zircon grains for the Siou granodiorite. (f) U-Pb concordia plots of zircons from the Siou granodiorite (sample I1C25B). Green and white ellipsoids were used in the $^{207}Pb/^{206}Pb$ weight mean age calculations. Blue ellipsoids are excluded from the calculation, as they are inherited age data. (g) Distribution histogram for the Siou granodiorite analyzed sample I1C25B. (h) Backscattered electron image of zircon grains of the Kokoï diorite. (i) U-Pb concordia plots of zircons from Kokoï diorite (sample I1C20B).

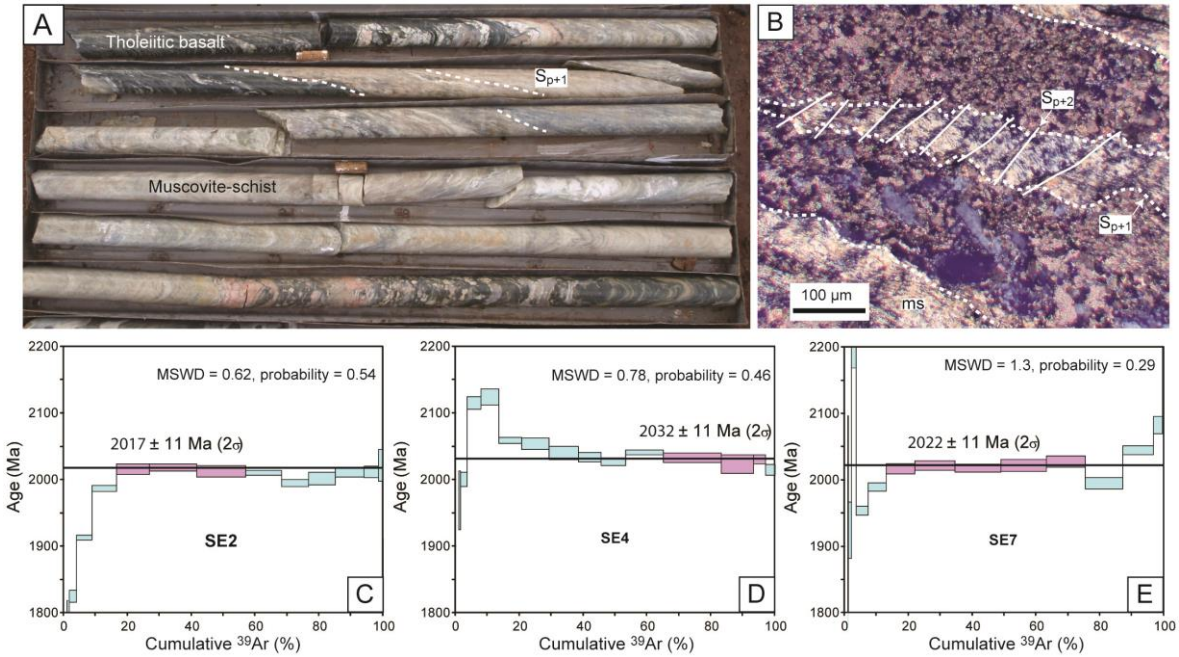

Figure 3.8 (a) Muscovite-schists hosted by tholeiitic basalts along the Wona-Kona major deformation zone defining the S_{p+1} schistosity. (b) Microphotograph of muscovite-schist (ms) defining S_{p+1} schistosity and crosscut by S_{p+2} crenulation cleavages, polarized transmitted light. (c to e) $^{40}Ar/^{39}Ar$ age spectra vs. ^{39}Ar released (%) for three hydrothermal muscovite samples (SE2, SE4, SE7) of the Wona-Kona gold deposit. Plateau steps are magenta-colored and rejected steps are cyan-colored.

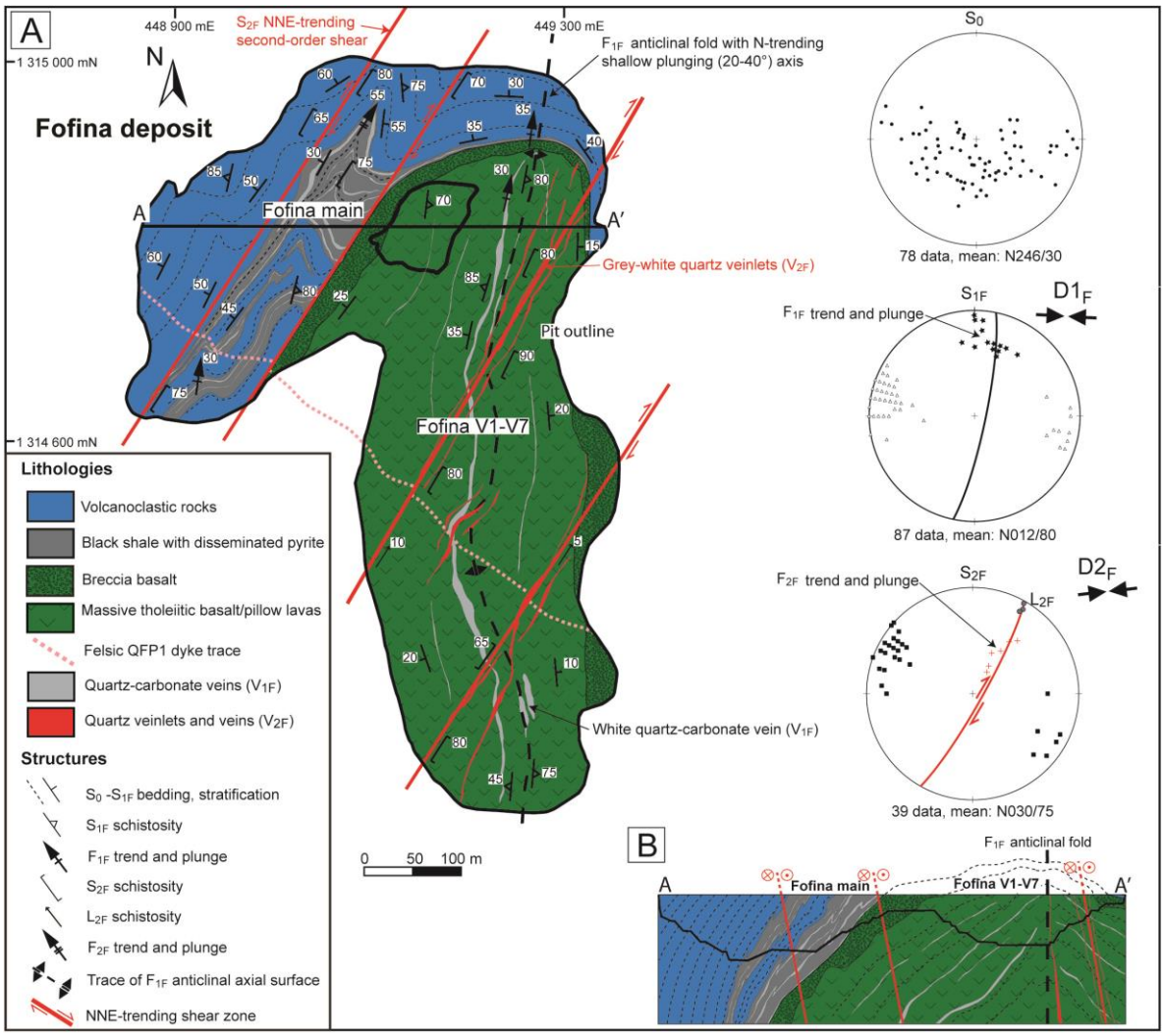

Figure 3.9 Plan and cross-section of the Fofina gold deposit. (a) Geological map of the Fofina deposit showing the surface expression of gold mineralization and the structural features. Structural data are presented as equal area lower hemisphere stereoplots. (b) Geological cross-section through the main anticlinal of the Fofina main and Fofina V1-V7 pits.

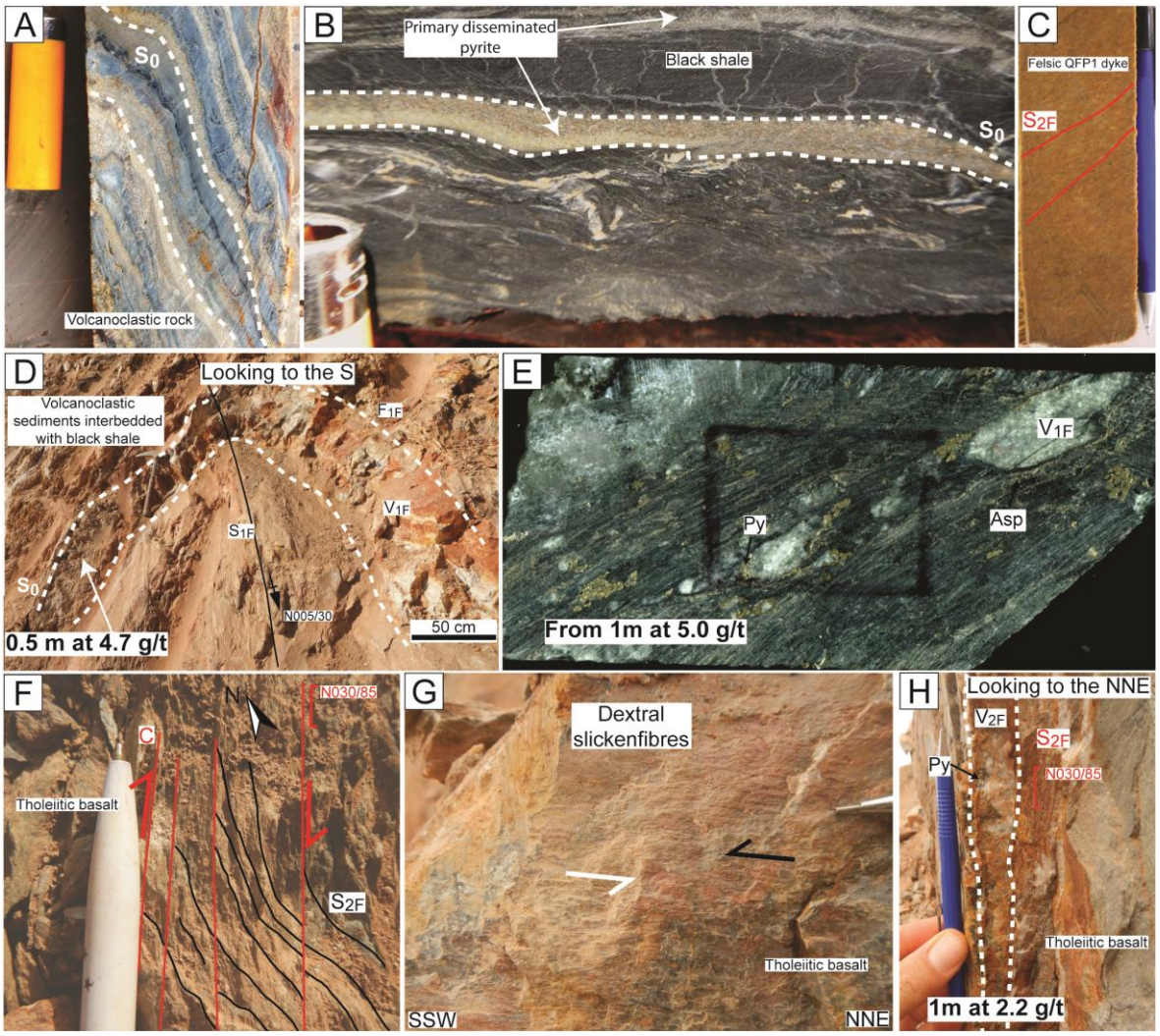

Figure 3.10 (a) Volcanoclastic rocks showing the S_0 folding. (b) Primary disseminated pyrite parallel to the bedding in the black shale unit. (c) Felsic QFP1 dyke affected by the S_{2F} schistosity from the drill core. (d) Field photograph illustrating the early quartz-carbonate vein (V_{1F}) folded by the axial planar schistosity S_{1F} in volcanoclastic rocks in the main Fofina pit. (e) Core photograph showing a quartz-carbonate vein (V_{1F}) with mineral assemblage of pyrite and arsenopyrite hosted in pillow basalt in the Fofina V1-V7 pit. (f) Field photography illustrating the C-S_{2F} fabric relationship compatible with a dextral displacement. (g) Subvertical NNE-trending fault wall with slickenfibres indicating horizontal movements. Black arrow indicates displacement of the missing block. (h) Typical view of a late NNE-trending quartz vein (V_{2F}) with mineral assemblage of pyrite (Py) along the S_{2F} schistosity marked by chlorite, muscovite and iron carbonates (Fofina V1-V7 pit).

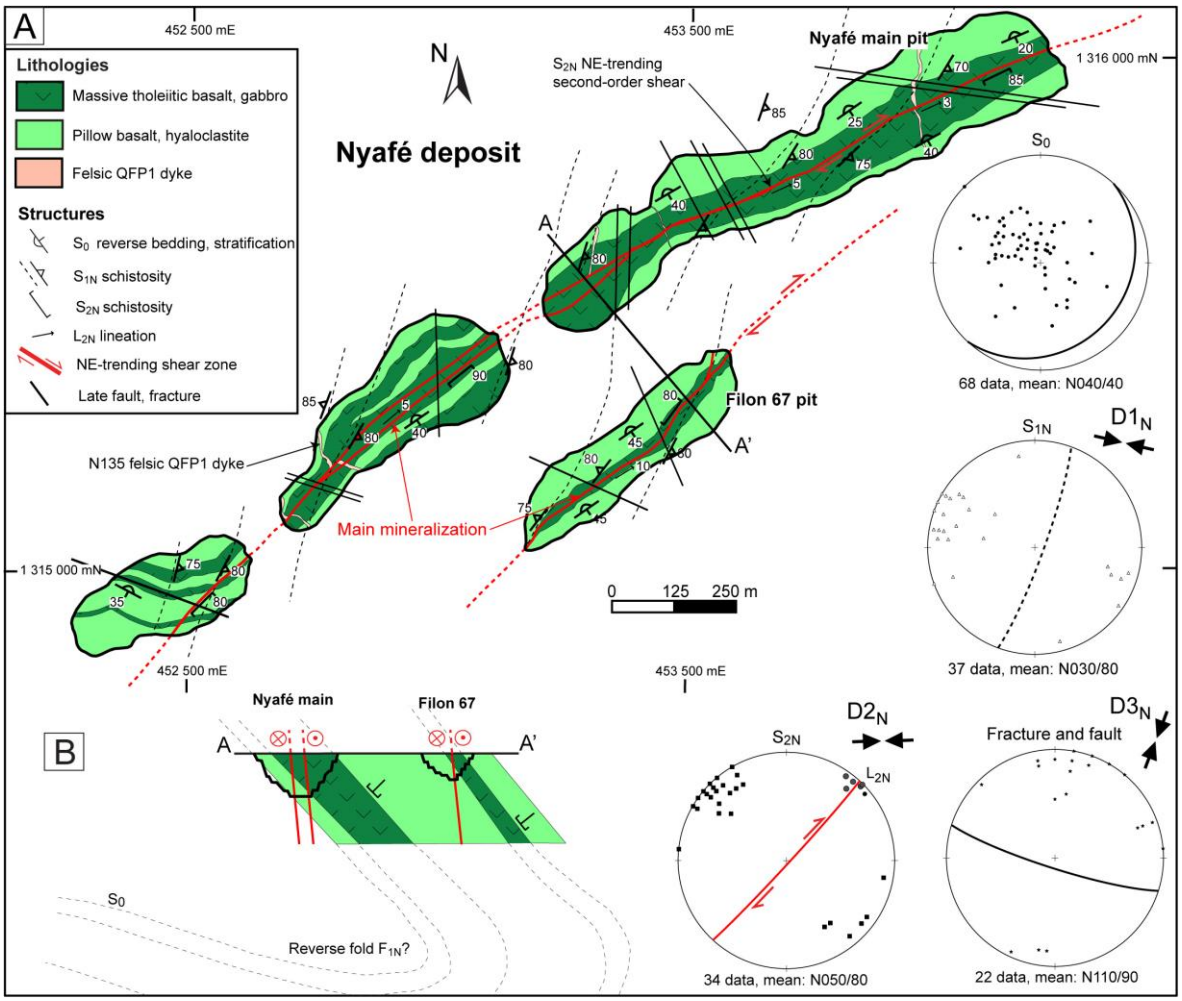

Figure 3.11 Plan and cross-section of the Nyafé gold deposit. (a) Geological and structural map of the Nyafé main and Filon 67 pits. Structural data are presented as equal area lower hemisphere stereoplots. (b) Geological cross-section of the Nyafé main and Filon 67 gold deposits.

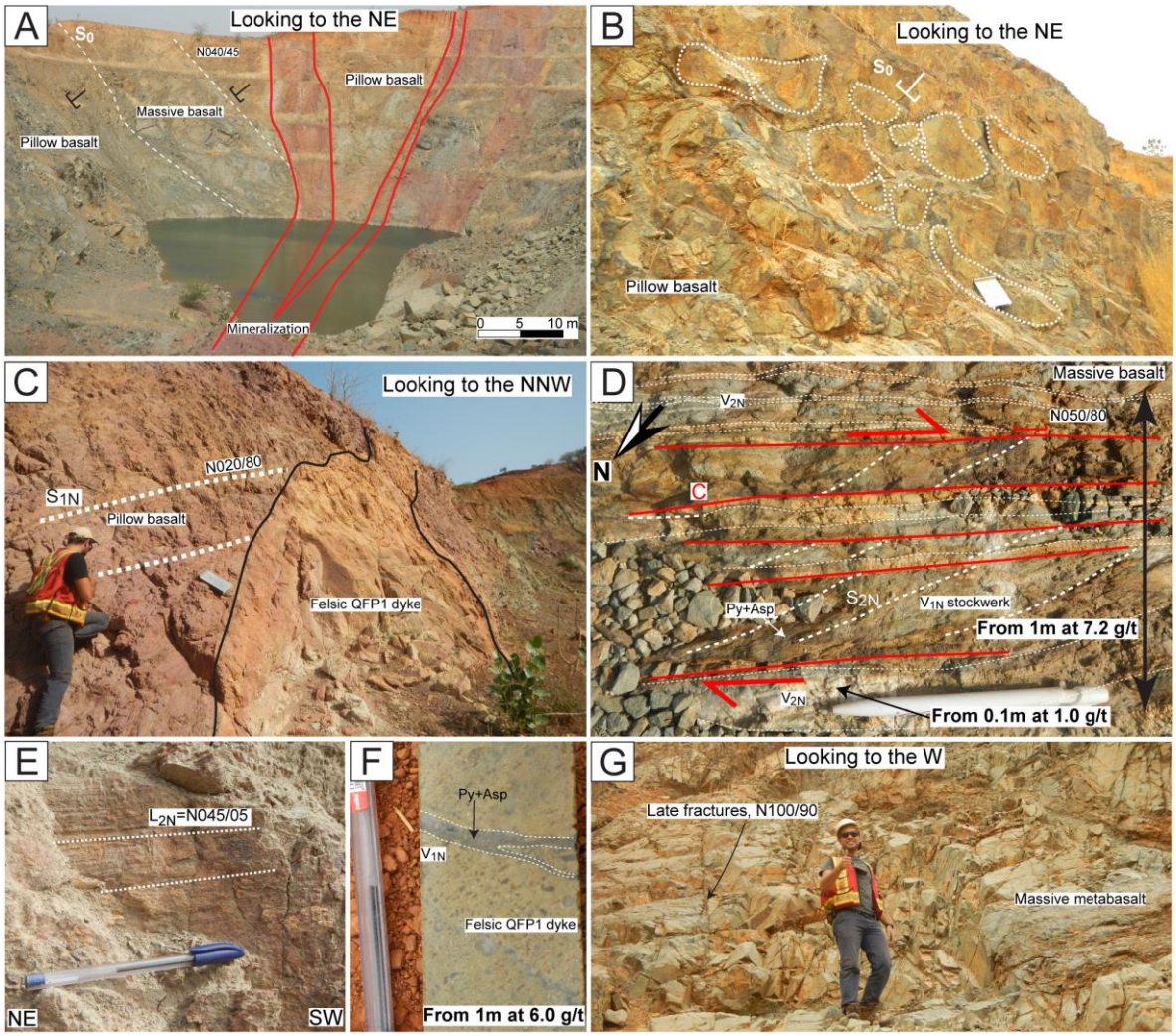

Figure 3.12 Field photographs illustrating structural features in relation to gold mineralization at Nyafé. (a) Field photography of gold mineralization and the reverse polarity of the basaltic sequence in the Nyafé main pit. (b) Metric pillow lavas showing convex-upward shapes indicating a reverse polarity of bedding that is plunging gently (40-50°) to the SE in the Filon 67 pit. (c) NNE-trending S_{1N} schistosity developed in the massive basalt but lacking in the SE-trending felsic QFP1 dyke in the Nyafé main pit. (d) Relationship with C-S_{2N} fabric and the quartz veinlets (V_{1N}) forming a stockwork and quartz-carbonate veins (V_{2N}) compatible with a dextral kinematic. (e) Subhorizontal striation lineation (L_{2N}) on the C-S_{2N} fabric in the Nyafé main pit. (f) Core photograph of high grade quartz veinlets (V_{1N}) with mineral assemblage of pyrite (Py) and arsenopyrite (Asp), which crosscut a muscovite felsic QFP1 dyke. (g) Late fractures (N100/90) in the massive tholeiitic basalt, Filon 67 pit.

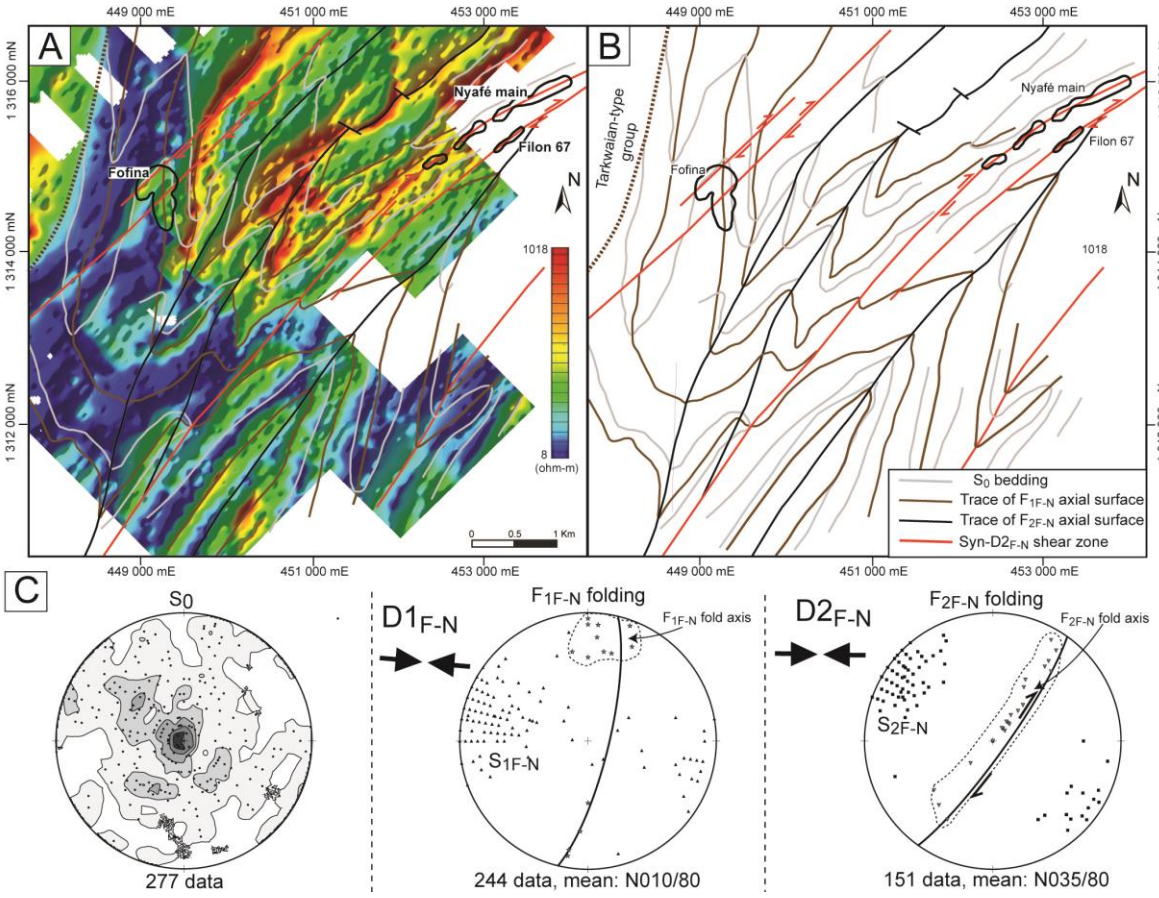

Figure 3.13 Structural framework of the Fofina and Nyafé area. (a) Detailed electrical resistivity map showing the high and low resistivity distribution. (b) Structural interpretation with the main S_0 bedding deformed by isoclinal $F_{1F\text{-}N}$ folds and then by $F_{2F\text{-}N}$ folds. The brown dashed line on the northwestern part of the sketch image represents the contact between the Lower Birimian and the younger Tarkwaian-type group. (c) Structural data are represented as equal area lower hemisphere stereoplots.

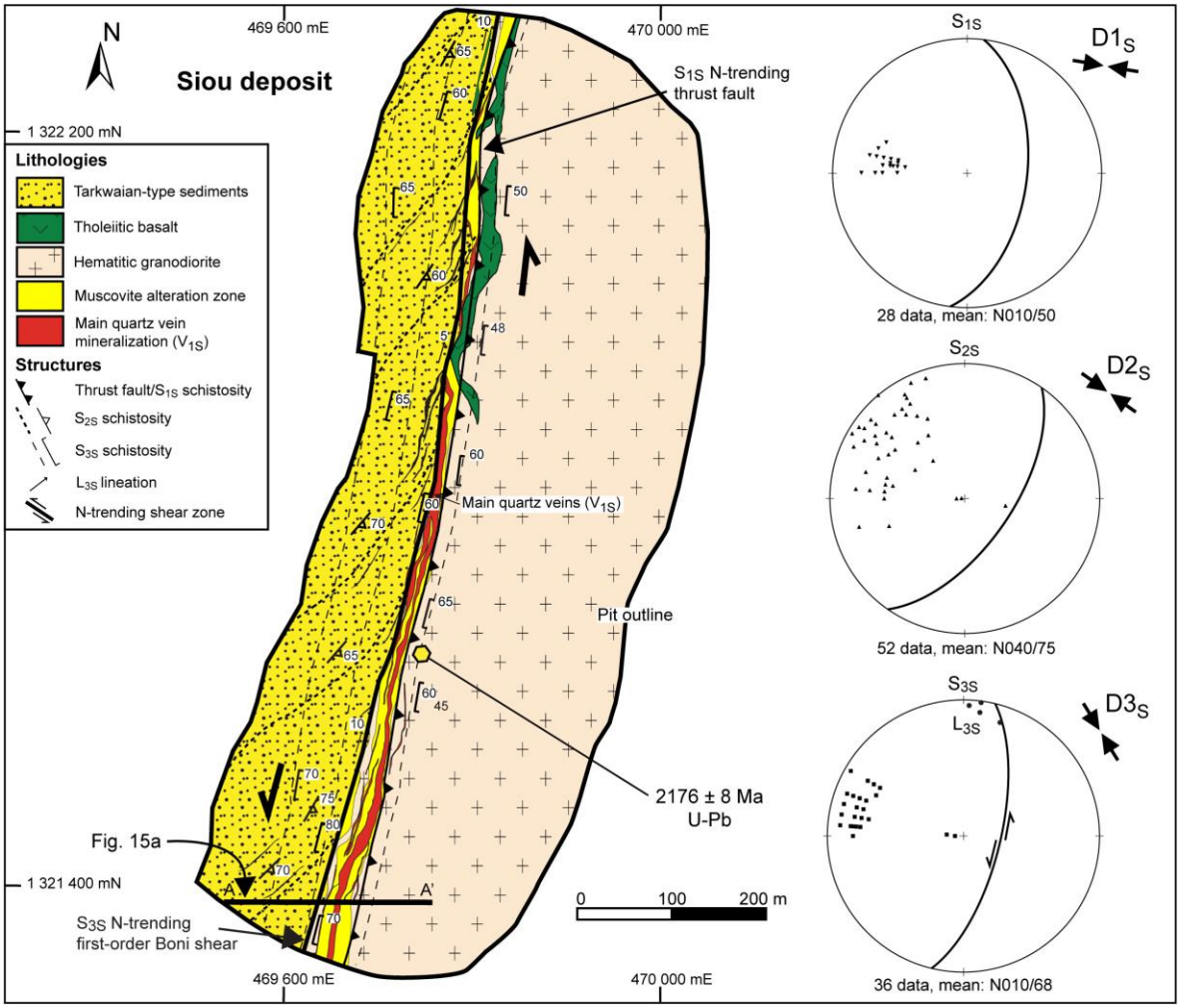

Figure 3.14 Geological map of the Siou deposit showing the surface expression of gold mineralization and the structural features. Structural data are presented as equal area lower hemisphere stereoplots. The mineralization seems to follow the contact between the Siou pluton and the Tarkwaian-type rocks. Enclaves of basaltic rocks occur close to the contact.

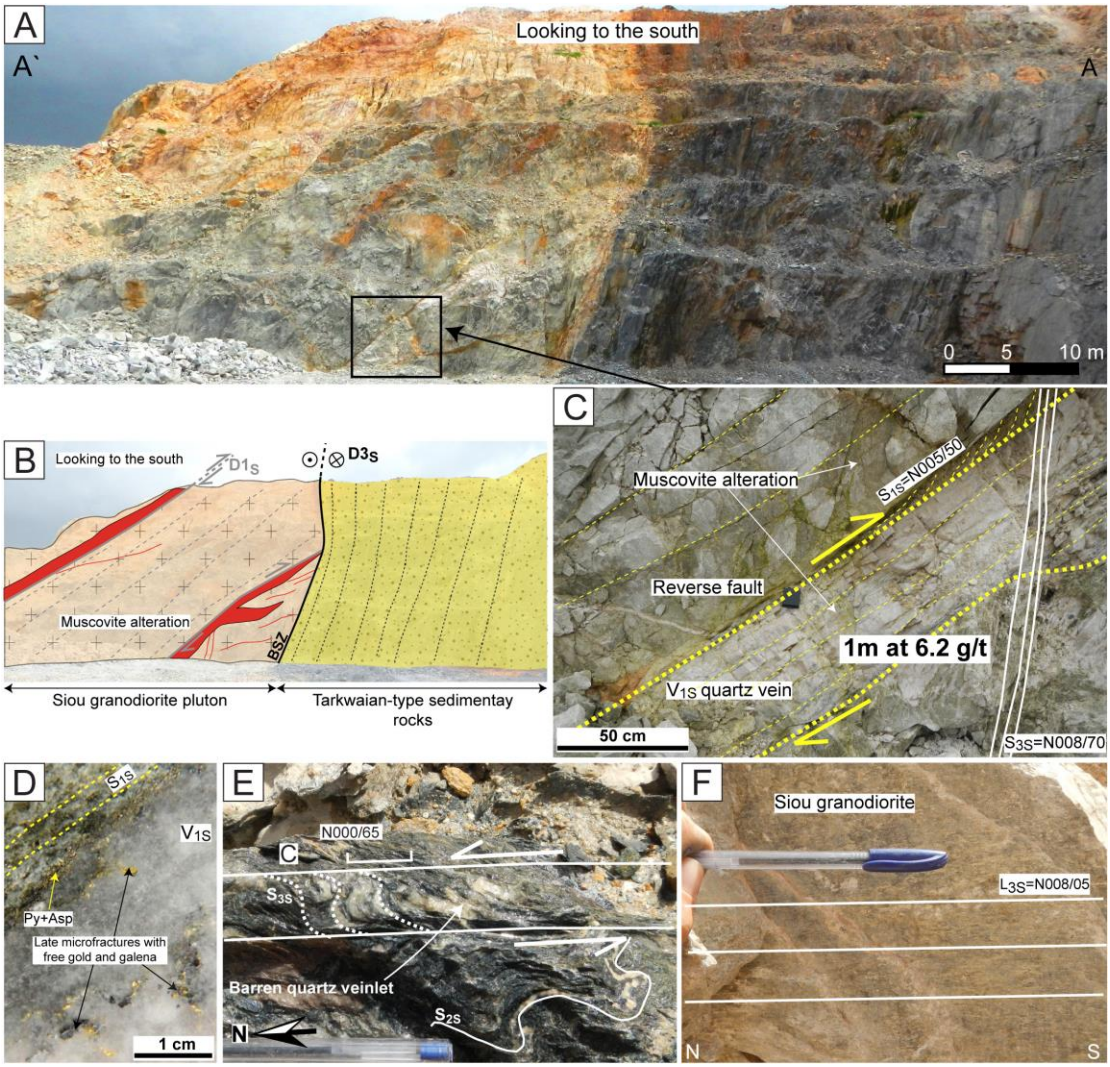

Figure 3.15 Field photographs illustrating the structural relationships with the Siou gold mineralization. (a-b) Photograph and interpretation sketch image of the south wall of the Siou pit illustrating the faulted contact (BSZ) between the Tarkwaian-type sedimentary rocks to the west and the Siou granodiorite pluton to the east (see Fig. 3.14 for the location of the cross-section). Gold mineralization is associated with quartz veins (V_{1S}) controlled by N-trending reverse brittle faults (N010/50) hosted in the Siou pluton and surrounded by muscovite alteration. (c) Quartz vein (V_{1S}) confined within the reverse fault (S_{1S}) in the granodiorite and cut by the N-trending (N008/70) S_{3S} fabric of the BSZ. (d) Free visible gold and galena in late microfractures of the V_{1S} quartz vein from a drill core. Pyrite and arsenopyrite occur along of the S_{1S} fabric. (e) C-S_{3S} fabric relationships compatible with a sinistral displacement in the Tarkwaian-type sedimentary rocks. (f) Stretching lineation (L_{3S}) along the S_{3S} fabric in the Siou pit.

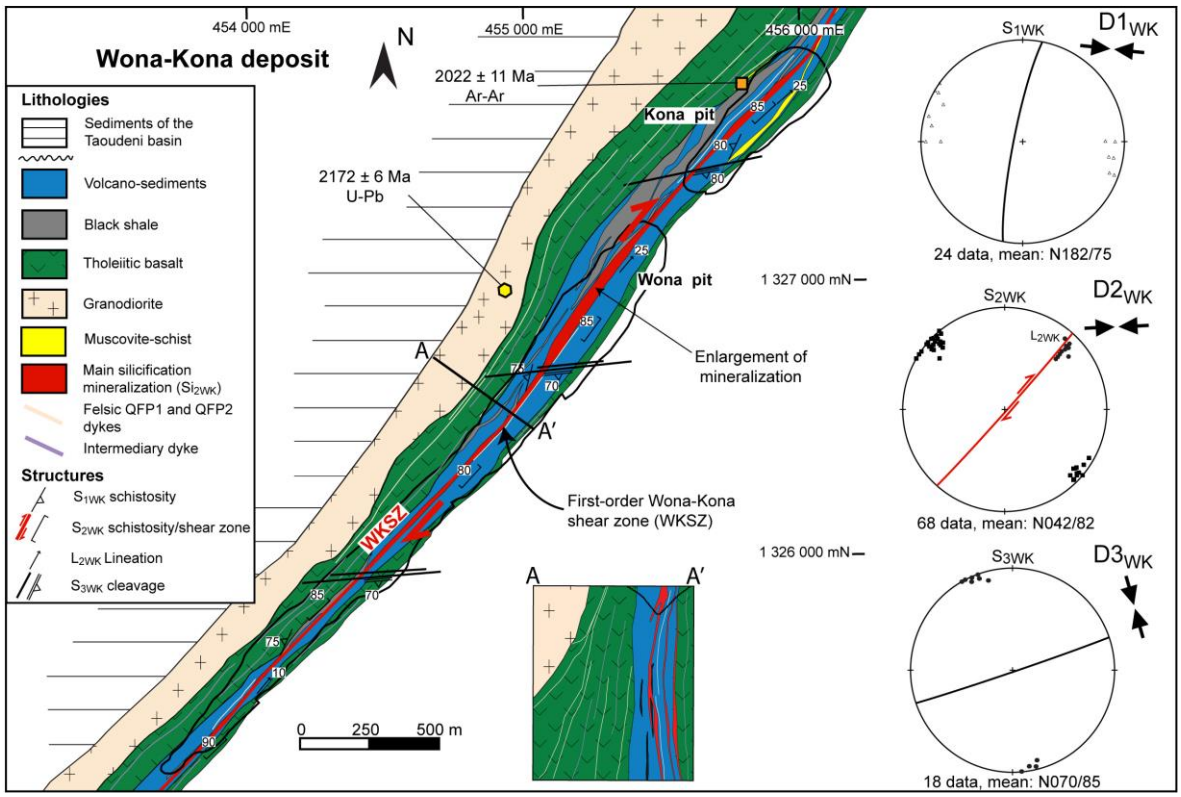

Figure 3.16 Simplified geological map and cross-section of the Wona-Kona deposit. Structural data recorded during field mapping are presented as equal area lower hemisphere stereoplots. Note the very continuous mineralization for over 5 km, hosted in strongly deformed and verticalized Lower Birimian strata. The thickening of the mineralization is related to a flexure compatible with a sinistral displacement.

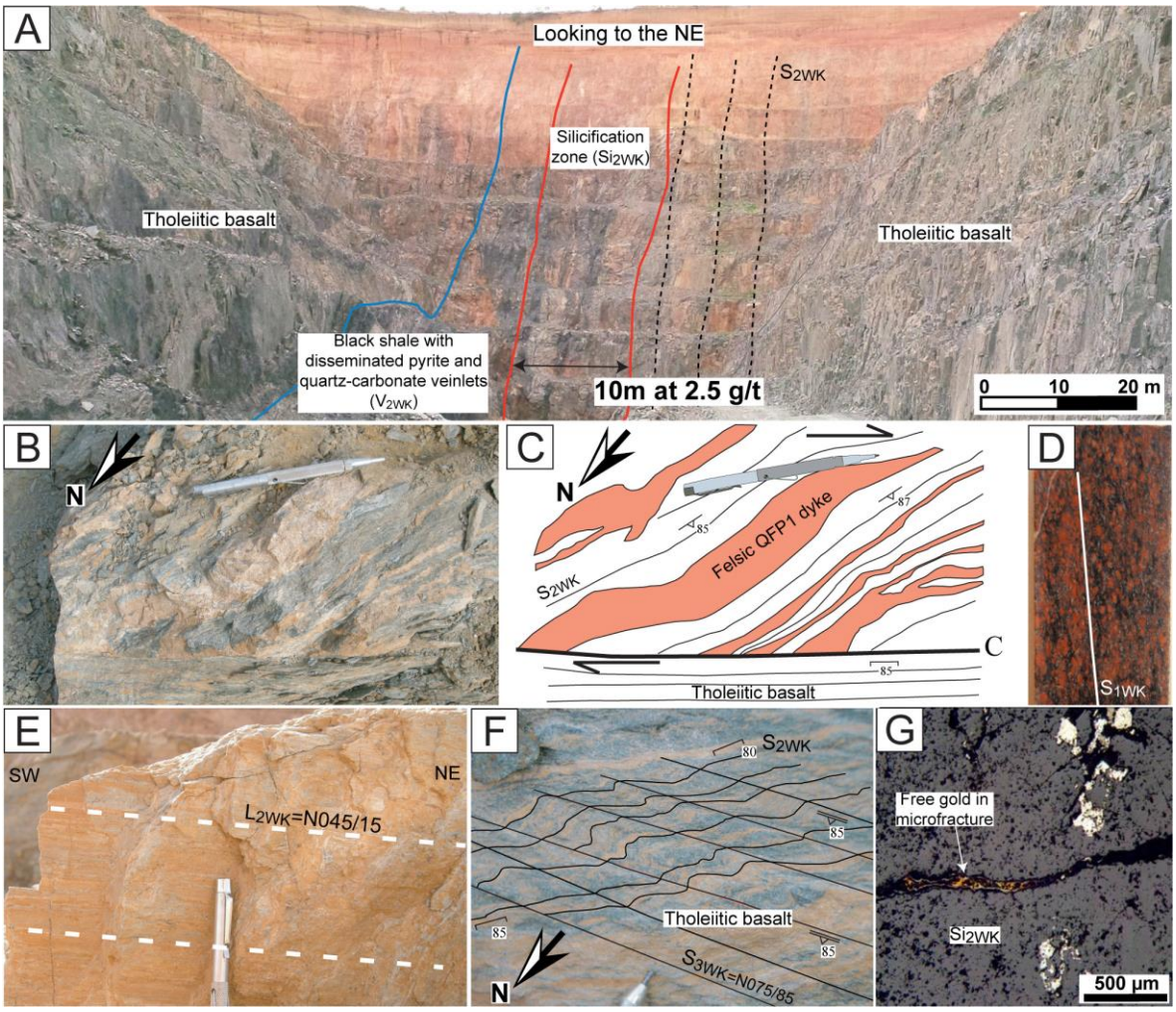

Figure 3.17 Field photographs of the structural relationships at the Wona-Kona deposit. (a) Typical view of the northeast Wona pit showing the main silicified orebody (Si_{2WK}), host rocks and the structural framework dominated by S_{2WK} schistosity. (b-c) Field photograph and interpretation sketch image showing the C-S_{2WK} fabric that affected the felsic QFP1 dyke and tholeiitic basalt compatible with a dextral displacement. (d) Wona-Kona hematitic granodiorite crosscut by the S_{1WK} foliation as seen in the drill core. (e) Subhorizontal striation lineation (L_{2WK}) along NE-trending subvertical S_{2WK} schistosity. (f) Penetrative schistosity (S_{2WK}) in tholeiitic basalt affected by late steeply dipping crenulation cleavages S_{3WK}. The brown bands are associated with iron carbonates along the S_{2WK}. (g) Reflected light image of late free gold in a microfracture crosscutting the silicification (Si_{2WK}).

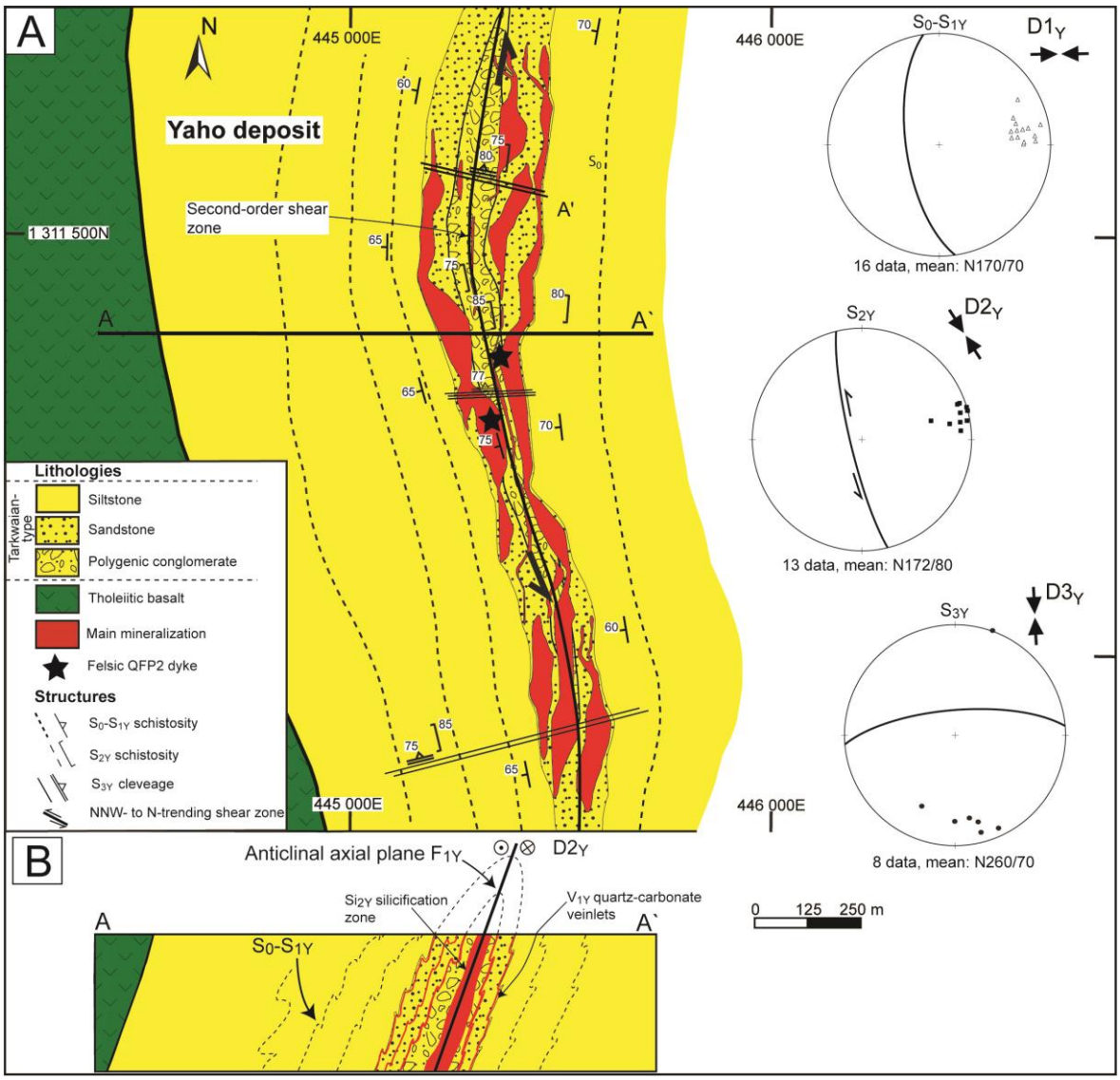

Figure 3.18 Simplified geological map and cross-section of the Yaho deposit. (a) Geological and structural map of the Yaho deposit. Structural data are presented as equal area lower hemisphere stereoplots. (b) Geological cross-section of the Yaho deposit. The gold mineralization is centered on the detrital sedimentary rocks (sandstone, polygenic conglomerate) defining an interpreted anticlinal fold.

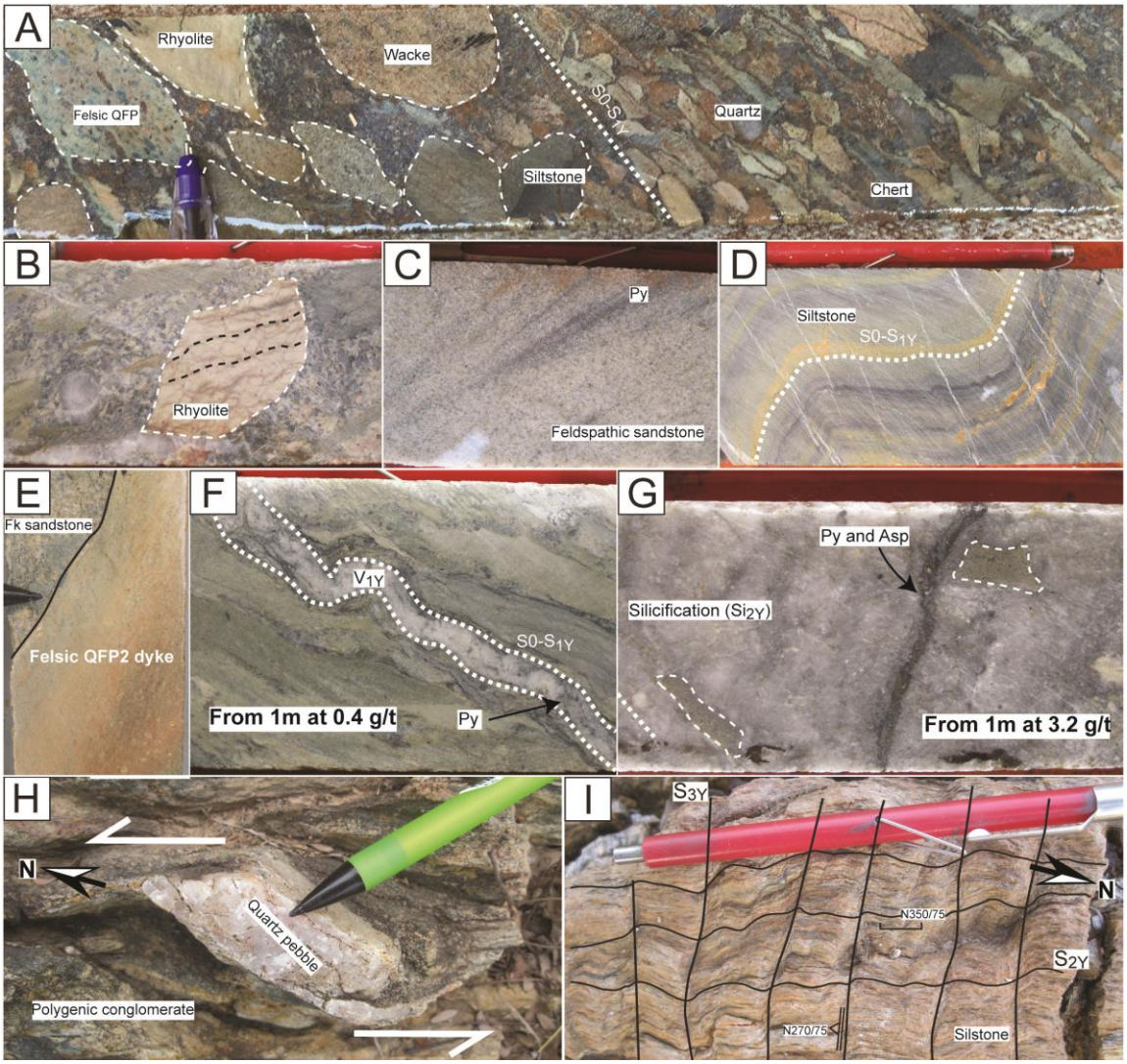

Figure 3.19 (a) Diamond drill core of the polygenic conglomerates with the presence of various kinds of pebbles, such as rhyolite, felsic QFP, siltstone, quartz, chert and wacke. (b) Centimetric rhyolite pebble showing an early schistosity formed before the sedimentation. (c) Feldspathic sandstone with cross-bedding structure associated with bands of hematite and disseminated pyrite grains (Py). (d) Siltstone interbedded with thin beds of wackes defining a folded S_0-S_{1Y} fabric. The white veinlets are along the S_{2Y} fabric. (e) Felsic QFP2 dyke intrudes the feldspathic sandstone and is affected by a planar fabric. (f) Quartz veinlet (V_{1Y}) with pyrite (Py) parallel to the bedding. (g) Silicified main zone (Si_{2Y}) hosted in polygenic conglomerates. Gold is associated with pyrite (Py) and arsenopyrite (Asp). (h) Sinistral sigma-shaped centimetric quartz-pebble hosted in a polygenic conglomerate unit as exposed on the field. (i) Typical relationship between the S_{2Y} schistosity and the S_{3Y} crenulation cleavage in a feldspathic sandstone unit.

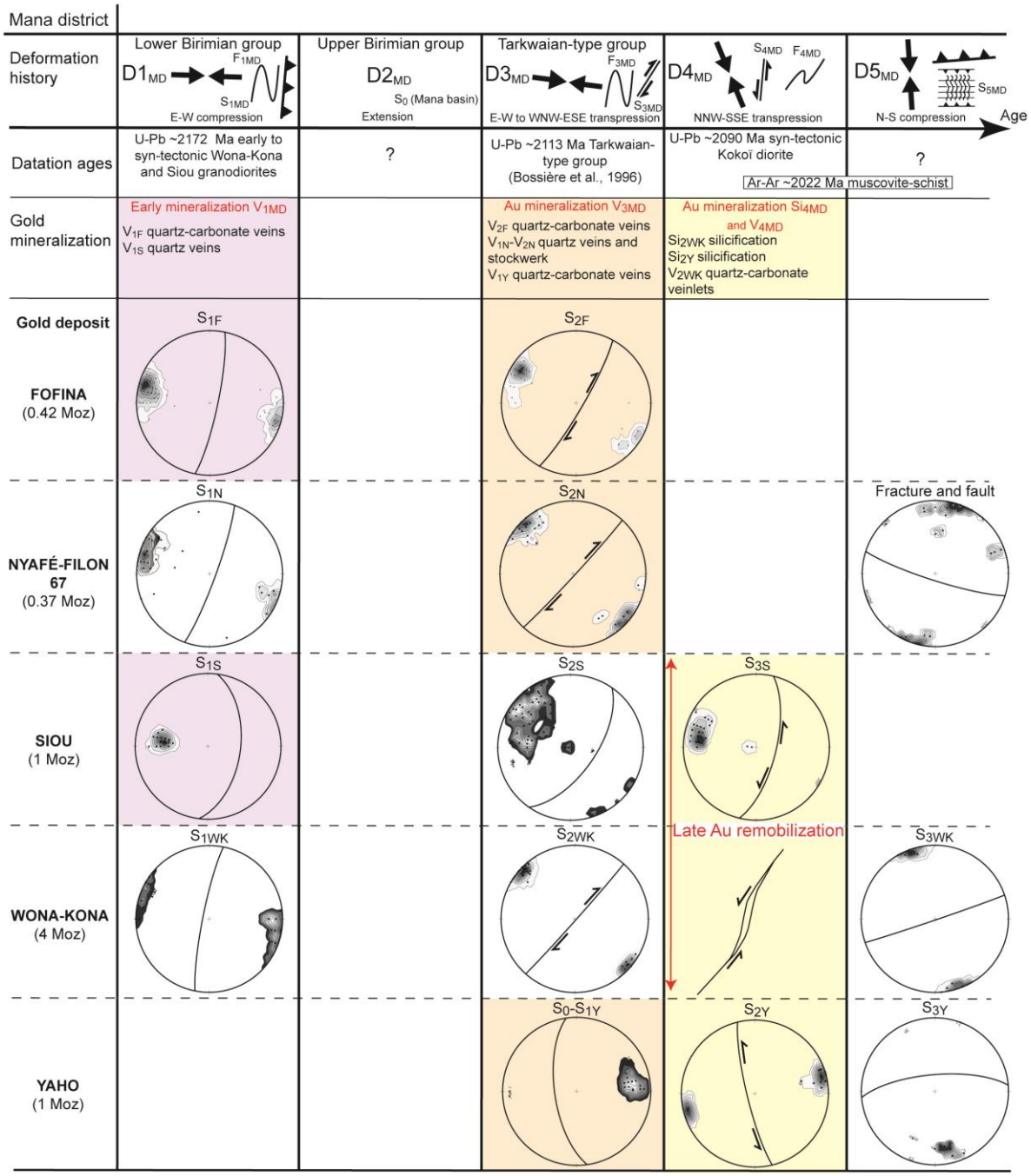

Figure 3.20 Stereoplot diagrams of the structural data collected over the Mana gold deposits, representing the evolution of the 5 deformational and 4 gold mineralizing events.

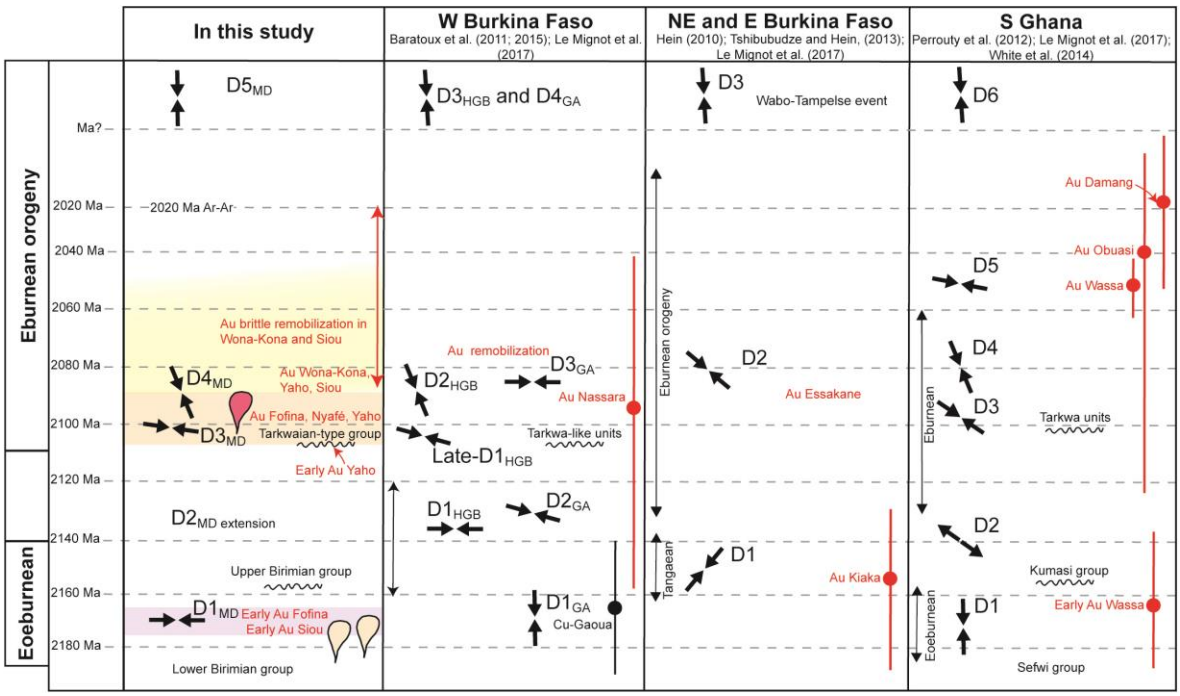

Figure 3.21 Correlations between deformation events and timing of the mineralization in the Mana district compared to western and northeastern Burkina Faso (Hein, 2010; Baratoux et al., 2011; Tshibubudze and Hein, 2013; Le Mignot et al., 2017) and southern Ghana (Perrouty et al., 2012; White et al., 2014; Le Mignot et al., 2017).

TABLEAUX DU CHAPITRE 3

Table 3.1 Geological characteristics of gold deposits from the Mana district.

Gold deposits	Gold	Host rock	Structural context	Metamorphic facies	Mineralization style	Major sulfides phases	Alteration assemblage (In decreasing abundance)
Fofina	0.42 Moz at 3.6 g/t	Voplcanoclastic rocks, black shale, tholeiitic basalt, felsic QFP1 dyke	Anticlinal fold and second-order dextral shear zone	Greenschist	Stratiform disseminated and quartz-sulfides veins	Pyrite, arsenopyrite	Chlorite Muscovite Iron carbonates
Nyafé	0.37 Moz at 6.0 g/t	Tholeiitic basalt, felsic QFP1 dyke	Second-order dextral shear zone	Greenschist	Stockworks and quartz veins	Pyrite, arsenopyrite	Chlorite Muscovite Epidote Carbonates
Siou	1 Moz at 5.0 g/t	Granodiorite, tholeiitic basalt, Tarkwaian-type sedimentary rocks	Thrust and regional sinistral shear zone (Boni fault)	Greenschist	Quartz veins and free gold	Pyrite	Muscovite Chlorite Iron carbonates
Wona-Kona	4 Moz at 2.3 g/t	Granodiorite, tholeiitic basalt, volcanoclastic rocks, black shale, Felsic QFP1-2 dykes	Regional dextral Shear zone (Wona-Kona fault)	Greenschist	Silicification, quartz-sulfides veins and free gold	Pyrite, arsenopyrite, chacopyrite, sphalerite	Silicification Muscovite Iron carbonates Chlorite Epidote
Yaho	1 Moz at 1.0 g/t	Tarkwaian-type sedimentary rocks, felsic QFP2 dyke	Fold and second-order sinsitral shear zone (Wona-Kona fault)	Greenschist	Disseminated and quartz-sulfides veins	Pyrite, arsenopyrite	Silicification Muscovite Iron carbonates

Table 3.2 Selected major oxides (wt.%) and trace element (ppm) data for the Wona-Kona and Siou granodiorites and the Kokoï diorite.

Sample	215496	215497	215526	215527	8215	8216	8217	8218	215683	215689
Rock type	grano.	grano.	grano.	grano.	grano.	grano.	grano.	grano.	diorite	diorite
Locality	Wona-Kona	Wona-Kona	Wona-Kona	Wona-Kona	Siou	Siou	Siou	Siou	Kokoï	Kokoï
SiO_2	71.6	73.2	71.6	70.3	70.1	72.0	70.8	69.2	62.6	62.2
TiO_2	0.26	0.26	0.19	0.28	0.25	0.29	0.27	0.35	0.81	0.73
Al_2O_3	14.25	14.15	13.8	14.75	13.6	14.75	14.1	13.85	14.7	14.7
Fe_2O_3	2.9	2.39	2.84	3.27	2.33	2.68	2.78	2.71	6.38	5.81
MnO	0.03	0.03	0.04	0.04	0.03	0.04	0.03	0.04	0.08	0.07
MgO	0.99	0.61	0.82	1.04	0.45	0.54	0.79	0.59	2.6	2.34
CaO	2.14	2.4	2.43	2.44	1.65	1.98	1.13	1.66	5.13	3.46
Na_2O	4.53	4.66	4.18	4.34	4.82	5.23	4.89	4.19	3.98	3.35
K_2O	2.2	1.82	1.65	1.63	2.35	2.47	2.27	2.57	0.82	2.43
P_2O_5	0.06	0.04	0.05	0.06	0.08	0.09	0.08	0.1	0.26	0.23
SrO	0.03	0.05	0.03	0.03	0.05	0.07	0.04	0.02	0.07	0.04
LOI	0.69	0.3	2.76	1.87	2.41	1.62	2.23	3.33	2.7	5.32
TOTAL	**99.8**	**100**	**100.5**	**100**	**98.1**	**101.85**	**99.37**	**98.68**	**100.18**	**100.69**
Mg#	40.3	33.6	36.4	38.6	27.7	28.5	36.0	30.1	56.4	58.4
V	40.0	39.0	15.0	25.0	28.0	34.0	30.0	40.0	134.0	126.0
Cr	20.0	40.0	20.0	10.0	10.0	20.0	10.0	10.0	100.0	60.0
Co	6.9	5.4	4.4	5.3	3.9	4.5	4.5	5.3	21.9	18.8
Rb	82.4	74.4	48.4	59.6	91.1	78.9	90.5	109.5	23.5	66.4
Sr	292	434	248	273	433	590	390	198.5	587	323
Ba	645	553	496	472	0.08	0.09	0.06	0.07	293	471
Y	4.7	5.6	4.2	6.4	5.7	6.3	6.1	6.9	13.1	13.7
Zr	138.0	174.0	138.0	170.0	120.0	130.0	110.0	130.0	170.0	200.0
Hf	3.9	4.6	4	4.6	3.5	3.5	3.3	3.7	4.4	4.4
Nb	5.3	4.9	2.1	5.8	4.8	5.6	4.6	5.3	7.1	7.6
Ta	0.5	0.5	0.1	0.4	0.5	0.5	0.4	0.5	0.4	0.6
Cs	2.15	1.96	1.62	1.38	1.86	2.29	2.23	2.74	0.51	1.29
Pb	6.0	9.0	5.0	4.0	9.0	12.0	8.0	6.0	5.0	6.0
Ga	20.2	21.2	16.2	18.7	22.3	23.5	23	23	20.3	20.9
Th	6.13	4.61	3.3	6.53	3.61	3.36	4.19	3.01	2.53	3.92
U	1.42	1.86	0.59	0.76	1.88	1.66	2.17	0.91	0.89	1.63
La	18.2	18.8	16.5	31.5	19	21.1	17.4	20.1	28.2	27.8
Ce	31.8	53.7	29.3	55.6	37	40.5	33.6	39	55	55.8
Pr	3.28	3.33	3.04	5.81	4.56	4.94	4.06	4.76	7.14	6.99
Nd	11.2	11.5	10.5	19.6	17.0	18.2	14.9	17.9	26.0	25.8
Sm	1.89	2.14	1.74	3.1	3.16	3.28	2.77	3.22	4.82	4.48
Eu	0.58	0.61	0.68	0.85	0.87	0.94	0.77	0.93	1.44	1.44
Gd	1.41	1.54	1.37	2.24	2.03	2.08	1.78	2.17	3.63	3.53
Tb	0.16	0.19	0.16	0.26	0.26	0.27	0.24	0.27	0.52	0.48
Dy	0.98	1.04	0.78	1.29	1.25	1.27	1.23	1.4	2.65	2.54
Ho	0.17	0.2	0.14	0.23	0.2	0.22	0.22	0.24	0.5	0.48
Er	0.46	0.53	0.38	0.6	0.49	0.54	0.57	0.59	1.34	1.38
Tm	0.07	0.07	0.05	0.08	0.07	0.08	0.08	0.09	0.2	0.19
Yb	0.46	0.49	0.34	0.53	0.4	0.5	0.51	0.55	1.18	1.19
Lu	0.07	0.08	0.06	0.08	0.06	0.07	0.07	0.07	0.18	0.17
W	2.0	1.0	5.0	1.0	3.0	-	1.0	6.0	1.0	3.0
$(La/Yb)_N$	28.38	27.52	34.81	42.63	34.07	30.27	24.47	26.21	17.14	16.76
$(Gd/Yb)_N$	4.2	3.44	2.89	3.26	4.2	3.44	2.89	3.26	2.54	2.45
Eu/Eu*	1.04	0.98	1.3	0.94	0.98	1.03	0.99	1.01	1.01	1.07

Table 3.3 Major oxide (wt.%) and trace element (ppm) data for the two types of felsic QFP dykes (QFP1 and QFP2) of the Mana district.

Sample	270992	279993	1289963	1289964	215163	215166	215330	215243	215511
Rock type	QFP1	QFP1	QFP1	QFP1	QFP2	QFP2	QFP1	QFP1	QFP2
Locality	Fofina	Fofina	Nyafé	Nyafé	Wona	Wona	Kona	Kona	Yaho
SiO_2	68.4	70.3	71.5	70.7	75.6	72.4	69.2	70	76.6
TiO_2	0.28	0.27	0.3	0.31	0.08	0.16	0.17	0.16	0.07
Al_2O_3	14.5	13.95	14.4	14.8	13.5	14.2	14.35	13.5	13.2
Fe_2O_3	2.25	2.19	2.29	2.3	1.02	1.4	1.53	1.64	1.25
MnO	0.06	0.1	0.04	0.04	0.04	0.04	0.06	0.04	0.03
MgO	0.86	0.65	0.65	1.07	0.32	0.56	0.93	0.83	0.16
CaO	1.97	1.47	2.05	1.21	0.63	1.31	1.58	1.27	0.38
Na_2O	2.73	4.6	2.52	1.88	3.74	3.78	3.88	3.58	3.6
K_2O	2.01	1.74	3.15	3.7	4.24	3.79	2.61	2.86	4.37
P_2O_5	0.07	0.06	0.09	0.09	<0.01	0.04	0.07	0.08	0.01
SrO	0.02	0.01	0.01	0.01	0.01	0.03	0.02	0.02	0.01
LOI	3.98	3.81	3.1	3.51	1.39	1.89	2.89	2.49	1.39
TOTAL	**97.2**	**99.2**	**100.2**	**99.7**	**100.5**	**99.7**	**97.4**	**96.5**	**101**
Mg#	38.41	21.86	35.98	47.95	14.48	22.68	32.18	31.46	8.09
V	34	26	27	30	-	5	9	10	-
Cr	10	10	10	10	10	-	10	10	10
Co	4.7	3.6	4.1	4.9	0.9	1.9	2.8	2.4	1
Rb	56.5	65.7	112	157.5	170	133.5	83.8	99.8	213
Sr	132.5	114.5	81.1	42.9	84.1	199.5	202	163	49.4
Ba	560	733	660	694	368	949	635	661	202
Y	6.8	6.9	6.7	7.7	18.3	21.7	8.3	8.9	23.5
Zr	143	105	130	146	47	134	122	127	49
Hf	4.4	3.3	3.7	3.9	2.5	4.3	3.7	3.8	2.4
Nb	5.3	4.7	6.8	8.2	11.7	10.3	7.3	7.7	14.1
Ta	0.6	0.5	0.5	0.7	1.1	0.8	0.8	0.8	1.3
Cs	9.77	16.25	14.6	23.8	3.57	2.18	1.81	1.94	6.31
Pb	7	8	9	9	12	25	5	22	18
Ga	18.8	18.3	16.7	19.7	15.6	17.3	16.1	17.1	16.9
Th	6.48	6.37	8.68	10	6.53	10.7	6.66	7.65	5.63
U	2.99	2.82	4.2	4.81	3.71	3.91	3.32	3.5	4.24
La	16.2	15.7	21.6	24.1	14.9	44	22.5	23.8	11.6
Ce	29.7	29.3	40.5	44.4	33	87.4	40.5	43.1	25
Pr	3.45	3.23	4.31	4.76	4.03	9.97	4.08	4.6	3.13
Nd	12.1	11.9	15.4	16.5	14.8	36.7	14.3	15	11.4
Sm	2.37	2.02	2.55	2.98	3.72	6.96	2.33	2.66	3.17
Eu	0.53	0.53	0.61	0.69	0.67	1.42	0.61	0.64	0.53
Gd	2.08	1.9	1.83	2.08	3.38	4.41	1.78	1.73	3.59
Tb	0.25	0.24	0.27	0.28	0.57	0.71	0.26	0.28	0.6
Dy	1.35	1.22	1.22	1.49	3.24	3.61	1.36	1.46	3.82
Ho	0.26	0.21	0.25	0.28	0.65	0.69	0.26	0.27	0.75
Er	0.75	0.62	0.64	0.77	1.89	1.98	0.79	0.79	2.23
Tm	0.1	0.09	0.09	0.1	0.28	0.29	0.12	0.12	0.32
Yb	0.67	0.6	0.62	0.67	1.92	1.97	0.86	0.87	2.25
Lu	0.11	0.08	0.1	0.09	0.3	0.31	0.14	0.14	0.33
W	4	2	5	7	1	2	4	4	4
$(La/Yb)_N$	17.34	18.77	24.99	25.81	5.57	16.02	18.76	19.62	3.69
$(Gd/Yb)_N$	2.57	2.62	2.44	2.57	1.45	1.85	1.71	1.64	1.32
Eu/Eu*	0.71	0.81	0.82	0.81	0.57	0.73	0.88	0.85	0.48

Table 3.4 LA-ICP-MS U-Pb isotopic data of zircons from the plutons of the Mana district.

Sample	U (ppm)	Th (ppm)	Pb*	Th/U	$^{206}Pb/^{238}U$	± 1σ (%)	$^{207}Pb/^{235}U$	± 1σ (%)	$^{207}Pb/^{206}Pb$	± 1σ (%)	Rho	$^{206}Pb/^{238}U$	± 1σ (Ma)	$^{207}Pb/^{206}Pb$	± 1σ (Ma)	Conc. (%)
I1C24B Wona-Kona granodiorite																
r4g1	68	43	30	0.64	0.3862	0.0038	7.2178	0.0908	0.1355	0.0011	0.79	2105	18	2171	14	3.0
r4g2	160	36	74	0.23	0.3998	0.0040	7.4817	0.0953	0.1357	0.0011	0.79	2168	18	2173	14	0.2
r4g3	109	65	47	0.60	0.3918	0.0038	7.2931	0.0894	0.1350	0.0010	0.78	2131	17	2164	13	1.5
r4g4	98	58	45	0.60	0.3941	0.0045	7.3480	0.1069	0.1352	0.0012	0.79	2142	21	2167	16	1.2
r4g5	112	3	45	0.03	0.3989	0.0037	7.4531	0.0886	0.1355	0.0010	0.78	2164	17	2171	13	0.3
r4g6	85	44	37	0.52	0.3945	0.0039	7.4117	0.0934	0.1363	0.0011	0.78	2144	18	2180	14	1.7
r4g11	71	16	29	0.22	0.3952	0.0041	7.3831	0.0984	0.1355	0.0011	0.78	2147	19	2170	14	1.1
r4g12	77	35	34	0.45	0.3874	0.0040	7.2478	0.0947	0.1357	0.0011	0.78	2111	18	2173	14	2.9
r4g14	83	29	38	0.35	0.4154	0.0040	7.8248	0.0975	0.1366	0.0011	0.78	2240	18	2185	14	-2.5
r4g15	54	25	23	0.47	0.3937	0.0044	7.3888	0.1058	0.1361	0.0012	0.78	2140	20	2179	16	1.8
r3gr1	117	28	49	0.24	0.3971	0.0043	7.3956	0.1035	0.1351	0.0012	0.78	2156	20	2165	15	0.4
r3gr2	66	38	28	0.57	0.3889	0.0045	7.2516	0.1065	0.1352	0.0012	0.78	2118	21	2167	16	2.3
r3gr3	117	28	48	0.24	0.3958	0.0040	7.4095	0.0958	0.1358	0.0011	0.77	2149	18	2174	14	1.1
r3gr4	46	12	20	0.25	0.3848	0.0050	7.2068	0.1189	0.1358	0.0014	0.78	2099	23	2175	18	3.5
r3gr5-1c	171	113	87	0.66	0.4045	0.0042	7.5349	0.1004	0.1351	0.0011	0.77	2190	19	2165	15	-1.1
r3gr5-2r	118	17	51	0.14	0.4105	0.0044	7.6764	0.1064	0.1356	0.0012	0.77	2217	20	2172	15	-2.1
r3gr6	180	125	87	0.69	0.4021	0.0050	7.5319	0.1206	0.1359	0.0014	0.78	2179	23	2175	18	-0.2
r3gr7	156	53	70	0.34	0.4004	0.0046	7.5106	0.1127	0.1360	0.0013	0.77	2171	21	2177	17	0.3
r3gr9	36	14	16	0.39	0.3978	0.0058	7.4252	0.1395	0.1354	0.0016	0.78	2159	27	2169	21	0.5
r3gr10	35	12	15	0.34	0.3900	0.0053	7.3081	0.1281	0.1359	0.0015	0.77	2123	24	2176	19	2.4
r3gr11	212	29	97	0.13	0.4136	0.0050	7.6928	0.1207	0.1349	0.0014	0.77	2231	23	2163	18	-3.2
r3gr12	20	10	9	0.49	0.3983	0.0087	7.4108	0.2079	0.1349	0.0024	0.78	2161	40	2163	31	0.1
r3gr13	86	55	43	0.64	0.4034	0.0057	7.5967	0.1389	0.1366	0.0016	0.77	2185	26	2184	20	0
r3gr14	73	25	31	0.34	0.3984	0.0047	7.4833	0.1162	0.1362	0.0014	0.76	2162	22	2180	18	0.8
r3gr15-1r	95	18	36	0.19	0.3696	0.0044	6.8971	0.1088	0.1354	0.0014	0.76	2027	21	2169	18	6.5
r3gr15-2c	134	77	69	0.58	0.4101	0.0055	7.6654	0.1340	0.1356	0.0015	0.77	2215	25	2171	20	-2.0

Sample	U (ppm)	Th (ppm)	Pb*	Th/U	$^{206}Pb/^{238}U$	± 1σ (%)	$^{207}Pb/^{235}U$	± 1σ (%)	$^{207}Pb/^{206}Pb$	± 1σ (%)	Rho	$^{206}Pb/^{238}U$	± 1σ (Ma)	$^{207}Pb/^{206}Pb$	±1σ (Ma)	Conc. (%)
I1C25B Siou granodiorite																
r1g1-1r	477	113	214	0.24	0.3932	0.0034	7.1993	0.0766	0.1328	0.0008	0.80	2137	15	2135	11	-0.1
r1g1-2c	513	106	247	0.21	0.4042	0.0039	7.5586	0.0941	0.1356	0.0011	0.77	2188	18	2172	14	-0.7
r1g1-3c	374	72	156	0.19	0.4007	0.0041	7.4913	0.0985	0.1356	0.0011	0.77	2172	19	2172	15	0
r1g2-1r	326	52	135	0.16	0.3928	0.0033	7.1873	0.0745	0.1327	0.0008	0.80	2136	15	2134	11	-0.1
r1g2-2r	331	57	131	0.17	0.3935	0.0038	7.2191	0.0902	0.1331	0.0011	0.77	2139	17	2139	14	0
r1g3-1r	210	9	84	0.04	0.3930	0.0035	7.1823	0.0796	0.1326	0.0009	0.80	2137	16	2132	12	-0.2
r1g3-2c	419	23	125	0.06	0.2974	0.0029	5.7127	0.0717	0.1393	0.0011	0.76	1678	14	2219	14	24.4
r1g4	797	74	238	0.09	0.2907	0.0026	5.8519	0.0660	0.1460	0.0010	0.80	1645	13	2300	12	28.5
r1g5	464	85	185	0.18	0.3833	0.0032	7.1692	0.0747	0.1357	0.0009	0.80	2092	15	2173	11	3.7
r1g6	405	96	181	0.24	0.4044	0.0034	7.5787	0.0802	0.1359	0.0009	0.80	2189	16	2176	11	-0.6
r1g7	386	69	166	0.18	0.3956	0.0034	7.4174	0.0796	0.1360	0.0009	0.80	2149	16	2177	11	1.3
r1g8	385	54	165	0.14	0.4030	0.0034	7.6722	0.0803	0.1381	0.0009	0.80	2183	15	2203	11	0.9
r1g15	192	56	88	0.29	0.4012	0.0039	7.5156	0.0907	0.1359	0.0010	0.80	2174	18	2175	13	0
r2g1	470	109	151	0.23	0.3034	0.0026	5.9381	0.0630	0.1419	0.0009	0.79	1708	13	2251	11	24.1
r2g3	270	49	116	0.18	0.3916	0.0035	7.3664	0.0821	0.1364	0.0009	0.79	2130	16	2182	12	2.4
r2g9	392	75	153	0.19	0.3542	0.0030	6.7961	0.0739	0.1392	0.0009	0.79	1955	14	2217	12	11.8
r2g12	251	35	115	0.14	0.4260	0.0038	8.6167	0.0965	0.1467	0.0010	0.79	2288	17	2308	12	0.9
r2g15	45	13	19	0.30	0.3966	0.0043	7.4114	0.1030	0.1355	0.0012	0.79	2154	20	2171	15	0.8
r3g2	373	86	172	0.23	0.4104	0.0037	7.8854	0.0901	0.1394	0.0010	0.78	2217	17	2219	12	0.1
r3g4-1r	16	4	6	0.25	0.3917	0.0065	7.1711	0.1522	0.1328	0.0017	0.79	2131	30	2135	23	0.2
r3g4-2c	19	5	7	0.29	0.3680	0.0056	6.8596	0.1341	0.1352	0.0016	0.78	2020	26	2167	21	6.8
r3g5	235	71	104	0.30	0.4026	0.0038	7.5766	0.0907	0.1365	0.0010	0.78	2181	17	2183	13	0.1
r3g6	307	46	138	0.15	0.3974	0.0038	7.5623	0.0932	0.1380	0.0011	0.78	2157	18	2202	13	2.0
r3g7	316	57	125	0.18	0.3560	0.0033	7.0472	0.0834	0.1436	0.0011	0.77	1963	15	2271	13	13.5
r3g8	1223	740	273	0.61	0.2268	0.0021	4.3526	0.0510	0.1392	0.0010	0.77	1318	11	2217	13	40.6
r3g9	154	95	69	0.61	0.3941	0.0038	7.3685	0.0931	0.1356	0.0011	0,77	2142	18	2172	14	1.4

Sample	U (ppm)	Th (ppm)	Pb*	Th/U	$^{206}Pb/^{238}U$	± 1σ (%)	$^{207}Pb/^{235}U$	± 1σ (%)	$^{207}Pb/^{206}Pb$	± 1σ (%)	Rho	$^{206}Pb/^{238}U$	± 1σ (Ma)	$^{207}Pb/^{206}Pb$	± 1σ (Ma)	Conc. (%)
IC20B Kokoï diorite																
oc23	198.6	100.3	78.2	0.51	0.2567	0.0181	4.6380	0.3316	0.1310	0.0014	0.99	1473	92	2111	19	69.8
oc24	152.9	108.2	95.8	0.71	0.3824	0.0058	6.8930	0.1118	0.1307	0.0007	0.94	2087	27	2108	10	99.0
oc27	97.7	52.7	62.1	0.54	0.4183	0.0070	7.4883	0.1330	0.1298	0.0008	0.94	2252	31	2095	10	107.5
oc28	14.0	142.5	12.5	10.15	0.1755	0.0060	3.2460	0.1407	0.1341	0.0035	0.79	1042	33	2152	45	48.4
oc29	42.4	17.6	21.0	0.41	0.3231	0.0078	5.7318	0.1463	0.1287	0.0010	0.95	1804	38	2080	14	86.8
oc30	70.6	32.5	46.1	0.46	0.4328	0.0032	7.6383	0.0747	0.1280	0.0008	0.76	2318	14	2070	11	111.9
oc32	91.4	45.5	57.0	0.50	0.4098	0.0052	7.2787	0.1027	0.1288	0.0008	0.90	2213	23	2082	11	106.3
oc33	66.3	31.2	43.7	0.47	0.4318	0.0077	7.6642	0.1444	0.1287	0.0008	0.94	2313	34	2080	11	111.2
oc35	120.6	93.1	71.8	0.77	0.3696	0.0103	6.6182	0.1891	0.1299	0.0008	0.98	2027	48	2096	10	96.7

Table 3.5 $^{40}Ar/^{39}Ar$ analytical results for Wona-Kona samples SE2, SE4 and SE7.

Step	Temp	Cum.%	^{40}Ar		^{39}Ar		^{38}Ar		^{37}Ar		^{36}Ar								
no.	(˚C)	^{39}Ar	(x10^{-13} moles)	± 2σ	(x10^{-14} moles)	± 2σ	(x10^{-16} moles)	± 2σ	(x10^{-16} moles)	± 2σ	(x10^{-16} moles)	± 2σ	Ca/K	± 2σ	%^{40}Ar*	$^{40}Ar^*/^{39}Ar$	± 2σ	Age (Ma)	± 2σ
Sample SE2																			
J-value = 0.0250452 ± 0.00006																			
1	550	0.67	0.2659	0.0006	0.0389	0.0004	0.0004	0.0087	5.7885	0.0604	0.0078	0.0069	2.6059	0.0362	99.1	67.81	0.82	1790.7	13.8
2	600	3.03	0.9587	0.0013	0.1366	0.0005	0.0516	0.0142	16.6828	0.1730	0.0158	0.0033	2.1378	0.0233	99.5	69.86	0.27	1825.0	4.4
3	650	7.98	2.1649	0.0024	0.2863	0.0002	0.0789	0.0093	12.7292	0.1405	0.0208	0.0060	0.7779	0.0086	99.7	75.39	0.12	1914.0	1.9
4	700	15.76	3.6060	0.0041	0.4495	0.0007	0.1302	0.0091	2.4724	0.1057	0.0000	0.0016	0.0963	0.0041	100.0	80.22	0.15	1988.4	2.3
5	750	26.29	5.0220	0.0062	0.6093	0.0017	0.2258	0.0301	1.7486	0.0305	0.0646	0.0256	0.0502	0.0009	99.6	82.11	0.28	2016.6	4.1
6	800	40.98	6.9977	0.0092	0.8494	0.0014	0.2781	0.0248	1.9285	0.1579	0.0277	0.0234	0.0397	0.0033	99.9	82.29	0.19	2019.3	2.8
7	850	56.61	7.4396	0.0091	0.9037	0.0006	0.3271	0.0382	1.6961	0.2258	0.1250	0.0799	0.0328	0.0044	99.5	81.91	0.29	2013.7	4.2
8	900	67.75	5.2894	0.0060	0.6443	0.0006	0.2403	0.0205	1.3763	0.0604	0.0781	0.0088	0.0374	0.0016	99.6	81.74	0.12	2011.1	1.9
9	950	76.49	4.1070	0.0051	0.5059	0.0004	0.2078	0.0349	1.1823	0.0556	0.0774	0.0203	0.0409	0.0019	99.4	80.74	0.17	1996.1	2.5
10	1000	84.80	3.9134	0.0047	0.4804	0.0015	0.1944	0.0248	0.8942	0.1202	0.0446	0.0195	0.0326	0.0044	99.7	81.18	0.30	2002.8	4.5
11	1050	93.99	4.3560	0.0056	0.5313	0.0010	0.2084	0.0232	0.7345	0.1324	0.0404	0.0253	0.0242	0.0044	99.7	81.77	0.23	2011.6	3.4
12	1100	98.55	2.1704	0.0025	0.2642	0.0009	0.1612	0.0086	0.8544	0.0424	0.0264	0.0078	0.0566	0.0028	99.6	81.86	0.30	2012.9	4.4
13	1150	99.60	0.5067	0.0011	0.0604	0.0004	0.0460	0.0146	0.7358	0.0546	0.0288	0.0116	0.2133	0.0159	98.3	82.51	0.80	2022.6	11.9
14	1450	100.00	0.3876	0.0014	0.0233	0.0003	0.1758	0.0143	1.9958	0.0368	0.7586	0.0174	1.5015	0.0338	42.2	70.26	2.46	1831.4	40.4

Step	Temp	Cum.%	^{40}Ar		^{39}Ar		^{38}Ar		^{37}Ar		^{36}Ar								
no.	(˚C)	^{39}Ar	(x10^{-13} moles)	± 2σ	(x10^{-14} moles)	± 2σ	(x10^{-16} moles)	± 2σ	(x10^{-16} moles)	± 2σ	(x10^{-16} moles)	± 2σ	Ca/K	± 2σ	%^{40}Ar*	^{40}Ar*/^{39}Ar	± 2σ	Age (Ma)	± 2σ
Sample SE4																			
J-values = 0.025058 ± 0.00006																			
1	550	0.62	0.3827	0.0014	0.0477	0.0003	0.0423	0.0220	25.3989	0.2084	0.0204	0.0216	9.3201	0.0948	98.4	78.99	1.45	1969.5	22.1
2	600	2.73	1.3990	0.0017	0.1635	0.0006	0.0831	0.0127	79.9310	0.3756	0.2482	0.0095	8.5576	0.0499	94.8	81.10	0.34	2001.4	5.2
3	650	7.12	3.0527	0.0036	0.3391	0.0008	0.1540	0.0339	71.5776	0.3045	0.1133	0.0233	3.6934	0.0182	98.9	89.03	0.32	2116.4	4.5
4	700	12.71	3.9143	0.0049	0.4317	0.0009	0.1141	0.0207	11.5610	0.1044	0.1453	0.0549	0.4687	0.0043	98.9	89.69	0.44	2125.6	6.1
5	750	19.76	4.7442	0.0053	0.5447	0.0008	0.1255	0.0210	8.4663	0.1639	0.3690	0.0172	0.2720	0.0053	97.7	85.10	0.18	2060.4	2.6
6	800	28.61	5.8147	0.0066	0.6830	0.0014	0.0748	0.0353	10.1632	0.2028	0.0866	0.0486	0.2604	0.0052	99.6	84.76	0.29	2055.4	4.2
7	850	37.77	5.9596	0.0067	0.7082	0.0022	0.1367	0.0180	11.7963	0.3453	0.0924	0.0436	0.2915	0.0086	99.5	83.77	0.33	2041.0	4.9
8	900	45.20	4.8342	0.0056	0.5740	0.0013	0.2534	0.0229	10.6143	0.1624	0.1666	0.0250	0.3236	0.0050	99.0	83.37	0.25	2035.0	3.7
9	950	52.73	4.8355	0.0056	0.5815	0.0010	0.1996	0.0251	11.4237	0.1615	0.0564	0.0187	0.3438	0.0049	99.7	82.87	0.19	2027.7	2.8
10	1000	64.66	7.7257	0.0094	0.9215	0.0006	0.2643	0.0499	19.8372	0.4080	0.0004	0.0009	0.3767	0.0078	100.0	83.84	0.12	2042.0	1.7
11	1050	82.89	11.7892	0.0150	1.4083	0.0035	0.6933	0.1031	34.1625	0.2525	0.2054	0.0505	0.4245	0.0033	99.5	83.28	0.25	2033.8	3.7
12	1100	93.36	6.7777	0.0194	0.8081	0.0033	0.4471	0.1110	25.0395	0.3954	0.3414	0.0582	0.5422	0.0088	98.5	82.62	0.46	2024.0	6.9
13	1150	97.03	2.4019	0.0030	0.2837	0.0005	0.0908	0.0048	9.9861	0.1042	0.1475	0.0117	0.6160	0.0065	98.2	83.12	0.22	2031.5	3.3
14	1450	100.00	2.1746	0.0030	0.2296	0.0003	0.3214	0.0181	9.0814	0.0595	0.9854	0.0175	0.6923	0.0046	86.6	82.05	0.28	2015.5	4.2

Step	Temp	Cum.%	^{40}Ar		^{39}Ar		^{38}Ar		^{37}Ar		^{36}Ar								
no.	(˚C)	^{39}Ar	(x10^{-13} moles)	± 2σ	(x10^{-14} moles)	± 2σ	(x10^{-16} moles)	± 2σ	(x10^{-16} moles)	± 2σ	(x10^{-16} moles)	± 2σ	Ca/K	± 2σ	%^{40}Ar*	^{40}Ar*/^{39}Ar	± 2σ	Age (Ma)	± 2σ
Sample SE7																			
J-value = 0.025048 ± 0.00006																			
1	550	0.21	0.0760	0.0002	0.0090	0.0002	0.0004	0.0003	4.0184	0.1144	0.0213	0.0149	7.7729	0.2699	91.7	77.08	5.11	1939.9	79.1
2	600	1.08	0.2880	0.0003	0.0369	0.0005	0.0132	0.0054	16.6643	0.1284	0.0256	0.0103	7.9124	0.1263	97.4	76.10	1.35	1924.6	21.1
3	650	2.59	0.6758	0.0016	0.0643	0.0010	0.0004	0.0083	0.0020	0.0007	0.0004	0.0007	0.0005	0.0002	100.0	105.09	1.73	2329.0	21.7
4	700	6.46	1.3022	0.0014	0.1649	0.0001	0.0531	0.0188	0.9999	0.0543	0.0515	0.0120	0.1061	0.0058	98.8	78.03	0.24	1954.4	3.6
5	750	12.32	2.0156	0.0023	0.2494	0.0005	0.0785	0.0229	1.1609	0.0416	0.0373	0.0070	0.0814	0.0029	99.5	80.36	0.21	1990.0	3.2
6	800	21.23	3.1203	0.0038	0.3794	0.0011	0.0267	0.0110	1.0867	0.0685	0.0004	0.0012	0.0501	0.0032	100.0	82.25	0.26	2018.1	3.8
7	850	33.74	4.4021	0.0053	0.5324	0.0013	0.1282	0.0202	1.3919	0.0593	0.0227	0.0147	0.0457	0.0020	99.8	82.56	0.23	2022.7	3.5
8	900	48.54	5.1972	0.0060	0.6304	0.0010	0.2244	0.0185	1.8888	0.1029	0.0324	0.0216	0.0524	0.0029	99.8	82.29	0.19	2018.8	2.9
9	950	62.62	4.9753	0.0067	0.5994	0.0019	0.2305	0.0276	2.0068	0.1065	0.0891	0.0166	0.0586	0.0031	99.5	82.56	0.29	2022.8	4.4
10	1000	74.96	4.3660	0.0053	0.5256	0.0011	0.1642	0.0357	1.8412	0.1444	0.0205	0.0321	0.0613	0.0048	99.9	82.96	0.27	2028.7	4.0
11	1050	87.16	4.2129	0.0127	0.5191	0.0008	0.2159	0.0203	2.2505	0.0837	0.0659	0.0235	0.0759	0.0028	99.5	80.78	0.31	1996.2	4.6
12	1100	96.62	3.4011	0.0042	0.4031	0.0003	0.1706	0.0309	2.7667	0.1748	0.0391	0.0268	0.1201	0.0076	99.7	84.10	0.23	2045.4	3.4
13	1150	99.41	1.0442	0.0012	0.1186	0.0002	0.0764	0.0083	3.1044	0.0486	0.0505	0.0171	0.4581	0.0072	98.6	86.79	0.47	2084.3	6.7
14	1450	100.00	0.4262	0.0005	0.0252	0.0005	0.2041	0.0198	17.1121	0.1477	0.6607	0.0129	11.8894	0.2604	54.2	91.71	2.40	2153.4	33.0

CHAPITRE 4

4. Multi-stage and multi-sourced fluid and gold in the formation of orogenic gold deposits in the world-class Mana district of Burkina Faso - revealed by LA-ICP-MS analysis of pyrites and arsenopyrites

Jérôme Augustin, Damien Gaboury

Soumis dans Economic Geology, septembre 2017.

4.1 RÉSUMÉ

Mana est un district d'or orogénique paléoprotérozoïque de classe mondiale (~8,0 Moz) qui comprend cinq gisements aurifères (Fofina, Nyafé, Siou, Wona-Kona et Yaho) encaissés dans diverses roches de la partie nord de la ceinture de roches vertes birimiennes de Houndé, soit à l'ouest du Burkina Faso. La minéralisation aurifère a enregistré différents styles de minéralisations associés avec des sulfures durant des évènements de déformation polyphasés. Les analyses pétrographiques détaillées et au LA-ICP-MS des pyrites et arsénopyrites composant la minéralisation principale de chaque gisement fournissent de nouvelles informations sur les sources potentielles de l'or et de l'arsenic et sur la chronologie des fluides responsables de la minéralisation à Mana et peuvent être utilisées pour évaluer le potentiel d'utilisation des éléments traces dans la pyrite comme un outil d'exploration pour l'exploration de l'or orogénique. Quatre évènements de fluides hydrothermaux associés à 2 réservoirs de sources distinctes et au moins 2 systèmes hydrothermaux ont été reconnus.

Cette étude révèle que la Py_{1WK} diagénétique framboïdale dans les shales noirs (groupe du Birimien inférieur) est enrichie en Au (médiane de 0,8 ppm) et faiblement en As (médiane de 70 ppm), ainsi qu'en d'autres éléments traces (Ni, Cu, Zn, Ag, Sb et Pb).

Le premier pulse de fluide hydrothermal a été généré lors de l'évènement de raccourcissement Éoéburnéen $D1_{MD}$ (~2172 Ma). Il est documenté dans les gisements de Fofina et Siou, et s'est produit dans des conditions métamorphiques aux faciès des schistes

verts. Les dépôts économiques aurifères à Fofina sont associés à la pyrite métamorphique disséminée (Py_{1F}) dans les shales noirs, à la pyrite zonée (Py_{2F}) enrichie en As, Ni, Cu, Ag, Sb, W, Au et Pb, et l'arsénopyrite dans les veines de quartz-carbonates V_{1F} plissées. À l'opposé, le gisement de Siou présente de l'or dans les cœurs des pyrites poreuses (Py_{1S}) qui sont associés avec Ag, Bi, Te et W (± Sb) dans des veines de quartz V_{1S} encaissées dans la granodiorite de Siou. Ces deux suites d'éléments traces sont interprétées comme ayant été induites par une source métamorphique pour le gisement de Fofina et par une contribution locale d'une source magmatique pour le gisement de Siou.

Le deuxième pulse de fluide hydrothermal s'est produit lors de l'évènement transpréssif $D3_{MD}$ (2113-2090 Ma) dans le gisement de Nyafé. Cet événement est défini par des couronnes riches en Au-As dans la pyrite hydrothermale (Py_{3N}) et par la co-précipitation de l'arsenopyrite riche en Au dans les veinules de quartz (V_{3N}) contrôlées par une zone de cisaillement dextre de second ordre.

Le troisième pulse et principal évènement de fluide hydrothermal est engendré durant l'évènement transpressif $D4_{MD}$ (~2090 Ma). Il se caractérise par le développement d'une forte silicification refermant des pyrites zonées (Py_{3WK} et Py_{2Y}) et des arsénopyrites riches en Au dans les gisements de Wona-Kona et Yaho. Ces pyrites se caractérisent par des couronnes tardives riches en Au-As. Les mêmes couronnes sont également développées sur les pyrites du gisement de Nyafé. Ces couronnes sont interprétées comme étant l'expression d'un même évènement hydrothermal, qui tire sa source d'or du réservoir métamorphique du

Birimien inférieur, incluant les shales noires (pyrite diagénétique framboïdale) et éventuellement les basaltes tholéiitiques.

L'évènement hydrothermal tardif est associé à la remobilisation de l'or libre dans les microfractures tardives dans les gisements de Wona-Kona et Siou lors de la réactivation des principales failles en cisaillement transpressif durant l'évènement $D4_{MD}$ ou l'évènement de raccourcissement $D5_{MD}$ (aussi tard que 2022 Ma).

Pour guider l'exploration, un diagramme binaire As/Ag vs. Sb/Bi apparait efficace pour séparer les pyrites diagénétiques, magmatiques et métamorphiques. Celui-ci pourrait être utilisé pour estimer les sources d'or potentielles pour une éventuelle remobilisation orogénique à l'échelle d'un gisement et d'un district.

4.2. ABSTRACT

Mana is a world-class Paleoproterozoic orogenic gold district (~8.0 Moz) that includes five gold deposits (Fofina, Nyafé, Siou, Wona-Kona and Yaho) hosted in various rocks in the northern part of the Birimian Houndé greenstone belt, western Burkina Faso. The gold mineralization recorded different styles of mineralization associated with sulfides during polyphase deformation events. Detailed petrographic and LA-ICP-MS analyses of pyrites and arsenopyrites from the main mineralization of each deposit provide new information on the potential gold and arsenic sources and timing of fluids responsible for mineralization at

Mana. Four hydrothermal fluid events associated with 2 distinct source reservoirs and at least 2 hydrothermal systems were recognized.

This study reveals that the diagenetic framboidal Py_{1WK} in black shale (Lower Birimian group) is enriched in Au (median of 0.8 ppm) and low of As (median of 70 ppm), along with other trace elements (Ni, Cu, Zn, Ag, Sb and Pb).

The first hydrothermal fluid event was generated during the Eoeburnean $D1_{MD}$ shortening event (~2172 Ma), observed in the Fofina and Siou deposits, and occurred under greenschist metamorphic facies conditions. Economic gold deposits at Fofina are associated with metamorphic disseminated pyrite (Py_{1F}) in black shale and zoned pyrite (Py_{2F}) enriched in As, Ni, Cu, Ag, Sb, W, Au and Pb and arsenopyrite in folded V_{1F} quartz-carbonate veins. In contrast, the Siou deposit exhibits Au in porous pyrite cores (Py_{1S}), which are associated with Ag, Bi, Te and W (± Sb) in V_{1S} quartz veins hosted in the Siou granodiorite. These two trace element suites are interpreted as having been induced by a metamorphic source in the Fofina deposit and by a local contribution of a magmatic source in the Siou deposit.

The second hydrothermal fluid event occurred during the Eburnean $D3_{MD}$ transpressional event (2113-2090 Ma) in the Nyafé deposit. This event is defined by Au-As-rich rims in hydrothermal pyrite (Py_{3N}) and by the co-precipitation of Au-rich arsenopyrite in the V_{3N} quartz veinlets (V_{3N}) controlled by a second-order dextral shear zone.

The third and main hydrothermal fluid event during the $D4_{MD}$ transpressional event (~2090 Ma) is characterized by the development of strong silicification and by zoned pyrites (Py_{3WK} and Py_{2Y}) and Au-rich arsenopyrite in the Wona-Kona and Yaho deposits. However, the same late Au-As-rich rims in hydrothermal pyrite are observed in both deposits and in the Nyafé deposit, and these rims are interpreted to be related to the same economic gold source related to the Lower Birimian metamorphic reservoir, composed of black shale (diagenetic framboidal pyrite) and tholeiitic basalts.

The late hydrothermal event is associated with free gold remobilization in late microfractures in the Wona-Kona and Siou deposit during the reactivation of major transcurrent shear zones during the $D4_{MD}$ event or the $D5_{MD}$ shortening event (as late as 2022 Ma).

A binary diagram of As/Ag vs. Sb/Bi appears to be effective at separating the diagenetic, magmatic and metamorphic pyrites and could be used in orogenic gold exploration to estimate the potential gold endowment at deposit and district scale.

4.3. INTRODUCTION

Pyrite is the most abundant sulfide phase in the Earth's crust and it is very common in hydrothermal deposits of various types (e.g. epithermal, BIF-hosted gold, SEDEX, porphyry, VMS, IRGS and orogenic gold; Large et al., 2011; Côté-Mantha et al., 2012;

Gregory et al., 2013; Steadman et al., 2014; Genna and Gaboury, 2015; Meffre et al., 2016; Mériaud and Jébrak, 2017). Numerous studies used the pyrite associated with orogenic gold deposits to decipher the hydrothermal evolution (Thomas et al., 2011; Lebrun et al., 2017), the fluid sources (Large et al, 2013; Steadman et al., 2015; Fuchs et al., 2016), and the source of gold (Large et al, 2013; Steadman et al., 2015; Fuchs et al., 2016; Hu et al., 2016) and to document specific gold remobilization processes (Simard et al., 2013; Fougerouse et al., 2017). However, the origin of the mineralizing fluids and the source of the gold remain debated (Tomkins, 2013). Some authors have proposed different models implying (1) a magmatic source (Bath et al., 2013; Xue et al., 2013; Lawrence et al., 2013b), (2) a mantle source (Mao et al., 2003; Graupner et al., 2006), (3) a crustal source during prograde metamorphism and devolatilization of carbonaceous sulfidic sedimentary rocks and/or mafic rocks (Goldfarb et al., 2005; Phillips and Powell, 2010; Large et al., 2011; Gaboury, 2013; Pitcairn et al., 2015; Goldfarb and Groves, 2015; Augustin and Gaboury, 2017), and (4) a subcrustal source (Colvin, 1989; Kerrich, 1999; Chen et al., 2008; Goldfarb and Groves, 2015).

Most, if not all, studies based on pyrite chemistry, have been conducted at the deposit scale, whereas most orogenic gold deposits are related to regional scale hydrothermal systems (Phillips and Powell, 2010). For exploration purposes, the potential sources of gold and fluids are important for developing exploration criteria. However, deciphering whether gold mineralizations at district scale are related to a single unique large hydrothermal system or small localized systems, or numerous overprinting systems, is of fundamental importance for interpreting the gold potential of a specific district.

The West African Craton (WAC) contains a wide spectrum of gold mineralization types, such as orogenic deposits (Lawrence et al., 2013a, b; Perrouty et al., 2015; White et al., 2015; Augustin et al., 2016; Salvi et al., 2016; Fontaine et al., 2017; Fougerouse et al., 2017; Lebrun et al., 2017; Masurel et al., 2017), intrusion-related deposits (McFarlane et al., 2011), porphyry Cu-Au deposits (Le Mignot et al., 2017) and paleoplacers (Davis et al., 1994; Hirdes and Nunoo, 1994). Recent studies by Lawrence et al. (2013a, b) have reported multiple mineralization styles and ore paragenesis in the Loulo gold district (Mali) resulting from hydrothermal systems that sourced fluids and metals from both metamorphic and magmatic reservoirs. These various gold- and fluid-related hydrothermal systems are considered the most favorable settings for forming large gold deposits and world-class districts (Meffre et al., 2016). The trace elements in pyrite are thus a useful tool for deciphering the characteristics, type and evolution of regional hydrothermal systems, and for designing the best exploration program.

In this paper, we investigate the trace element composition of pyrites and arsenopyrites from five orogenic gold deposits in the world-class Mana district of Burkina Faso using laser ablation-inductively coupled plasma-mass spectrometry (LA-ICP-MS) with the aim of characterizing the hydrothermal systems at the local- and district-scales and establishing the fluid evolution and sources. The Mana district is of special interest for such a study for several reasons: 1) it is, at present, the most gold endowed district at the country scale with total Au reserves and resources of > 8.0 Moz (Augustin et al., 2017); 2) each deposit, lying within < 20 km of each other, has a specific ore type, host rocks and structural setting

(Augustin et al., 2017); and 3) the introduction of gold is well constrained relative to tectonic history of the district (Augustin et al., 2017).

Pyrite and arsenopyrite textures and trace element composition and zonation were used to characterize the hydrothermal events and their genetic affiliation. It is demonstrated that each deposit has its own specific evolution with multi-stage gold introduction. Some deposits exhibit magmatic-sourced gold, but all have recorded metamorphic fluids probably sourced from a single regional hydrothermal system. Our results demonstrate the importance of multiple sources of gold and fluids and multi-stage mineralizing events for forming world-class deposits and districts.

4.4. REGIONAL GEOLOGY

The Mana district is located in the northern part of the Paleoproterozoic Birimian Houndé greenstone belt (HGB), which is part of the Baoulé-Mossi domain in the West African Craton (Fig. 4.1a). The Mana district consists of three distinct stratigraphic groups known as the Lower Birimian group, the Upper Birimian group and the Tarkwaian-type group (Fig. 4.1b), all metamorphosed under greenschist-facies conditions (Augustin et al., 2017). The Lower Birimian group, in the central and eastern domains, is composed at the base of a major tholeiitic basaltic suite that is intercalated with volcanoclastic and pelagic sedimentary rocks intruded by a swarm of meter-scale NE- to SE-trending felsic QFP dykes. The black shales in this group are carbonaceous and locally pyritic. Abundant meter-

scale layers of cherts (ferruginous and manganiferous) are associated with the volcano-sedimentary rocks. At the top, a calc-alkaline series is defined by andesitic, volcanoclastic flows and tuffaceous facies intruded by NE-trending dioritic dykes (Fig. 4.1b). This group was dated as being older than 2176 ± 4 Ma in the HGB (U-Pb on zircon: Le Métour et al., 2003). The Upper Birimian group, in the central domain, overlies the Lower Birimian group. It is characterized by volcano-sedimentary rocks with abundant interbeds of wackes, siltstones and feldspathic sandstones forming the Mana basin (Fig. 4.1b). The Mana basin is delimited by the NNE- to NE-trending Maoula shear zone (MLSZ) and Mana shear zone (MSZ) (Augustin et al., 2017). These rocks have been dated to ~2160 Ma to ~2124 Ma (U-Pb on zircon, Hirdes et al., 1996; Lüdtke et al., 1999; Castaing et al., 2003). The Tarkwaian-type group unconformably overlies the Birimian Supergroup (Lower and Upper Birimian groups) and is characterized by polygenic conglomerates with interbeds of feldspathic sandstones and siltstones. These rocks form two narrow NE- to NNE-trending basins in the western and eastern margins of the Mana district, controlled by the NE-trending Wona-Kona shear zone (WKSZ) and N-trending Boni shear zone (BSZ) (Fig. 4.1b). The eastern margin has been dated by U-Pb dating of detrital zircons to 2113 ± 23 Ma (Bossière et al., 1996), which is interpreted as the maximum deposition age of the Tarkwaian-type sedimentary rocks. The district was intruded by granodioritic plutons (Wona-Kona and Siou) and dioritic plutons (Mana and Kokoï) in two phases during the Eburnean orogeny (Bonhomme, 1962): an Eoeburnean phase (~2172 Ma) and an Eburnean phase (~2090 Ma) (U-Pb on zircon, Augustin et al., 2017). A late SE-trending dioritic dyke crosscuts all the Birimian groups (Fig. 4.1b).

Five deformation events are recognized by Augustin et al. (2017) in the Mana district (Fig. 4.2). The first event $D1_{MD}$, affected the metamorphosed volcanic and sedimentary rocks of the Lower Birimian group. This early deformation episode was correlated with the formation of gently N-plunging F_{1MD} folds and N-trending thrust faults coeval with the emplacement of the pre- to syn-kinematic Wona-Kona and Siou plutons (Eoeburnean magmatic phase). This episode was interpreted as the product of E-W shortening. The second event, $D2_{MD}$, corresponds to an extensional deformation event recorded by the deposition of the Upper Birimian group in the Mana basin controlled by MLSZ and MSZ (Fig. 4.1b). The Tarkwaian group deposition occurred at the end of the late $D2_{MD}$ or early $D3_{MD}$ controlled by the major bordering faults (WKSZ and BSZ), at ~2113 Ma (Fig. 4.1b). The third event, $D3_{MD}$, is associated with N- to NE-trending F_{3MD} folds and a S_{3MD} axial planar schistosity. The plunge of the F_{3MD} fold axes varies from sub-horizontal in the Upper Birimian and Tarkwaian groups to sub-vertical in the Lower Birimian group. Some of NE-trending dextral faults are also developed at the district scale. This event was interpreted as having been associated with an E-W to ESE-WNW transpressional regime bracketed between ~2113 and ~2090 Ma during the Eburnean phase. The fourth event, $D4_{MD}$, is associated with the development of brittle-ductile sinistral shear zones that reactivated $D3_{MD}$ faults and with asymmetric NNE-striking F_{4MD} folds with vertical axes. This event was interpreted as having been associated with NNW-SSE transpression between 2090 and 2022 Ma (U-Pb dating of zircon and Ar-Ar dating of muscovite: Augustin et al., 2017). The fifth and last deformation event, $D5_{MD}$, is more brittle and formed E-W subvertical crenulation cleavages, fractures and E-W thrust faults. This event was interpreted as having

been associated with minor N-S shortening that was either late-Eburnean (~2022 Ma) or perhaps even Pan-African in age.

In the western margin, Neoproterozoic sedimentary rocks of the Taoudeni basin unconformably overlie the Birimian basement (Deynoux, 1983; Bertrand-Sarfati et al., 1991) and are crosscut by a late SE-trending post-Eburnean doleritic dyke (Jessell et al., 2015) (Fig. 4.1b).

Hydrothermal activity is defined by four gold mineralizing events that are related to the $D1_{MD}$, $D3_{MD}$, $D4_{MD}$ and possibly $D5_{MD}$ deformation events (Augustin et al., 2017) (Fig. 4.2). The first gold mineralization, mainly characterized by quartz-carbonate to quartz veins (V_{1MD}) and disseminated pyrite, occurred during the $D1_{MD}$ event. The second gold event is defined by quartz-carbonate veins (V_{3MD}) and disseminated sulfides that are developed along the $D3_{MD}$ faults. The third and main gold mineralizing event is characterized by strong and pervasive silicification (Si_{4MD}) and by tiny quartz-carbonate veinlets (V_{4MD}) that developed along the transcurrent WKSZ during $D4_{MD}$ event (Fig. 4.1b). The last event induced higher gold grade mineralization and is defined by free gold remobilization related to late $D4_{MD}$ or $D5_{MD}$ along the WKSZ and BSZ (Fig. 4.2).

4.5. GEOLOGY OF THE MANA GOLD DEPOSITS

The Mana district contains 5 gold deposits: Fofina (0.42 Moz at average grade of 3.6 g/t), Nyafé (0.37 Moz at 6.0 g/t), Siou (1.0 Moz at 6.0 g/t), Wona-Kona (4.0 Moz at 2.3 g/t) and Yaho (1.0 Moz at 1.0 g/t) (SGS, 2009; Semafo Inc., 2013 - Table 4.1). All these numbers are from surface to depths of less than 200 m.

Augustin et al. (2017) described in detail the litho-structural and mineralization characteristics of each gold deposit and only the salient features are summarized below (Table 4.1 and Figs. 4.3, 4.4).

The Fofina deposit is hosted in the Lower Birimian group of the central domain (Fig. 4.1b), specifically in tholeiitic basalt overlain by volcano-sedimentary rocks with graphitic and pyrite-rich black shale. Mineralization is associated with $D1_{MD}$-related anticlinal folds (Figs. 4.3a, 4.4a). The first and main mineralization occurs in the Fofina main pit and is defined by boudinated and folded V_{1F} quartz-carbonate veins along the contact between the black shale and the tholeiitic basalt. The V_{1F} formed during the $D1_{MD}$ with associated chlorite and local silicification (Figs. 4.3, 4.4b). High grade gold (> 4.0 g/t) is related to euhedral pyrite and traces of arsenopyrite. The second gold mineralizing event occurred as fault-fill and extensional quartz veins (V_{3F}), referred to as Fofina V1-V7 veins (Fig. 4.4c). These veins are related to NNE-trending dextral shear zones formed during $D3_{MD}$ E-W shortening. The V_{3F} quartz veins are surrounded by a muscovite and carbonate alteration

assemblage. Gold is associated with minor sulfide phases, including pyrite and traces of arsenopyrite, with gold values ranging from 1 to 6.0 g/t Au.

The Nyafé deposit is hosted in a reversed sequence of tholeiitic basalt of the Lower Birimian group (central domain) related to either reverse folding or thrusting during the $D1_{MD}$ event (Fig. 4.3b). The main mineralization is controlled by two-brittle-ductile NE-trending dextral shear zones (Nyafé main and Filon 67) interpreted as $D3_{MD}$ structures (Fig. 4.3). The main mineralization style is dominated by high-grade quartz veinlets (V_{3N}) forming a stockwork that is crosscut by late quartz-carbonate veins (Late-V_{3N}) (Fig. 4.4d). The quartz veinlets (V_{3N}) are folded and are associated with disseminated arsenopyrite with minor pyrite and local chalcopyrite within an alteration assemblage of muscovite, chlorite and iron carbonates. These V_{3N} host the highest gold grade (> 7.0 g/t). The later quartz-carbonate veins (Late-V_{3N}) are boudinated and contain calcite with rare sulfides and minor gold values (< 1.0 g/t).

The Siou deposit is located in the eastern domain along the N-trending first-order BSZ (Fig. 4.1b). The host rocks comprise the metamorphosed detrital sedimentary rocks of the Tarkwaian-type group on the western side of the mineralization and the Siou granodiorite pluton to the east (Fig. 4.3c). The main mineralization is hosted in the Siou pluton and confined along two N-trending, moderately dipping reverse brittle faults related to the $D1_{MD}$ event. The mineralization occurs as boudinated white quartz veins (V_{1S}) with some interconnected veins surrounded by a muscovite halo (Figs. 4.3c, 4.4e). Sulfide phases consist of minor pyrite and trace sphalerite associated with bands of muscovite crosscutting

the V_{1S} veins. The major gold event is recorded as free gold and galena associated with muscovite in brittle fractures during the reactivation of the transcurrent BSZ during the late $D4_{MD}$ or $D5_{MD}$ event. Gold grades in this late event are commonly > 6.0 g/t Au (Fig. 4.4e).

The world-class Wona-Kona deposit lies within the major NE-trending regional-scale WKSZ in the western domain (Fig. 4.1b). The orebody is hosted along the vertical contact between an assemblage of tholeiitic basalts and volcano-sedimentary rocks containing layers of graphite-rich black shales with disseminated primary pyrites of the Lower Birimian group (Figs. 4.3d, 4.4f). The main mineralization is correlated with the reactivation of NE-trending transcurrent WKSZ during the $D4_{MD}$ event. The Si_{4WK} silicification with disseminated pyrite and arsenopyrite represents the main style of gold mineralization with late tiny quartz-carbonate veins (V_{4WK}) surrounded by a large hydrothermal alteration halo (muscovite and iron carbonates) (Fig. 4.4g). Free gold, occurring in late fractures with grades of > 3.5 g/t Au, is interpreted to be the result of gold remobilization during late $D4_{MD}$ or $D5_{MD}$ (Fig. 4.4g).

The Yaho deposit is located in the southwestern domain along a second-order shear zone connected with the WKSZ (Fig. 4.1b). The orebody is hosted within a slightly E-inclined F_{3Y} isoclinal antiformal fold affecting Tarkwaian-type sedimentary rocks (Fig. 4.3e) and formed during $D3_{MD}$. The first mineralization is characterized by bed-parallel quartz veins and quartz-carbonate veinlets (V_{3Y}) with minor disseminated pyrite and arsenopyrite within V_{3Y} and along the bedding of the host rocks (Fig. 4.4h). The gold grade is low at approximately 0.4 g/t (Fig. 4.4h). The alteration assemblage is defined by minor chlorite

and muscovite. The second and main mineralization style is similar to the Wona-Kona deposit and corresponds to a slight silicification (Si_{4Y}) surrounded by a muscovite alteration along a NNW- to N-trending sinistral shear zone related to the $D4_{MD}$ event (Fig. 4.4i). Pyrite and arsenopyrite occur within the silicified zone and contain the highest gold grade with an average of 2.0 g/t Au (Fig. 4.4i).

4.6. METHODOLOGY AND ANALYTICAL TECHNIQUES

4.6.1. SAMPLING APPROACH

A sampling approach was designed to characterize the signature of the hydrothermal systems that formed the four gold mineralization events recognized in the district (Augustin et al., 2017 - Fig. 4.2). Pyrite and arsenopyrite were sampled from the main gold mineralization of each deposit, from quartz-carbonate veins, quartz veins and silicification zones (Table 4.2). A total of 24 representative samples from 20 drill holes were used to produce polished thin sections. In total, this study examined the following samples: 4 samples of V_{1F} quartz-carbonate veins (Fig. 4.4b), and one sample of the pyritic black shale from the Fofina deposit (Fig. 4.4a); 5 samples of the V_{3N} quartz veinlets from the Nyafé deposit (Fig. 4.4d), 6 samples of the V_{1S} quartz veins from the Siou deposit (Fig. 4.4e); 4 samples of the Si_{4WK} silicification zone from the Wona-Kona deposit (Fig. 4.4g); and 5 samples of the Si_{4Y} silicification zone from the Yaho deposit (Fig. 4.4i). Only unweathered rocks from drill cores located below 100 m were selected.

All the samples were examined using reflected and transmitted light microscopy at the Université du Québec à Chicoutimi (UQAC), Canada. Petrographic examination was performed for defining the mineral assemblages, characterizing textures of sulfides and oxides and for selecting pyrite grains for LA-ICP-MS analysis and elemental mapping.

Data from previous studies (Béland, 2009; Augustin, 2011; Paulin-Bissonnette, 2012; Sinaré, 2013) on the trace elements in arsenopyrite from the Fofina, Nyafé, Wona-Kona and Yaho deposits were also used for comparison with the pyrite results.

4.6.2. ANALYTICAL METHOD

LA-ICP-MS was used to obtain quantitative line data and semi-quantitative element image maps of pyrite. The analyses were performed at LabMaTer (UQAC) using an Excimer 193 nm Resonetics Resolution M-50 laser ablation system coupled with an Agilent 7700x mass spectrometer. Counts of the following isotopes were measured: ^{28}Si, ^{33}S, ^{34}S, ^{51}V, ^{52}Cr, ^{55}Mn, ^{57}Fe, ^{59}Co, ^{60}Ni, ^{65}Cu, ^{66}Zn, ^{71}Ga, ^{72}Ge, ^{75}As, ^{82}Se, ^{107}Ag, ^{111}Cd, ^{115}In, ^{118}Sn, ^{121}Sb, ^{126}Te, ^{197}Au, ^{205}Tl, ^{208}Pb, and ^{209}Bi. Depending on the pyrite size, analyses were performed with laser beam diameters from 25 to 43 µm, a range of stage movement speeds from 2.5 to 5 µm/s, laser frequencies from 10 to 15 Hz and power from 4 to 5 mJ/pulse. For all pyrite grains, line analyses were made. Following 20 to 30 s of background acquisition of the gas blank, lines were ablated across pyrite over the course of at least 60 s. The ablated material

was then carried into the ICP-MS by an argon-helium gas mixture at a rate of 0.8 - 1.0 L/min for Ar and 350 mL/min for He.

In addition to the line analyses, numerous pyrite grains were mapped (n = 38) following the method of Dare et al. (2014). The morphology, internal structure and zoning of pyrites have been used here as a guide to determine 1) the trace element spatial distribution, and 2) the timing relationship between pyrite growth and gold events. Semi-quantitative mapping was performed by ablating a set of parallel lines arranged in a grid over the sample (~0.5 x 0.5 to 2 x 2 mm). The beam size (15 to 35 µm) and the stage movement speed (5 to 10 µm/s) were varied based on a compromise between the grain size and the resolution to optimize the spatial resolution and analysis time for grains of different sizes. A laser frequency of 15 Hz and a power of 5 mJ/pulse were used to map the pyrite grains in their entirety.

Both line and map analyses of pyrite were calibrated with MASS-1, which is a ZnCuFeS pressed powder pellet doped with 50-70 ppm of Ag, As, Bi, Pb, Re, Sb, Se, Sn and Te supplied by the United States Geological Survey (USGS), using values published by Wilson et al. (2002). Internal standardization was based on ^{57}Fe using stoichiometric iron values of pyrite. Data reduction was performed using the Iolite package for Igor Pro software (Paton et al., 2011). Results for the pyrite analyses are presented in Table 4.3. The full dataset is available in the Annexe 5.

4.7. PYRITE TEXTURES AND TRACE ELEMENT CHEMISTRY

As hydrothermal deposits are open geochemical systems, numerous elemental maps of pyrite were produced for each deposit (n ~ 8). For this study, only the most complexly zoned pyrites were selected (elemental maps provided as figure) in order to have the most representative evolution of the hydrothermal system. Quantitative data were extracted from these maps and from spot and line analyses on texturally comparable pyrites in order to have a statistically valuable and representative dataset.

4.7.1. FOFINA DEPOSIT

Three pyrite types (Py_{1F} to Py_{3F}) were defined in the Fofina deposit based on their texture and association with recognized mineralizing events (Figs. 4.3a, 4.5). The first pyrite type Py_{1F} is composed of fine-grained aggregate crystals (< 100 µm) commonly aligned parallel to bedding in the black shale matrix in the western part of the Fofina deposit (Figs. 4.4a, 4.5a). Based on previous studies (Large et al., 2009; Thomas et al., 2011), its origin can be interpreted as early synsedimentary/diagenetic pyrite in the Lower Birimian group. However, as the rocks are metamorphosed, this type could also be diagenetic-metamorphosed pyrite. Hydrothermal pyrite are zoned and associated with V_{1F} quartz-carbonate veins and arsenopyrite (Figs. 4.4b, 4.5b). The porous cores of these pyrites are rich in silicate inclusions (50 µm to 300 µm; Fig. 4.5c) and are interpreted as Py_{2F}. These cores are surrounded by euhedral Py_{3F} rims of variable size (100 µm to 2 mm).

The LA-ICP-MS line results show that a greater number of trace elements are present in Py_{1F} compared to Py_{2F} and Py_{3F} (Fig. 4.6). The Py_{1F} grains contain the highest contents of Cu, Zn, As, W, Pb, and Bi but moderate levels of Au (median of 0.9 ppm) and Ag (median of 0.8 ppm) (Fig. 4.6; Table 4.3).

The LA-ICP-MS mapping of the selected most complexly zoned pyrite (Fig. 4.7) revealed that the porous cores of Py_{2F} are overgrown by the euhedral Py_{3F}. The porous cores of Py_{2F} contain significantly higher concentration of trace elements compared to Py_{3F}, including Co, Ni, Cu, As, Ag, Sb, W, Au and Pb (Figs. 4.6, 4.7). Vanadium is concentrated in the silicate matrix whereas the Cu and Pb maps suggest the occurrence of micro-inclusions of chalcopyrite and galena, which are not visible under the microscope (Fig. 4.7). Selenium and Te images are below the detection limit. The Au image shows a spikey distribution due to inclusions of native gold, which is spatially associated with Ag (Fig. 4.7). The Py_{3F} overgrowth is defined by cyclic zoning of As, and it is depleted in the other elements including Au (< 0.17 ppm) (Figs. 4.6, 4.7).

4.7.2. NYAFÉ DEPOSIT

In the Nyafé deposit, hydrothermal zoned pyrite grains are widely distributed in the main V_{3N} quartz veinlets in association with arsenopyrite (Fig. 4.4d). Three subtypes (Fig. 4.8) were distinguished based on petrographic criteria.

Py_{1N} occurs as anhedral porous crystals with sizes ranging from 400 µm to 2 mm and containing silicate inclusions (Fig. 4.8a). Py_{2N} comprises euhedral crystals with sizes of 500 µm to 3 mm containing an earlier core of Py_{1N} (Fig. 4.8b). The outermost Py_{3N} occurs as coarser sub-euhedral crystals and is associated with an assemblage of chalcopyrite and arsenopyrite (Fig. 4.8c).

LA-ICP-MS mapping and line analyses (Figs. 4.9, 4.10; Table 4.3) highlight the complex zoning and show that each zone has different trace element chemistry. The core of the porous Py_{1N} is depleted in all elements except for Se (132 ppm), which is homogeneously distributed and minor Te (1.4 ppm) (Fig. 4.10). Gold and W are below the detection limit (Fig. 4.9). Some spikes of Pb are present and may be associated with micro-inclusions of galena (Fig. 4.10). The LA-ICP-MS map (Fig. 4.10) shows that Py_{2N} overgrows Py_{1N} and that it is defined by cyclic zoning of Co, Ni and Pb but without Au. The Cu, Zn and Pb maps suggest micro-inclusions of chalcopyrite, sphalerite and galena and these are not associated with Au (Fig. 4.10). The outermost Py_{3N} surrounding Py_{2N} is associated with an Au-As-rich rim with chalcopyrite inclusions (Cu) (Fig. 4.10). Gold content varies from 5.1 to 24.4 ppm with a median of 9.3 ppm, whereas the As content varies from 25,000 to 35,900 ppm with a mean of 33,050 ppm (Table 4.3).

4.7.3. SIOU DEPOSIT

In the Siou deposit, zoned pyrite occurs in V_{1S} quartz veins with sphalerite and free gold in late microfractures (Figs. 4.4e, 4.11). Two pyrite textures were identified (Fig. 4.11). Py_{1S} corresponds to fine anhedral porous crystals of variable size (200 µm to 1 mm) containing silicate and sulfides inclusions (Fig. 4.11a). Py_{2S} occurs as euhedral grains surrounding Py_{1S} and are coarser (500 µm to 2 mm) (Fig. 4.11b).

The LA-ICP-MS results show that the porous Py_{1S} is enriched in trace elements and that the overgrowth Py_{2S} exhibits cyclic zoning (Fig. 4.13). Py_{1S} contains higher concentrations of V (54 ppm), Cu (370 ppm), Zn (29.4 ppm), Ag (16.6 ppm), Sb (8.8 ppm), Te (29 ppm), W (34.2 ppm), Au (1.6 ppm), Pb (340 ppm) and Bi (37 ppm) compared to Py_{2S} (Figs. 4.11, 4.12; Table 4.3).

The LA-ICP-MS images show clear correlations of Au with Cu, Zn, Ag, Sb, Te, W, Pb and Bi but not with As (Fig. 4.13). These elements are associated with nanoparticles or micro-inclusions of galena (Pb-Ag), chalcopyrite (Cu) and sphalerite (Zn) and probably tellurides (Au-Ag-Te). The maps show that the outer Py_{2S} is defined by cyclic zoning of Co, Ni, As and Se, unlike the porous Py_{1S} (Fig. 4.13). The thin outermost rim from Py_{2S} displays nanoparticles or micro-inclusions of Ag, Te, W, Au and Bi (Fig. 4.13).

4.7.4. WONA-KONA DEPOSIT

Three pyrite types in the Wona-Kona deposit were identified (Augustin et al., 2016) (Fig. 4.14). The first type (Py_{1WK}) occurs as disseminated, porous and framboidal crystals (200 µm to 1 mm) oriented parallel to the bedding in the black shale and in the silicification zone (Si_{4WK}). Py_{1WK} is characterized by a high density of silicate inclusions (Fig. 4.14a). In the main silicification zone (Si_{4WK}), pyrite grains are associated with arsenopyrite, sphalerite and free gold in late microfractures (Fig. 4.14c, d). Two subtypes are identified Py_{2WK} and Py_{3WK}. Py_{2WK} includes euhedral crystals with sizes ranging from 400 µm to 2 mm and is overgrown by sub-euhedral Py_{3WK} (Fig. 4.14b, c). Py_{1WK} is interpreted by Augustin et al. (2016) as diagenetic, Py_{2WK} as metamorphic and Py_{3WK} as hydrothermal. Previous LA-ICP-MS spot analyses by Augustin et al. (2016) have shown that the early diagenetic pyrite (Py_{1WK}) contains a higher level of invisible gold (median of 0.75 ppm Au) compared with the later metamorphic/hydrothermal pyrites (Py_{2WK} and Py_{3WK}), which contain much less invisible gold (medians of 0.13 and 0.18 ppm Au, respectively). The new LA-ICP-MS maps provide more detail on the pyrite types at Wona-Kona especially for Py_{3WK}.

To precisely determine the hydrothermal evolution, 2 pyrite maps, selected from a total of 12 mapped grains, are used below. The first elemental map (Fig. 4.16) shows a framboidal Py_{1WK} crosscut by a euhedral crystal of Py_{2WK}. Py_{1WK} is enriched in Co, Ni, Cu, Zn, Sb and Pb (Figs. 4.15, 4.16). Gold (0.8 ppm) and Ag (3.9 ppm) are concentrated in the core of the Py_{1WK} grain. Gold and Ag maps show a clear correlation and both metals occur as micro-

inclusions in the core of the Py_{1WK} grain. In contrast, the Py_{2WK} grain is zoned, with concentric bands of Co, Ni and As but without significant Au (Figs. 4.15, 4.16).

The second map (Fig. 4.17) shows a zoned pyrite with a euhedral Py_{2WK} grain overgrown by a sub-euhedral Py_{3WK} crystal hosted in the main silicification zone. Py_{2WK} is composed of cyclic rims of Co and Ni with low contents of As but high contents of Se compared to the Py_{3WK} overgrowth. The Co, As, Sb, and Te maps highlight an arsenopyrite crystal. Antimony, Au and Pb are not observed due to the detection limit (Fig. 4.15). The Py_{3WK} overgrowth is defined by a clear rim (50 µm) enriched in Cu, As, Se, Ag, Sb, Au, Pb and Bi. Gold content varies from 2.8 to 20.3 ppm with a mean of 5.6 ppm, whereas As varies from 6,400 to 21,200 ppm with a mean of 8,200 ppm (Fig. 4.15; Table 4.3). The thin external rim from Py_{3WK} is enriched in Co and Ni.

4.7.5. YAHO DEPOSIT

Several generations of pyrites have been described by Sinaré (2013). The first pyrite type (Py_{1Y}) consists of anhedral porous crystals (300 µm to 1 mm) with silicate inclusions that are hosted in the sandstones and polygenic conglomerates (Fig. 4.18a). Py_{2Y} occurs as euhedral grains with sizes of 200 µm to 1 mm and is mainly hosted in the host rocks and quartz-carbonate veins. The last type is associated with zoned pyrite, which is defined by a porous core of Py_{1Y} and surrounded by a sub-euhedral coarser Py_{3Y} (300 µm to 2 mm) occurring in a silicification zone with arsenopyrite and higher gold grades (> 3.0 g/t) (Figs.

4.18b, c). Sinaré (2013) interpreted Py_{1Y} and Py_{3Y} as hydrothermal pyrite and Py_{2Y} as metamorphic pyrite. However, the trace element contents were similar for each type of pyrite. Consequently, Sinaré (2013) concluded that the gold was much more associated with arsenopyrite (median of 76.6 ppm vs. 0.5 ppm for pyrite).

In this study, LA-ICP-MS lines and a map of zoned pyrite were generated to investigate the trace element distribution between Py_{1Y} and Py_{3Y} (Figs. 4.19, 4.20). The imaging shows that the Py_{1Y} porous core is enriched in Co, Ni, Se, Sb, Pb and Bi with minor Au (1.1 ppm) compared to the outer Py_{3Y}. The Py_{3Y} overgrowth consists of an As-Au-rich rim with median values of 17.2 ppm Au and 21,200 ppm As (Figs. 4.19, 4.20; Table 4.3). The thin outermost rim on Py_{3Y} consists of Co and Ni (Fig. 4.20). For both pyrite types, Te and W are below the detection limit.

4.7.6. COMPOSITION OF ARSENOPYRITE COMPARED TO PYRITES

Arsenopyrite occurs in the ore in all the gold deposits studied (Table 4.1). However, at the Siou deposit, its proportion is in trace amounts only, and consequently no arsenopyrite was analyzed. It is of interest to compare the geochemical signatures of arsenopyrite and the genetically related pyrite because the latter can incorporate much more gold, as well as other trace elements, into its structure (Fleet and Mumin, 1997; Reich et al., 2005; Fougerouse et al., 2016). In short, the geochemical composition of pyrite can be strongly influenced by co-precipitation of arsenopyrite from the same hydrothermal fluid.

In the Fofina deposit, arsenopyrite occurs in the V_{1F} quartz-carbonate veins associated with zoned pyrite (Py_{2F} and Py_{3F}) (Fig. 4.5b). Compared to the zoned pyrite, V_{1F} arsenopyrite is enriched in Co, Ni, Cu, Zn, Sb, Te and Pb (Fig. 4.6). Gold and Ag concentrations are similar to those of Py_{2F}.

In the Nyafé deposit, arsenopyrite coexists with zoned pyrite in the V_{3N} quartz veinlets (Fig. 4.8b). The V_{3N} arsenopyrite contains higher Au and Sb concentrations (medians of 232 ppm and 507 ppm) compared to the zoned pyrite (Fig. 4.9). However, the concentrations of Co, Ni, Zn, and Ag are similar to those of Py_{3N}.

In the Wona-Kona deposit, arsenopyrite occurs with the zoned pyrite grains in the silicification zone (Si_{4WK}) (Fig. 4.14c). The arsenopyrite in Si_{4WK} is enriched in Co, Ni, Se, Sb, and Te and depleted in Bi compared to all generations of pyrites (Fig. 4.15). Gold content is similar to that of Py_{3WK} (median of 6.7 ppm vs. 5.6 ppm). These results support the co-precipitation of the Si_{4WK} arsenopyrite and the Py_{3WK} overgrowth from the hydrothermal fluids that also induced the silicification in the $D4_{MD}$ shear zone, as proposed by Augustin et al. (2016).

In the Yaho deposit, arsenopyrite occurs in the silicification zone (Si_{4Y}) with zoned pyrite (Fig. 4.18c). The arsenopyrite in Si_{4Y} is enriched in Ni (250 ppm), Sb (197 ppm) and Au (48 ppm) compared to the zoned pyrite (Fig. 4.19). The concentrations of Co, Zn, Ag and Bi are similar to those of Py_{2Y}.

In summary, the Au and Sb contents of arsenopyrite are systematically higher than in pyrite from the same deposit. Arsenopyrite represents the main form of gold enrichment in all the gold deposits except Siou.

4.8. DISCUSSION

4.8.1. DISCRIMINATING PYRITE ORIGINS

The LA-ICP-MS lines and maps of pyrite from the Mana gold deposits exhibit a wide variability in trace element contents associated with the polyphase hydrothermal activities at the district scale (Augustin et al., 2017). Numerous types of diagenetic pyrites and several subtypes of hydrothermal and metamorphic pyrites were distinguished based on their textures (Figs. 4.5, 4.8, 4.11, 4.14, 4.18). To precisely determine the pyrite origins, various geochemical diagrams were produced using discriminating elements such as Au, As, Ag, Sb, Bi, Ni and Co (Fig. 4.21), as proposed by previous studies (e.g. Thomas et al., 2011; Sack et al., 2014; Gregory et al., 2015).

The framboidal Py_{1WK} from the Wona-Kona has been identified as being of diagenetic origin by Augustin et al. (2016). Py_{1WK} is enriched in Ni, Cu, Zn, Ag, Te, Au, Pb and Bi but depleted in As (Fig. 4.15; Table 4.3). Vanadium and W are concentrated in silicate inclusions within the pyrite (Fig. 4.16). The median ratios of Ag/Au = 4.5, Co/Ni = 0.6 and As/Ag = 18.5 (Fig. 4.21) are similar to those in the Paleoproterozoic sedimentary pyrite

described by Gregory et al. (2015) and formed in suboxic to anoxic environments. In these submarine environments, Au and other trace elements interact with organic matter and are concentrated by various scavenging processes (Piper and Calvert, 2009; Hu et al., 2016), and they can be incorporated into pyrite as fine particles during diagenesis (Large et al., 2009).

The disseminated Py_{1F} hosted in the black shale of the Fofina deposit contains a wide range of trace elements (Ni, Cu, Zn, As, W, and Pb ± Au and, Ag) (Fig. 4.6). The ratios of As/Au (median of 12,720), Ag/Au (median of 0.9), As/Ag (median of 12,940), Sb/Bi (median of 299) and Co/Ni (median of 2.5) (Fig. 4.21a, c; Table 4.3) are not compatible with a sedimentary/diagenetic origin. According to the values provided by Thomas et al. (2011) and Gregory et al. (2015), these pyrites are metamorphic or hydrothermal in origin, even though they are hosted in black shale.

Hydrothermal zoned pyrite is ubiquitous in all the studied gold deposits associated with quartz-carbonate veins (V_{1F}), quartz veins (V_{1S}-V_{3N}) and silicification zones (Si_{4WK}-Si_{4Y}) (Figs. 4.5b, 4.8b, 4.11, 4.14c, 4.18c). These pyrites are generally associated with arsenopyrite except at the Siou deposit (Fig. 4.4). The zoned pyrites, such as Py_{2F} and Py_{1S}, display similar textures, defined by internal core rich in silicate inclusions containing gold inclusions (Figs. 4.7, 4.13). These pyrite cores are overgrown by several generations of pyrite with late Au-As-rich rims, such as Py_{3N}, Py_{3WK} and Py_{2Y} (Figs. 4.10, 4.17, 4.20). These overgrowth pyrites have characteristics typical of metamorphic-hydrothermal pyrites (Thomas et al., 2011; Velásquez et al., 2014; Zhang et al., 2014). Chemically, the zoned

pyrites have highly variable compositions but show distinct features (Fig. 4.21). The plot of As vs. Au shows that the zoned pyrites are enriched in Au and As and depleted in Ag compared to the diagenetic pyrite $Py_{1WK,}$ except for the zoned pyrites from Siou (Fig. 4.21a, b). The Ag vs. Au and As/Ag vs. Sb/Bi diagrams allow a clear separation of the zoned pyrites of Siou (Py_{1S}) from to the other zoned pyrites, including the disseminated pyrites Py_{1F} (Fig. 4.21b, c), due to the high Ag, Bi, and Te ± Sb and W values characterizing Py_{1S} (Fig. 4.13; Table 4.3). The origin of these trace elements in Py_{1S} is discussed below. Finally, the higher values of Co and Ni and the higher ratio value Co/Ni (mean of 2.3) for Py_{1S} could indicate an increase in the metamorphic or magmatic inputs (Sack et al., 2014; Zhang et al., 2014) (Fig. 4.21c).

Silver and Au contents in Py_{1N}, Py_{2S}, and Py_{2WK} ± Py_{2F} are below the detection limits, implying that the formation of these pyrites was not related to any gold mineralizing event. Consequently, they could be related to a metamorphic event (Craig and Vokes, 1993 - Fig. 4.21b).

From these data, the binary diagram As/Ag vs. Sb/Bi (Fig. 4.22) is proposed for discriminating among gold-bearing pyrite types. Diagenetic pyrite has a low As/Ag ratio and an intermediate Sb/Bi ratio (Fig. 4.22). Magmatic pyrite has low As/Ag and Sb/Bi ratios, whereas metamorphic pyrite has higher As/Ag and Sb/Bi ratios characteristic of orogenic gold deposits (Fig. 4.22).

4.8.2. METAMORPHOGENIC SOURCE FOR Au AND As

The Mana gold deposits are characterized by elevated Au and As, and their sources remain debated. The Mana district is defined by large volume of various host rocks including, volcanic volcano-sedimentary and sedimentary rocks and granitic plutons which have the potential to be the source of Au and As during the metamorphic history. The study by Augustin and Gaboury (2017) suggested that the gold endowment of the Mana district is mostly related to the occurrence to a large sequence (~8 km) of plume-related basaltic rocks, which may have served as an important metal stock and thus a viable source for As and Au. Gaboury (2013) documented C_2H_6 in fluid inclusions from the Mana gold deposits and argued that gold was extracted during the metamorphism of primary gold-enriched pyrite occurring in the black shales. Nevertheless, these two sources are not exclusive, since early seafloor hydrothermal activity overprinting the plume-related basalts also has the potential for upgrading the gold background of primary pyrite in black shales (Augustin and Gaboury, 2017).

The results of the present study support this conclusion and add more specific information on potential metal sources. The data provided above show that the framboidal Py_{1WK} in the black shale has hight Au (median of 0.8 ppm) and low As (median of 70 ppm) contents (Table 4.3). Hence, the framboidal pyrite is a potential source of Au and As in the Lower Birimian metamorphic pile of the Mana district, comparable to the Victorian gold field of Australia (Thomas et al., 2011).

The LA-ICP-MS maps show that the Au-As association is observed in the disseminated pyrite Py_{1F} and zoned pyrites (Fofina, Nyafé, Wona-Kona and Yaho) associated with arsenopyrite precipitation (Figs. 4.7, 4.10, 4.13, 4.17, 4.20). Consequently, two different Au-As distributions are observed: 1) in the core of Py_{2F} (Fofina deposit) and 2) as the late Au-As-rich rims of Py_{3F}, Py_{3WK} and Py_{2Y}. The multi-element diagram in figure 4.23a, shows that Py_{1F} and Py_{2F} have similar trace element patterns implying a similar source origin, in agreement with the As vs. Au diagram (Fig. 4.21a). The later Au-As-rich rims observed in the zoned pyrites also have very similar trace element patterns (Fig. 4.23b). Furthermore, these patterns are comparable to the Py_{1F} and Py_{2F} patterns (Fig. 4.21a). All these pyrites having similar geochemical signatures (Fig. 4.23), implying that their formation is related to the same hydrothermal system operating at the district scale (Fig. 4.23c). Nevertheless, in the Fofina deposit, Au and As are associated with the cores of Py_{2F} (Fig. 4.7) suggesting that Au and As were available earlier for this deposit.

The Au-As association has been described in many orogenic gold deposits and is interpreted as being related to the metamorphic devolatilization of metasedimentary rocks, especially carbonaceous metasedimentary rocks, with abundant syngenetic/diagenetic pyrite (Large et al., 2009; Thomas et al., 2011, Steadman and Large, 2016). However, the Mana district hosts a large volume of tholeiitic basalts, which are also potential sources of Au and As. Phillips et al. (1987) demonstrated through a mass balance calculation that, even at 1-2 ppb levels in basaltic to andesitic volcanic rocks, sufficient gold could be liberated during metamorphism to form giant gold deposits. Conversely, the recent study of Pitcairn et al. (2015) suggested that basaltic rocks in New Zealand did not provide

sufficient As and S to account for the documented values in orogenic gold deposits. Consequently, it is interpreted that Au and As were extracted from the Lower Birimian sequence, especially from the black shales and in part from the plume-related tholeiitic basalts and mobilized during metamorphism.

4.8.3. MAGMATIC SOURCE FOR Au, Ag, Bi, Te, AND W

In contrast to the other deposits, the zoned pyrites of the Siou deposit do not display the Au-As association (Fig. 4.13). Conversely, gold is associated with Ag in the core of Py_{1S} with granophile trace elements (Bi, Te, and W) compared to the other zoned pyrites (Figs. 4.21c, 4.23c), implying a different source. The low concentrations of As, Au and Sb in the Siou deposit compared to the other deposits (Fig. 4.23c; Table 4.3) are also consistent with the rarity of arsenopyrite, which is commonly enriched in these elements (Figs. 4.6, 4.9, 4.15, 4.19). The source of Ag, Bi, Te and W has received little attention in the literature and thus remains uncertain.

Early Au-Sb-Bi-(Te-W) mineralization is documented at the Morila deposit in southeast Mali and interpreted to be intrusion-related (McFarlane et al., 2011). Another source is proposed by Pitcairn et al. (2006) for the Otago Schist, where As, Bi, Sb, Te and W were liberated during the progressive metamorphism of a sedimentary sequence. Large et al. (2009) showed that Te is also enriched in diagenetic pyrite, making this type of pyrite a potential source reservoir of this element.

Augustin et al. (2017) showed that the early mineralization at Siou formed during the $D1_{MD}$ deformation event prior to or during emplacement of the Siou granodiorite, which had the potential to release magmatic-fluids. The Au association with nanoparticles and/or inclusions of galena, chalcopyrite, sphalerite and tellurides (Fig. 4.13) appear to be consistent with a magmatic source, such as in the Canadian Malartic deposit (Helt et al., 2014). As such, the cores of Py_{1S} plot in a distinctive field in the binary diagram As/Ag vs. Sb/Bi (Fig. 4.22) and are considered to be magmatic. However, the main economic gold concentration is associated with free gold and sericite in late microfractures that formed during later deformation of the district (Fig. 4.11c - Augustin et al., 2017). The thin outermost rims of Py_{2S} (Fig. 4.13) contain nanoparticles of Au, Ag, Te and Bi which could have been remobilized or introduced by another source as observed for the overgrowth Py_{3WK} (Fig. 4.17).

4.8.4. HYDROTHERMAL EVOLUTION OF THE MANA DISTRICT

According the previous study of Augustin et al. (2017), the Mana district has recorded at least four hydrothermal events during a period of over 150 Ma (Fig. 4.2). From the LA-ICP-MS and the pyrite formation sequence presented here, we have refined the ore-forming processes as follow.

The early event started with the formation of the early synsedimentary to diagenetic gold-bearing fluid in the Lower Birimian carbonaceous black shale (< 2170 Ma) which is

manifested as the precipitation of diagenetic framboidal Py_{1WK} (Figs. 4.14a, 4.24a). The observations from the LA-ICP-MS maps show that Py_{1WK} is pre-concentrated in Au and by features characteristic suite of trace elements (Ni, Cu, Zn, Ag, Au, Pb, and Bi - Figs. 4.15, 4.16).

The first hydrothermal event occurred during the $D1_{MD}$ E-W shortening (~2172 Ma - Eoeburnean phase) correlated with the folding of the Lower Birimian group in the central domain and the development of thrust faults (Augustin et al., 2017). Metamorphic-hydrothermal fluids were focused within the F_{1MD} anticlinal fold of the Fofina deposit (Fig. 4.3a) and produced the economic V_{1F} quartz-carbonate veins and disseminated Py_{1F} (Fig. 4.4a, b). At deeper depth, later fluids may have leached the framboidal Py_{1WK} from the black shales and released Au and As into the hydrothermal-metamorphic fluids in association with the precipitation of Py_{1F}, Py_{2F} and arsenopyrite (Fig. 4.24b). At the same time in the Siou deposit, magmatic-hydrothermal fluids enriched in Au, Ag, Bi, W, and Te were generated and channeled in the $D1_{MD}$ reverse fault along the pre- to syn-kinematic Siou granodiorite (Fig. 4.24b). The V_{1S} quartz veins were produced (Fig. 4.4e) with the precipitation of porous Py_{1S} without arsenopyrite. In both deposits, the overprinting of Au-rich core pyrites formed the metal-depleted overgrowths of Py_{3F} and Py_{2S} (Figs. 4.7, 4.13). These pyrites are depleted in all elements except for As ± Ni, and Co and could be related to the regional greenschist metamorphic event of unknown age (Fig. 4.24b).

The second hydrothermal event is associated with the $D3_{MD}$ E-W to WNW-ESE transpression (~2113-2090 Ma - Eburnean phase) associated with folds and the activation

of NNE- to NE-trending dextral shear zones as observed in the Nyafé deposit (Figs. 4.1, 4.3b, 4.24c). Hydrothermal-metamorphic fluids were generated along the dextral shear zone in association with V_{3N} quartz veinlets forming a stockwork (Fig. 4.4d). Multiple Ni-Co rims in the zoned pyrites (Fig. 4.10: Py_{1N} and Py_{2N}) indicate fluctuations in the metamorphic-hydrothermal fluids during pyrite growth, as documented by Velásquez et al. (2014). The late stage is defined by an Au-As-rich rim of Py_{3F} and by the co-precipitation of Au-rich arsenopyrite and chalcopyrite, which represent the most economical gold mineralization (Figs. 4.8c, 4.9). The origin of the metamorphic-hydrothermal fluids is consistent with leaching of the Lower Birimian group (black shale), as interpreted for the Fofina deposit (Fig. 4.23c). However, the enrichment of Au and As at the end of the hydrothermal system could be related to a later event (see below). The high Cu (median of 450 ppm) concentration compared to the other deposits (Fig. 4.23b; Table 4.3) could be related to a tholeiitic basaltic source or fluid/rock interactions with tholeiitic basalts.

The third and main hydrothermal event is correlated with the $D4_{MD}$ NNW-SSE transpression (~2090 Ma) with the development of folds and sinistral shearing along the major transcurrent faults and folds as documented in the Wona-Kona and Yaho deposits (Figs. 4.1, 4.3d, e, 4.24d). This event is considered the main gold-bearing event in the western margin of the district. In both deposits, the gold mineralization is characterized by a strong silicification (Si_{4WK} and Si_{4Y}) associated with zoned pyrites and arsenopyrites (Fig. 4.4g, i). However, the earlier Py_{2WK} and Py_{1Y} are depleted in all elements (Figs. 4.17, 4.20) suggesting that they are not related to the main gold-bearing event. Gold-As-rich rims on

the pyrites (Py_{3WK} and Py_{2Y}) indicate that the main episode of hydrothermal gold and arsenic transfer occurred during the final stage of deformation in association with the co-precipitation of Au-rich arsenopyrites (Figs. 4.15, 4.17, 4.19, 4.20). Their similar trace element patterns imply that a large metamorphic-hydrothermal fluid reservoir became available to source gold and arsenic from the black shales and tholeiitic basalts deeper in the Lower Birimian sequence (Fig. 4.23b), probably during the maximum shortening of the Mana district (Fig. 4.24d). Notably, the same Au-As-rich rims on pyrite are observed in the Nyafé deposit, which is interpreted as being related to a late reactivation of the Nyafé shear zone during the $D4_{MD}$ event, as suggested by Augustin et al. (2017).

The fourth hydrothermal event occurred during the late $D4_{MD}$ or $D5_{MD}$ N-S shortening (~2022 Ma) with a brittle reactivation of the major transcurrent faults (WKSZ and BSZ) in the Wona-Kona and Siou deposits (Figs. 4.2, 4.24e). The mineralization corresponds to late high-grade free gold enrichment infilling late microfractures (Figs. 4.11c, 4.14d). Two hypotheses can be proposed to explain this gold infilling. First, new gold input may be related to the late syn-$D4_{MD}$ or $D5_{MD}$ hydrothermal event. Secondly, gold may have been remobilized during this deformation event from the various generations of gold-bearing pyrites and arsenopyrites. Such remobilization is documented in several orogenic gold deposits (Cook et al., 2013; Simard et al., 2013; Fougerouse et al., 2016).

4.8.5. IMPLICATIONS FOR GOLD EXPLORATION

This study shows that the gold endowment of the Mana district is associated with multiple gold mineralizing events and with multiple fluid sources throughout a complex and polyphase accretionary tectonic history. Our results imply a single large metamorphic hydrothermal system enriched in Au, As, Ni and Co which operated for a long time and mineralized active fault systems. Magmatism related hydrothermal system with Au, Bi, Sb, Te and W contributed locally to the gold endowment of the Siou deposit, where the highest gold grade is recorded.

The main contribution of this paper resides in the development of a binary diagram As/Ag vs. Sb/Bi (Fig. 4.22) that can be used to discriminate among the diagenetic, magmatic and hydrothermal origins of gold-bearing pyrites. By using this diagram, one can determine whether there are one or numerous sources of fluids involved in the formation of a specific gold deposit. Consequently, the fertility of a large area (district) can be addressed by examining various gold deposits to determine whether there is: 1) gold-bearing primary-diagenetic pyrite in the environment, which can constitute a gold source for metamorphic gold liberation during the metamorphic pyrite-to-pyrrhotite transition at depth (Finch and Tomkins, 2017); 2) a single large hydrothermal system, which would imply that a large volume of rock was involved in generating abundant gold-bearing fluids during regional deformation and metamorphism (Phillips and Powell 2010); and 3) more localized fluid and gold inputs from magmatic degasification. All together, these multiple gold- and fluid-sourcing hydrothermal systems are more apt to generate the multi-stage enrichment

processes necessary for forming large gold-bearing deposits and districts, as documented recently (Meffre et al., 2016).

4.9. CONCLUSION

The LA-ICP-MS study of trace element compositions of sulfides (especially pyrite) was used to: 1) decipher the hydrothermal evolution; 2) recognize multiple stages of gold mineralization; and 3) trace the various sources of fluids and gold for the formation of the gold deposits in the Mana district.

The LA-ICP-MS lines and maps revealed at least 2 sources of gold and at least 2 different hydrothermal systems at the district scale. Gold was sourced from primary to diagenetic pyrite and from a magmatic source. During the first shortening deformation event ($D1_{MD}$), metamorphic devolatilization of the volcano-sedimentary rocks in Lower Birimian group induced the generation of the first-stage Au- and As-bearing metamorphic hydrothermal fluids, which were focused in the Fofina deposit. At Siou, magmatic-hydrothermal fluids characterized by Au, Ag, Bi, Te, and W formed during the pre- to syn-tectonic emplacement of the Siou granodiorite related to $D1_{MD}$. During the $D3_{MD}$ and $D4_{MD}$ shortening events, the main metamorphic-hydrothermal fluids, enriched in Au and As, were released and channeled along the major transcurrent faults. This hydrothermal system generated the most economic gold-bearing event at the district scale. The source of gold for this regional scale system is interpreted to be derived from the primary gold-bearing

sedimentary pyrite and from the direct leaching of plume-related gold-enriched tholeiitic basalts (Augustin and Gaboury, 2017). The late free-gold event is not clearly constrained and could be related to remobilization processes or a new hydrothermal input, without pyrite formation, during the late $D4_{MD}$ or $D5_{MD}$ events.

This study supports the concept that orogenic gold districts can form from a variety of fluid and metal sources, including metamorphic, magmatic and primary sedimentary-diagenetic processes. Diagram based on the ratios As/Ag and Sb/Bi can be used for the orogenic gold exploration to discriminate among diagenetic, magmatic and metamorphic gold-bearing pyrites and to ascertain the potential of a specific area.

4.10. ACKNOWLEDGMENTS

The data presented in this paper are from a Ph.D. project by the first author, which is part of a larger research program on the Mana District supervised by Prof. D. Gaboury (UQAC) since 2007 in collaboration with SEMAFO Inc. We are grateful to SEMAFO Inc. for granting access to their technical data, permitting field work and for authorizing the publication of these results. Many thanks to the senior geologists at SEMAFO Inc, particularly to M.A. Crevier, R. Roy, D. Lalonde, D. Bondé, F. Yameogo and D. Boisvert (now at Endeavour Mining Corporation) for their enthusiasm for this study. Our special thanks are extended to Dany Savard and Salia Mehdi for their assistance at the LA-ICP-MS facility at UQAC.

4.11. REFERENCES

Augustin, J., 2011. Facteurs de contrôle et processus métallogéniques des minéralisations aurifères du gisement de Wona, mine Mana, Burkina Faso. Unpublished M.Sc. thesis, Université du Québec à Chicoutimi, p. 1-220.

Augustin, J., Gaboury, D., Crevier, M., 2016. The world-class Wona-Kona gold deposit, Burkina Faso. Ore Geology Reviews 78, 667-672.

Augustin, J., Gaboury, D., 2017. Paleoproterozoic Plume-related basaltic rocks in the Mana gold district in Western Burkina Faso, West Africa: Implications for exploration and the source of gold in orogenic deposits. Journal of African Earth Sciences 129, 17-30.

Augustin, J., Gaboury, D., Crevier, M., 2017. Structural and gold mineralizing evolution of the world-class orogenic Mana District, Burkina Faso: Multiple mineralizing events during 150 million years. Ore Geology Reviews, doi.org/10.1016/j.oregeorev.2017.08.007.

Bath, A.B., Walshe, J.L., Cloutier, J., Verall, M., Cleverley, J.S., Pownceby, M.I., Macrae, C.M., Wilson, N.C., Tunjic, J., Nortje, G.S., 2013. Biotite and apatite as tools for tracking pathways of oxidizied fluids in the Archean East Repulse gold deposit, Australia. Economic Geology 108, 667-690.

Béland, J., 2009. Caractérisation gîtologique du gisement aurifère Nyafé, Burkina Faso. Unpublished B.Sc. report, Université du Québec à Chicoutimi, p. 1-19.

Bertrand-Sarfati, J., Moussine-Pouchkine, A., Affaton, P., Trompette, R., Bellion, Y., 1991. Cover sequences of the West African craton. In: Dallmeyer, R.D., Lecorche, J.P. (Eds.), The West African Orogens and Circum-Atlantic Correlatives. Springer-Verlag, p. 65-82.

Bonhomme, M., 1962. Contribution à l'étude géochronologique de la plate-forme de l'Ouest Africain. Ann. Fac. Sci. Univ. Clermont-Ferrand, p. 1-62.

Bossière, G., Bonkoungou, I., Peucat, J.J., Pupin, J.P., 1996. Origin and age of Paleoproterozoic conglomerates and sandstones of the Tarkwaian Group in Burkina Faso, West Africa. Precambrian Research 80, 153-172.

Castaing, C., Billa, M., Milési, J.P., Thiéblemont, D., Le Métour, J., Egal, E., Donzeau, M., Guerrot, C., Cocherie, A., Chèvremont, P., Tegyey, M., Itard, Y., Zida, B., Ouedraogo, I., Koté, S., Kaboré, B.E., Ouedraogo, C., Ki, J.C., Zunino, C., 2003. Notice explicative de la carte géologique et minière du Burkina Faso à 1/1,000,000. BRGM BUMIGEB, p. 1-147.

Chen, Y.J., Pirajno, F., Qi, J.P., 2008. The Shanggong gold deposit, Eastern Qinling Orogen, China: Isotope geochemistry and implication for ore genesis. Journal of Asian Earth Sciences 33, 252-266.

Colvin, E.T.C., 1989. An empirical model for the formation of Archean gold deposits-products final cratonization of the Superior province, Canada. Economic Geology 6, 37-53.

Cook, N.J., Ciobanu, C.L., Meria, D., Silcock, D., Wade, B., 2013. Arsenopyrite-pyrite association in an orogenic gold ore: Tracing mineralization history from textures and trace elements. Economic Geology 108, 1273-1283.

Côté-Mantha, O., Daigneault, R., Gaboury, D., Chartrand, F., Pilote, P., 2012. Geology, alteration, and origin of Archean Au-Ag-Cu mineralization associated with the synvolcanic Chibougamau pluton: The Brosman prospect, Abitibi greenstone belt, Canada. Economic Geology 107, 909-934.

Craig, J.R., Vokes, F.M., 1993. The metamorphism of pyrite and pyritic ores: An overview. Mineralogical Magazine 57, 3-18.

Dare, S. A. S., Barnes, S.-J., Beaudoin, G., Méric, J., Boutroy, E., Potvin-Doucet, C., 2014. Trace elements in magnetite as petrogenetic indicators. Mineralium Deposita 49, 785-796.

Davis, D., Hirdes, W., Schaltegger, U., Nunoo, E., 1994. U-Pb age constraints on deposition on provenance of Birimian and gold-bearing Tarkwaian sediments in Ghana, West Africa. Precambrian Research 67, 89-107.

Deynoux, M., 1983. Les formations de plate-forme d'âge Précambrien supérieur et Paléozoïque dans l'Ouest africain corrélation avec les zones mobiles. Pergamon Press, Oxford, United Kingdom.

Finch, E.G., Tomkins, A.G., 2017. Pyrite-pyrrhotite stability in a metamorphic aureole: Implications for orogenic gold genesis. Economic Geology 112, 661-674.

Fleet, M.E., Mumin, A.H., 1997. Gold-bearing arsenian pyrite and marcasite and arsenopyrite from Carlin Trend gold deposits and laboratory synthesis. American Mineralogist 82, 182-193.

Fontaine, A., Eglinger, A., Ada, K., André-Mayer, A.S., Reisberg L., Siebenaller, L., Le Mignot, E., Ganne, J., Poujol, M., 2017. Geology of the world-class Kiaka polyphase gold deposit, West African Craton, Burkina Faso. Journal of African Earth Sciences 126, 96-122.

Fougerouse, D., Micklethwaite, S., Tomkins, A.G., Mei, Y., Kilburn, M., Guagliardo, P., Fisher, L.A., Halfpenny, A., Gee, M., Paterson, D., Howard, D.L., 2016. Gold remobilization and formation of high grade ore shoots driven by dissolution-reprecipitation replacement and Ni substitution into auriferous arsenopyrite. Geochimica et Cosmochimica Acta 178, 143-159.

Fougerouse, D., Micklethwaite, S., Ulrich, S., Miller, J., Godel, B., Adams, D.T., McCuaig, T.C., 2017. Evidence for two stages of mineralization in West Africa's largest gold deposit: Obuasi, Ghana. Economic Geology 112, 3-22.

Fuchs, S., Williams-Jones, A.E., Przybylowicz, W.J., 2016. The origin of the gold and uranium ores of the Black Reef Formation, Transvaal Supergroup, South Africa. Ore Geology Reviews 72, 149-164.

Gaboury, D., 2013. Does gold in orogenic deposits come from pyrite in deeply buried carbon-rich sediments?: Insight from volatiles in fluid inclusions. Geology 41, 1207-1210.

Genna, D., Gaboury, D., 2015. Deciphering the hydrothermal evolution of a VMS system by LA-ICP-MS using trace elements in pyrite: An example from the Bracemac-McLeod deposits, Abitibi, Canada, and implications for exploration. Economic Geology 110, 2087-2108.

Goldfarb, R., Baker, T., Dubé, B., Groves, D.I., Hart, C.J., Gosselin, P., 2005. Distribution, character and genesis of gold deposits in metamorphic terranes. Economic Geology 100th Anniversary volume, 407-450.

Goldfarb, R.J., Groves, D.I., 2015. Orogenic gold: Common or evolving fluid and metal sources through time. Lithos 233, 2-26.

Graupner, T., Niedermann, S., Kempe, U., Klemd, R., Bechtel, A., 2006. Origin of ore fluids in the Muruntau gold system: Constraints from noble gas, carbon isotope and halogen data. Geochimica et Cosmochimica Acta 70, 5356-5370.

Gregory, M., Lang, J.R., Gilbert, S., Hoal, K.O., 2013. Geometallurgy of the pebble porphyry copper-gold-molybdenum deposit, Alaska: Implications for gold distribution and paragenesis. Economic Geology 108, 463-482.

Gregory, D.D., Large, R.R., Halpin, J.A., Lounejeva-Baturina, E., Lyons, T.W., Wu, S., Sack, P.J., Chappaz, A, Maslennikov, V.V., Bull, S.W., 2015. Trace element content of background sedimentary pyrite in black shales. Economic Geology 110, 1389-1410.

Helt, K.M., Williams-Jones, A.E., Clark, J.R., Wing, B.A., Wares, R.P., 2014. Constraints on the genesis of the Archean oxidized, intrusion-related Canadian Malartic gold deposit, Québec, Canada. Economic Geology 109, 713-735.

Hirdes, W., Nunoo, B., 1994. The Proterozoic paleoplacers at Tarkwa gold mine, SW Ghana; sedimentology, mineralogy, and precise age dating on the main Reef and West Reef, and bearing of the investigations on source area aspects. Geologisches Jahrbuch D 100, 247-311.

Hirdes, D., Davis, D., Lüdtke, G., Konan, G., 1996. Two generations of Birimian (Paleoproterozoic) volcanic belts in northeastern Côte d'Ivoire (West Africa): Consequences for the Birimian controversy. Precambrian Research 80, 173-191.

Hu, S.Y., Evans, K., Fisher, L., Rempel, K., Craw, D., Evans, N.J., Cumberland, S., Robert, A., Grice, K., 2016. Associations between sulfides, carbonaceous material, gold and other trace elements in polyframboids: Implications for the source of orogenic gold deposits, Otago Schist, New Zealand. Geochimica et Cosmochimica Acta 180, 197-213.

Jessell, M., Santoul, J., Baratoux, L., Youbi, N., Ernst, R. E., Metelka, V., Miller, J., Perrouty, S., 2015. An updated map of West African mafic dykes. Journal of African Earth Sciences 112, 440-450.

Kerrich, R., 1999. Nature's gold factory. Science 284, 2101-2102.

Large, R.R., Danyushevsky L.V., Hollit, C., Maslennikov, V., Meffre, S., Gilbert, S., Bull, S., Scotte, R., Emsbo, P., Thomas, H., Foster, J., 2009. Gold and trace element zonation in pyrite using a laser imaging technique: Implications for the timing of gold in orogenic and Carlin-style sediment-hosted deposits. Economic Geology 104, 635-668.

Large, R.R., Bull, S.W., Maslennikov, V.V., 2011. A carbonaceous sedimentary source-rock model for Carlin-type and orogenic gold deposits. Economic Geology 106, 331-358.

Large, R.R., Meffre, S., Burnett, R., Guy, B., Bull, S., Gilbert, S., Goemann, K., Danyushevsky, L., 2013. Evidence for an Intrabasinal source and multiple concentration processes in the formation of the carbon leader reef, Witwatersrand supergroup, South Africa. Economic Geology 108, 1215-1241.

Lawrence, D.M., Treloar, P.J., Rankin, A.H., Harbridge, P., Holliday, J., 2013a. The geology and mineralogy of the Loulo mining district, Mali, West Africa: Evidence for two distinct styles of orogenic gold mineralization. Economic Geology 108, 199-227.

Lawrence, D.M., Treloar, P.J., Rankin, A.H., Boyce, A., Harbidge, P., 2013b. A fluid inclusion and stable isotope study at the Loulo mining district, Mali, West Africa: Implications for multifluid sources in the generation of orogenic gold deposits. Economic Geology 108, 229-257.

Lebrun, E., Thébaud, N., Miller, J., Roberts, M., Evans, N., 2017. Mineralisation footprints and regional timing of the world-class Siguiri orogenic gold district (Guinea, West Africa). Mineralium Deposita 52, 539-564.

Le Métour, J., Chèvremont, P., Donzeau, M.E., Thiéblemont, E., Tegey, D., Guerrot, M.C.M., Itard, B., Castaing, Y., Delpont, C., Ki, G., Zunino, J.C.C., 2003. Notice explicative de la carte géologique du Burkina Faso au 1/200,000. Feuille Houndé, p. 1-82.

Le Mignot, E., Siebenaller, I., Béziat, D., André-Mayer, A.S., Reisberg, L., Salvi, S., Velásquez, G., Zimmermann, C., Naré, A., 2017. The Paleoproterozoic copper-gold deposits of the Gaoua district, Burkina Faso: Superposition of orogenic gold on a porphyry copper occurrence? Economic Geology 112, 99-122.

Lüdtke, G., Hirdes, W., Konan, G., Koné, Y., N'da, D., Traoré, Y., Zamblé, Z., 1999. Géologie de la région Haute Comoé Sud-feuilles Dabakala (2b, d et 4b, d). Direction de la Géologie Abidjan Bulletin, p. 1-176.

Mao, J., Li, Y., Goldfarb, R.J., He, Y., Zaw, K., 2003. Fluid inclusion and noble gas studies of the Dongping gold deposit, Hebei province, China: A mantle connection for mineralization? Economic Geology 98, 517-534.

Masurel, Q., Thébaud, N., Miller, J., Ulrich, S., Hein, K.A.A., Cameron, G., Béziat, D., Bruguier, O., Davis, J.A., 2017. Sadiola Hill: A world-class carbonate-hosted gold deposit in Mali, West Africa. Economic Geology 112, 23-47.

McFarlane, C.R., Mavrogenes, J., Lentz, D., King, K., Allibone, A., Holcombe, R., 2011. Geology and intrusion-related affinity of the Morila gold mine, southeast Mali. Economic Geology 106, 727-750.

Meffre, S., Large, R.R., Steadman, J.A., Gregory, D.D., Stepanov, A.S., Kamenetsky V.S., Ehrig, K., Scott, R.J., 2016. Multi-stage enrichment processes for large gold-bearing ore deposits. Ore Geology Reviews 76, 268-279.

Mériaud, N., Jébrak., M., 2017. From intrusion-related to orogenic mineralization: The Wasamac deposit, Abitibi greenstone belt, Canada. Ore Geology Reviews 84, 289-308.

Milési, J.P., Feybesse, J.L., Pinna, P., Deschamps, Y., Kampunzu, H., Muhongo, S., Lescuyer, J.L., Le Goff, E., Delor, C., Billa, M., Ralay, F., Heinry, C., 2004. Geological map of Africa 1:10,000,000. SIGAfrique Project. <http://www.sigafrique.net>

Paton, C., Hellstrom, J., Paul, B., Woodhead, J., Hergt, J., 2011. Iolite: Freeware for the visualisation and processing of mass spectrometric data. Journal of Analytical Atomic Spectrometry 26, 2508-2518.

Paulin-Bissonnette, A., 2012. Caractérisation de l'habitus de l'or dans les sulfures provenant des zones Fobiri et Fofina au Burkina Faso. Unpublished B.Sc. report, Université du Québec à Chicoutimi, p. 1-49.

Perrouty, S., Jessell, M.W., Bourassa, Y., Miller, J., Apau, D., Siebenaller, L., Velásquez G., Baratoux, L., Aillères, L., Béziat, D., Salvi, S., 2015. The Wassa deposit: A poly-deformed orogenic gold system in southwest Ghana-Implication for regional exploration. Journal of African Earth Sciences 112, 536-547.

Phillips, G.N., Groves, D.I., Brown, I.J., 1987. Source requirements for the Golden Mile, Kalgoorlie: Significance to the metamorphic replacement model for Archean gold deposit. Canadian Journal of Earth Sciences 24, 1642-1651.

Phillips, G.N., Powell, R., 2010. Formation of gold deposits: A metamorphic devolatilization model. Journal of Metamorphic Geology 28, 689-718.

Piper, D.Z., Calvert, S.E., 2009. A marine biogeochemical perspective on black shale deposition. Earth-Science Reviews 95, 63-96.

Pitcairn, I.K., Teagle, D.A.H., Craw, D., Olivo, G.R., Kerrich, R., Brewer, T.S., 2006. Sources of metals and fluids in orogenic gold deposits: Insights from the Otago and Alpine Schists, New Zealand. Economic Geology 101, 1525-1546.

Pitcairn, K.I., Craw, D., Teagle, D.A.H., 2015. Metabasalts as sources of metals in orogenic gold deposits. Mineralium Deposita 50, 373-390.

Reich, M., Kesler, S.E., Utsunomiya, S., Palenik, C.S., Chryssoulis, S.L., Ewing, R.C., 2005. Solubility of gold in arsenian pyrite. Geochimica et Cosmochimica Acta 69, 2781-2796.

Sack, P.J., Danyushevsky, L.V., Large, R.R., Gilbert, S., Gregory, D., 2014. Sedimentary pyrite as a gold-source in sediment-hosted gold occurrences in the Selwyn basin area, eastern Yukon. Yukon Exploration and Geology 2013, 195-220.

Salvi, S., Velásquez, G., Miller, J.M., Béziat, D., Siebenaller, L., Bourassa, Y., 2016. The Pampe gold deposit (Ghana): Constraints on sulfide evolution during gold mineralization. Ore Geology Reviews 48, 673-686.

Semafo Inc., 2013. Advanced Technical Report, Mana Property, Burkina Faso Reserve and Resource, p. 1-157.

SGS, 2009. Technical report on the resources and reserves of the Mana gold deposits, Burkina Faso, p. 1-101.

Simard, M., Gaboury, D., Daigneault, R., Mercier-Langevin, P., 2013. Multistage gold mineralization at the Lapa mine, Abitibi Subprovince: Insights into auriferous hydrothermal and metasomatic processes in the Cadillac-Larder Lake Fault Zone. Mineralium Deposita 48, 883-905.

Sinaré. M., 2013. Métallogénie du gisement aurifère de Yaho, ceinture birimienne de Houndé, Burkina Faso. Unpublished M.Sc. thesis, Université du Québec à Chicoutimi, p. 1-266.

Steadman, J.A., Large, R.R., Davidson, G.J., Bull, S.W., Thompson, J., Ireland, T.R., Holden, P., 2014. Paragenesis and composition of ore minerals in the Randalls BIF-hosted gold deposits, Yilgarn Craton, Western Australia: Implications for the timing of deposit formation and constraints on gold sources. Precambrian Research 243, 110-132.

Steadman, J.A., Large, R.R., Meffre, S., Olin, P.H., Danyushevsky, L.V., Gregory, D.D., Holden, P., 2015. Synsedimentary to early diagenetic gold in black shale-hosted pyrite nodules at the Golden Mile Deposit, Kalgoorlie, Western Australia. Economic Geology 110, 1157-1191.

Steadman, J.A., Large, R.R., 2016. Synsedimentary, diagenetic, and metamorphic pyrite, pyrrhotite, and marcasite at the Homestake BIF-hosted gold deposit, south Dakota, USA: Insights on Au-As ore genesis from textural and LA-ICP-MS trace element studies. Economic Geology 111, 1731-1752.

Thomas, H.V., Large, R.R., Bull, S.W., Maslennikov, V., Berry, R.F., Fraser, R., Froud, S., Moye, R., 2011. Pyrite and Pyrrhotite textures and composition in sediments, laminated quartz veins, and reefs at Bendigo gold mine, Australia: Insights for ore genesis. Economic Geology 106, 1-31.

Tomkins, A.G., 2013. On the source of orogenic gold. Geology 41, 1255-1256.

Velásquez, G., Béziat, D., Salvi, S., Siebenaller, L., Borisova, A.Y., Porkrovski, G.S., De Parseval, P., 2014. Formation and deformation of pyrite and implications for gold mineralization in the El Callao district, Venezuela. Economic Geology 109, 457-486.

White, A.J.R., Waters, D.J., Robb, L., 2015. Exhumation-driven devolatilization as a fluid source for orogenic gold mineralization at the Damang deposit, Ghana. Economic Geology 110, 1009-1025.

Wilson, S.A., Ridley, W.I., Koenig, A.E., 2002. Development of sulfide calibration standards for the laser ablation inductively-coupled plasma mass spectrometry technique. Journal of Analytical Atomic Spectrometry 17, 406-409.

Xue, Y., Campbell, I., Ireland, T.R., Holden, P., Armstrong, R., 2013. No mass-independent S isotope fractionation in auriferous fluids support a magmatic origin for Archean gold deposits. Geology 41, 791-794.

Zhang, J., Deng, J., Chen, H.Y., Yang, L.Q., Cooke, D., Danyushevsky, L., Gong, Q.J., 2014. LA-ICP-MS trace element analysis of pyrite from the Chang`an gold deposit, Sanjiang region, China: Implication for ore-forming process. Gondwana Research 26, 557-575.

FIGURES DU CHAPITRE 4

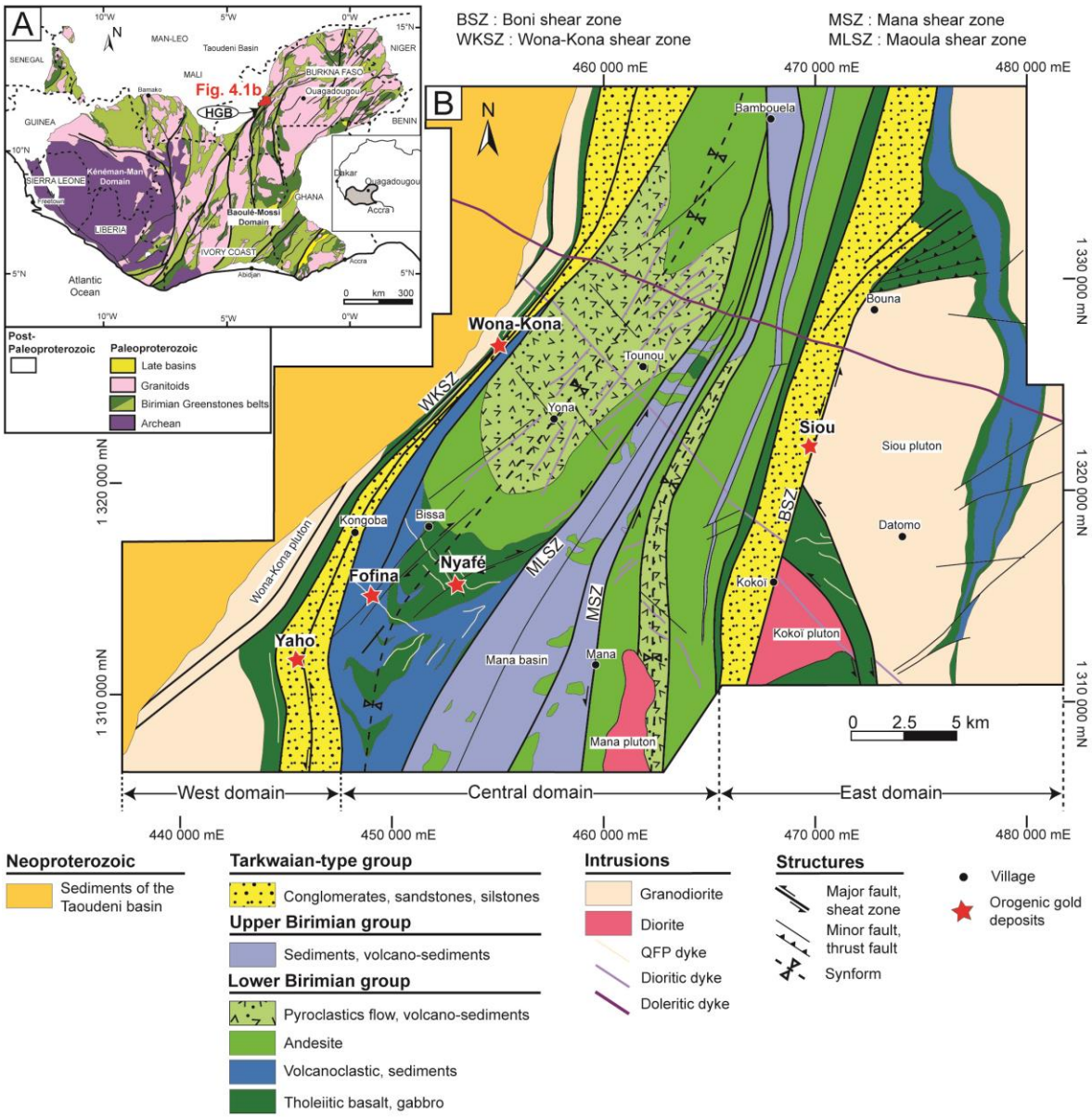

Figure 4.1 (a) Geology of the West African Craton, modified after Milési et al. (2004). (b) Simplified geological map of the Mana district, showing the 5 orogenic gold deposits studied (red stars), modified after Augustin et al. (2017).

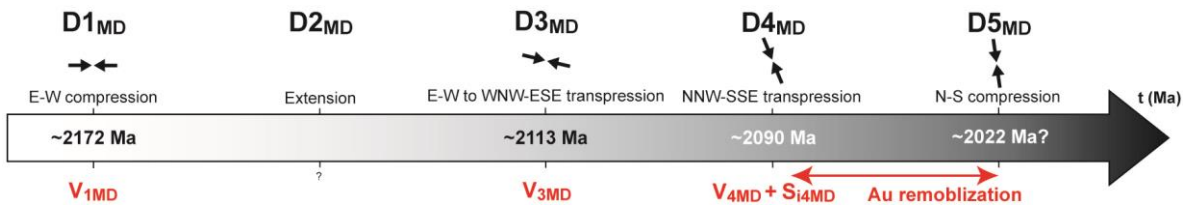

Figure 4.2 Schematic structural evolution associated with gold mineralizing events, as interpreted for the Mana district by Augustin et al. (2017).

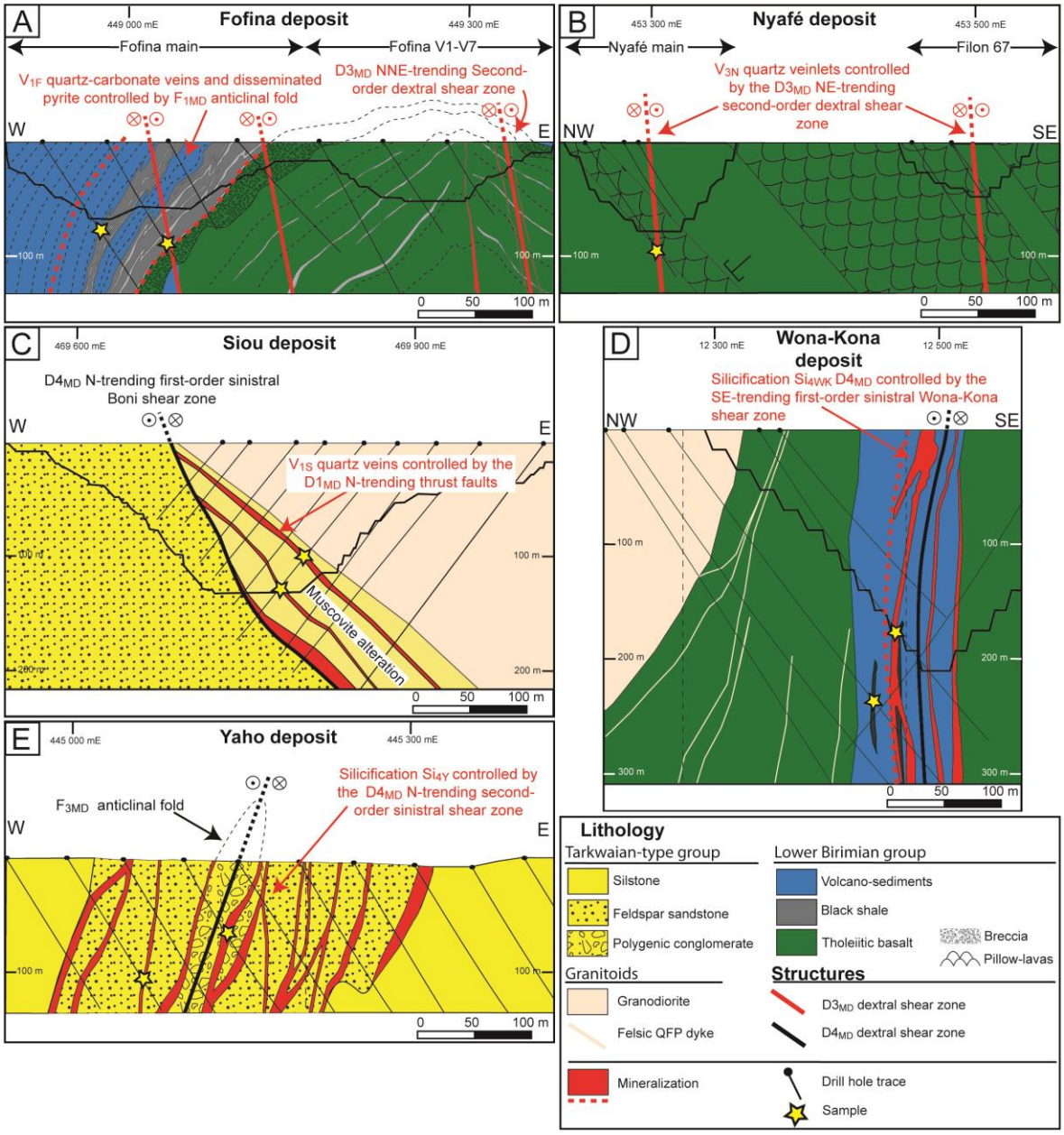

Figure 4.3 (a-e) Geological cross-sections and structural interpretation of the Mana gold deposits showing the geometry of the main gold mineralization and host rocks, modified after Augustin et al. (2017).

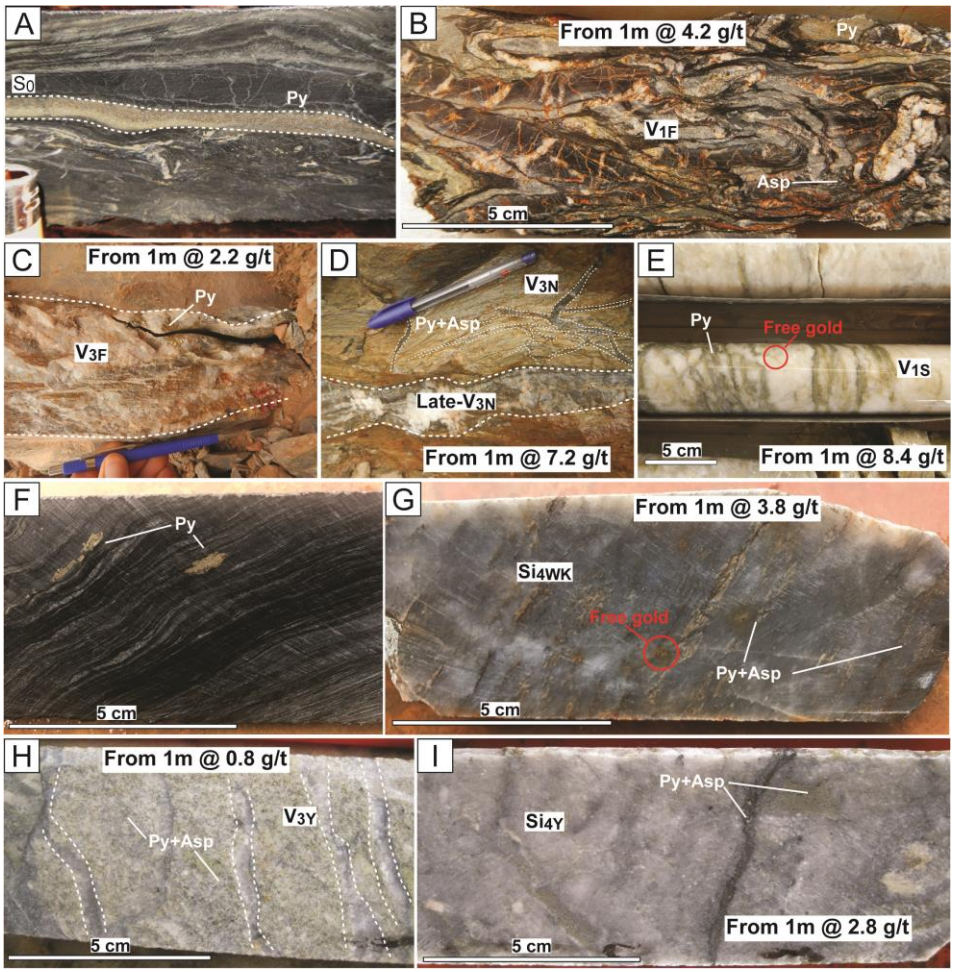

Figure 4.4 Macroscopic drill core observations and fields photographs of the different main mineralization facies of the Mana gold deposits. (a) Bedding-parallel bands of disseminated pyrite in black shale of the Fofina main pit. (b) Early folded quartz veins (V_{1F}) with pyrite (Py) and arsenopyrite (Asp) in the black shale unit (Fofina main). (c) Late quartz vein (V_{3F}) with pyrite in the Fofina V1-V7 veins. (d) Quartz veinlets (V_{3N}) associated with arsenopyrite and minor pyrite, surrounded by a muscovite-chlorite alteration assemblage and crosscut by a late quartz-carbonate vein (Late-V_{3N}) with minor pyrite in the Nyafé main pit. (e) White quartz vein (V_{1S}) with minor pyrite surrounded by muscovite alteration from the Siou pit. Some visible free gold occurs in the late microfracture and yields the highest gold grade. (f) Diagenetic pyrite hosted in the black shale of the Wona pit. (g) Main silicification (Si_{4WK}) associated with pyrite, arsenopyrite and free gold in late microfractures in the Wona-Kona deposit. (h) Disseminated pyrite and arsenopyrite in sandstone with quartz-carbonate veins (V_{3Y}) surrounded by muscovite alteration from the Yaho deposit. (i) Main silicification (Si_{4Y}) with pyrite and arsenopyrite in the Yaho deposit.

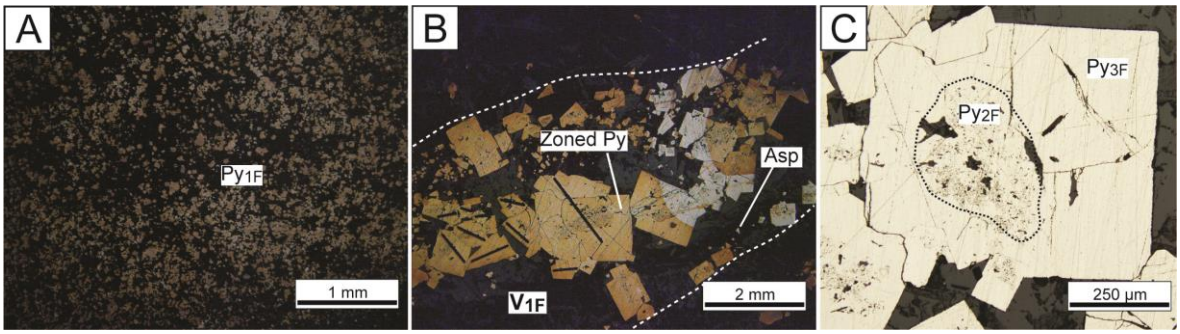

Figure 4.5 Photomicrographs of the various textural aspects of the pyrite types in the Fofina deposit. (a) Fine-grained (< 100 µm) pyrite interpreted as the earliest generation of pyrite in the black shale (Py_{1F}). (b) Quartz-carbonate vein (V_{1F}) with idiomorphic zoned pyrite and arsenopyrite. Zoning is highlighted by the different tint of oxidation in the thin section. (c) Zoned pyrite composed of porous pyrite (Py_{2F}) overgrown by coarser euhedral pyrite (Py_{3F}).

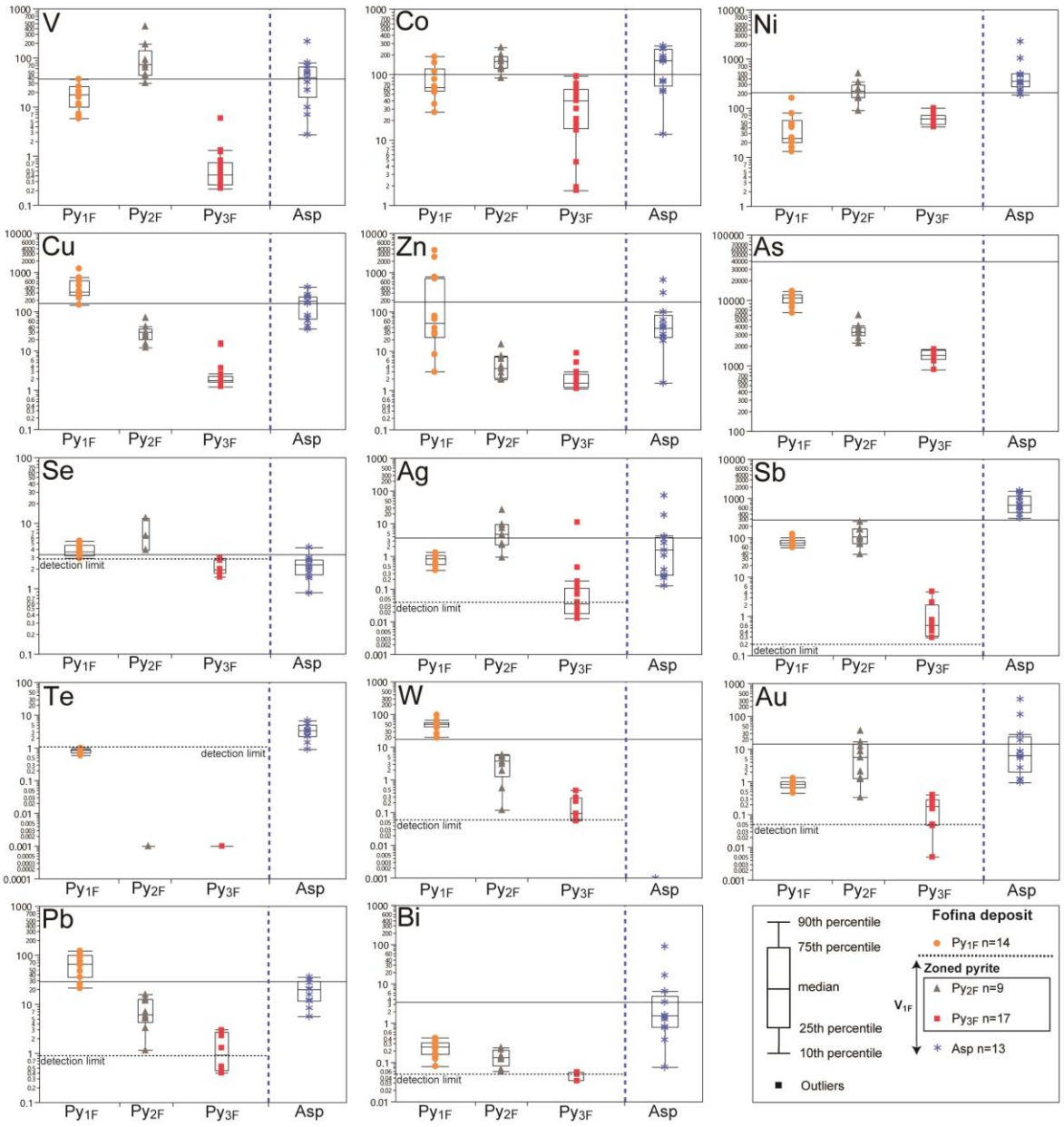

Figure 4.6 Statistical representation of the LA-ICP-MS data from different types of pyrite from the Fofina deposit. Detection limits are shown when they are close to the concentrations measured in pyrite. Data for the Fofina arsenopyrite are from Paulin-Bissonette (2012).

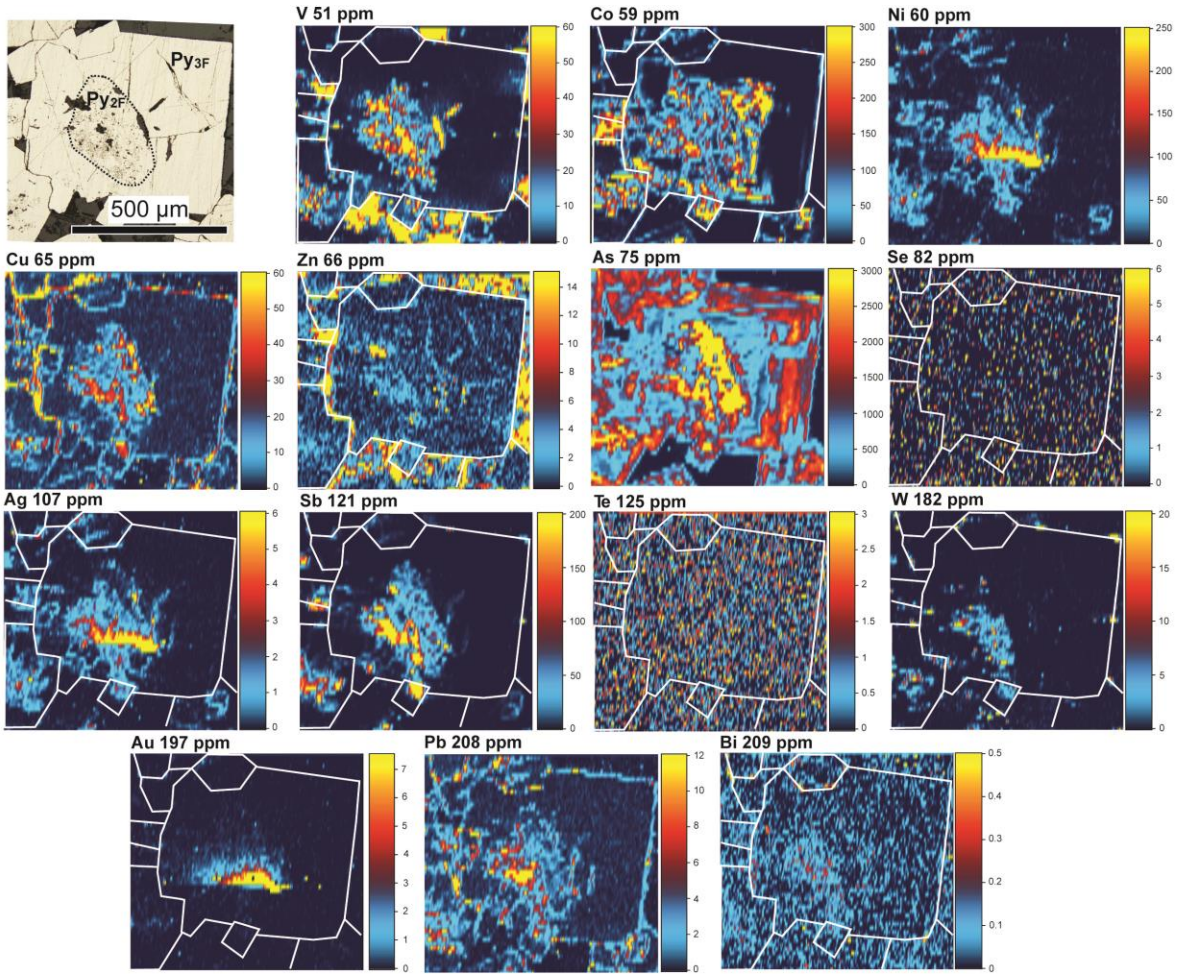

Figure 4.7 Trace element LA-ICP-MS maps of zoned pyrite in a quartz-carbonate vein (V_{1F}) from the Fofina deposit. Zoned pyrite exhibits a porous core Py_{2F} surrounded by a euhedral Py_{3F}. The core contains inclusions of silicates enriched in V and micro-inclusions of galena, chalcopyrite and native gold. The gold image shows yellow spots in the core due to inclusions of native gold. The light blue halo is due to gold splatter caused by the laser ablation process. The images show that the inclusion-rich pyrite core contains elevated V, Cu, As, Ag, Sb, W and Pb. The euhedral pyrite overgrowth shows cyclic zoning of Ni and As. White lines show the grain outline.

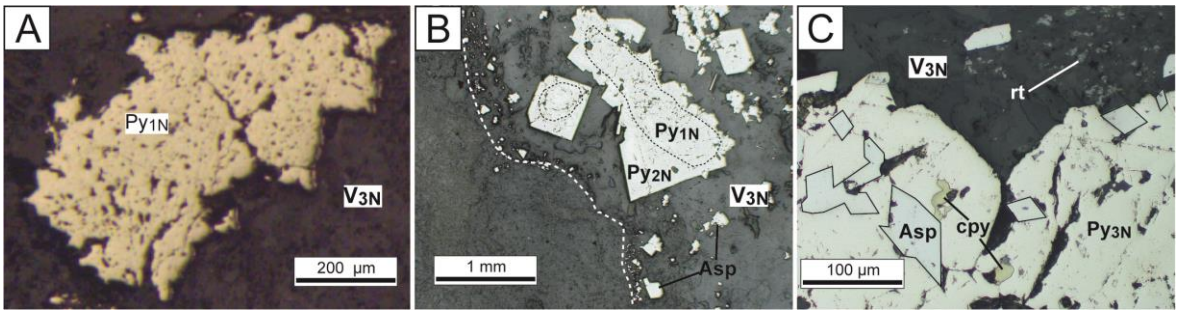

Figure 4.8 Photomicrographs of the various textural aspects of the pyrite types in the Nyafé deposit. (a) Anhedral porous pyrite (Py_{1N}) with silicate inclusions in the quartz veinlets (V_{3N}). (b) Quartz veinlets (V_{3N}) with idiomorphic zoned pyrite (Py_{1N} and Py_{2N}) and arsenopyrite. (c) Quartz veinlets (V_{3N}) with sub-euhedral pyrite (Py_{3N}), arsenopyrite (Asp), chalcopyrite (cpy) and rutile (rt).

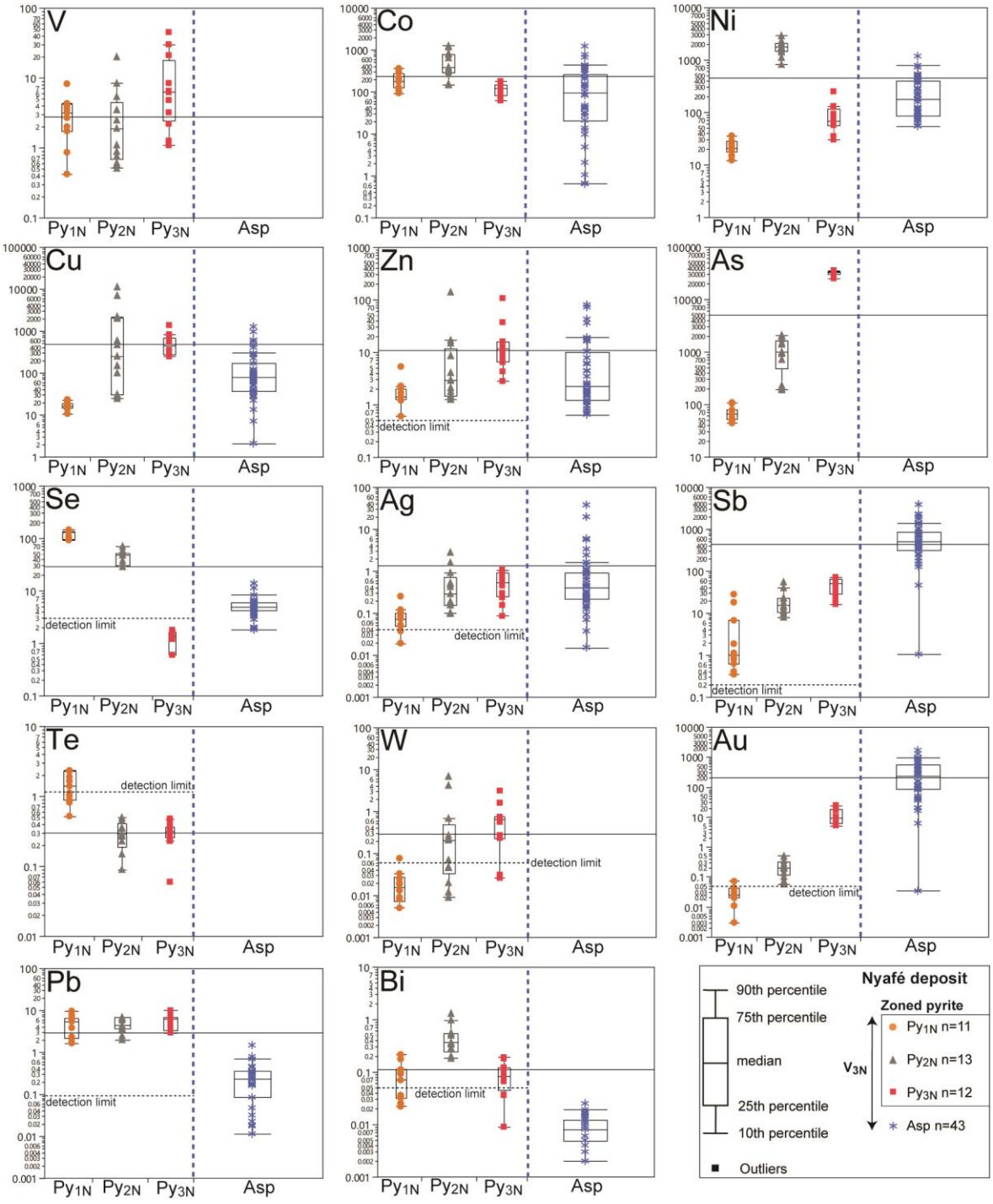

Figure 4.9 Statistical representation of the LA-ICP-MS data from different types of pyrite from the Nyafé deposit. Detection limits are shown when they are close to the concentrations measured in pyrite. Data for the Fofina arsenopyrite are from Béland (2009).

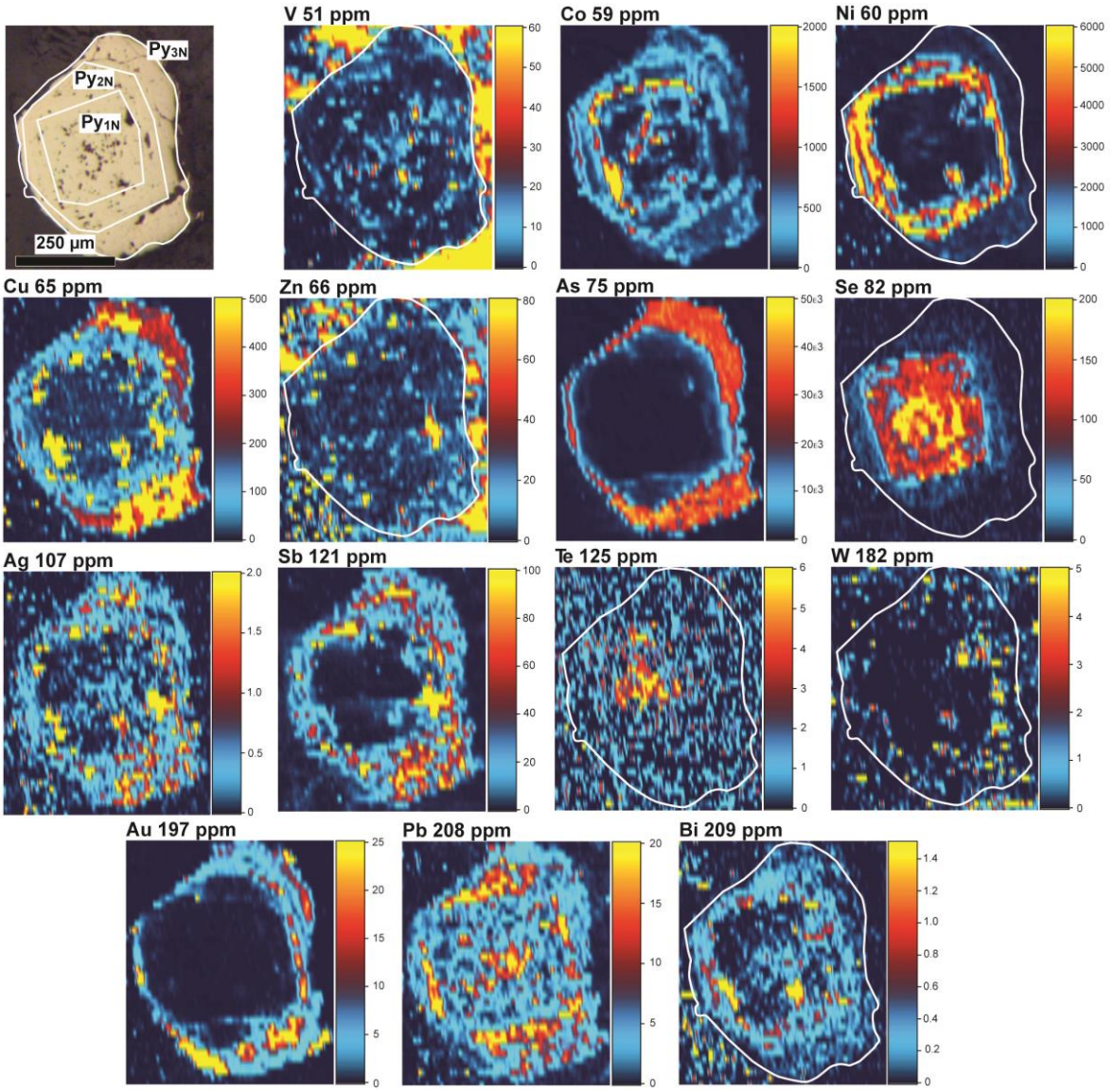

Figure 4.10 Trace element LA-ICP-MS maps of zoned pyrite in a quartz veinlet (V_{1N}) from the Nyafé deposit. Zoned pyrite exhibits a porous core Py_{1N} surrounded by a euhedral Py_{2N} and outermost euhedral Py_{3N}. Py_{1N} core is enriched in Se and minor Te compared to the surrounding Py_{2N}. Py_{2N} shows cyclic zoning of Co and Ni and contains micro-inclusions enriched in Cu (chalcopyrite) and Pb (galena). Py_{3N} forms a rim enriched in Cu, As and Au. White lines show the grain outline.

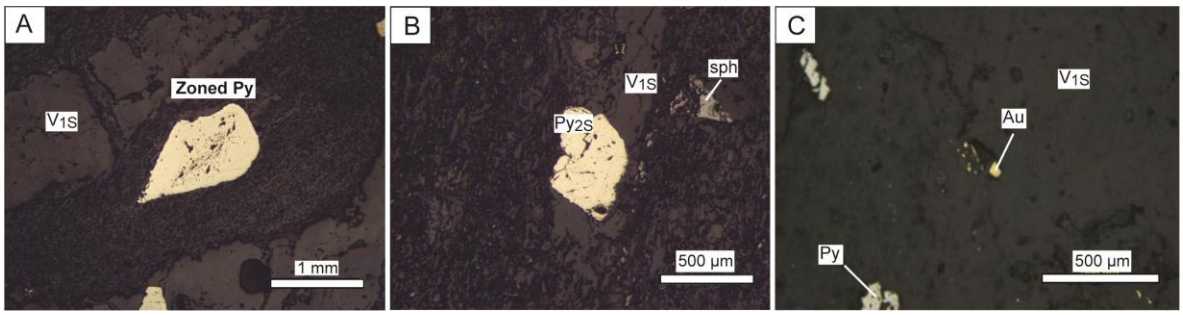

Figure 4.11 Photomicrographs in reflected light of different types of pyrites observed in the main quartz vein (V_{1S}) of the Siou deposit. (a) Sub-euhedral zoned pyrite (Py_{1S} and Py_{2S}) associated with a muscovite band. (b) Sub-euhedral Py_{2S} and sphalerite (sph). (c) Late free gold (Au) in a fracture crosscutting quartz vein (V_{1S}).

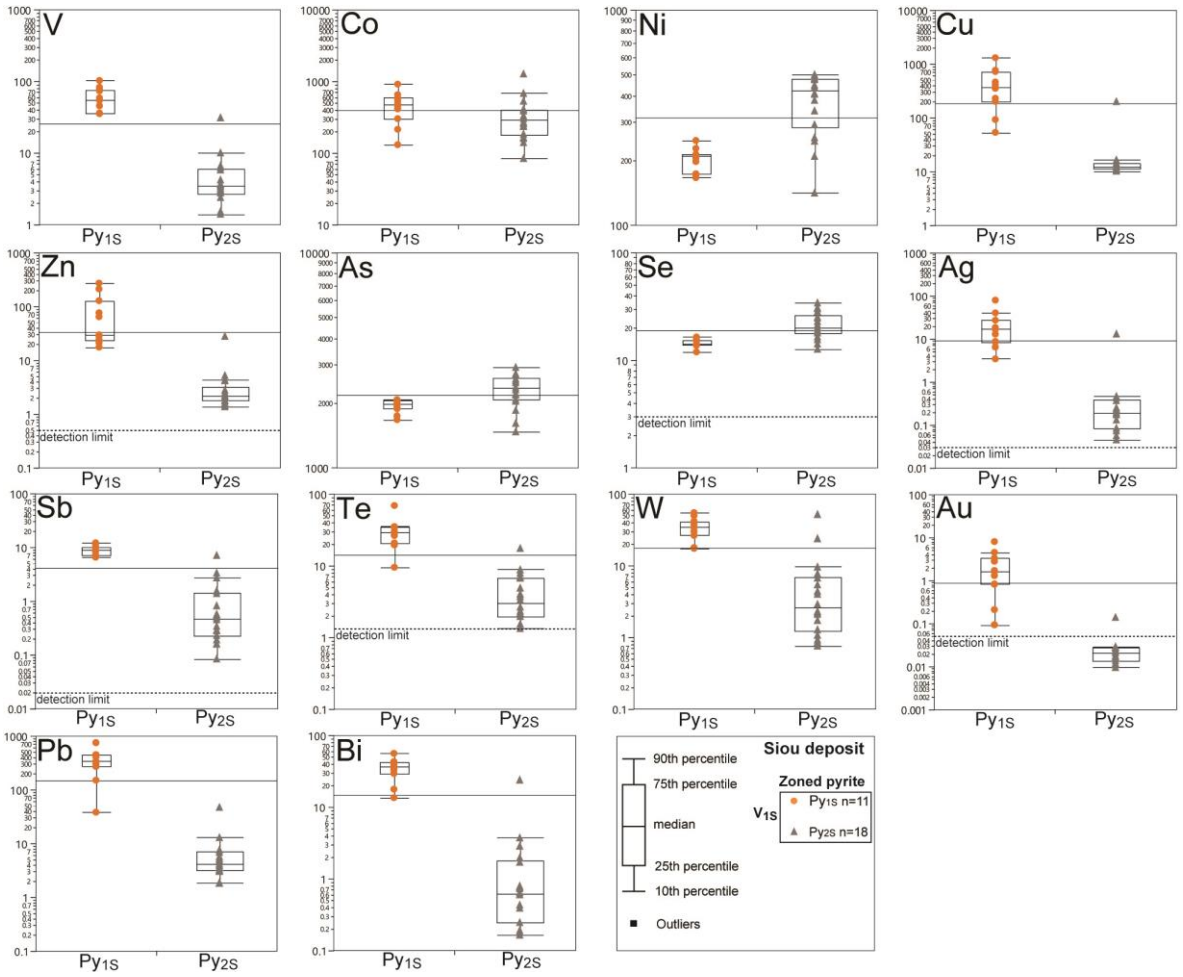

Figure 4.12 Statistical representation of the LA-ICP-MS data from different types of pyrite from the Siou deposit. Detection limits are shown when they are close to the concentrations measured in pyrite.

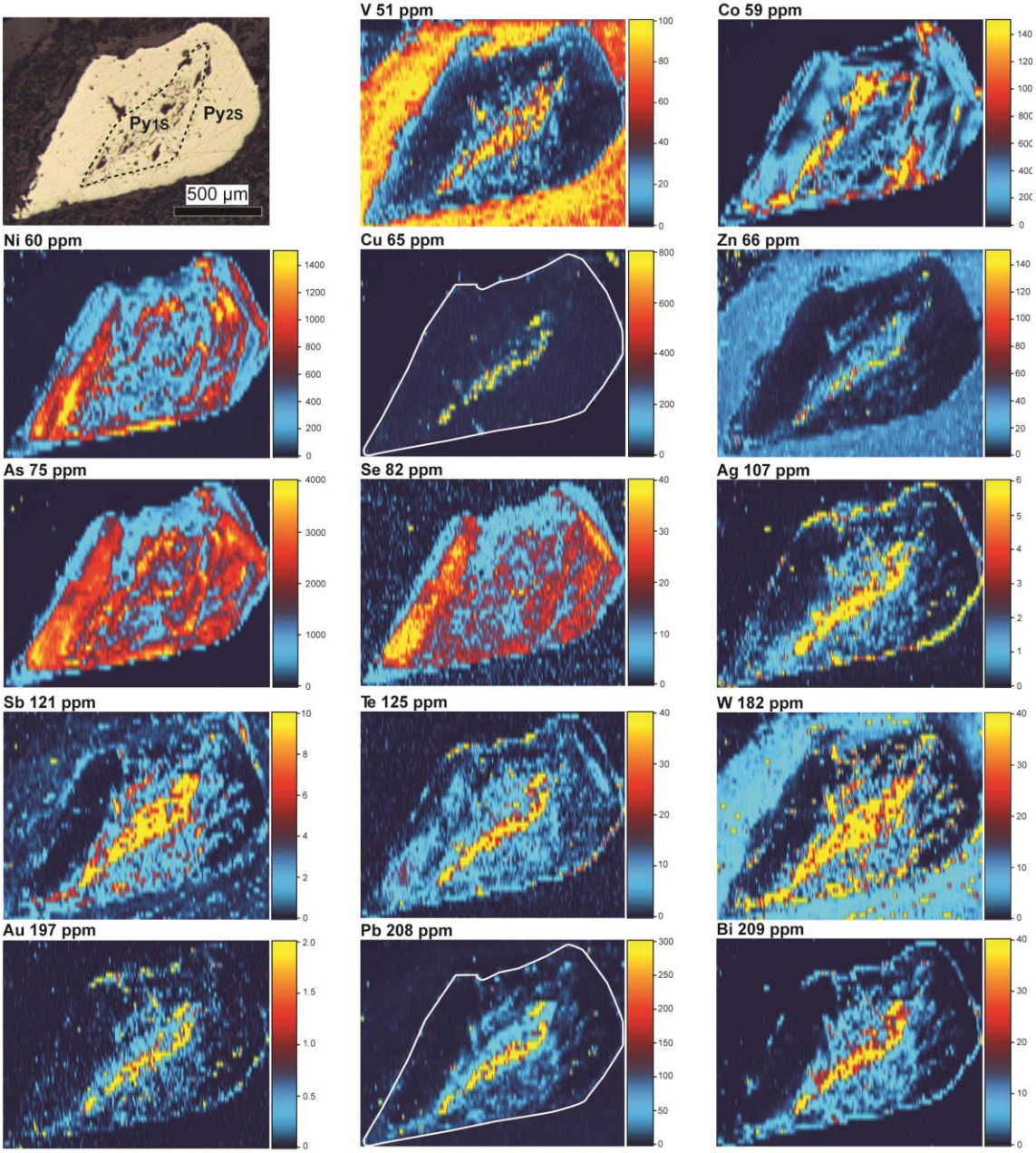

Figure 4.13 Trace element LA-ICP-MS maps of zoned pyrite in a quartz veinlet (V_{1S}) from the Siou deposit. Zoned pyrite exhibits a porous core Py_{1S} surrounded by euhedral Py_{2S}. The porous Py_{1S} core contains elevated values of V, Ag, Sb, Te, W, Au and Bi. Cu, Zn and Pb show spikey distribution due to micro-inclusions of chalcopyrite, sphalerite and galena in the core. The outer Py_{2S} shows cyclic zoning of Co, Ni, As and Se. The thin outermost rim of Py_{2S} contains nanoparticles or micro-inclusions of Ag, Te, W, Au and Bi. White lines show the grain outline.

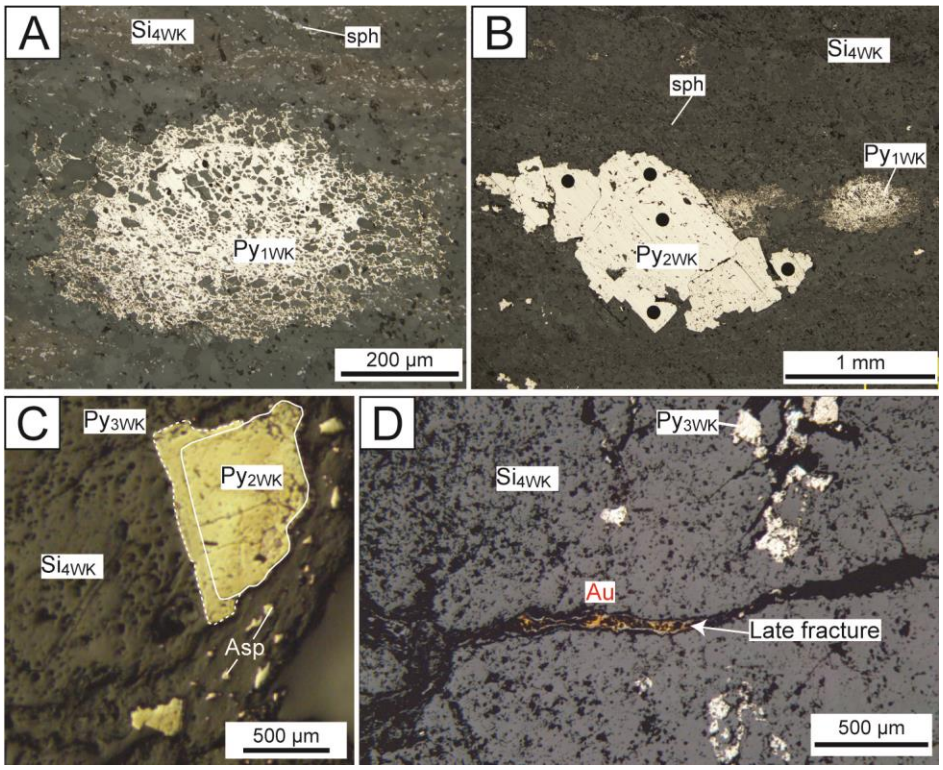

Figure 4.14 Photomicrographs of the various textural aspects of the pyrite types in the Wona-Kona deposit. (a) Framboidal pyrite (Py_{1WK}) with silicate inclusions and bands of sphalerite (sph) from the silicification zone overprinting black shale. (b) The temporal relationship is established by the cutting of the framboidal Py_{1WK} by an aggregate of Py_{2WK}. (c) Zoned pyrites defined by a euhedral Py_{2WK} core surrounded by sub-euhedral Py_{3WK} associated with arsenopyrite. (d) Late free gold (Au) in a fracture crosscutting the silicification Si_{4WK}.

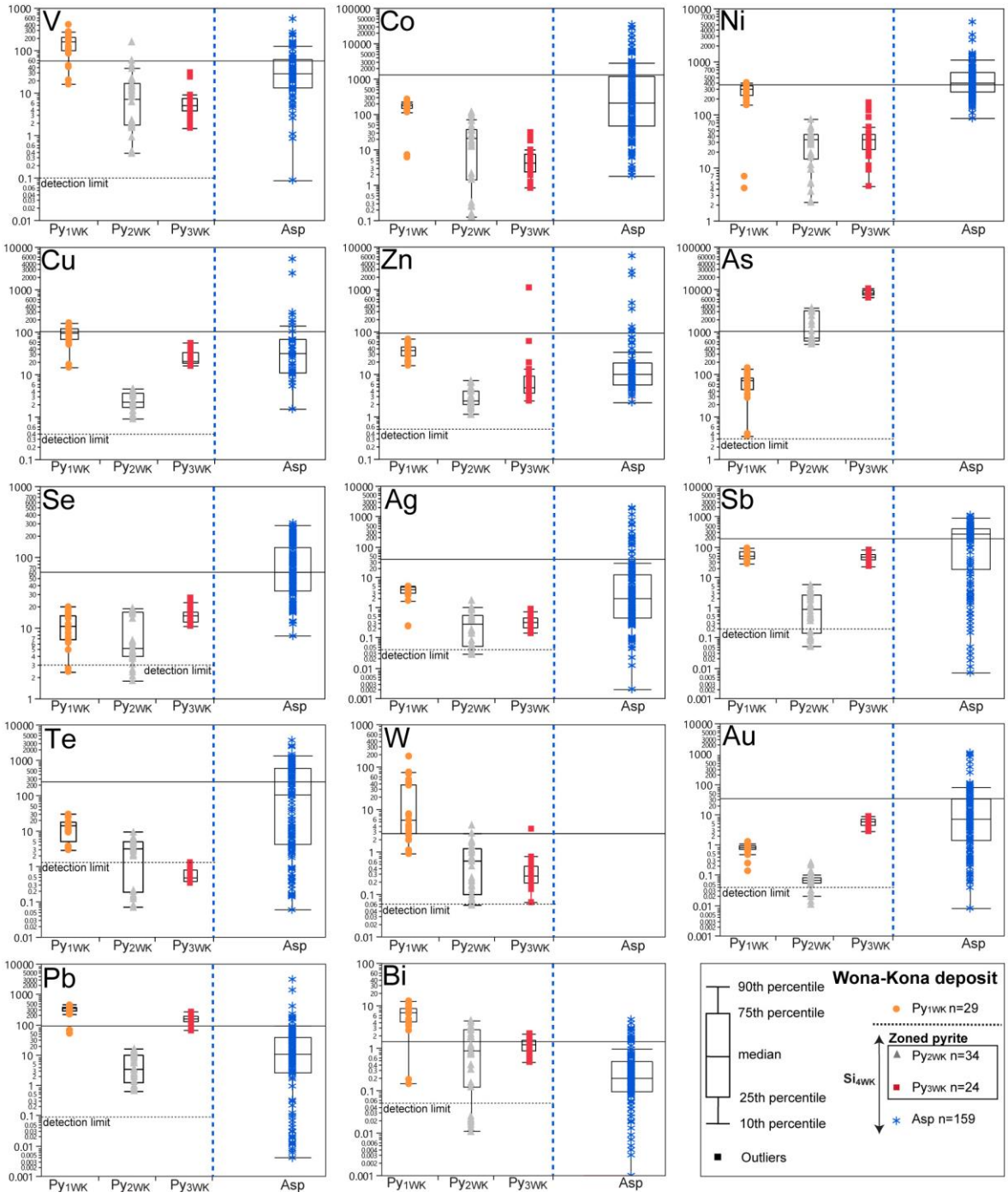

Figure 4.15 Statistical representation of the LA-ICP-MS data from different types of pyrite from the Wona-Kona deposit. Detection limits are shown when they are close to the concentrations measured in the pyrite. Data for the Wona-Kona arsenopyrite are from Augustin (2011).

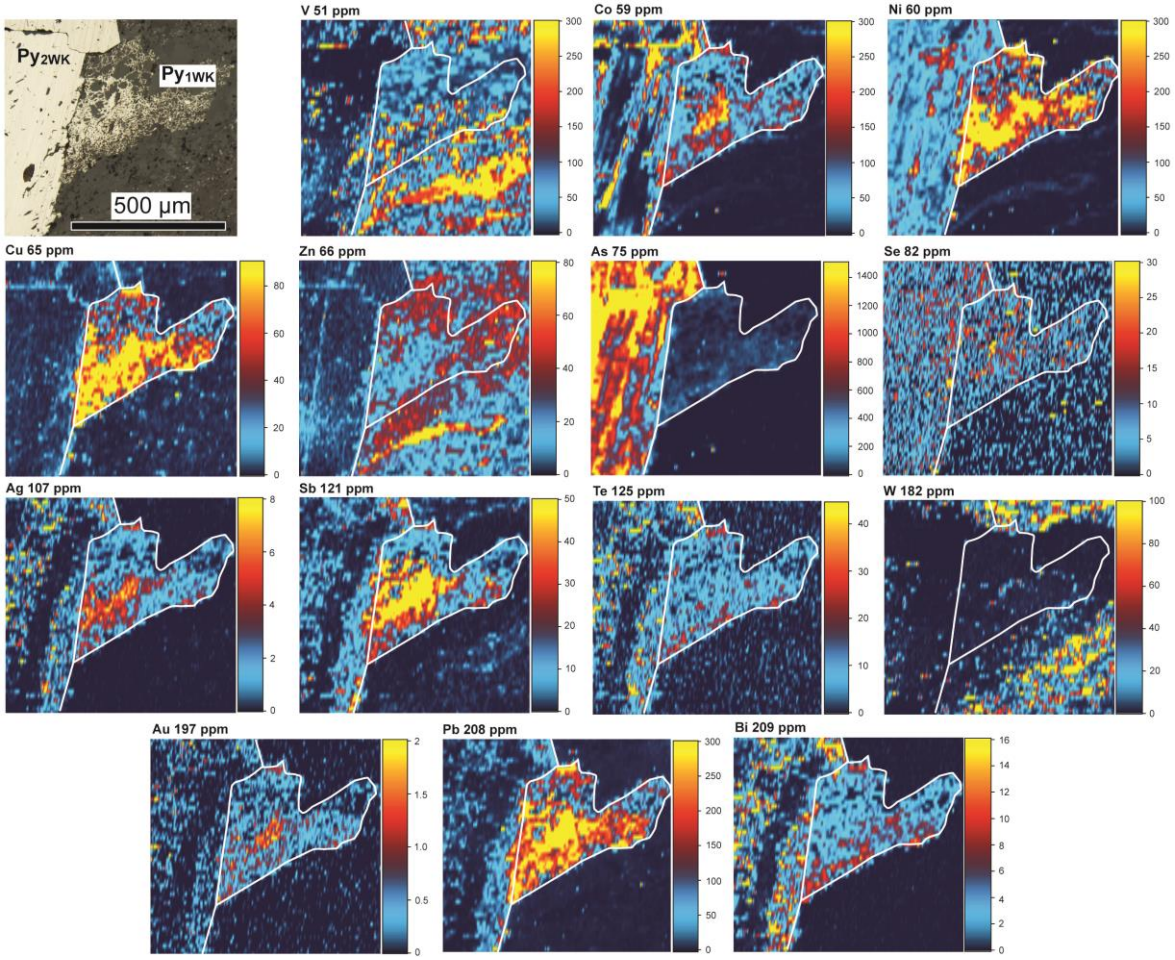

Figure 4.16 Trace element LA-ICP-MS maps of pyrites from the Wona-Kona deposit. Framboidal Py_{1WK} is enriched in Co, Ni, Cu, Zn, Ag, Sb, Au and Pb. Euhedral Py_{2WK} crosscuts Py_{1WK} and is defined by cyclic zoned Co, Ni and As. High concentrations of Zn are due to bands of sphalerite in the silicification zone. White lines show the grain outline.

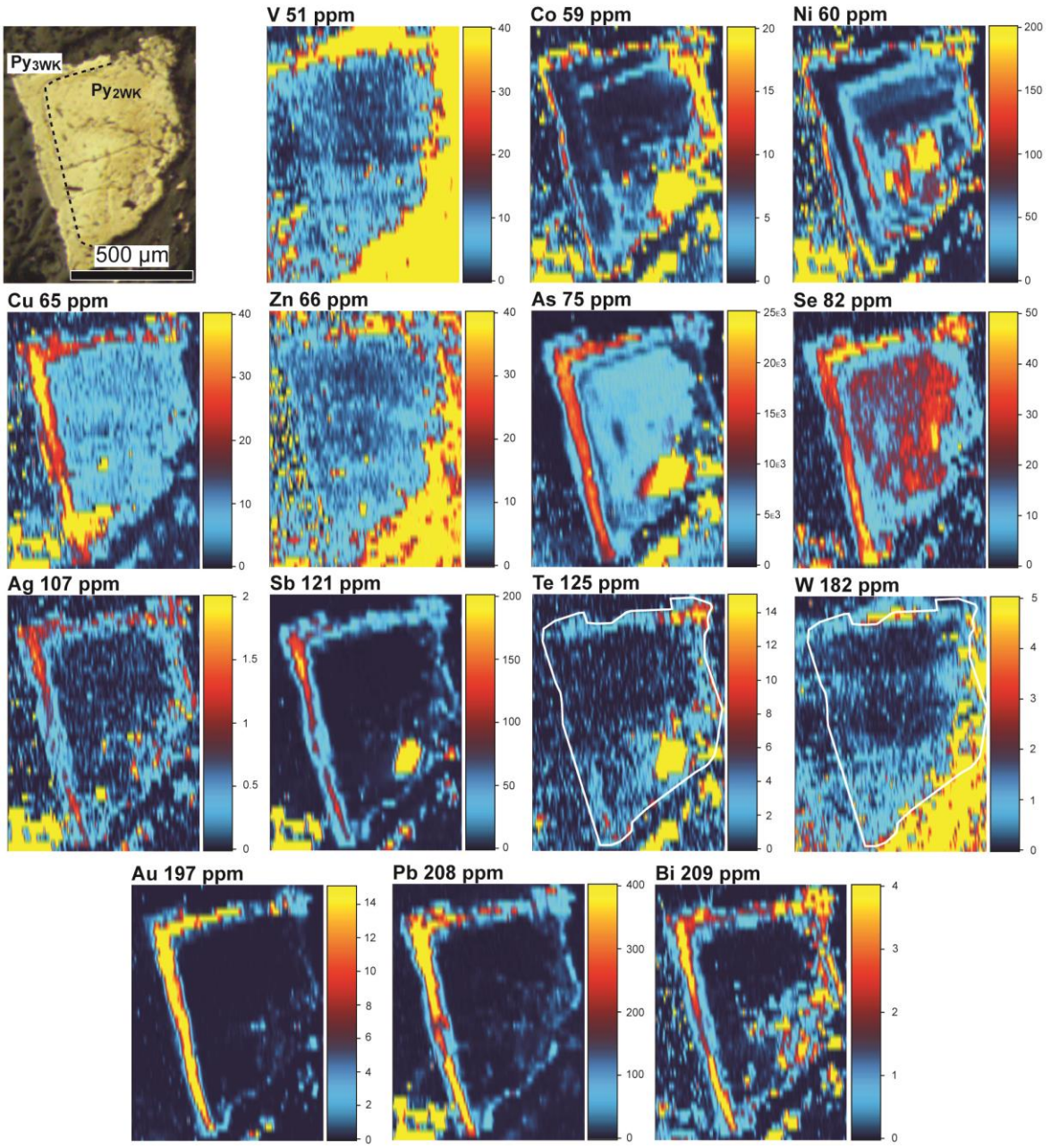

Figure 4.17 LA-ICP-MS elemental maps of a pyrite grain from the Wona-Kona deposit hosted in the silicified ore (Si_{4WK}). Euhedral Py_{2WK} is surrounded by late sub-euhedral Py_{3WK}. Py_{2WK} shows zoning of Co and Ni and the core is enriched in Se. The maps of Co, As, Sb and Te highlight an arsenopyrite crystal. The Py_{3WK} overgrowth is composed of an Au-As rim with elevated values of Cu, Se, Ag, Sb, Pb and Bi. The thin outermost rim on Py_{3WK} consists of Co and Ni. White lines show the grain outline.

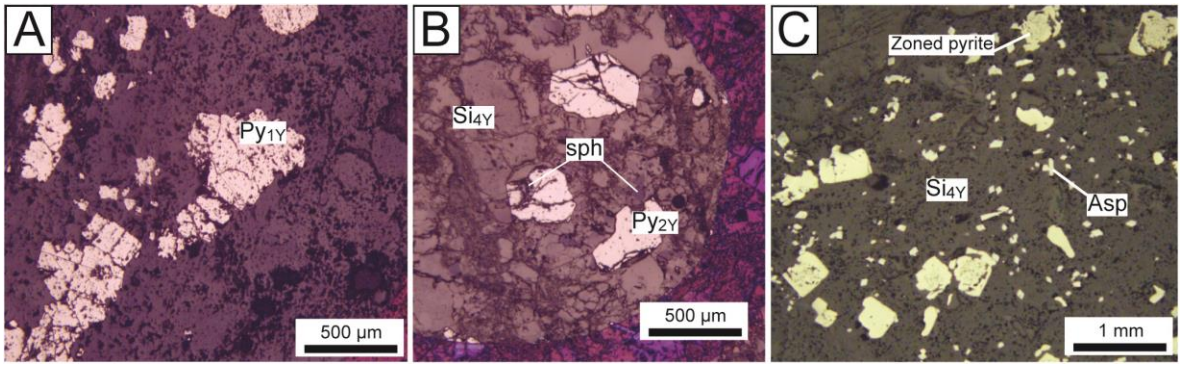

Figure 4.18 Photomicrographs of the various textural aspects of the pyrite types in the Yaho deposit. (a) Anhedral porous Py_{1Y} with silicate inclusions hosted in conglomerate. (b) Euhedral Py_{2Y} associated with sphalerite in fractures from the silicified ore (Si_{4Y}). (c) Zoned pyrite with a porous core containing silicate- and sulfide-bearing inclusions (Py_{1Y}) surrounded by euhedral Py_{2Y}. Arsenopyrite coexists with the zoned pyrite in the silicified ore (Si_{4Y}).

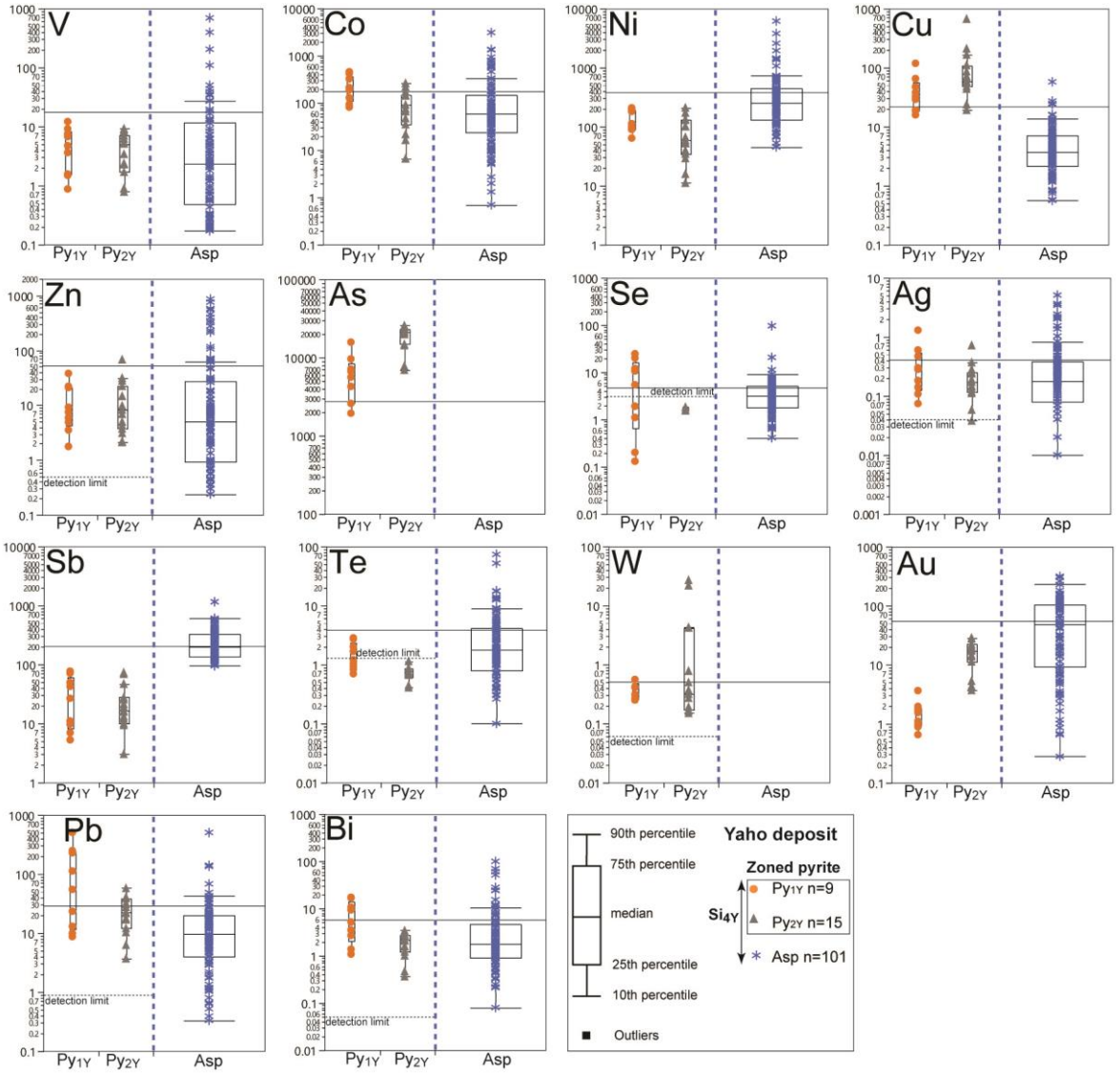

Figure 4.19 Statistical representation of the LA-ICP-MS data from different types of pyrite from the Yaho deposit. Detection limits are shown when they are close to the concentrations measured in the pyrite. Data on the Yaho arsenopyrite are from Sinaré (2013).

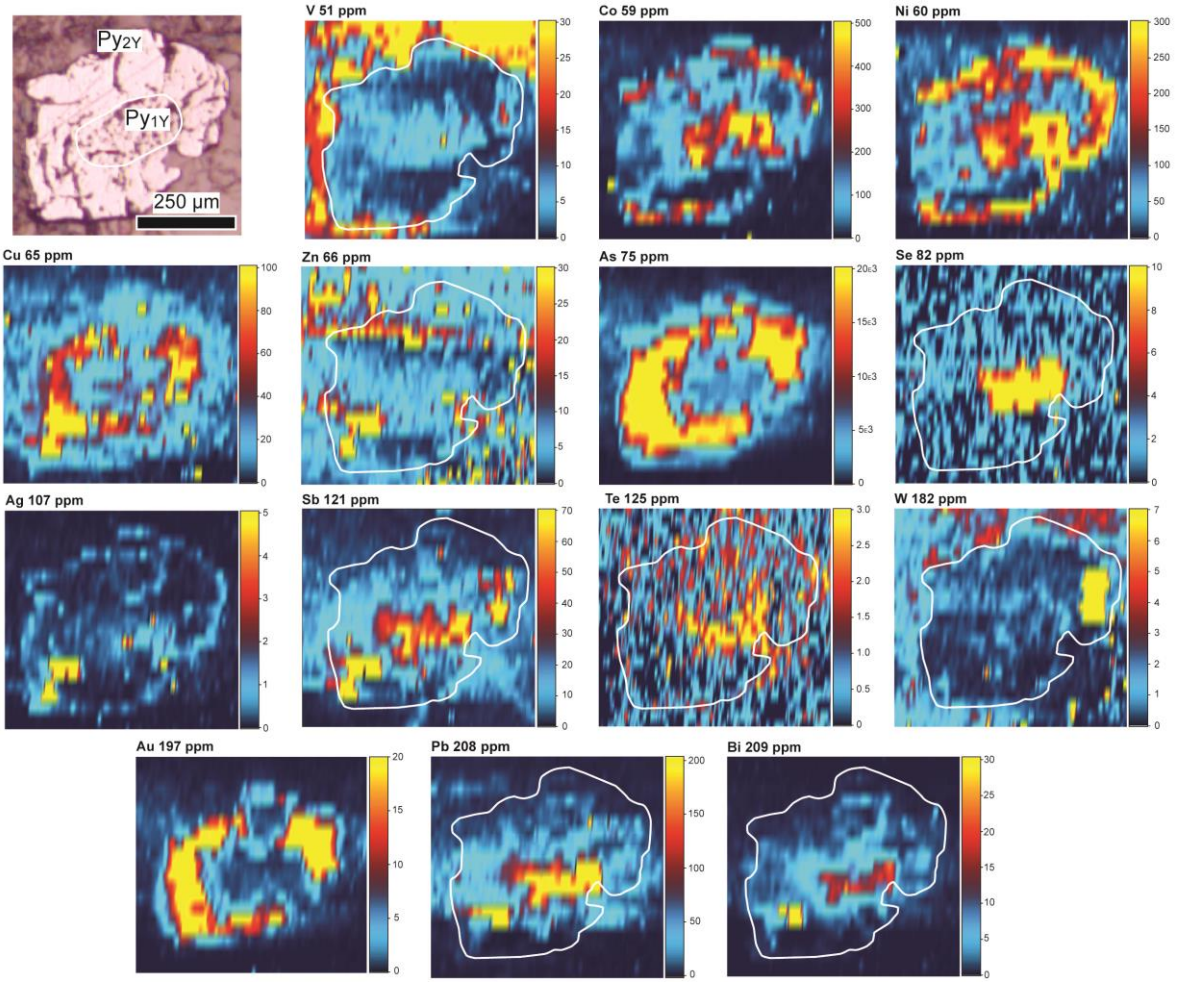

Figure 4.20 LA-ICP-MS elemental maps of pyrite grain from the Yaho deposit in the main silicified zone (Si_{4Y}). Anhedral porous Py_{1Y} is overgrowth by sub-euhedral Py_{2Y}. The core of Py_{1Y} is enriched in Co, Ni, Se, Sb, Pb and Bi. Py_{2Y} is characterized by Au-As-rich rims. The thin outermost rim on Py_{3WK} consists of Co and Ni. The white line delimits the grain boundary.

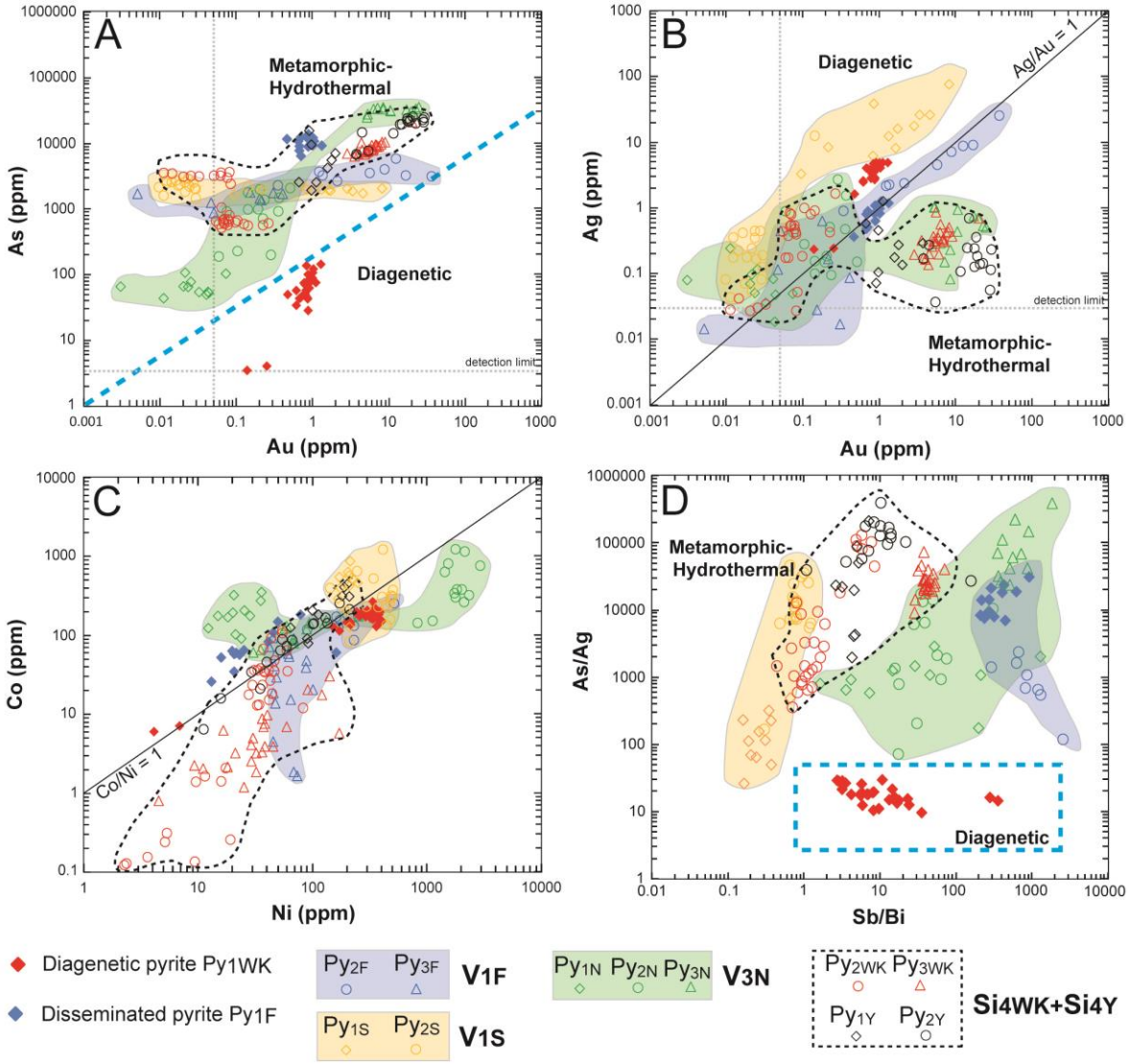

Figure 4.21 Discrimination binary diagrams of the different pyrite types from the Mana gold deposits. (a) Au vs. As. (b) Au vs. Ag. (c) Co vs. Ni. (d) As/Ag vs. Sb/Bi. These diagrams show that the pyrite compositions from V_{1F}, V_{1N} and Si_{4WK}-Si_{4Y} plot in the same area whereas the other pyrite generations (diagenetic Py_{1WK} and V_{1S}) plot in another area of the diagrams.

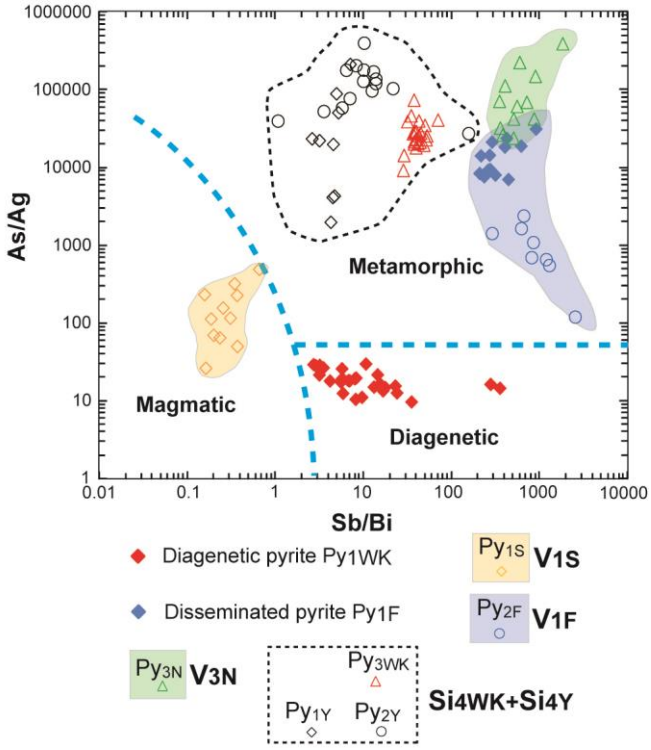

Figure 4.22 Discrimination binary diagram of As/Ag vs. Sb/Bi for gold-bearing pyrites (> 0.8 ppm Au) from the Mana gold deposits. This diagram provides a coherent grouping of the various pyrites and it is proposed as tool for distinguishing among the pyrite types.

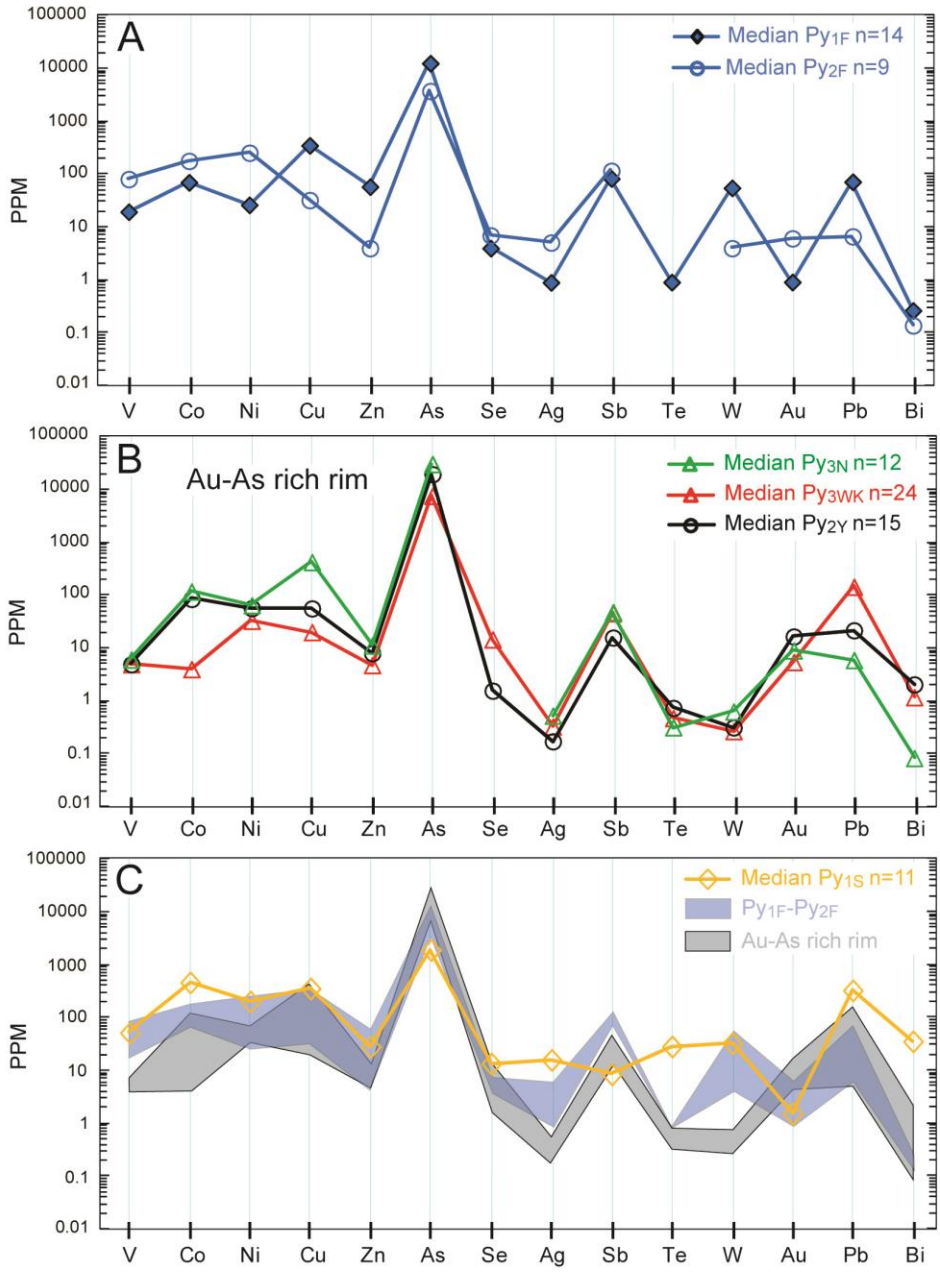

Figure 4.23 Multi-element diagrams of gold-bearing pyrites (> 0.8 ppm Au) from the Mana gold deposits showing median values of the LA-ICP-MS analyses for specific pyrite types. (a) Disseminated Py_{1F} and porous core Py_{2F} from the Fofina deposit showing similar trace element concentrations. (b) Similar patterns between Au-As rich rims of late zoned pyrites from the Nyafé, Wona-Kona and Yaho deposits. (c) Differences in trace elements between Py_{1S} (Siou), considered to have formed from magmatic fluids, and the hydrothermal pyrite types from the other deposits.

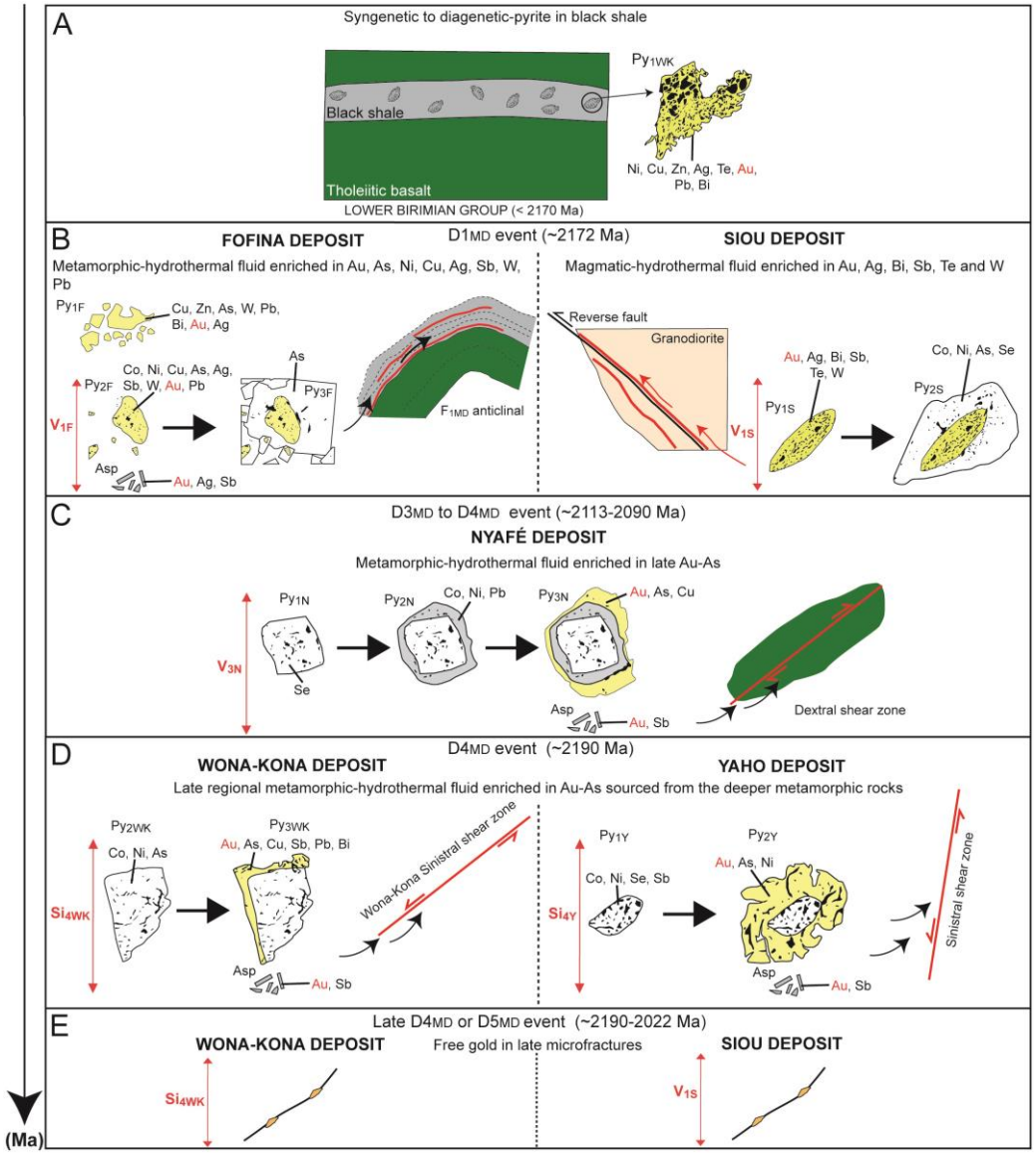

Figure 4.24 Synthesis of the trace element compositions of pyrite and arsenopyrite in association with the hydrothermal system evolution and deformation events. (a) Syngenetic accumulation of Au and As in pyrite developed in organic-rich black shale. Gold was scavenged by the diagenetic framboidal pyrite (Py_{1WK}). (b) During the first deformation event ($D1_{MD}$), metamorphic-hydrothermal fluids in the Fofina deposit and magmatic-hydrothermal fluid in the Siou deposit formed the primary hydrothermal pyrites. (c-d) The third and fourth deformation events ($D3_{MD}$ and $D4_{MD}$) are related to the same metamorphic-hydrothermal system, and fluids were channeled by active shear zones in the Nyafé, Wona-Kona and Yaho deposits. (e) The late stage is associated with free gold infilling late microfractures in the Wona-Kona and Siou deposits during the $D4_{MD}$ or $D5_{MD}$ event.

TABLEAUX CHAPITRE 4

Table 4.1 Geological characteristics of gold deposits from the Mana district.

Gold deposits	Size	Host rock	Metamorphic facies	Structural context	Mineralization style	Major sulfide phases	Alteration assemblage (In decreasing abundance)
Fofina	0.42 Moz at 3.6 g/t	Volcanoclastic rocks, black shale, tholeiitic basalt. Felsic QFP dykes	Greenschist	$D1_{MD}$ anticlinal fold	Stratiform disseminated $D1_{MD}$ quartz-carbonate vein	Pyrite Arsenopyrite	Weak silicification Iron carbonates
				Second-order $D3_{MD}$ dextral shear zone	$D3_{MD}$ quartz veinlets	Pyrite and minor arsenopyrite	Chlorite Muscovite
Nyafé	0.37 Moz at 6.0 g/t	Tholeiitic basalts. Felsic QFP dykes	Greenschist	Second-order $D3_{MD}$ dextral shear zone	$D3_{MD}$ stockworks and quartz veins	Pyrite Arsenopyrite Chalcopyrite	Chlorite Muscovite Epidote Iron carbonates
Siou	1.0 Moz at 6.0 g/t	Granodiorite, tholeiitic basalt. Tarkwaian-type sedimentary rocks	Greenschist	$D1_{MD}$ thrust fault	$D1_{MD}$ quartz vein	Pyrite and minor arsenopyrite	Muscovite Chlorite Iron carbonates
				Regional $D4_{MD}$ sinistral shear zone (Boni Fault)	$D4_{MD}$ to $D5_{MD}$ late free gold	Galena	Muscovite
Wona-Kona	4.0 Moz at 2.3 g/t	Granodiorite, tholeiitic basalt, volcanoclastic rocks, black shale. Felsic QFP dykes	Greenschist	Regional $D4_{MD}$ sinistral shear zone (Wona-Kona Fault)	$D4_{MD}$ silicification, quartz-sulfide veins and late $D4_{MD}$ or $D5_{MD}$ free gold	Pyrite Arsenopyrite Chacopyrite Sphalerite	Silicification Muscovite Iron carbonates Chlorite Epidote
Yaho	1.0 Moz at 1.0 g/t	Tarkwaian-type sedimentary rocks. Felsic QFP dyke	Greenschist	$D3_{MD}$ anticlinal fold	$D3_{MD}$ quartz-carbonate veins	Minor pyrite	Muscovite
				$D4_{MD}$ sinistral shear zone	$D4_{MD}$ silicification	Pyrite Arsenopyrite	Muscovite Iron carbonates Silicification

Table 4.2 Sample selection methodology used for the LA-ICP-MS analyses.

Deposit	**Fofina**		**Siou**	**Nyafé**	**Wona-Kona**	**Yaho**
Ore deposit	**Stratiform n=1**	**V_{1F} n=3**	**V_{1S} n=6**	**V_{3N} n=5**	**Si_{4WK} n=4**	**Si_{4Y} n=5**
Sulfide mineralogy	py	py+asp	py	py+cpy+asp	py+asp+cp+sph	py+asp+sph
Lithologies	Sample from the black shale beds in the Lower Birimian group	Sampled from tholeiitic basalt and black shale in the Lower Birimian group	Sampled from the Siou granodiorite	Sampled from the tholeiitic basalt in the Lower Birimian group	Sampled from the volcano-sedimentary rocks, tholeiitic basalt and black shale in the Lower Birimian group	Sampled from polygenic conglomerate in the Tarkwaian-type group

py = pyrite, asp = arsenopyrite; cpy = chalcopyrite; sph = sphalerite

Table 4.3 Trace element concentrations (ppm) for each pyrite type from the Mana gold deposits.

Deposit	Pyrite type		V	Mn	Co	Ni	Cu	Zn	As	Se	Mo	Ag	Sn	Sb	Te	W	Au	Pb	Bi
	Average detection limit		0.104	1.92	0.031	0.111	0.423	0.565	3.629	3.014	0.09	0.036	0.215	0.229	1.302	0.063	0.057	0.091	0.051
Fofina	Py_{1F} n=14	Median	17.8	48.4	63.4	23.95	312.5	52.5	10870	3.69	0.2485	0.84	0.55	74.7	bdl	49.95	0.8545	64.95	0.25
		sd	10.2	108.1	52.6	39.7	296.2	1124.1	2219.5	0.8	0.2	0.3	1.8	18.6	bdl	18.2	0.2	33.3	0.1
		Max	37.1	360.2	187.4	160.3	1250	3700	13880	5.3	0.9	1.3	7.1	125.4	bdl	96.6	1.3	122.3	0.42
		Min	5.8	19.4	26.5	13.4	149.1	3.0	6460	bdl	0.1	0.4	0.3	57.1	bdl	19.4	0.5	21.3	0.1
	Py_{2F} n=9	Median	73.1	18.3	160.4	228.3	29.5	3.7	3280	6.4	bdl	4.7	0.9	104.3	bdl	3.7	5.6	6.13	0.131
		sd	129.9	12.6	50.6	123.5	17.1	4.2	1061	4.2	bdl	7.9	0.8	66.9	bdl	2.2	11.5	4.9	0.06
		Max	440	49.1	260	510	70.1	15.1	5960	12.2	bdl	26.4	1.5	258	bdl	5.8	36.3	15.8	0.3
		Min	31.6	9.7	89	89	12.3	1.9	2220	3.9	bdl	0.9	0.4	38.8	bdl	0.1	0.3	1.2	0.06
	Py_{3F} n=17	Median	0.4	2.3	40	61.5	1.8	1.5	1440	bdl	bdl	0.036	0.3	0.6	bdl	0.1	0.2	0.9	0.05
		sd	1.3	2.2	29.8	17.8	4.4	2.0	284.7	bdl	bdl	2.6	0.2	1.4	bdl	0.1	0.1	1.1	0.01
		Max	5.9	8.0	95.2	100.1	15.6	9.2	1800	bdl	bdl	11.6	0.6	4.4	bdl	0.5	0.4	3.6	0.06
		Min	0.2	bdl	1.7	41.7	1.2	1.1	870	bdl	bdl	bdl	0.3	0.3	bdl	0.06	bdl	0.41	bdl
Nyafé	Py_{1N} n=11	Median	3.2	434.3	180.1	21.1	15.8	1.4	65.3	132.6	bdl	0.07	bdl	1.0	1.4	bdl	bdl	5.5	0.07
		sd	2.1	11.9	87.4	7.5	3.2	1.2	21.2	20.8	bdl	0.06	bdl	9.1	0.6	bdl	bdl	2.6	0.06
		Max	8.2	452.7	360.4	35.6	23.2	5.3	108.5	146.1	bdl	0.3	bdl	23.4	2.4	bdl	bdl	9.7	0.2
		Min	0.4	407.3	93.4	12.2	10.6	0.6	43.9	92.7	bdl	bdl	bdl	0.3	bdl	bdl	bdl	1.6	bdl
	Py_{2N} n=13	Median	1.9	438.3	390.2	1760	250.9	2.9	990.2	48.4	bdl	0.3	bdl	15.1	bdl	0.2	0.2	4.4	0.4
		sd	5.4	17.9	369.1	527.8	3408	37.8	655.9	13.2	bdl	0.8	bdl	13.6	bdl	2.1	0.1	1.8	0.3
		Max	20.4	445.6	1260	2890	11200	140.4	2100	71.8	bdl	2.8	bdl	55.8	bdl	6.9	0.6	6.9	1.3
		Min	0.5	392.1	147.3	820.1	24.5	1.26	190.3	29.4	bdl	0.1	bdl	8.1	bdl	bdl	0.06	2.1	0.2
	Py_{3N} n=12	Median	6.2	431.4	123.5	67.7	450.4	11.6	33050	bdl	bdl	0.5	bdl	50.1	bdl	0.6	9.3	6.1	0.083
		sd	13.7	31.9	38.8	59.4	331.4	28.8	3154	bdl	bdl	0.3	bdl	18.7	bdl	0.9	6.8	2.1	0.055
		Max	45.1	530	179.4	250.4	1370	107.5	35900	bdl	bdl	1.1	bdl	72.3	bdl	3.1	24.4	9.9	0.191
		Min	1.1	412	62.3	30.2	245.1	2.81	25100	bdl	bdl	0.09	bdl	16.4	bdl	bdl	5.1	2.9	bdl
Siou	Py_{1S} n=11	Median	54	369.1	480.3	209.7	370.1	29.4	1970	14.1	0.124	16.6	0.48	8.8	29.6	34.2	1.6	340.7	37.1
		sd	22.2	7.4	216.5	24.6	361.5	86.3	129.7	1.2	0.21	21.6	0.24	1.7	14.8	11.8	2.3	215.9	11.8
		Max	102.2	374	910.6	247	1300	270	2070	16.4	0.71	79.2	0.89	12.1	69.3	54.8	8.5	750.3	56.6
		Min	35.6	349	130.4	166	53.3	17.4	1670	11.9	bdl	3.4	0.22	6.5	9.5	17.4	0.093	38.4	13.5
	Py_{2S} n=18	Median	3.4	358.5	286.4	423.3	12.1	2.1	2340	20.1	bdl	0.2	bdl	0.5	3.1	2.6	bdl	4.1	0.6
		sd	6.7	18.7	271.3	110.9	44.2	6.1	414.7	6.1	bdl	3.1	bdl	1.7	3.9	12.4	bdl	10.4	5.5
		Max	31.1	415.2	1270	501.6	200.1	28.3	2930	34.2	bdl	13.1	bdl	7.1	17.5	52.1	0.1	47.2	23.9
		Min	1.3	332.3	84.1	141	10.1	1.3	1470	12.7	bdl	0.05	bdl	bdl	1.3	0.8	bdl	1.8	0.2

Deposit	Pyrite type		V	Mn	Co	Ni	Cu	Zn	As	Se	Mo	Ag	Sn	Sb	Te	W	Au	Pb	Bi
Wona-Kona	Py_{1WK} n=29	Median	159.1	3980	174.5	304.3	97.2	37.1	70.1	10.5	0.33	3.8	0.7	50.5	13.7	5.6	0.8	347.1	6.8
		sd	87.1	1872	53.7	101.2	36.4	12.5	33.4	4.7	13.7	1.2	0.4	17.4	7.8	37.5	0.2	86.5	3.2
		Max	410.1	9840	269.4	403.3	165.6	67.3	143.3	19.9	71.1	5.3	1.8	92.2	29.5	180.4	1.3	445.2	13.5
		Min	16.3	1570	6.1	4.1	14.7	16.4	3.4	bdl	bdl	0.23	0.5	28.1	2.9	0.9	0.14	51.3	0.1
	Py_{2WK} n=34	Median	7.3	35.6	21.3	34.3	2.2	2.3	705.5	5.1	bdl	0.3	bdl	0.9	3.1	0.6	0.07	3.3	0.9
		sd	28.9	181.9	31.3	19.2	1.1	1.5	1233	6.3	bdl	0.4	bdl	1.4	2.7	0.9	0.05	4.5	1.4
		Max	160.3	424.3	118.6	82.4	4.6	7.6	3670	19.3	0.1	1.7	bdl	5.6	9.3	4.3	0.3	15.9	4.5
		Min	0.38	7.4	0.126	2.2	0.9	1.1	517.3	bdl	bdl	0.03	bdl	bdl	bdl	0.06	bdl	0.6	bdl
	Py_{3WK} n=24	Median	5.1	390.5	4.1	34.1	20.8	4.9	8200	15.1	0.2	0.3	0.3	47.6	bdl	0.3	5.6	152	1.2
		sd	7.7	13.4	7.1	41.9	11.6	223.1	1272	4.1	0.4	0.2	3.4	13.9	bdl	0.7	1.6	50.6	0.5
		Max	30.3	415.6	31.3	170.5	55.4	1100	21200	26.8	1.5	0.9	15.6	79.4	bdl	3.5	20.3	264.6	2.2
		Min	1.5	366.3	0.82	4.5	15.8	2.3	6400	10.6	0.12	0.1	bdl	22.9	bdl	0.07	2.8	64.4	0.5
Yaho	Py_{1Y} n=9	Median	4.7	3.6	211.1	112.4	32.4	7.5	5600	5.4	bdl	0.3	0.6	26.7	bdl	0.3	1.1	55.1	5.1
		sd	3.8	4.6	138.3	56.2	32.3	11.9	4350	9.1	bdl	0.4	1.0	27.9	bdl	0.1	0.9	168.9	6.3
		Max	12.1	13.4	455	208	118	38	15700	24.6	bdl	1.3	3.5	77.1	bdl	0.6	3.6	510.3	17.3
		Min	0.9	bdl	81,0	63.7	15.8	1.8	1935	bdl	bdl	0.07	bdl	5.3	bdl	0.3	0.6	8.7	1.1
	Py_{2Y} n=15	Median	5.1	2.9	89.3	59.6	59.1	8.3	21200	bdl	0.02	0.2	0.6	16.4	bdl	0.3	17.2	22.6	2.1
		sd	2.9	14.1	76.3	58.8	161.5	17.5	5822	bdl	0.051	0.1	0.7	21.8	bdl	8.4	8.1	14.9	0.9
		Max	9.2	57.4	261.6	209.4	670.4	68.6	25700	bdl	0.2	0.7	3.4	73.6	bdl	27.8	28.6	57.6	3.4
		Min	0.78	bdl	6.6	11.1	19.1	2.1	6900	bdl	bdl	0.04	0.3	3.2	bdl	0.1	3.7	3.7	0.4

n = number of analysis; sd = standard deviation; bdl = below detection limit; min = minimum value; max = maximum value.

CHAPITRE 5

5. DISCUSSION

5.1. INTRODUCTION

Ce projet avait pour objectif de déterminer les signatures géochimiques qui traduisent l'évolution d'un système hydrothermal, afin d'élaborer un modèle métallogénique et structural dans le but de proposer des guider d'exploration à l'échelle régionale. Afin d'atteindre ce but, 5 objectifs avaient été définis :

- ➢ Identifier la nature des roches encaissantes susceptibles d'être la source de l'or.
- ➢ Caractériser la chronologie relative des épisodes de déformation en lien avec les minéralisations.
- ➢ Déterminer la source des fluides hydrothermaux à travers l'étude des minéralisations.
- ➢ Déterminer le rôle génétique des granitoïdes afin d'expliquer leur rôle spatio-temporel avec les minéralisations.
- ➢ Formuler des guides d'exploration applicables aux gisements aurifères orogéniques.

Les résultats de cette étude répondent aux objectifs fixés dans le cadre de ce projet. Une synthèse des éléments pertinents est présentée ci-dessous en lien avec les différentes thématiques.

5.2. LITHOSTRATIGRAPHIE ET SOURCE DE L'OR

L'origine de la source de l'or est un problème récurrent dans les gisements aurifères orogéniques plus particulièrement dans les ceintures de roches vertes birimiennes d'Afrique de l'Ouest où peu d'études ont été réalisées sur cette problématique. Le district de Mana a permis de répondre à cette problématique par l'étude du log lithostratigraphique couplé aux données de géophysiques, de géochronologies et à des analyses lithogéochimiques. Ainsi trois principaux groupes stratigraphiques, marquant l'évolution géodynamique de la ceinture de Houndé, ont été identifiés:

- ➢ Le Birimien inférieur (< 2172 Ma) composé à sa base de roches basaltiques en alternance avec des roches volcano-sédimentaires recoupées par des dykes felsiques porphyriques (QFP) et d'une séquence calco-alcaline andésitique dans sa partie sommitale.
- ➢ Le Birimien supérieur (~2172-2113 Ma) en lien avec un bassin sédimentaire en discordance sur le Birimien inférieur dans la partie centrale du district (bassin de Mana).
- ➢ Le groupe du type Tarkwaïen (~2113 Ma) composé de roches sédimentaires détritiques en discordance sur les deux groupes précédents, mais développé essentiellement le long des failles sur les bordures du district.

Notre étude s'est plus particulièrement centrée sur le Birimien inférieur qui apparaissait comme le réservoir aurifère majeur du district de Mana. Les études lithogéochimiques sur les basaltes ont permis de démontrer leur affinité tholéiitique, mais surtout de documenter

leur formation en tant que plateau océanique en lien avec une plume mantéllique. Cette interprétation avait déjà été proposée pour d'autres ceintures de roches vertes en Afrique de l'Ouest (Abouchami et al., 1990; Boher et al., 1992). Elle avait également été suggérée pour la ceinture de Houndé par Baratoux et al. (2011). Hormis une implication directe sur la géodynamique du district, ce type de basalte est communément enrichie en or (Bierlein and Pisarevsky 2008; Weber et al., 2013). Ces basaltes peuvent donc constituer une source aurifère lors de la dévolatisation métamorphique. Les travaux de gravimétrie de Baratoux et al. (2011) estiment une épaisseur de plus de 8 km dans la ceinture de roches vertes de Houndé, ce qui pourrait ainsi représenter le plus vaste réservoir de métaux à l'échelle du district.

La séquence basaltique est interlitée par des niveaux de roches volcano-sédimentaires incluant des niveaux de shales noirs riches en pyrites diagénétiques. Bien que l'épaisseur des shales noirs soit indéterminée, les études au LA-ICP-MS ont révélées que ces pyrites à texture framboïdale (Py_{1WK}) étaient enrichies en une suite d'éléments traces (Co, Ni, Cu, Zn, Sb, Pb, Ag) et également en or (médiane de 0,6 ppm). Les shales sont reconnus comme étant une source d'or majeure du district de Mana (Gaboury, 2013), en accord avec les travaux de Large et al. (2009) et Thomas et al. (2011).

La séquence sommitale calco-alcaline andésitique ne semble pas être fertile car aucune minéralisation n'a pour le moment été observée. Les groupes du Birimien supérieur et du type Tarkwaïen sont essentiellement composés de roches sédimentaires détritiques jeunes et faiblement enfouies par rapport au Birimien inférieur. En conséquence, elles ne sont pas

considérées ici comme des roches sources potentielles pour libérer l'or lors du métamorphisme.

5.3. ÉVOLUTION STRUCTURALE EN LIEN AVEC LES MINÉRALISATIONS

Les travaux de cartographie à l'échelle régionale et locale en lien avec la description des forages ont permis d'identifier une histoire structurale polyphasée définie par 5 déformations et 4 épisodes de minéralisation.

La première phase de déformation $D1_{MD}$ est un raccourcissement régional de direction E-W associé à l'épisode Éoéburnéen et daté à ~2172 Ma par la granodiorite de Wona-Kona. Cette première déformation développe une série de plis F_{1MD} à axe subhorizontal à plongement N et des failles inverses de direction N-S dans le groupe du Birimien inférieur. La mise en place des granodiorites de bordures de Wona-Kona et Siou est interprétée comme étant pré- à syn-tectonique de cette déformation. Cet épisode provoque un métamorphisme prograde et permet le développement du premier pulse aurifère documenté dans les gisements de Fofina et de Siou, correspondant à des sulfures disséminés et des veines de quartz (V_{1S}) et quartz-carbonates (V_{1F}). Cet épisode minéralisateur précoce est l'événement le plus ancien documenté au Burkina Faso et pourrait être l'équivalent temporel de la minéralisation du gisement d'or de Wassa au Ghana (2164 ± 24 Ma - Le Mignot et al., 2017).

La deuxième phase de déformation $D2_{MD}$ est documentée dans le bassin de Mana durant une période d'extension de direction E-W permettant le dépôt des roches sédimentaires du Birimien supérieur. Cette sédimentation est contrôlée par l'activation des failles de 2ème ordre de Mana (MSZ) et de Maoula (MLSZ). Bien qu'aucune datation n'ait été réalisée, nous proposons un âge de dépôt entre 2172 et 2113 Ma selon le cadre chronologique régional. Ainsi, la fin de l'épisode $D2_{MD}$ est en lien avec la sédimentation des roches détritiques de type Tarkwaïen sur les bordures est et ouest du district. Cette sédimentation clastique est contrôlée par les failles de Boni (BSZ) et de Wona-Kona (WKSZ) et datée à 2113 Ma par Bossière et al. (1996). Aucune minéralisation n'a été documentée dans le Birimien supérieur.

Le début de l'épisode Éburnéen (2113-2090 Ma) est marqué par une phase de déformation $D3_{MD}$ en transpression de direction E-W à WNW-ESE qui affecte l'ensemble des groupes stratigraphiques du Birimien et du type Tarkwaïen. Dans le Birimien inférieur, la déformation $D3_{MD}$ réactive les plis F_{1MD} pour former des plis F_{3MD} à axe vertical de plan axial à la mise en place de failles en cisaillement dextre de direction NE-SW. Ces failles sont documentées dans les gisements de Fofina et Nyafé. Elles encaissent le deuxième pulse aurifère du district correspondant à des veines de quartz (V_{3F}) dans le gisement de Fofina et de stockwerks à sulfures (V_{3N}) dans le gisement de Nyafé. Dans la bordure ouest du district, la réactivation de la faille de 1er ordre de Wona-Kona est documentée avec possiblement le début d'un apport aurifère. Dans le Birimien supérieur et le type Tarkwaïen, des plis isoclinaux kilométriques F_{3MD} de direction N-S à NNE-SSW à axe

horizontal sont observés. Dans le gisement de Yaho, des veines de quartz (V_{3Y}) en lien avec des sulfures disséminés constituent une première minéralisation aurifère à faible teneur.

La quatrième phase de déformation $D4_{MD}$ durant un régime transpressif NNW-SSE induit la réactivation en cisaillement sénestre des failles majeures de bordures ainsi que celles du bassin de Mana en lien avec le développement de plis F_{4MD} à axe vertical dans le Birimien supérieur. Cette phase est datée à 2090 Ma par l'intermédiaire du pluton dioritique de Kokoï. La bordure ouest du district enregistre le troisième pulse aurifère défini par une silicification massive à sulfures (pyrite et arsénopyrite). Elle est enregistrée dans les gisements de Wona-Kona (Si_{4WK}) et Yaho (Si_{4Y}). Le gisement de Nyafé enregistre également une réactivation tardive en cisaillement senestre. Cet épisode aurifère est reconnu à l'échelle du craton ouest africain dans de nombreux gisements d'or orogéniques (Baratoux et al., 2001, 2015; Perrouty et al., 2012; Le Mignot et al., 2017).

La cinquième et dernière phase de déformation $D5_{MD}$ a un caractère cassant défini par des clivages de crénulation N080, des failles inverses et des fractures sous un régime compressif N-S qui affecte l'ensemble du district de Mana. Dans le gisement de Wona-Kona, les schistes à muscovite datés à 2022 Ma sont affectés par des clivages de crénulation qui pourraient représenter l'âge de la déformation $D5_{MD}$. Le dernier pulse aurifère est associé à de l'or libre que l'on retrouve dans les corps minéralisés des gisements de Wona-Kona et Siou en association avec de la muscovite. Cet épisode pourrait être en lien avec la fin de la déformation $D4_{MD}$ ou $D5_{MD}$.

5.4. DÉTERMINER LA SOURCE DES FLUIDES HYDROTHERMAUX

L'identification de la source des fluides hydrothermaux du district de Mana a été réalisée sur les 5 gisements à travers l'étude des minéralisations et plus particulièrement par l'étude texturale des pyrites et des arsénopyrites et de leur chimie. Les études au LA-ICP-MS ont permis d'identifier la distribution spatiale des éléments traces et de définir des cortèges métalliques spécifiques afin de déchiffrer l'évolution hydrothermale du district de Mana. Notre étude démontre la présence de plusieurs pulses aurifères définis par de 2 systèmes hydrothermaux en lien avec 2 sources aurifères distinctes (Fig. 5.1).

Durant la phase de déformation $D1_{MD}$, la dévolatilisation métamorphique des unités volcano-sédimentaires (shales noirs riches en pyrites diagénétiques) du Birimien inférieur a permis la génération des premiers fluides métamorphiques enrichis en Au et As (Fig. 5.1). Les pyrites résultantes constituent une partie de la minéralisation au gisement de Fofina. Cet épisode s'accompagne de la précipitation de pyrites disséminées (Py_{1F}) et de pyrites zonées (Py_{2F} et Py_{3F}) en lien avec des arsénopyrites dans les veines de quartz-carbonates (V_{1F}). Ces pyrites sont caractérisées par la présence d'un large spectre d'éléments (As, Au, Ni, Cu, Ag, Sb, W et Pb). Durant la déformation $D1_{MD}$, des fluides magmatiques enrichis en Au, Ag, Bi, W et Te ont été produits et sont à l'origine d'une partie de la minéralisation au gisement Siou (Fig. 5.1). Ces fluides ont été canalisés le long des failles inverses encaissées dans la granodiorite pré- à syn-cinématique de Siou. Cette signature métallique a déjà été documentée en Afrique de l'Ouest dans le gisement de Morila (Mali) et est interprétée par McFarlane et al. (2011) comme d'affiliation magmatique.

Durant les déformations $D3_{MD}$ et $D4_{MD,}$ la plus grande contribution d'or économique à l'échelle du district est introduite par des fluides hydrothermaux métamorphiques enrichis en Au et As (Fig. 5.1). Ceux-ci ont été canalisés par les failles actives en cisaillement de 1er et 2ème ordre. Ces enrichissements se traduisent par la précipitation de pyrites zonées ayant des couronnes tardives à Au-As dans les gisements de Nyafé, Wona-Kona et Yaho (Fig. 5.1). L'association Au-As est reconnue dans de nombreux gisements d'or orogéniques (Large et al., 2009; Thomas et al., 2011) et est interprétée comme provenant du lessivage des pyrites primaires diagénétiques et des basaltes tholéiitiques sous-jacents aux gisements. Dans le cas présent, il s'agit du Birimien inférieur.

Le dernier pulse aurifère est défini par de l'or libre dans les gisements de Wona-Kona et Yaho lors de la fin de la déformation $D4_{MD}$ ou durant $D5_{MD}$ (Fig. 5.1). Cependant son origine reste indéterminée, car aucun sulfure n'est associé à cette minéralisation. Cette introduction d'or pourrait être liée simplement à des processus de remobilisation de l'or existant, ou à un nouvel apport externe d'or provenant d'une autre source hydrothermale.

5.5. DÉTERMINER LE RÔLE DES GRANITOÏDES

L'étude pétrographique, géochronologique et structurale des granitoïdes de Mana a permis d'identifier deux pulses magmatiques durant l'orogénèse Éburnéenne.

Le premier pulse magmatique se déroule pendant la phase Éoéburnéenne avec la mise en place des plutons granodioritiques de Wona-Kona et Siou datés respectivement à 2176 Ma et 2172 Ma. La découverte d'une contribution en fluides magmatiques dans le gisement de Siou indique que le pluton de Siou est probablement la source de ces fluides pendant la déformation $D1_{MD}$ (Fig. 5.1). Dans la partie ouest du district, les fluides magmatiques n'ont pas été documentés mais la mise en place du pluton de Wona-Kona a probablement contribué à l'activation d'un système hydrothermal précoce le long de la faille de 1er ordre de Wona-Kona. Outre l'aspect hydrothermal, ces plutons ont joué un rôle clé dans l'architecture du district. Puisent-ils contrôlent en partie la localisation des failles majeures de bordures, ils ont donc induit des contrastes rhéologiques permettant la canalisation des fluides hydrothermaux en lien avec les épisodes de déformation. C'est dans ces failles majeures que sont localisés les plus gros gisements orogéniques du district (Siou, Wona-Kona et Yaho).

Le deuxième pulse magmatique est documenté durant la phase Éburnéen, dans la partie est du district, avec la mise en place du pluton dioritique de Kokoï daté à ~2090 Ma. Ce pluton est syn-tectonique à la déformation $D4_{MD}$ qui est reconnu comme étant le principal événement aurifère économique du district. Son impact sur les minéralisations aurifères est pour le moment inconnu, mais il contrôle la mise en place de failles NNW en cisaillement senestre qui elles, sont reconnues comme hôtes de minéralisation aurifère dans le district de Yaramoko (Hein, 2016).

5.6. IMPLICATIONS POUR L'EXPLORATION

Les implications pour l'exploration qui résultent de cette thèse sont multiples. D'un point de vue des lithologies, nous avons mis en lumière la présence de basalte tholéiitique de type plateau océanique pouvant avoir un impact important sur le stock aurifère de la ceinture de roches vertes de Houndé. Pour identifier ces roches potentiellement fertiles en or, deux diagrammes géochimiques basés sur les éléments Zr, Y, Nb, Th ont été développés. Il est ainsi proposé qu'à un stade précoce de l'exploration, la reconnaissance de roches basaltiques de plateau soit considérée comme un critère de sélection pour le potentiel en gisements aurifères orogéniques à l'échelle des ceintures.

Les déformations polyphasées du district de Mana indiquent également que les phases de déformation $D1_{MD}$ et $D4_{MD}$ contribuent principalement à la mise en place des minéralisations aurifères. Il est donc conseillé de focaliser l'exploration dans le groupe du Birimien inférieur ainsi que le long des failles de bordures qui ont constitué des canalisations importantes pour les fluides hydrothermaux. De plus, ces mêmes failles ont également enregistré l'événement tardif à d'or libre à la fin de la $D4_{MD}$ voir de la $D5_{MD}$.

La signature géochimique des pyrites a permis de définir la présence de fluides syn-diagénétiques, de fluides métamorphiques et magmatiques. Ces fluides ont contribué à l'enrichissement aurifère du district de Mana à différentes périodes. Un diagramme de discrimination binaire As/Ag vs Sb/Bi a été développé pour identifier les types de pyrite. Pour l'exploration, cette possibilité d'identifier rapidement les pyrites a au moins deux

implications : 1) déceler des enrichissements aurifères dans les pyrites primaires – celles-ci pourraient constituer une source importante d'or lors du métamorphisme en profondeur; et 2) déceler différentes générations de pyrites de sources différentes – indiquant des venues multiples de fluides et d'or, ajoutant ainsi au potentiel économique des minéralisations (multi-stages).

5.7. RÉFÉRENCES

Abouchami, W., Boher, M., Michard, A., Albarède, F., 1990. A major 2.1 Ga event of mafic magmatism in Western Africa: An early stage of crustal accretion. Journal of Geophysical Research 95, 17605-17629.

Baratoux, L., Metelka, V., Naba, S., Jessell, M.W., Grégoire, M., Ganne, J., 2011. Juvenile Paleoproterozoic crust evolution during the Eburnean orogeny (~2.2-2.0 Ga), western Burkina Faso. Precambrian Research 191, 18-45.

Baratoux, L., Metelka, V., Naba, S., Ouiya, P., Siebenaller, L., Jessell, M.W., Naré, A., Salvi, S., Béziat, D., Franceschi, G., 2015. Tectonic evolution of the Gaoua region, Burkina Faso: Implications for mineralization. Journal of African Earth Sciences 112, 419-439.

Bierlein, F.P., Pisarevsky, S., 2008. Plume-related oceanic plateaus as a potential source of gold mineralization. Economic Geology 103, 425-430.

Boher, M., Abouchami, W., Michard, A., Albarède, F., Arndt, N., 1992. Crustal growth in West Africa at 2.1 Ga. Journal of Geophysical Research 97, 345-369.

Bossière, G., Bonkoungou, I., Peucat, J.J., Pupin, J.P., 1996. Origin and age of Paleoproterozoic conglomerates and sandstones of the Tarkwaian group in Burkina Faso, West Africa. Precambrian Research 80, 153-172.

Gaboury, D., 2013. Does gold in orogenic deposits come from pyrite in deeply buried carbon-rich sediments?: Insight from volatiles in fluid inclusions. Geology 42, 1207-1210.

Hein, K.A.A., 2016. The Bagassi gold deposits on the eastern margin of the Houndé greenstone belt, Burkina Faso. Ore Geology Reviews 78, 660-666.

Large, R.R., Danyushevsky, L., Hollit, C., Maslennikov, V., Meffre, S., Gilbert, S., Bull, S., Scott, R., Emsbo, P., Thomas, H., 2009. Gold and trace element zonation in pyrite using a laser imaging technique: Implications for the timing of gold in orogenic and Carlin-style sediment-hosted deposits. Economic Geology 104, 635-668.

Le Mignot, E., Reisberg, L., André-Mayer, A.-S., Bourassa, Y., Fontaine, A., Miller, J., 2017. Re-Os geochronological evidence for multiple Paleoproterozoic gold events at the scale of the West African craton. Economic Geology 112, 145-168.

McFarlane, C.R., Mavrogenes, J., Lentz, D., King, K., Allibone, A., Holcombe, R., 2011. Geology and intrusion-related affinity of the Morila gold mine, southeast Mali. Economic Geology 106, 727-750.

Thomas, H.V., Large, R.R., Bull, S.W., Maslennikov, V., Berry, R.F., Fraser, R., Froud, S., Moye, R., 2011. Pyrite and pyrrhotite textures and composition in sediments, laminated quartz veins, and reef at Bendigo gold mine, Australia: Insights for ore genesis. Economic Geology 106, 1-31.

Webber, A.P., Roberts, S., Taylor, R.N., Pitcairn, I.K., 2013. Golden plumes: Substantial golf enrichment of oceanic crust during ridge-plume interaction. Geology 41, 87-90.

FIGURE DU CHAPITRE 5

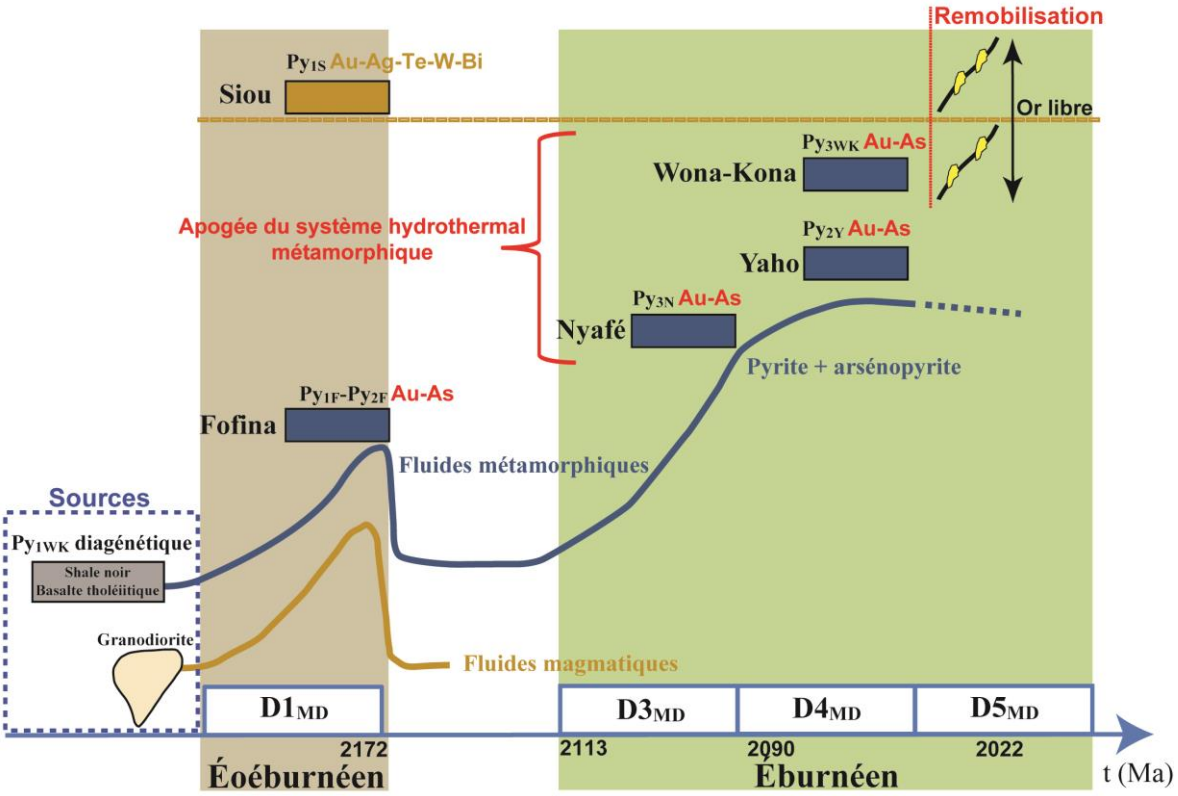

Figure 5.1 Synthèse de l'évolution hydrothermale du district de Mana.

CHAPITRE 6

6. CONCLUSIONS

Ce projet de doctorat est la première synthèse métallogénique et structurale d'un district aurifère dans la partie ouest du Burkina Faso. Ce projet avait pour objectifs de reconstituer l'histoire structurale et hydrothermale du district de Mana et de déterminer l'origine de la source de l'or qui a conduit à la formation des gisements aurifères orogéniques économiques. Cette approche académique a permis de développer des outils d'exploration directement applicables afin d'estimer rapidement la fertilité aurifère d'une ceinture de roches vertes à l'échelle régionale. Cette approche est possiblement applicable au reste de l'Afrique de l'Ouest.

Les principales contributions de ce projet sont sous la forme de 3 articles scientifiques, dont 2 publiés et 1 soumis. Les principaux résultats et implications sont présentés ci-dessous :

1) Trois groupes stratigraphiques ont été identifiés dans le district de Mana. À la base, le Birimien inférieur (< 2172 Ma) est composé de roches basaltiques tholéiitiques formées en contexte de plateau océanique, intercalées avec des roches volcano-sédimentaires contenant des niveaux de shales noirs enrichis de pyrites diagénétiques recoupées par des dykes felsiques porphyriques (QFP). La partie sommitale est définie par un complexe calco-alcalin andésitique qui vient sceller ce groupe. En discordance, le Birimien supérieur forme un bassin sédimentaire dans la partie centrale du district (Bassin de Mana). L'âge de sédimentation est interprété entre 2172 et 2113 Ma. Le dernier groupe, qui correspond à des dépôts clastiques de type Tarkwaïen (2113 Ma), forme des bassins sédimentaires linéaires en discordance, développés le long des failles majeures en bordure de la ceinture.

2) Le groupe du Birimien inférieur représente la principale source d'or lors de la dévolatilisation métamorphique à l'échelle du district. Les shales noirs par l'intermédiaire des pyrites diagénétiques aurifères sont interprétés comme la source d'or principale. Les basaltes tholéiitiques ont également le potentiel d'être pré-enrichis en or. Ceux-ci peuvent contribuer directement en or lors du métamorphisme ou en encore être lessivés durant l'activité hydrothermale précoce de fond océanique. Dans ce dernier cas, les pyrites diagénétiques dans les shales noirs devraient s'enrichir en or de cette activité de lessivages des basaltes. Les éléments Zr, Y, Nb, Th peuvent être utilisés en exploration pour identifier rapidement la présence de roches basaltiques de plateau, et donc identifier rapidement des séquences potentiellement source d'or.

3) L'histoire structurale polyphasée du district de Mana s'étend sur une période de près de 150 Ma et ne se limite pas à une simple phase durant l'orogénèse Éburnéenne. Au contraire, elle peut être subdivisée en deux phases, Éoéburnéenne et Éburnéenne. L'étude structurale a mis en évidence 5 évènements de déformation distincts et 4 épisodes de minéralisation aurifère.

4) Les phases Éoéburnéenne et Éburnéenne sont toutes deux associées à un magmatisme dans le district de Mana. Les granodiorites de bordures sont pré- à syn-tectoniques à la déformation $D1_{MD}$ (Éoéburnéen) alors que la diorite de Kokoï se met en place pendant la déformation $D4_{MD}$ (Éburnéen).

5) L'étude de la chimie des sulfures et plus particulièrement des pyrites a permis d'identifier 4 pulses hydrothermaux associés à 2 réservoirs de sources distinctes et à au moins 2 systèmes hydrothermaux (métamorphique et magmatique). Une suite d'éléments As, Ag, Sb et Bi peut être utilisée en exploration pour discriminer les pyrites diagénétiques, magmatiques et métamorphiques, afin d'estimer les sources d'or potentielles et de déceler si les minéralisations sont polyphasées. Dans ce dernier cas, elles devront être considérée comme plus intéressantes au stade d'exploration, car formées par de multiples pulses.

ANNEXES

ANNEXE 1 : GÉOCHIMIE ROCHE TOTALE DES BASALTES DU DISTRICT DE MANA

Sample	263992	268999	271995	271996	271997	271998	271999	272000	274992	263999	272992
Major elements (wt. %)											
SiO_2	49.3	47.8	47.6	47.9	47.6	48.1	49.6	49.7	49	49.5	52.6
Al_2O_3	13.65	15.6	14.05	13.9	12.95	14.95	12.8	13.65	14.25	14	13.9
Fe_2O_3	13.1	10.7	12.2	11.5	12.9	11.6	14.6	13.1	12.2	12.85	12.7
FeO	11.79	9.63	10.98	10.35	11.61	10.44	13.14	11.79	10.98	11.565	11.43
CaO	10.35	12.7	12.25	10.15	10.35	12.25	9.72	11.6	9.38	10.15	7.32
MgO	7.54	8	7.58	7.67	7.19	7.76	6.42	6.55	7.73	7.33	6.75
Na_2O	1.7	2.09	1.01	2.06	1.55	1.69	2.05	1.57	2.7	2.19	3.48
K_2O	0.03	0.03	0.08	0.08	0.06	0.08	0.06	0.04	0.12	0.04	0.03
TiO_2	1.12	0.77	1.04	0.93	1.06	0.93	1.32	1.19	0.98	1.08	1.13
MnO	0.2	0.17	0.19	0.19	0.21	0.18	0.23	0.22	0.2	0.2	0.17
LOI	3	2.95	2.88	2.47	1.6	2.29	2.38	2.7	2.88	2.64	2.68
Mg#	53.26	59.68	55.16	56.91	52.46	56.98	46.54	49.75	55.65	53.04	51.28
TOTAL	100	101	99	97	95.6	100	99.3	100.5	99.6	100	101
Trace elements (ppm)											
Ba	7.4	10	19	19.3	12.8	17.8	17	15.6	28.2	10.9	14.4
Rb	0.5	0.4	1.6	1.3	0.8	1.1	0.8	0.5	2.4	1	0.3
Sr	164.5	188.5	198	129	134	153.5	91.5	132.5	116.5	138.5	114
Cr	250	730	250	520	80	470	30	260	230	250	250
V	300	233	274	267	294	242	340	311	259	289	300
Cu	114	71	97	124	114	102	111	107	102	108	105
Co	50.7	46.4	50.9	47	46.9	46.1	50.4	48.6	49.1	51.6	52.1
Ni	128	140	140	119	71	132	55	90	151	148	121
Zn	105	66	82	82	90	74	111	95	93	102	103
Th	0.25	0.17	0.28	0.25	0.24	0.21	0.34	0.28	0.23	0.23	0.27
Nb	2.8	1.7	2.5	2.2	2.4	2.2	3.4	2.8	2.4	2.6	2.7
Zr	54	36	54	47	51	43	71	60	47	52	55
Hf	1.8	1.2	1.7	1.5	1.6	1.4	2.2	1.8	1.7	1.7	1.8
Y	21.4	13.7	18.6	17.2	18.9	15.9	24.2	20.1	18	20.6	20.4
La	3.4	2.1	3.2	2.9	3	2.6	4	3.3	2.9	3.3	3.6
Ce	8.9	5.4	8.2	7.3	7.8	6.8	10.4	8.7	7.1	8.4	9
Pr	1.34	0.89	1.29	1.16	1.23	1.08	1.64	1.39	1.1	1.31	1.36
Nd	6.8	4.7	6.6	6.2	6.6	5.8	8.8	7.4	5.6	6.7	7.2
Sm	2.29	1.58	2.17	1.98	2.1	1.87	2.8	2.38	1.84	2.29	2.3
Eu	0.9	0.66	0.84	0.84	0.85	0.76	1.08	0.95	0.84	0.9	0.87
Gd	2.78	2	2.77	2.61	2.78	2.28	3.55	3.11	2.41	2.74	3.01
Tb	0.56	0.37	0.5	0.46	0.49	0.43	0.65	0.55	0.48	0.54	0.55
Dy	3.82	2.51	3.43	3.25	3.48	2.92	4.46	3.83	3.18	3.69	3.86
Ho	0.8	0.54	0.72	0.67	0.73	0.61	0.94	0.8	0.68	0.77	0.77
Er	2.48	1.59	2.15	2.05	2.2	1.88	2.84	2.41	2.13	2.38	2.31
Yb	2.29	1.57	2.12	2.02	2.14	1.87	2.81	2.3	1.94	2.22	2.26
Lu	0.34	0.24	0.31	0.3	0.33	0.28	0.42	0.36	0.3	0.34	0.34
Ce/Nb	3.18	3.18	3.28	3.32	3.25	3.09	3.06	3.11	2.96	3.23	3.33
Th/Nb	0.09	0.1	0.112	0.11	0.1	0.09	0.1	0.1	0.1	0.09	0.1
Zr/Nb	19.28	21.18	21.6	21.36	21.25	19.54	20.88	21.43	19.58	20	20.37
Nb/Th	11.2	10	8.93	8.8	10	10.47	10	10	10.43	11.31	10
Nb/Y	0.13	0.12	0.13	0.13	0.13	0.14	0.14	0.14	0.13	0.13	0.13
Zr/Y	2.52	2.63	2.91	2.73	2.7	2.71	2.93	2.98	2.61	2.52	2.69
$(La/Nb)_N$	1.06	0.96	1.08	1.03	1.01	0.99	1.02	1.03	1.07	1.07	1.14
Eu/Eu*	1.09	1.13	1.04	1.13	1.07	1.12	1.04	1.07	1.22	1.09	1.01

Sample	272994	272996	272997	275000	291995	291998	291999	292000	292996	292997	297997
Major elements (wt. %)											
SiO_2	47.4	50.9	51	49.1	48.9	50.2	50.2	50.1	50.9	51	49.7
Al_2O_3	13.75	14.7	13.8	13.7	12.95	13.85	13.8	13.9	14.7	13.8	14.2
Fe_2O_3	12.6	12.05	12.45	13	11.55	13.1	12.2	12.65	12.05	12.45	13.05
FeO	11.34	10.845	11.205	11.7	10.395	11.7	10.98	11.385	10.845	11.205	11.745
CaO	11.7	9.58	9.02	11.4	8.91	10.3	11	10.35	9.58	9.02	10.95
MgO	6.96	7.38	7.56	6.6	7.71	7.14	6.32	7.07	7.38	7.56	6.63
Na_2O	1.68	2.22	2.22	1.68	2.58	1.88	2.1	1.69	2.22	2.22	2.01
K_2O	0.03	0.02	0.03	0.03	0.06	0.04	0.04	0.02	0.02	0.03	0.02
TiO_2	1.1	1.03	1.11	1.1	0.94	1.12	1.07	1.13	1.03	1.11	1.05
MnO	0.18	0.2	0.19	0.19	0.18	0.19	0.19	0.19	0.2	0.19	0.17
LOI	2.08	2.5	2.69	2.86	2.67	2.49	2.5	2.55	2.5	2.69	2.8
Mg#	52.24	54.81	54.59	50.13	56.92	52.09	50.64	52.53	54.81	54.59	50.15
TOTAL	97.6	100.5	100	99.8	96.6	100.5	99.6	99.8	100.5	100	100.5
Trace elements (ppm)											
Ba	11.5	9.6	14.8	10.6	15	14.7	16.4	11.5	9.6	14.8	11.2
Rb	0.2	0.3	0.4	0.4	1.1	0.6	0.3	0.2	0.3	0.4	0.4
Sr	238	221	191.5	166	152.5	237	180.5	207	221	191.5	195.5
Cr	250	240	260	250	220	250	240	250	240	260	250
V	291	278	305	299	247	299	281	295	278	305	269
Cu	66	103	117	113	85	111	103	112	103	117	93
Co	52	52.2	52.2	51.2	47.4	49.2	51.1	49.8	52.2	52.2	46.4
Ni	131	142	116	132	149	104	122	110	142	116	106
Zn	96	97	106	108	90	103	98	106	97	106	90
Th	0.28	0.25	0.27	0.23	0.22	0.28	0.26	0.26	0.25	0.27	0.27
Nb	2.7	2.5	2.7	2.8	2.2	2.7	2.6	2.7	2.5	2.7	2.9
Zr	56	52	57	53	45	57	52	55	52	57	57
Hf	1.8	1.6	1.8	1.7	1.4	1.8	1.7	1.8	1.6	1.8	1.6
Y	20	18.7	20.9	21.6	16.6	20.3	19.1	20.2	18.7	20.9	19.5
La	3.4	3.2	3.4	3.5	3	3.4	3.1	3.2	3.2	3.4	3.1
Ce	8.7	8	8.9	8.9	7.2	8.7	8.2	8.4	8	8.9	8.6
Pr	1.34	1.22	1.34	1.33	1.1	1.33	1.27	1.3	1.22	1.34	1.35
Nd	7.1	6.6	7.3	6.6	5.8	7.1	6.7	6.9	6.6	7.3	6.9
Sm	2.21	2.15	2.4	2.31	1.89	2.3	2.19	2.26	2.15	2.4	2.17
Eu	0.91	0.9	0.96	0.95	0.77	0.91	0.86	0.98	0.9	0.96	0.96
Gd	2.93	2.77	3.09	2.72	2.37	2.89	2.79	2.95	2.77	3.09	2.58
Tb	0.54	0.5	0.57	0.55	0.45	0.55	0.51	0.54	0.5	0.57	0.55
Dy	3.78	3.51	3.93	3.65	3.05	3.79	3.6	3.76	3.51	3.93	3.88
Ho	0.76	0.7	0.79	0.75	0.61	0.75	0.72	0.77	0.7	0.79	0.76
Er	2.26	2.12	2.37	2.38	1.84	2.28	2.16	2.25	2.12	2.37	2.16
Yb	2.24	2.11	2.36	2.22	1.81	2.19	2.12	2.27	2.11	2.36	2.14
Lu	0.33	0.3	0.35	0.33	0.26	0.34	0.3	0.33	0.3	0.35	0.32
Ce/Nb	3.22	3.2	3.29	3.18	3.27	3.22	3.15	3.11	3.2	3.3	2.96
Th/Nb	0.1	0.1	0.1	0.08	0.1	0.11	0.1	0.09	0.1	0.1	0.09
Zr/Nb	20.74	20.8	21.11	18.93	20.45	21.11	20	20.37	20.8	21.11	19.65
Nb/Th	9.64	10	10	12.17	10	9.64	10	10.38	10	10	10.74
Nb/Y	0.13	0.13	0.13	0.13	0.13	0.13	0.14	0.13	0.13	0.13	0.15
Zr/Y	2.8	2.78	2.72	2.45	2.71	2.81	2.72	2.72	2.78	2.72	2.92
$(La/Nb)_N$	1.09	1.09	1.03	1.13	1.19	1.11	1.05	1.01	1.09	1.03	1.04
Eu/Eu*	1.09	1.13	1.08	1.16	1.11	1.08	1.06	1.16	1.13	1.08	1.24

Samples	297998	298994	299996	453695
Major elements (wt. %)				
SiO_2	49	48.1	47.8	47.2
Al_2O_3	13.8	13.6	13.8	14.05
Fe_2O_3	13.35	13	13.85	13.2
FeO	12.015	11.7	12.465	11.88
CaO	10.9	10.3	9.95	10.2
MgO	7.27	7.3	7.17	7.65
Na_2O	1.51	2.19	1.88	2.72
K_2O	0.02	0.03	0.01	0.2
TiO_2	1.06	1.04	1.09	1.16
MnO	0.19	0.18	0.19	0.21
LOI	2.6	2.2	3	2.9
Mg#	51.88	52.65	50.62	53.43
TOTAL	99.8	98	98.9	99.61
Trace elements (ppm)				
Ba	7.4	15.1	7.2	83.7
Rb	0.3	<0.2	0.2	3.3
Sr	178.5	196	278	124.5
Cr	260	240	260	300
V	280	265	268	341
Cu	104	99	94	103
Co	48.2	47.5	49.3	54.9
Ni	109	108	102	133
Zn	92	91	99	95
Th	0.27	0.25	0.28	0.28
Nb	2.9	2.8	3	3
Zr	58	56	59	63
Hf	1.7	1.7	1.8	1.8
Y	19.6	19.3	19.8	21.3
La	3	2.9	3.2	3.4
Ce	8.5	8.1	8.8	9.2
Pr	1.31	1.28	1.38	1.51
Nd	6.9	6.6	7.2	7.6
Sm	2.27	2.1	2.26	2.47
Eu	0.9	0.94	0.99	0.9
Gd	2.45	2.46	2.68	3.44
Tb	0.58	0.53	0.6	0.58
Dy	3.91	3.64	4.03	3.79
Ho	0.77	0.75	0.8	0.82
Er	2.18	2.13	2.29	2.46
Yb	2.14	2.08	2.21	2.32
Lu	0.33	0.32	0.35	0.37
Ce/Nb	2.93	2.89	2.93	3.06
Th/Nb	0.09	0.09	0.09	0.09
Zr/Nb	20	20	19.67	21
Nb/Th	10.74	11.2	10.71	10.71
Nb/Y	0.15	0.14	0.15	0.14
Zr/Y	2.96	2.91	2.98	2.96
$(La/Nb)_N$	1	1	1.04	1.05
Eu/Eu*	1.16	1.26	1.23	0.94

ANNEXE 2 : METHODOLOGIE DU CHAPITRE 3

Whole rock analysis

Rocks pulps were desiccated at 60°C. 0.20 g of each sample was added to 0.90 g of lithium metaborate ($LiBO_2$) flux and fused in a furnace at 1000°C. The resulting melt was then cooled and dissolved in 100 ml of 4% nitric acid (HNO_3), filtered, and diluted to a concentration of 2% HNO_3. The major elements were analyzed using inductively coupled plasma-atomic emission spectroscopy (ICP-AES) and the results were corrected for spectral inter-element interferences. Trace elements, including the rare-earth elements, were determined by inductively coupled plasma-mass spectrometry (ICP-MS) using an Agilent 750#0a instrument.

Zircon U-Pb

Samples were first crushed, and only the powder fraction with a diameter < 250 µm was kept. Heavy minerals were subsequently concentrated by a Wilfey table. Magnetic minerals were then removed with an isodynamic Frantz separator. Zircon grains selected from visual sorting were mounted in epoxy blocks, polished, coated with palladium for conductivity and observed with a 2013 Zeiss EVO MA15-HD scanning electron microscope at IOS Services Géoscientifiques Inc. (Québec, Canada). Imaging for internal structures of individual zircon grains and for selecting spots for laser ablation dating was performed with

a CZBSD sector backscattered electron detector coupled with a VP-SE detector, which is equivalent to a cathodoluminescence detector (Fornelli et al., 2014). The electron gun was operated under high vacuum at 20 kV and with a working distance of approximately 11.5 mm. Laser ablation was conducted using a Geolas automated platform housing a 193 nm CompEx 102 laser from LambdaPhysik. Samples were analyzed using an Element XR sector field single-collector ICP-MS (see Bosch et al., 2011 for more details). U-Th-Pb analyses were performed under helium in a 15 cm^3 circular shaped cell using an energy density of 12 J/cm^2 at a frequency of 4 Hz. The laser spot sizes were 26 µm. Data were acquired in the peak jumping mode measuring the ^{202}Hg, $^{204}(Pb + Hg)$, ^{206}Pb, ^{207}Pb, ^{208}Pb and ^{238}U isotopes. A signal was acquired after 10 pulses of pre-ablation to allow for crater stabilization and to remove surface contamination as well as fall-out from previous analyses. This was followed by 15 seconds of gas blank measurement and 45 seconds of signal acquisition. The Pb/Pb and U/Pb isotopic ratios of unknowns were calibrated against the G91500 zircon standard (Wiedenbeck et al., 1995) as an external standard, which was measured four times for each five unknowns using the bracketing technique. Data were reduced using the Glitter software program to check for heterogeneities in the signal. Accurate common lead correction during laser ablation analyses is difficult to achieve, mainly because of the isobaric interference of ^{204}Hg on ^{204}Pb. The contribution of ^{204}Hg on ^{204}Pb was estimated by measuring the ^{202}Hg and assuming a $^{204}Hg/^{202}Hg$ natural isotopic composition of 0.2298 (Bruguier et al., 2001). This allows monitoring the common lead content of the analyzed grains, but corrections often resulted in spurious ages. Analyses yielding ^{204}Pb close to or above the limit of detection were thus rejected. Table 3.4 displays

only analyses for which ^{204}Pb was below the detection limit, and the quoted $^{207}Pb/^{206}Pb$ ratios correspond to measured ratios, corrected from background and mass discrimination. Ages quoted in the text and in the diagram were calculated using the ISOPLOT (MS Excel add-ins by Ludwig, 2003 and 2009) and are reported at the 2σ level, whereas the analytical data are listed in Table 3.4 at the 1σ level. Throughout the text, analyses are considered as concordant when the discordance degree does not exceed 5% (disc % = 100 – [100 x {$^{206}Pb/^{238}U$ age} / {$^{207}Pb/^{206}Pb$ age}]), in which case the $^{207}Pb/^{206}Pb$ age is a good approximation of the age of the analyzed grain.

Ar-Ar dating

The muscovite samples SE2, SE4 and SE7, together with aliquots of the Fish Canyon Tuff sanidine fluence monitor (28.02 Ma; Renne et al., 1998), were packaged in aluminum foil packets and co-irradiated in the CLICIT facility of the Oregon State University reactor for 100 MWH. After irradiation, the FCT sanidine grains and muscovite samples were loaded into a copper holder. The holder was placed into the stainless steel sample chamber with a ZnS cover slip and baked at ~180˚C overnight. Once extraction line ^{40}Ar rate-of-rise levels had decreased to <1fA/min, the sample chamber was exposed to the getters and the sanidine grains were outgassed using the CO_2 laser. Air aliquots from the automated pipette system were analyzed prior to the standard and sample analyses to monitor mass discrimination and detector bias. Following purification, the gas was expanded online into a

multi-collector Thermo Fisher Scientific ARGUSVI mass spectrometer for multi-collector analysis of the five argon isotopes in the Melbourne University. Peak signals were collected for a period of 300 s and regressed to time zero. Line blanks were analyzed between every 1 to 3 sample analyses and were typically <1.5 fA for ^{40}Ar, compared to >1000 fA for FCT sanidine analyses. Line blanks were subtracted from succeeding sample data. The argon isotopic data have been corrected for system blanks, radioactive decay, isotopic interferences and mass discrimination (including H1/CDD bias). Ca/K/Cl salts/glasses included in the irradiation package give average interference correction values for the OSU CLICIT facility of: $(^{39}Ar/^{37}Ar)_{Ca}$ = (6.5075 ± 0.0067) x 10^{-4}; $(^{36}Ar/^{37}Ar)_{Ca}$ = (2.7703 ± 0.0033) x 10^{-4}; and $(^{40}Ar/^{39}Ar)_{K}$ = (5.88 ± 0.34) x 10^{-4}. Ages were calculated using the decay constants recommended by Steiger and Jager (1977). Plateau and mean ages were calculated using ISOPLOT (Ludwig, 2003) and are defined as including > 50% of the total ^{39}Ar released, distributed over at least 3 contiguous steps, with $^{40}Ar^*/^{39}Ar$ ratios within agreement of the mean at the 95% confidence level (see McDougall and Harrison, 1999). The analytical data are presented in Table 3.5. Unless otherwise stated, calculated ages are reported at the 2σ level and include uncertainties in the J-values, but they exclude errors associated with the age of the fluence monitor and the decay constants.

References

Bosch, D., Garrido, C.J., Bruguier, O., Dhuime, B., Bodinier, J.L., Padròn-Navarta, J.A., Galland, B., 2011. Building an island-arc crustal section: Time constraints from a LA-ICP-MS zircon study. Earth and Planetary Science Letters 309, 268-279.

Bruguier, O., Télouk, P., Cocherie, A., Fouillac, A. M., Albarède, F., 2001. Evaluation of Pb-Pb and U-Pb Laser Ablation ICP-MS Zircon Dating using Matrix-Matched Calibration Samples with a Frequency Quadrupled (266 nm) Nd-YAG Laser. Geostandards and Geoanalytical Research 25, 361-373.

Fornelli, A., Piccarreta, G., Micheletti, F., 2014. In situ U-Pb dating combined with SEM imaging on zircon - A analytical bond for effective geological reconstructions. Geochrnology-Methods and Case studies, Edited by Nils-Axel Morner, chapter 5, p. 109-139.

Ludwig, K.R., 2003. Isoplot 3.00: A geochronological toolkit for Microsoft Excel. Berkeley Geochronology Center Special Publication 4, p. 1-71.

Ludwig, K.R., 2009. Users' Manual for Isoplot/Ex rev. 3.27. Berkeley Geochronology Center Special Publication.

McDougall, I., Harrison, T.M., 1999. Geochronology and thermochronology by the $^{40}Ar/^{39}Ar$ method (2^{nd} ed.) Oxford Univ. Press, Oxford, p. 1-269.

Renne, P.R., Swisher, C.C., Deino, A.L., Karner, D.B., Owens, T.L., DePaolo, D.J., 1998. Intercalibration of standards, absolute ages and uncertainties in $^{40}Ar/^{39}Ar$ dating. Chemical Geology 145, 117-152.

Steiger, R.H., Jäger, E., 1977. Subcommission on geochronology: Convention on the use of decay constants in geo- and cosmochronology. Earth and Planetary Science Letters 36, 359-362.

Wiedenbeck, M., Allé, P., Corfu, F., Griffin, W.L., Meier, M., 1995. Three natural zircon standards for U-Th-Pb, Lu-Hf, trace element and REE analyses. Geostandards Newletter 19, 1-23.

ANNEXE 3 : GÉOCHIMIE ROCHE TOTALE DES GRANITES DU DISTRICT DE MANA

Sample	8219	8220	819801	819802	819803	819805	819808	819810	819811	819812
Rock type	grano.	grano.	grano.	grano.	grano.	grano.	grano.	grano.	grano.	grano.
Locality	Siou	Siou	Siou	Siou	Siou	Siou	Siou	Siou	Siou	Siou
SiO_2	70.6	70.2	71.5	69.9	71.1	68.6	71.2	69.4	67.9	72.1
TiO_2	0.29	0.31	0.28	0.35	0.27	0.32	0.22	0.24	0.35	0.2
Al_2O_3	14.1	13.65	13.6	14.4	14.35	14.45	13.95	14.35	16.5	14.05
Fe_2O_3	2.55	2.9	2.7	3.01	2.35	2.86	2.26	2.3	2.97	2.4
MnO	0.03	0.04	0.03	0.04	0.02	0.04	0.03	0.03	0.03	0.03
MgO	0.35	0.82	0.53	0.61	0.49	0.55	0.41	0.63	0.65	0.54
CaO	1.81	1.95	1.82	2.28	1.37	2.06	1.66	2.01	2.4	1.21
Na_2O	5.2	4.71	5.08	5.14	4.78	4.27	4.98	4.83	5.63	5.0
K_2O	2.15	2.29	2.23	2.16	2.64	2.46	2.51	2.46	2.33	2.88
P_2O_5	0.08	0.08	0.06	0.1	0.07	0.14	0.05	0.05	0.08	0.03
SrO	0.06	0.04	0.06	0.07	0.05	0.04	0.06	0.05	0.08	0.06
LOI	2.43	3.54	1.57	2.03	1.92	3.17	0.99	2.64	1.78	1.22
TOTAL	**99.72**	**100.62**	**99.53**	**100.15**	**99.49**	**99.02**	**98.39**	**99.06**	**100.83**	**99.81**
Mg#	21.37	35.89	27.99	28.64	29.22	27.58	26.43	35.16	30.23	30.82
V	34.0	37.0	27.0	31.0	30.0	29.0	22.0	33.0	30.0	19.0
Cr	20.0	10.0	20.0	10.0	20.0	20.0	20.0	30.0	20.0	20.0
Co	3.7	5.2	4.2	5.0	3.4	3.6	3.2	4.7	4.4	2.6
Rb	87.2	100.5	70.8	73.2	96.4	83.8	65.8	111.5	83.7	83.7
Sr	491	349	484	563	411	360	534	515	627	485
Ba	0.07	0.09	592	496	746	534	625	688	1095	724
Y	6.1	5.9	5.8	6.9	4.7	6.9	7.5	7.3	5.4	4.3
Zr	130	120	104	126	121	120	105	134	131	100
Hf	3.6	3.5	3.2	3.6	3.5	3.4	3.5	4.1	3.9	3.1
Nb	5.0	4.5	4.1	5.3	3.9	4.9	5.8	5.4	3.3	3.7
Ta	0.5	0.4	0.4	0.5	0.4	0.5	0.8	0.7	0.3	0.4
Cs	2.51	3.26	1.52	2.48	2.46	1.52	1.16	2.49	2.26	1.17
Pb	11.0	5.0	10.0	8.0	8.0	7.0	12.0	12.0	9.0	7.0
Ga	22.4	22.1	20.1	20.8	21.2	20.7	22	24.2	21.9	19.6
Th	3.63	3.52	3.17	3.2	3.7	2.52	4.04	5.33	3.93	3.72
U	1.36	1.11	1.21	1.55	1.81	0.63	3.36	2.42	1.77	2.04
La	19.8	19.7	17.5	19.8	20.9	16.1	15.8	18.7	14.9	16.9
Ce	37.5	37.1	34.3	39.5	40.1	33.1	31.8	35.2	29.9	32.1
Pr	4.52	4.35	3.89	4.4	4.46	3.71	3.67	3.95	3.4	3.46
Nd	16.7	16.2	14.2	17.1	16.6	14.9	14.8	14.8	13.5	12.4
Sm	3.07	2.86	2.41	2.79	2.77	2.55	2.54	2.51	2.33	2.16
Eu	0.87	0.83	0.71	0.89	0.73	0.75	0.75	0.84	0.9	0.6
Gd	1.93	1.74	1.96	1.95	1.75	1.87	2.12	1.97	1.73	1.53
Tb	0.25	0.23	0.25	0.27	0.21	0.27	0.27	0.27	0.23	0.19
Dy	1.28	1.15	1.23	1.46	1.03	1.37	1.41	1.32	1.12	0.9
Ho	0.22	0.2	0.22	0.24	0.17	0.24	0.24	0.25	0.19	0.15
Er	0.56	0.54	0.53	0.68	0.46	0.61	0.72	0.66	0.52	0.46
Tm	0.08	0.08	0.09	0.1	0.07	0.09	0.1	0.12	0.08	0.08
Yb	0.49	0.5	0.55	0.55	0.41	0.57	0.67	0.61	0.53	0.37
Lu	0.07	0.07	0.08	0.08	0.07	0.08	0.09	0.1	0.09	0.07
W	2.0	9.0	1.0	-	2.0	30.0	-	1.0	1.0	-
$(La/Yb)_N$	28.98	28.26	22.82	25.82	36.56	20.26	16.92	21.99	20.17	32.76
$(Gd/Yb)_N$	3.26	2.88	2.95	2.93	3.53	2.71	2.62	2.67	2.70	3.42
Eu/Eu*	1.02	1.05	0.97	1.11	0.95	1.00	0.96	1.11	1.31	0.96

Sample	819813	819816	819817	819819	819821	819822	819823	819825	215682	215690
Rock type	grano.	grano.	grano.	grano.	grano.	grano.	grano.	grano.	diorite	diorite
Locality	Siou	Siou	Siou	Siou	Siou	Siou	Siou	Siou	Kokoï	Kokoï
SiO_2	71.4	70.4	71.7	74.1	70.6	71.4	70.5	73.3	58.8	58.4
TiO_2	0.23	0.27	0.24	0.21	0.27	0.25	0.28	0.16	0.73	0.78
Al_2O_3	14.9	14.5	14.4	14.25	14.15	14.55	13.95	14.2	13.85	14.9
Fe_2O_3	2.38	2.74	2.36	2.23	2.56	2.36	2.5	2.03	6.06	5.76
MnO	0.04	0.04	0.04	0.02	0.04	0.03	0.03	0.03	0.07	0.08
MgO	0.94	0.49	1.02	0.65	0.75	0.96	0.47	0.23	2.43	2.71
CaO	1.34	1.72	1.35	0.75	1.62	1.58	1.96	1.54	4.73	4.13
Na_2O	5.41	4.75	5.12	3.68	4.85	3.44	5.41	5.34	3.54	3.23
K2O	2.42	2.26	1.96	2.66	2.16	3.05	1.85	1.94	1.91	2.71
P_2O_5	0.06	0.08	0.06	0.06	0.08	0.08	0.08	0.02	0.25	0.23
SrO	0.04	0.04	0.04	0.03	0.05	0.02	0.05	0.04	0.04	0.03
LOI	2.26	2.91	2.65	2.22	2.97	3.41	2.93	1.94	6.87	7.01
TOTAL	**101.49**	**100.26**	**101.01**	**100.93**	**100.18**	**101.21**	**100.07**	**100.84**	**99.33**	**100.03**
Mg#	43.88	26.15	46.11	36.59	36.71	44.61	27.13	18.32	57.61	62.42
V	24.0	21.0	22.0	22.0	27.0	27.0	28.0	12.0	121.0	119.0
Cr	20.0	20.0	30.0	30.0	20.0	20.0	20.0	40.0	90.0	60.0
Co	3.6	3.8	2.3	2.6	3.6	4.8	3.8	2.2	20.7	18.8
Rb	102	70.9	72.5	90.7	85.1	120.5	68.5	86.1	54.9	64.7
Sr	365	293	305	221	436	151	443	425	303	249
Ba	611	470	599	629	638	715	525	686	291	415
Y	6.0	5.6	5.6	6.2	4.9	6.0	6.1	7.5	12.8	13.9
Zr	121	114	109	122	116	125	123	126	190	200
Hf	3.7	3.5	3.2	3.7	3.1	3.6	3.5	4.1	4.8	4.4
Nb	4.3	4.1	3.1	4.8	2.7	3.7	3.7	6.3	7.0	7.3
Ta	0.7	0.4	0.4	0.6	0.3	0.4	0.4	1.0	0.5	0.6
Cs	2.27	1.28	2.02	1.61	2.38	2.15	1.22	1.09	0.96	1.27
Pb	6.0	8.0	5.0	6.0	6.0	-	5.0	12.0	-	-
Ga	21.6	19.1	18.3	20.5	19.6	20.6	19	22.3	19.3	21.8
Th	4.84	3.38	2.44	4.59	2.22	2.7	2.37	5.02	2.3	3.14
U	2.6	0.78	0.88	0.82	0.6	0.77	0.74	1.77	0.77	1.09
La	18.1	18	15	18.2	14.8	14.1	17.1	18.8	27.9	25.9
Ce	34.3	35.1	28.9	36.1	28.4	28	33.9	35.1	54.6	54.4
Pr	3.73	4.01	3.31	4.02	3.09	3.24	3.89	3.87	7.05	6.76
Nd	14.2	15.3	12.8	15.3	12	12.7	14.7	14.1	25.6	25.5
Sm	2.42	2.55	2.28	2.57	1.97	2.26	2.55	2.41	4.55	4.4
Eu	0.75	0.72	0.68	0.73	0.71	0.68	0.84	0.69	1.32	1.28
Gd	1.95	1.9	1.86	1.94	1.37	1.71	1.8	2.01	3.37	3.57
Tb	0.26	0.24	0.23	0.28	0.19	0.23	0.26	0.27	0.47	0.47
Dy	1.24	1.16	1.14	1.23	0.96	1.15	1.25	1.33	2.5	2.49
Ho	0.22	0.19	0.2	0.2	0.17	0.21	0.21	0.26	0.48	0.51
Er	0.57	0.55	0.53	0.61	0.45	0.57	0.56	0.69	1.28	1.39
Tm	0.1	0.1	0.09	0.1	0.08	0.1	0.09	0.11	0.19	0.19
Yb	0.53	0.51	0.5	0.56	0.45	0.56	0.46	0.58	1.14	1.19
Lu	0.08	0.09	0.08	0.08	0.08	0.07	0.08	0.09	0.17	0.17
W	-	20.0	2.0	7.0	3.0	5.0	16.0	3.0	3.0	11.0
$(La/Yb)_N$	24.50	25.32	21.52	23.31	23.59	18.06	26.66	23.25	17.55	15.61
$(Gd/Yb)_N$	3.04	3.08	3.08	2.87	2.52	2.53	3.24	2.87	2.45	2.48
Eu/Eu*	1.02	0.96	0.98	0.96	1.25	1.02	1.14	0.93	0.99	0.96

ANNEXE 4 : GÉOCHIMIE ROCHE TOTALE DES DYKES FELSIQUES PORPHYRIQUES (QFP) DU DISTRICT DE MANA

Sample	294995	298997	215116	215495
Rock type	QFP1	QFP1	QFP1	QFP2
Locality	Fofina	Fofina	Wona	Wona
SiO_2	69.4	68.3	72.7	74.3
TiO_2	0.27	0.25	0.19	0.1
Al_2O_3	14.55	13.45	13.7	13.05
Fe_2O_3	2.16	2.38	1.93	1.36
MnO	0.09	0.17	0.04	0.04
MgO	1.14	1.28	0.87	0.46
CaO	2.51	2.2	1.2	0.7
Na_2O	1.03	3.26	2.07	3.64
K_2O	2.85	1.82	3.47	4.3
P_2O_5	0.08	0.01	0.07	0.02
SrO	0.01	0.01	0.01	0.01
LOI	5.59	4.18	3.39	1.18
TOTAL	**99.8**	**97.4**	**99.7**	**99.3**
Mg#	68.67	43.74	45.42	20.01
V	28	31	15	13
Cr	10	20	10	20
Co	3.8	7.1	11	1.1
Rb	107.5	61.9	119	165
Sr	127.5	106.5	124.5	129
Ba	742	882	858	855
Y	6.2	6.3	8.8	18.8
Zr	110	104	124	89
Hf	3.4	3	3.8	3.2
Nb	5	5	7	11.3
Ta	0.5	0.6	0.8	1
Cs	18.7	11.5	2.6	3.53
Pb	7	5	6	7
Ga	19.7	17.8	16.8	16.8
Th	6.87	5.96	7.19	8.85
U	3.12	2.62	3.57	3.52
La	16.8	13.7	24.5	31
Ce	30.2	25.4	42.3	60.1
Pr	3.2	2.71	4.7	6.59
Nd	11.7	10	15.7	23.4
Sm	2.01	1.9	2.68	4.72
Eu	0.56	0.49	0.65	0.99
Gd	1.88	1.71	2.18	3.8
Tb	0.23	0.27	0.31	0.56
Dy	1.24	1.31	1.59	3.24
Ho	0.22	0.24	0.28	0.63
Er	0.62	0.63	0.82	1.85
Tm	0.09	0.09	0.13	0.26
Yb	0.6	0.62	0.88	1.79
Lu	0.09	0.09	0.15	0.29
W	6	4	8	2
$(La/Yb)_N$	20.08	15.85	19.97	12.42
$(Gd/Yb)_N$	2.59	2.28	2.05	1.76
Eu/Eu*	0.87	0.81	0.79	0.69

ANNEXE 5 : ANALYSES LA-ICP-MS DE PYRITES

Fofina

Hole ID	Type	^{51}V	^{52}Cr	^{55}Mn	^{59}Co	^{60}Ni	^{65}Cu	^{66}Zn	^{75}As	^{82}Se	^{95}Mo	^{107}Ag	^{118}Sn	^{121}Sb	^{125}Te	^{182}W	^{197}Au	^{208}Pb	^{209}Bi
WDC239-2-1	Py_{1F}	15.8	bdl	79	152	49.4	267	65	9100	4.3	0.9	0.5	0.5	69	1.7	58	0.7	25.6	0.2
WDC239-2-2	Py_{1F}	19.9	bdl	68	61.5	21.4	340	31	6460	3.6	0.3	0.9	0.8	125	2.9	68	0.7	101	0.3
WDC239-2-3	Py_{1F}	11.8	bdl	19	66.4	25	740	69	8970	3.5	0.2	1.1	0.5	98.5	bdl	53.4	0.9	89.8	0.3
WDC239-2-4	Py_{1F}	26	bdl	220	111	45.1	700	27	9300	3.6	0.3	1.2	1	98.3	bdl	96	1.3	122	0.4
WDC239-2-5	Py_{1F}	37	bdl	22	187	78	269	8.3	13880	2.9	0.2	0.7	0.5	64.5	bdl	49	0.9	47.9	0.2
WDC239-2-6	Py_{1F}	37	bdl	22	187	78	269	8.3	13880	2.8	0.2	0.7	0.5	64.5	bdl	49	0.9	47.9	0.2
WDC239-2-7	Py_{1F}	21	bdl	30	62	160	305	29	9390	4.1	0.3	1	7	78.8	bdl	57.5	1	76.1	0.3
WDC239-2-8	Py_{1F}	11	bdl	47	35.5	20.5	1250	700	10860	3.2	0.2	0.6	0.7	76.8	2	39.1	0.6	35.7	0.1
WDC239-2-9	Py_{1F}	7.3	bdl	200	59.3	20.6	226	39	10880	5	0.3	1.3	0.3	75.5	1.8	25.8	1	100.2	0.4
WDC239-2-10	Py_{1F}	19.6	bdl	360	26.5	13	149	2.9	11700	3	0.1	0.4	0.7	72.5	1.6	43	0.5	21.3	0.1
WDC239-2-11	Py_{1F}	26.3	bdl	240	57.9	22.9	320	79	12000	5.4	0.4	0.8	3.1	57.1	bdl	49.9	0.8	62.9	0.3
WDC239-2-12	Py_{1F}	16	bdl	32	85	40.8	245	780	12240	3.3	0.3	0.9	0.6	82.9	2.9	57	1	67	0.3
WDC239-2-13	Py_{1F}	5.8	bdl	28	53.5	15.8	600	3700	7800	4.5	0.2	0.8	0.5	64	1.8	50	0.7	112	0.2
WDC239-2-14	Py_{1F}	6.5	bdl	49	64.8	19.7	460	2500	12470	4.6	0.1	0.5	0.4	60.3	bdl	19.4	0.7	35.7	0.1
WDC244-1-1	Py_{2F}	42	35	36	135	228	29.7	4.2	3150	bdl	bdl	26.4	bdl	169	bdl	3.1	36.3	5.2	0.1
WDC244-1-2	Py_{2F}	73	97	18.3	260	510	70.1	3.7	5960	bdl	bdl	9.1	bdl	258	bdl	5.4	12.2	15.8	0.2
WDC244-1-3	Py_{2F}	92	34	15	89	228	15.3	1.9	3280	bdl	0.1	9.4	bdl	73	bdl	0.1	16.5	1.2	bdl
WDC244-1-4	Py_{2F}	73	59	13.6	201	338	41.7	15	4070	bdl	bdl	7.4	bdl	163	bdl	5	8.6	13.2	0.1
WDC244-1-5	Py_{2F}	190	148	23.7	180	248	30.2	7.6	3260	6.4	0.5	4.7	0.4	110	bdl	5.8	5.6	12	0.1
WDC244-1-6	Py_{2F}	46	41	27	129	167	23.7	2.9	2660	bdl	bdl	2.5	bdl	104	bdl	5.7	2.1	5.4	0.1
WDC244-1-7	Py_{2F}	64	52	15.4	176	160	25.8	2.1	3670	bdl	bdl	2.2	bdl	92	bdl	3.7	1.2	6	0.1
WDC244-1-8	Py_{2F}	440	310	49	160	172	29.5	6.4	3300	12	bdl	2.3	1.5	69	bdl	1.9	1.3	7	0.2
WDC244-1-9	Py_{2F}	31	17.9	9.7	121	89	12.3	1.9	2220	3.9	bdl	0.9	bdl	38.8	bdl	0.6	0.3	3.3	0.1
WDC244-2-1	Py_{3F}	0.6	bdl	2.3	55	62	1.6	1.3	1580	bdl	bdl	bdl	bdl	bdl	bdl	bdl	bdl	bdl	bdl
WDC244-2-2	Py_{3F}	0.5	bdl	1.9	15.7	64	1.5	1.5	1740	2.9	bdl	bdl	bdl	bdl	bdl	bdl	bdl	bdl	bdl
WDC244-2-3	Py_{3F}	0.6	4	6.7	40	87	1.8	1.5	1770	bdl	bdl	bdl	bdl	bdl	bdl	bdl	0.3	bdl	bdl
WDC244-2-4	Py_{3F}	0.4	bdl	2.1	49	88	1.9	1.2	1720	bdl	bdl	0.1	bdl	0.7	bdl	bdl	0.4	0.4	bdl
WDC244-2-5	Py_{3F}	0.4	bdl	bdl	1.9	68	1.7	1.5	1720	bdl	bdl	bdl	bdl	bdl	bdl	bdl	bdl	bdl	bdl
WDC244-2-6	Py_{3F}	1.2	bdl	2.4	93	68	14.7	2.7	880	bdl	bdl	0.5	bdl	2.3	bdl	0.1	0.1	2.3	bdl
WDC244-2-7	Py_{3F}	0.8	7.2	8	60	61	3.7	9	1460	bdl	bdl	11	0.6	4.3	bdl	0.2	0.2	3	0.1
WDC244-2-8	Py_{3F}	1.3	3.3	4.5	21	100	15.6	1.8	1370	bdl	bdl	0.2	0.3	0.5	bdl	0.1	0.2	2.9	bdl
WDC244-2-9	Py_{3F}	0.4	2	2.9	1.7	73	2.6	1.8	1800	bdl	bdl	bdl	0.2	bdl	bdl	bdl	0.2	0.4	bdl
WDC244-2-10	Py_{3F}	0.2	3.9	4	42	46.1	1.9	5.2	1250	3.2	bdl	0.1	bdl	0.8	bdl	bdl	bdl	1.3	bdl
WDC244-2-11	Py_{3F}	0.3	2.3	2	58	47	1.7	3	1180	bdl	bdl	bdl	bdl	0.3	bdl	0.3	bdl	0.5	bdl
WDC244-2-12	Py_{3F}	0.3	1.5	3.4	14.1	47	2	1.8	1350	bdl	bdl	0.1	bdl	0.3	bdl	bdl	bdl	0,5	bdl
WDC244-2-13	Py_{3F}	5.9	3	6.7	73	41.7	1.8	2.4	1280	bdl	bdl	0.1	bdl	0.4	bdl	0.5	bdl	bdl	bdl
WDC244-2-14	Py_{3F}	0.2	2.7	bdl	4.6	45	1.7	1.3	1540	bdl	bdl	bdl	bdl	bdl	bdl	0.1	bdl	bdl	0.1
WDC244-2-15	Py_{3F}	0.2	1.7	bdl	19	45.3	1.5	1.1	1440	bdl	bdl	bdl	bdl	bdl	bdl	0.1	bdl	bdl	bdl
WDC244-2-16	Py_{3F}	0.2	2.1	2.1	30	48.1	1.7	1.1	1400	bdl	bdl	bdl	bdl	bdl	bdl	bdl	bdl	bdl	bdl
WDC244-2-17	Py_{3F}	0.5	1.6	bdl	95	44.6	1.2	101	870	bdl	bdl	bdl	bdl	bdl	bdl	bdl	bdl	bdl	bdl

Nyafé

Hole ID	Type	^{51}V	^{52}Cr	^{55}Mn	^{59}Co	^{60}Ni	^{65}Cu	^{66}Zn	^{75}As	^{82}Se	^{95}Mo	^{107}Ag	^{118}Sn	^{121}Sb	^{125}Te	^{182}W	^{197}Au	^{208}Pb	^{209}Bi
10ALP1-1	Py_{1N}	0.9	bdl	452	198	20	20	1.4	104	98	0.1	0.1	bdl	28	1.9	bdl	0.1	1.7	bdl
10ALP1-2	Py_{1N}	1.7	bdl	439	105	21.1	18.3	1.2	108	92.7	0.1	0.1	bdl	6.7	1.3	bdl	bdl	2.3	bdl
10ALP1-3	Py_{1N}	0.4	1.4	407	93	23.7	17.1	0.6	54.9	103.5	0.1	bdl	bdl	1.9	bdl	bdl	bdl	1.7	bdl
10ALP1-4	Py_{1N}	2	3.2	430	330	20.4	14.9	2.3	53	95.4	0.1	bdl	bdl	1.1	bdl	bdl	bdl	2.1	bdl
10ALP1-5	Py_{1N}	4.3	7.6	435	173	18.1	13.9	1.7	54.5	108.6	0.1	bdl	bdl	0.9	bdl	0.1	bdl	5.4	bdl
10ALP1-6	Py_{1N}	3.6	bdl	428	180	28.3	17.5	1.4	65.3	135	0.1	0.1	bdl	1	1.4	bdl	bdl	3.8	0.1
10ALP1-7	Py_{1N}	3.9	2	434	360	35.6	15.5	1.4	66.5	136	0.1	0.1	bdl	0.4	1.7	bdl	bdl	5.9	0.1
10ALP1-8	Py_{1N}	8.2	4.3	443	280	35	15.8	2	78	138	0.1	0.1	bdl	0.6	2.3	bdl	bdl	9.6	0.2
10ALP1-9	Py_{1N}	4.2	bdl	421	126	12.2	15.7	1.7	66	142	0.1	0.1	bdl	0.3	2.3	bdl	bdl	7.7	0.2
10ALP1-10	Py_{1N}	2.7	bdl	423	211	25.2	10.6	1.2	49.8	146	0.1	0.1	bdl	0.8	2.4	bdl	bdl	5.6	0.1
10ALP1-11	Py_{1N}	3.2	1.3	434	180	14.8	23	5.3	43.9	132	0.1	0.3	bdl	18	bdl	bdl	bdl	6.4	0.1
10ALP7-2-1	Py_{2N}	1.9	16	438	780	2890	7000	140	1500	57	0.1	1.6	0.2	23.2	bdl	bdl	0.4	2.5	0.4
10ALP7-2-2	Py_{2N}	8.4	59	447	147	820	250	4.1	2100	49	bdl	0.2	bdl	18	bdl	4.2	0.5	3.6	0.5
10ALP7-2-3	Py_{2N}	1.1	bdl	423	270	2090	470	8.6	920	29	bdl	0.4	bdl	11.1	bdl	bdl	0.1	3.8	0.2
10ALP7-2-4	Py_{2N}	0.6	bdl	409	330	2310	31	1.5	2000	38	0.1	0.2	bdl	55	bdl	bdl	0.2	4.2	0.2
10ALP7-2-5	Py_{2N}	0.6	4.4	435	390	1810	28	1.5	1400	38	bdl	0.1	bdl	9.9	bdl	bdl	0.2	2	0.2
10ALP7-2-6	Py_{2N}	0.8	bdl	441	350	1720	24.5	1.8	1000	33	bdl	0.2	bdl	13.8	bdl	bdl	0.2	6.4	0.4
10ALP7-2-7	Py_{2N}	0.5	bdl	441	310	1760	27	1.3	1800	29	0.1	0.1	bdl	11.6	bdl	bdl	0.1	6.7	0.3
10ALP7-2-8	Py_{2N}	0.9	b	392	390	2000	150	1.3	990	29	0.2	0.2	bdl	8	bdl	bdl	0.1	3.8	0.3
10ALP7-2-9	Py_{2N}	2.5	6	435	650	1420	2200	2.9	720	48	bdl	0.5	bdl	15.2	bdl	0.7	0.2	6.9	1
10ALP7-2-10	Py_{2N}	5.4	8	455	1180	2120	11200	17	201	60	0.1	2.8	bdl	22.5	bdl	0.2	0.3	6.8	1.3
10ALP7-2-11	Py_{2N}	3.5	4.7	416	1260	1760	590	2.1	230	49	0.1	0.3	bdl	9.8	bdl	0.3	0.1	4.4	0.6
10ALP7-2-12	Py_{2N}	2.5	4.7	447	830	1520	2000	15	190	71	0.1	0.9	bdl	15.1	bdl	bdl	0.1	6.9	0.5
10ALP7-2-13	Py_{2N}	20	1	447	156	1110	100	3	930	49	0.1	0.5	0.3	40	bdl	6.9	0.4	5.9	0.5
10ALP7-2-R1	Py_{2N}	3.2	1.9	431	134	59	300	2.8	33600	bdl	bdl	0.3	bdl	26.6	bdl	0.7	6.2	3.2	0.1
10ALP7-2-R2	Py_{3N}	6.5	3	431	125	56.5	263	8.2	34800	bdl	0.2	0.2	bdl	21.3	bdl	0.3	7	3.6	bdl
10ALP7-2-R3	Py_{3N}	21	3.8	454	62	30.2	245	14	33300	bdl	0.1	0.1	0.4	16.4	bdl	bdl	8.3	3	bdl
10ALP7-2-R4	Py_{3N}	1.3	1.7	436	67	35	267	4.3	35500	bdl	bdl	0.2	bdl	33	bdl	bdl	8.3	2.9	bdl
10ALP7-2-R5	Py_{3N}	8.4	6.4	458	179	250	350	16	31200	bdl	bdl	1	bdl	64	bdl	0.7	10.4	7.5	0.2
10ALP7-2-R6	Py_{3N}	45	11	530	145	126	300	107	28000	bdl	bdl	1.1	0.2	72	bdl	bdl	5.2	6.7	0.2
10ALP7-2-R7	Py_{3N}	30	bdl	412	159	131	670	37	25100	bdl	0.1	1.1	0.4	62	bdl	0.2	5.1	9.9	0.1
10ALP7-2-R8	Py_{3N}	4.8	bdl	429	147	93	690	6.7	32800	bdl	0.1	0.8	0.5	54	bdl	3.1	16.8	6.7	0.1
10ALP7-2-R9	Py_{3N}	1.1	bdl	421	122	88	1370	6.4	32000	bdl	0.1	0.5	0.6	42.9	bdl	0.6	10.3	5	0.1
10ALP7-2-R10	Py_{3N}	6.3	1.4	414	81	68.4	650	14.7	33700	bdl	0.1	0.6	bdl	48	bdl	0.6	22.3	5.8	0.1
10ALP7-2-R11	Py_{3N}	6.2	0.8	441	89	67	550	12.9	35900	bdl	0.1	0.5	0.3	52	bdl	1.6	24.4	6.3	0.1
10ALP7-2-R12	Py_{3N}	2.2	1.2	418	81	65.9	820	10.3	30400	bdl	0.1	0.7	0.3	68	bdl	0.7	19.2	6.4	0.1

Siou

Hole ID	Type	^{51}V	^{52}Cr	^{55}Mn	^{59}Co	^{60}Ni	^{65}Cu	^{66}Zn	^{75}As	^{82}Se	^{95}Mo	^{107}Ag	^{118}Sn	^{121}Sb	^{125}Te	^{182}W	^{197}Au	^{208}Pb	^{209}Bi
WDC621-1-1	Py_{1S}	45	179	371	910	213	760	24	2060	14	bdl	18.3	0.3	7.2	27	17.4	2.8	330	39
WDC621-1-2	Py_{1S}	35	173	360	590	209	720	64	1950	13.7	bdl	8.4	0.3	6.7	29	17.8	1.6	410	43
WDC621-1-3	Py_{1S}	45.2	337	364	530	227	53	21	2000	13.9	0.3	40	0.8	6.5	35	26.3	0.8	38	17.7
WDC621-1-4	Py_{1S}	35.9	210	360	213	197	92	17.4	1670	15.1	bdl	3.4	0.2	8.8	9.5	29.9	0.1	150	13.5
WDC621-1-5	Py_{1S}	73	281	369	130	209	200	23	1970	15.7	bdl	8.7	0.3	12.1	19.4	34.2	0.2	750	33.2
WDC621-1-6	Py_{1S}	58.3	231	374	410	173	229	29.4	2050	15.3	0.1	6.4	0.4	10	30	39.9	0.8	270	29.3
WDC621-1-7	Py_{1S}	54	223	370	570	171	350	28	2000	15	0.4	12.8	0.5	8.6	20.7	34.2	1.3	450	34
WDC621-1-8	Py_{1S}	76	361	349	300	166	410	210	1740	13.8	0.3	27	0.9	9.3	29	41.5	4.5	420	40
WDC621-1-9	Py_{1S}	102	520	373	650	204	370	270	1880	11.9	0.7	27	0.8	8.3	34	54.8	3.3	340	42
WDC621-1-10	Py_{1S}	82	340	371	480	247	1300	127	2070	14.1	0.6	79	0.6	9	69	36.8	8	740	56
WDC621-1-11	Py_{1S}	35.1	221	363	440	210	460	76	1920	16.4	0.1	16.6	0.6	11.3	26.4	50	1.7	300	37
WDC621-2-1	Py_{2S}	2.4	3.9	378	165	483	11.2	2.1	2590	21.4	bdl	0.1	bdl	0.5	2.3	2.1	bdl	3.2	0.8
WDC621-2-2	Py_{2S}	15	4	359	140	438	10.6	1.6	2310	20	bdl	0.1	bdl	0.6	2	1.7	bdl	3.3	0.6
WDC621-2-3	Py_{2S}	3.2	5.6	363	84	209	10.9	2.2	1610	18.7	bdl	bdl	0.4	bdl	2	1.3	bdl	1.8	0.2
WDC621-2-4	Py_{2S}	10	142	366	680	246	13.8	4.3	1850	15.6	bdl	0.3	bdl	1.6	2.3	9.6	bdl	7.6	2
WDC621-2-5	Py_{2S}	1.4	8.5	361	184	255	11.2	1.4	2040	19.1	bdl	0.1	0.3	0.5	1.3	2.3	bdl	3.9	0.6
WDC621-2-6	Py_{2S}	1.4	6.2	364	239	293	10.2	1.4	2170	18.9	bdl	0.1	bdl	0.8	1.5	5.4	bdl	4.2	0.7
WDC621-2-7	Py_{2S}	31	220	415	1270	410	200	28	2180	12.7	bdl	13	0.2	7.1	17.5	52	0.1	47.2	23.9
WDC621-2-8	Py_{2S}	5.8	20.7	366	410	141	12.9	4.2	1470	14.2	bdl	0.2	bdl	2.7	3.4	7.7	bdl	12.9	3.7
WDC621-2-9	Py_{2S}	2.8	14.7	357	160	381	11.9	1.8	2080	20.2	bdl	0.1	bdl	0.3	2.7	4	bdl	3.1	0.4
WDC621-2-10	Py_{2S}	6.3	7.4	374	234	448	10.9	2	2490	24.8	bdl	0.2	bdl	0.3	3.7	2.2	bdl	3.6	0.4
WDC621-2-11	Py_{2S}	4.2	13.3	332	256	436	12.5	2.4	2370	23	bdl	0.2	bdl	0.6	4	4.4	bdl	5.7	0.8
WDC621-2-12	Py_{2S}	3.4	8.9	358	530	340	11.3	2.2	2210	16.5	bdl	0.2	bdl	1.4	2	6.7	bdl	6.9	1.7
WDC621-2-13	Py_{2S}	3.6	11.7	342	318	493	12.1	1.8	2590	25.2	bdl	0.2	bdl	0.3	4.9	2.9	bdl	3	0.4
WDC621-2-14	Py_{2S}	3.2	4.6	346	331	484	12.1	1.8	2740	30.2	bdl	0.4	bdl	bdl	7	0.8	bdl	1.9	0.2
WDC621-2-15	Py_{2S}	6.6	14.1	340	318	406	16.4	5.2	2930	34.2	0.8	0.5	0.8	0.2	8.8	0.9	bdl	5.2	0.2
WDC621-2-16	Py_{2S}	3	5.11	336	302	479	12.3	2	2710	28.3	bdl	0.4	bdl	bdl	6.7	1.1	bdl	4.8	0.2
WDC621-2-17	Py_{2S}	3.7	5	352	270	475	14.3	2.5	2920	30.8	bdl	0.4	bdl	bdl	7.9	0.9	bdl	3.6	0.2
WDC621-2-18	Py_{2S}	3.4	35	357	388	501	15.8	2.8	2540	18	0.1	0.5	bdl	3.3	2.2	23.9	bdl	12.9	2.9

Wona-Kona

Hole ID	Type	^{51}V	^{52}Cr	^{55}Mn	^{59}Co	^{60}Ni	^{65}Cu	^{66}Zn	^{75}As	^{82}Se	^{95}Mo	^{107}Ag	^{118}Sn	^{121}Sb	^{125}Te	^{182}W	^{197}Au	^{208}Pb	^{209}Bi
WDC196-3-1	Py_{1WK}	20.3	9.4	5200	7.2	6.9	17.3	39	4.1	19.9	0.3	0.2	bdl	50.8	bdl	7.5	0.3	66	0.2
WDC196-3-2	Py_{1WK}	16	9.5	4200	6.1	4.1	14.7	39.7	bdl	15.4	0.3	0.2	bdl	50.8	bdl	7.3	0.1	51	0.1
WDC196-3-3	Py_{1WK}	85	18.1	2980	115	172	50.9	30.6	33.8	16.4	03	2.5	bdl	55.1	3.1	7.4	0.6	218	3.3
WDC196-3-4	Py_{1WK}	119	25.7	3980	178	256	57.1	38	57	16.7	0.5	2.6	0.6	60.8	2.9	44	0.6	299	4.2
WDC196-3-5	Py_{1WK}	98	28.5	2810	201	242	72	28.1	48.7	14.3	0.2	3.3	0.5	75.9	3.6	37	0.8	347	4.5
WDC196-3-6	Py_{1WK}	121	31.2	2870	149	199	60.4	29.9	42.6	16.7	0.2	2.8	0.9	84	3.4	69	0.9	292	3.7
WDC196-3-7	Py_{1WK}	117	27.5	1620	129	152	57.4	19.9	28.2	18.4	bdl	2.9	0.6	92.2	bdl	41	0.9	262	2.6
WDC196-3-8	Py_{1WK}	280	73	1650	182	252	71.6	18.8	45	14.8	0.2	3.6	1.8	80.1	bdl	180	0.8	320	3.4
WDC196-3-9	Py_{1WK}	169	44	2490	197	271	77.6	26.5	51.6	14.8	0.3	3.5	1	75.4	bdl	76	0.8	352	4.3
WDC196-3-10	Py_{1WK}	97	25.2	2750	185	247	72.1	27.6	57.7	10.6	0.4	3.5	0.9	70.8	2.9	45	0.8	354	4.6
WDC196-3-11	Py_{1WK}	115	29	2390	269	335	101.4	26.4	75	14	71	5	1.3	84.8	3.7	51	1.1	445	6.5
WDC196-2-1	Py_{1WK}	246	35	3800	222	353	165	39.6	143	bdl	0.6	5	bdl	38.2	29.5	2	1.3	404	12.1
WDC196-2-2	Py_{1WK}	238	39	5000	210	300	159	46.8	136	bdl	0.7	4.8	0.7	36.9	25.4	3.5	0.8	362	13
WDC196-2-3	Py_{1WK}	197	17	6700	148	215	134	59	121	6.7	0.8	4.1	1.4	28	25.2	1.9	1	337	10.4
WDC196-2-4	Py_{1WK}	275	33	5400	162	337	134	54	100	4.9	0.6	3.8	bdl	31.7	17.7	3.1	0.9	350	91
WDC196-2-5	Py_{1WK}	173	20.1	5400	174	317	124.6	47.9	106	7.5	0.4	4.9	0.5	35.4	24.7	3.1	1	360	11.3
WDC196-2-6	Py_{1WK}	212	25.5	2830	185	379	122.8	28.2	88	6.2	0.2	4.9	0.6	38.5	17.8	4.3	1	350	9.3
WDC196-2-7	Py_{1WK}	185	18.7	1930	145	385	102.1	26	62	6.2	0.2	5	bdl	40.1	13.5	1.1	0.9	292	6.9
WDC196-2-8	Py_{1WK}	109	9.5	2300	154	403	83.4	21	43	8.5	0.2	4.1	bdl	38.9	9.7	0.9	0.7	250	4.8
WDC196-2-9	Py_{1WK}	99	14.6	1570	131	361	90.6	16	44.6	10.5	0.1	4	bdl	44	10.3	1.9	0.7	240	4.6
WDC196-2-10	Py_{1WK}	205	23.8	4400	178	340	108.1	39	79.6	6.3	0.9	4.1	bdl	64	17.7	2.5	0.9	335	7.8
WDC196-2-11	Py_{1WK}	169	16.7	5440	191	337	111.8	41.3	73.6	8.4	24	4.1	0.6	53.2	15	5.6	0.8	370	8
WDC196-2-12	Py_{1WK}	248	25.2	5350	190	304	125	46.9	81	9.9	0.4	4.2	0.7	50.3	18	3.4	0.9	377	8.8
WDC196-2-13	Py_{1WK}	410	44	4750	174	291	116	41.4	82	9.7	0.4	4.6	0.8	48.4	14.4	3.4	0.9	372	8.9
WDC196-2-14	Py_{1WK}	126	14.3	4280	167	322	97.3	37.1	70	14.7	0.3	3.9	bdl	50.5	11.8	5.6	0.8	362	7.3
WDC196-2-15	Py_{1WK}	159	25.1	3700	173	358	97.2	34	70.3	13.6	0.3	3.7	bdl	54.2	13.9	7.9	0.8	350	6.9
WDC196-2-16	Py_{1WK}	176	32	4120	200	359	112.5	35.1	81	11.3	0.2	4.7	0.6	46.8	17	7.3	1	330	8.5
WDC196-2-17	Py_{1WK}	44.7	10.9	9840	201	387	94	67.3	74.3	7	0.5	2.9	bdl	41.9	13.6	4	0.8	366	7.4
WDC196-2-18	Py_{1WK}	41	4.2	7120	138	215	66.1	56	49.4	10.2	0.3	1.7	bdl	46.7	9.1	1.1	0.5	272	4.4

Wona-Kona

Hole ID	Type	^{51}V	^{52}Cr	^{55}Mn	^{59}Co	^{60}Ni	^{65}Cu	^{66}Zn	^{75}As	^{82}Se	^{95}Mo	^{107}Ag	^{118}Sn	^{121}Sb	^{125}Te	^{182}W	^{197}Au	^{208}Pb	^{209}Bi
WDC196-1-1	Py_{2WK}	160	21	35.7	94	43	3.6	4.8	520	4.9	bdl	0.2	0.6	5.6	4	1.4	0.1	9.8	3.1
WDC196-1-2	Py_{2WK}	22.6	bdl	40.5	109	54	1.4	7	607	3.7	bdl	0.1	0.3	0.5	bdl	1	bdl	1.4	0.3
WDC196-1-3	Py_{2WK}	14	7.5	29.1	36	37.5	1.4	6.7	517	4.2	0.1	0.1	bdl	1.3	bdl	4.3	bdl	2.4	0.7
WDC196-1-4	Py_{2WK}	14.8	bdl	26	118	54	1.4	5.1	630	bdl	bdl	0.2	bdl	1.2	2.2	2.8	0.1	3.1	0.9
WDC196-1-5	Py_{2WK}	15.1	bdl	22.9	36	60	1.8	4.5	670	bdl	bdl	1	bdl	3.1	6.3	0.7	0.1	14.1	2.8
WDC196-1-6	Py_{2WK}	25	6.4	35.5	37	41.2	1.9	4.3	594	bdl	bdl	0.8	bdl	4.3	6.6	1.2	0.1	12	3.4
WDC196-1-7	Py_{2WK}	46	6.6	41	36	46.2	1.9	4.2	627	3.9	bdl	0.6	bdl	2.5	3.4	0.7	0.1	10.7	2.2
WDC196-1-8	Py_{2WK}	11.2	bdl	27.5	15.6	41.3	1.9	6.3	664	6.7	bdl	0.5	bdl	1.2	2	1.1	bdl	5.8	1.2
WDC196-1-9	Py_{2WK}	9.8	2.8	29	13.5	33.8	2.3	3	593	6.4	bdl	0.2	bdl	0.8	bdl	1.4	bdl	3.4	0.8
WDC196-1-10	Py_{2WK}	16.9	3.8	47	24	29.6	2.1	3.2	562	3.1	bdl	0.9	0.4	2.6	6.7	1.7	0.1	9	3.2
WDC196-1-11	Py_{2WK}	8.4	2.7	44	37	32.9	1.8	3.2	649	4	bdl	0.4	bdl	0.8	3	0.8	0.1	5.4	1.8
WDC196-1-12	Py_{2WK}	59	5.8	28.9	37	30.7	3.1	2.9	572	bdl	bdl	0.6	bdl	3.3	4.5	1.9	0.1	9.7	3.2
WDC196-1-13	Py_{2WK}	21	bdl	16.1	18.1	27.5	2.4	2.3	571	4.5	bdl	0.4	0.4	2.3	3.3	0.5	0.2	8.2	1.9
WDC196-1-14	Py_{2WK}	6.2	bdl	21	13.3	32.6	2.3	2.5	597	5.4	bdl	0.6	bdl	2	4.6	0.3	0.1	10l8	2.7
WDC196-1-15	Py_{2WK}	12.3	4.3	15.9	24	36.2	2.5	2.2	611	4.8	bdl	1.7	bdl	3.1	9.3	0.6	0.3	15.9	4.5
WDC196-1-16	Py_{2WK}	14.6	bdl	12.8	35	37.9	2.3	2.4	711	3.9	bdl	0.8	bdl	3	5	1.8	0.1	11	3.2
WDC196-1-17	Py_{2WK}	16.8	bdl	11.2	39	34.9	2.3	2.2	700	5.4	bdl	0.5	bdl	2.8	2.7	1.1	0.1	9.1	1.9
WDC196-1-18	Py_{2WK}	38	7.5	38	27.4	42.4	2.1	2.2	672	4.4	bdl	0.9	bdl	3.8	5.5	1.1	0.1	10.6	4.1
WDC196-1-19	Py_{2WK}	1.7	2.5	32	69	36.8	1.2	1.7	810	4.5	bdl	0.4	bdl	1.8	bdl	0.1	0.1	6.7	1.1
WDC196-1-20	Py_{2WK}	0.9	bdl	7.4	49	46.1	1.1	1.1	790	4.7	bdl	0.1	bdl	0.5	bdl	bdl	bdl	1.9	0.2
WDC196-1-21	Py_{2WK}	0.4	bdl	10.5	66	59	0.9	1.2	1058	5.9	bdl	0.4	bdl	0.5	bdl	0.1	0.1	3.2	0.8
WDC196-1-22	Py_{2WK}	0.4	7.7	14.4	18.7	44	1.4	2.3	1490	4.8	bdl	0.2	bdl	0.4	bdl	bdl	bdl	2	0.4
WDC196-1-23	Py_{2WK}	0.4	5.3	13.8	12.3	82	1.4	1.5	1810	6.5	bdl	0.1	bdl	0.6	bdl	bdl	bdl	2.6	0.8
WDC423-5-1	Py_{2WK}	2.3	bdl	420	2.1	17.3	3.9	2.5	2430	13.7	bdl	0.1	bdl	1	bdl	0.1	0.1	3.6	0.1
WDC423-5-2	Py_{2WK}	1.9	bdl	414	1.5	15.8	3.9	2.3	3210	16.5	0.1	0.1	bdl	0.2	bdl	0.1	bdl	1	bdl
WDC423-5-3	Py_{2WK}	2.3	bdl	412	1.7	11.4	3.6	1.9	3670	18.3	bdl	bdl	bdl	0.2	bdl	0.1	0.1	0.8	bdl
WDC423-5-4	Py_{2WK}	2.1	1.6	424	1.4	9.5	3.5	1.7	3580	18.8	0.1	bdl	bdl	bdl	bdl	0.1	bdl	0.8	bdl
WDC423-5-5	Py_{2WK}	2	bdl	424	0.2	5.1	3.6	1.7	3600	18.4	bdl	bdl	bdl	bdl	bdl	0.1	0.1	0.6	bdl
WDC423-5-6	Py_{2WK}	1.9	bdl	405	0.2	3.6	3.9	2.1	3500	19	bdl	0.1	bdl	bdl	bdl	0.2	bdl	0.8	bdl

Wona-Kona

Hole ID	Type	^{51}V	^{52}Cr	^{55}Mn	^{59}Co	^{60}Ni	^{65}Cu	^{66}Zn	^{75}As	^{82}Se	^{95}Mo	^{107}Ag	^{118}Sn	^{121}Sb	^{125}Te	^{182}W	^{197}Au	^{208}Pb	^{209}Bi
WDC423-5-7	Py_{2WK}	1.8	bdl	390	0.1	2.3	3.2	1.8	3230	17.4	bdl	bdl	bdl	bdl	bdl	0.2	0.1	0.7	bdl
WDC423-5-8	Py_{2WK}	1.6	2.2	411	0.1	2.4	3.9	2	3010	17.2	0.1	bdl	bdl	bdl	bdl	0.2	0.1	1.3	bdl
WDC423-5-9	Py_{2WK}	1.6	1.5	408	0.3	5.3	4.6	4	3230	17.9	0.1	bdl	0.5	0.2	bdl	0.2	0.1	2.3	bdl
WDC423-5-10	Py_{2WK}	1.5	bdl	394	0.1	9.3	3.9	2.6	3130	15.8	bdl	bdl	bdl	bdl	bdl	0.1	bdl	1	bdl
WDC423-5-11	Py_{2WK}	1.8	bdl	391	0.3	19	4.1	2.2	3160	16.7	bdl	0.1	bdl	bdl	bdl	0.1	bdl	0.7	bdl
WDC423-1-1	Py_{3WK}	30.3	7.2	413	7.8	38	19.6	9	8350	22.4	0.2	0.6	0.2	49.6	1.4	0.4	6.2	159	1.7
WDC423-1-2	Py_{3WK}	24	3.7	402	6.4	16.5	20.6	3.4	10510	26.8	0.1	0.5	0.2	57.3	bdl	0.3	8	194	1.5
WDC423-1-3	Py_{3WK}	6.7	1.6	404	2.3	9.2	18.7	2.4	10500	23.2	0.2	0.4	bdl	59	bdl	0.1	8.8	200	1.3
WDC423-1-4	Py_{3WK}	3.8	1.4	384	0.8	4.5	15.8	2.4	7600	11.9	bdl	0.3	bdl	48	bdl	0.1	5.3	174	1.2
WDC423-1-5	Py_{3WK}	5.2	3	415	7.1	37	21.7	3.3	7900	14.9	0.2	0.4	bdl	57	bdl	0.3	6.1	195	1.5
WDC423-1-6	Py_{3WK}	5.2	2.4	393	3.3	21	22.7	3.8	9100	15.9	bdl	0.4	1.4	69	bdl	0.2	7.3	232	1.6
WDC423-1-7	Py_{3WK}	5.7	2.3	409	21	90	45	4.8	21200	15.6	bdl	0.7	0.7	79	bdl	0.2	20	264	2.1
WDC423-1-8	Py_{3WK}	6.4	1.8	387	9	36	23.8	3.6	9700	17.2	0.2	0.5	bdl	65	bdl	0.5	7.8	226	1.7
WDC423-1-9	Py_{3WK}	3.9	4.3	391	4.2	29	21.1	8.6	9600	15.5	0.4	0.3	1.3	49	bdl	0.4	6.6	172	1.2
WDC423-1-10	Py_{3WK}	4.2	2.5	391	2.1	11	21.2	5.3	9500	15.3	0.3	0.3	0.5	52	bdl	0.4	6.8	177	1.4
WDC423-1-11	Py_{3WK}	2.3	bdl	366	1.2	25	18.7	2.7	8900	11.8	bdl	0.3	bdl	47	bdl	0.2	6.9	165	1.2
WDC423-1-12	Py_{3WK}	2.8	2	374	5.1	30	18.7	4.5	8200	13.4	0.1	0.4	0.2	38	bdl	0.1	5.8	127	1
WDC423-1-13	Py_{3WK}	7.7	9	392	18	120	52	19	8200	19	bdl	0.9	9	62	bdl	0.5	5.4	200	2.2
WDC423-1-14	Py_{3WK}	1.9	1.6	390	1.9	32	18.4	3.8	7600	12.4	0.1	0.3	0.3	38	bdl	0.2	5.3	124	0.9
WDC423-1-15	Py_{3WK}	1.5	2.5	392	3.3	32	19.2	3.9	7300	12.5	0.1	0.3	0.6	41	bdl	0.1	5	126	0.8
WDC423-1-16	Py_{3WK}	8	9	392	7.1	59	35	11	7800	16.2	0.4	0.4	15	44.3	bdl	0.3	5	136	1.1
WDC423-1-17	Py_{3WK}	3.9	2.1	376	2.6	29	20.1	6.6	6800	10.7	0.1	0.3	0.2	34.5	bdl	0.2	4.8	87	0.7
WDC423-1-18	Py_{3WK}	9	1.6	373	10	40	36	1100	6900	13.7	bdl	0.2	0.4	44	bdl	0.3	3.9	105	0.6
WDC423-1-19	Py_{3WK}	4.7	6.6	373	4	38	29	5.4	6400	10.6	bdl	0.3	0.2	43	bdl	0.2	3.5	108	0.9
WDC423-1-20	Py_{3WK}	6.6	3	378	3.4	36	18.1	13.4	7000	11.9	1.2	0.2	2.9	23.3	bdl	0.6	2.8	64	0.5
WDC423-1-21	Py_{3WK}	4.8	2.3	385	4	45	43	6.9	7200	13.1	0.1	0.2	1.1	22.9	bdl	0.4	3.7	79	0.5
WDC423-1-22	Py_{3WK}	2.9	2.4	393	5.9	170	18.1	4.1	8000	15.9	0.1	0.2	0.5	26.7	1.7	0.5	4.4	127	0.9
WDC423-1-23	Py_{3WK}	4.5	2.4	379	2.2	18	17.7	5.1	9400	16.9	0.2	0.2	0.2	36	bdl	0.8	5.9	133	1
WDC423-1-24	Py_{3WK}	26	12	370	31	140	55	60	10300	12	1.5	0.1	2	47	1.3	3.5	4.3	145	1.3

Yaho

Hole ID	Type	^{51}V	^{52}Cr	^{55}Mn	^{59}Co	^{60}Ni	^{65}Cu	^{66}Zn	^{75}As	^{82}Se	^{95}Mo	^{107}Ag	^{118}Sn	^{121}Sb	^{125}Te	^{182}W	^{197}Au	^{208}Pb	^{209}Bi
WDC450-1-1	Py_{1Y}	4.7	6.2	5.4	187	112	37.9	7.5	5600	12	bdl	0.3	0.4	42.4	1.7	0.2	1.8	113	9.4
WDC450-1-2	Py_{1Y}	7.5	11.4	9.9	318	208	118	38	2570	20	bdl	1.3	0.6	71	2.7	0.4	1.1	510	16.8
WDC450-1-3	Py_{1Y}	12.1	12.8	13.4	322	180	47.3	5.9	1935	24.6	bdl	0.5	0.6	77.1	2.8	0.4	1	249	17.3
WDC450-1-4	Py_{1Y}	9.1	11.6	9.1	455	200	32.4	4.9	2580	10.6	bdl	0.6	0.6	49.8	2	0.3	0.7	230	10.7
WDC450-1-5	Py_{1Y}	6.7	10.5	3.6	417	188	28.9	3.5	7100	5.4	bdl	0.1	0.6	26.7	1.2	0.6	2	55.1	5.2
WDC450-1-6	Py_{1Y}	3.6	5	1.7	211	99	65	1.8	6650	1.9	bdl	0.3	0.2	11	bdl	0.6	3.6	23.4	3.5
WDC450-1-7	Py_{1Y}	1.5	2.3	bdl	128	63.7	15.8	21	4260	bdl	bdl	0.2	3.5	7	1.8	0.3	1.6	13	2.7
WDC450-1-8	Py_{1Y}	0.9	2.9	bdl	93	89	19	22.1	15700	bdl	bdl	0.1	bdl	9.7	bdl	0.2	0.9	9.9	1.4
WDC450-1-9	Py_{1Y}	1.6	1.7	1.9	81	91	18.5	9.2	9600	bdl	bdl	0.1	1	5.3	bdl	0.3	1	8.7	1.1
WDC450-2-1	Py_{2Y}	2.3	2.2	1.7	16.3	15.7	110	28	19720	bdl	bdl	0.7	0.3	73	bdl	0.3	14.6	6.3	0.5
WDC450-2-2	Py_{2Y}	0.9	1.5	1.5	6.6	11.1	56.1	3.7	22300	bdl	bdl	0.1	0.2	15.9	bdl	0.2	17.2	22	1.2
WDC450-2-3	Py_{2Y}	3.4	2.3	5.7	21.6	34.6	210	22.4	24200	bdl	bdl	0.3	0.7	27.7	bdl	0.2	17.2	39.8	2.2
WDC450-2-4	Py_{2Y}	2.4	1.6	2.1	35	29	55	9.8	22900	bdl	bdl	0.2	0.8	21.4	bdl	0.2	18.7	27.5	1.6
WDC450-2-5	Py_{2Y}	5.3	4.4	4.6	75	59	43.6	8.3	19600	bdl	bdl	0.3	0.5	19.1	bdl	0.3	13.8	57.6	2.7
WDC450-2-6	Py_{2Y}	5.1	3.1	3.2	47	39.5	48	5	25700	bdl	bdl	0.1	0.3	13.2	bdl	0.2	20.3	39	2.1
WDC450-2-7	Py_{2Y}	7	35	5.1	145	102	165	3.1	20300	bdl	bdl	0.1	0.9	47	bdl	22	22.2	41	3.4
WDC450-2-8	Py_{2Y}	8.3	28	8	142	100	670	2.1	24900	bdl	0.2	0.2	0.5	69	bdl	27	28.6	30.9	3.2
WDC450-2-9	Py_{2Y}	8.9	5.9	2.9	89	66	59.1	4.3	21600	bdl	bdl	0.4	0.6	12	bdl	0.8	18.1	22.6	2.1
WDC450-2-10	Py_{2Y}	5.4	9.5	2.2	91	54	72	2.2	23100	bdl	bdl	0.1	0.9	16.4	1.7	4.2	27.5	17.8	1.6
WDC450-2-11	Py_{2Y}	1.7	5.3	bdl	66	52	55.3	14.7	21200	bdl	bdl	0.1	0.5	25.6	bdl	4.3	28.1	32.4	2.6
WDC450-2-12	Py_{2Y}	1.7	1.8	1.9	146	134	69	31.4	14300	bdl	bdl	0.1	0.5	10	bdl	0.3	11.3	10.4	1
WDC450-2-13	Py_{2Y}	0.8	2	2.1	171	129	19.1	6.9	6900	bdl	bdl	0.2	3.4	3.1	bdl	0.2	3.7	17	2.9
WDC450-2-14	Py_{2Y}	6.2	5.4	6.1	218	209	86	68	14800	bdl	bdl	0.3	0.6	9.3	bdl	0.4	4.4	12.1	2.6
WDC450-2-15	Py_{2Y}	9.2	6.3	57	261	171	23.7	8.3	7780	bdl	bdl	0.1	0.7	3	bdl	0.5	5.3	3.7	0.4

ANNEXE 6 : ARTICLE DE MAÎTRISE PUBLIÉ DANS ORE GEOLOGY REVIEWS

Ore Geology Reviews 78 (2016) 667–672

Contents lists available at ScienceDirect

Ore Geology Reviews

journal homepage: www.elsevier.com/locate/oregeorev

The world-class Wona-Kona gold deposit, Burkina Faso

Jérôme Augustin [a,b,c,*], Damien Gaboury [a,b], Michel Crevier [c]

[a] UQAC, Université du Québec à Chicoutimi, 555 Boulevard de l'Université, Chicoutimi, Québec G7H 2B1, Canada
[b] LAMEQ, Laboratoire de Métallogénie Expérimentale et Quantitative, Université du Québec à Chicoutimi (UQAC), 555 Boulevard de l'Université, Chicoutimi, Québec G7H 2B1, Canada
[c] SEMAFO Inc. Société d'Exploitation Minérale en Afrique de l'Ouest, 100 Boulevard Alexis-Nihon, 7e Étage, St-Laurent, Québec H4M 2P3, Canada

ARTICLE INFO

Article history:
Received 6 May 2015
Received in revised form 14 September 2015
Accepted 14 October 2015
Available online 23 October 2015

Keywords:
Birimian
Shear zone
Gold
Silicification
Burkina Faso
West African Craton

ABSTRACT

The world-class >4 Moz Wona-Kona gold deposit is hosted within the Paleoproterozoic Birimian Houndé greenstone belt which is the most important gold mineralized belt in the western part of Burkina Faso, with a cumulative reserve of ~11 Moz. The mineralization consists of a pervasive silicification with disseminated pyrite–arsenopyrite crosscut by quartz–carbonate veinlets (1 to 10 cm wide) forming a vertical, thick (up to 40 m) and laterally extensive (5 km) northeast trending orebody hosted within a large (200 m wide) shear zone of regional extent. Gold occurs in association with 3 generations of pyrite and 2 generations of arsenopyrite. Free gold, interpreted as the last mineralizing event, occurs as late fracture filling in the pervasive silicification zone.

1. Exploration and exploitation history

The world-class Wona-Kona gold deposit, one of the largest gold deposits in Burkina Faso (Augustin, 2011), is located within the Houndé greenstone belt (HGB) situated about 260 km from Ouagadougou (Fig. 1). Exploration by SEMAFO Inc. (Société d'Exploration Minière en Afrique de l'Ouest) on the Mana property started in October 1997. The Wona prospect was discovered with trenches in 2000 following a BLEG (bulk leach extractable gold) regional soil geochemistry program that yielded isolated and weak anomalies (>20 ppb including a peak anomaly of 64 ppb). Detailed work on the target started in 2001 with gradient IP (induced polarization), trenches, RC (reverse circulation) holes, RAB (rotary air blast), CIL (carbon in leach) tests on RC drill hole material and a first resource estimate. Results confirmed the extension of the Wona structure over a 1.6 km strike length open in a NE trend. As a result, an application for the Kona permit to the northeast was reached in 2001. Certification of the Wona resources was completed in 2003. A formal feasibility and environmental impact study was initiated in 2004, and positively completed in 2006. Production started on February 15, 2008, and the first gold bar was poured on March 31, 2008. At this time, estimated mine life was 8 years from the start of operations in early 2008 (SGS, 2008).

Since 2008, the Wona-Kona gold deposit has produced 1,160,700 oz, and at the end of 2014, the Wona-Kona reserves stood at 13,275,500 t at a grade of 2.27 g/t Au for 970,100 oz (www.semafo.com). Measured and indicated resources stand at 1,787,000 oz (Table 1). All these gold ounces were defined only for the first 150 m of depth for a very long deposit, hence justifying the "world-class" classification.

Intensive mapping, auger, diamond and reverse circulation drilling, trench sampling and geophysical surveys over the years, have provided a better understanding of the structural control and origin of gold mineralization at the Wona-Kona deposit at property scale. This methodology has been successful for SEMAFO Inc. with the discovery of many other gold deposits in the Mana district: Nyafé (1999), Maoula (2000), Fofina (2010), Fobiri (2010), Yaho (2011: Sinaré, 2012) and Siou (2012).

2. Regional geology

The Wona-Kona gold deposit is located in the Paleoproterozoic Baoulé-Mossi domain of the West African Craton in the northwest branch of the Birimian Houndé greenstone belt (HGB) (western Burkina Faso). The HGB is a north to northeast trending structure comprising a basal unit of tholeiitic basalt and gabbro and interbedded greywacke–siltstone–shale units (Baratoux et al., 2011). These are overlain by andesites and volcanic rocks, composed of massive, pillowed, brecciated and tuffaceous facies, which occur in the central and southern part overlaying the tholeiitic unit (Baratoux et al., 2011). Abundant layers of cherts (ferruginous and manganiferous) and quartz veins injections are associated with the volcano-sedimentary rocks. The basalt mafic unit is bound to the east by the Boni shear zone, which defines the contact with the late Tarkwaian-type sediments (Baratoux et al.,

* Corresponding author at: UQAC, Université du Québec à Chicoutimi, 555 Boulevard de l'Université, Chicoutimi, Québec G7H 2B1, Canada.
E-mail address: jerome.augustin@gmail.com (J. Augustin).

http://dx.doi.org/10.1016/j.oregeorev.2015.10.017
0169-1368/

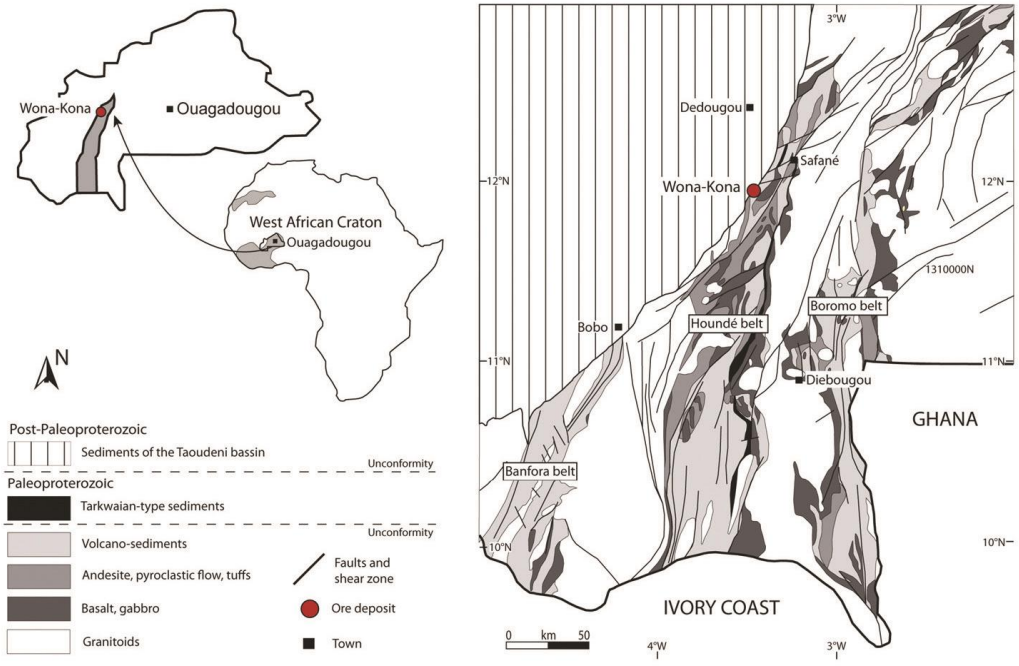

Fig. 1. Regional geology of western Burkina Faso showing major shear systems and Wona-Kona deposit. Modified from Baratoux et al. (2011).

2011) with a maximum deposition age between 2171 ± 7 to 2113 ± 23 Ma (Bonkoungou, 1994; Bossière et al., 1996). In the West, the Birimian basement is unconformably overlain by Neoproterozoic sediments of the Taoudeni basin (Deynoux, 1983; Bertrand-Sarfati et al., 1990).

The tectonometamorphic evolution is polycyclic with at least three deformation events; greenschist-facies metamorphism with amphibolite facies assemblages locally occur in contact with some granitoids. The principal deformation imprint of the Eburnean orogenesis (2160–2110 Ma, Baratoux et al., 2011) is related to the first and second deformation phases (D1–D2). The D1 event resulted in E–W to WNW oriented compression characterized by isoclinal folds and local shear zones (Baratoux et al., 2011). The D2 event consisted of regional sinistral N–S trending or dextral ENE-trending anastomosing shear zones. Late-Eburnean or perhaps even Pan-African D3 deformation is recorded in some lithologies (post 2109 Ma; Baratoux et al., 2011).

The HGB is intruded by multiple episodes of granitoid intrusions including a tonalite–trondhjemite–granodiorite suite (TTG) and granitic intrusions. Late swarm doleritic and gabbro dykes transect all of the present lithologies and are currently dated at 215 ± 15 Ma (Hottin and Ouedraogo, 1992).

Table 1
Production and location summary of the Wona-Kona deposit.

Deposit name	Wona-Kona
Commodity of exploitation	Au
Longitude	−3.413360
Latitude	11.990166
Geographic location	The project is situated in Western Burkina Faso at 260 km west of Ouagadougou
Geological location	West African Craton; Leo-Man Shield; Baoulé-Mossi domain; NE-striking Houndé greenstone belt
Deposit status	Mined since 2008
Deposit type	Shear zone-hosted quartz–carbonate veins and silicification; volcano-sedimentary rock/tholeiitic basalt/granodiorite hosted
Current owner	Semafo Inc.
Average grade	2.27 g/t
Proven and indicated	2.8 Moz proven and indicated resource (2014)
Past production	1.2 Moz (2008 to 2014)

3. Host rocks and hydrothermal alteration

The Wona-Kona gold deposit is situated along the contact between a granodiorite batholith (Wona intrusion) and an assemblage of tholeiitic basalt and volcano-sedimentary rocks. The tholeiitic basalt has an aphanitic texture with various proportions of epidote, chlorite, actinolite and albite. The volcano-sedimentary rocks are constituted by interbedded mafic volcanoclastic rocks and graphitic black shales rich in sulfides. They are crosscut by felsic to intermediate dyke swarms (Augustin, 2011, Fig. 2). Felsic porphyry dykes contain quartz and plagioclase feldspar porphyroblasts (1 to 3 mm) in a quartz–muscovite matrix. Dioritic dykes include plagioclase feldspar, chlorite and ankerite.

The Wona-Kona orebody is hosted along a major northeast trending and steeply dipping shear zone. Three deformation events (D1–D3) can be distinguished. The first deformation (D1) is characterized by a main vertical planar fabric trending NNE–SSW related to the regional shortening associated with the accretion during the D1 Eburnean orogeny. D2 is evident in a S2 fabric with a shallow plunging stretching lineation oriented NE–SW and the geometry of sigmoidal dipping quartz veins indicating dextral shear movement. D3 is characterized by an E–W trending subvertical cleavage (S3) only developed in highly strained

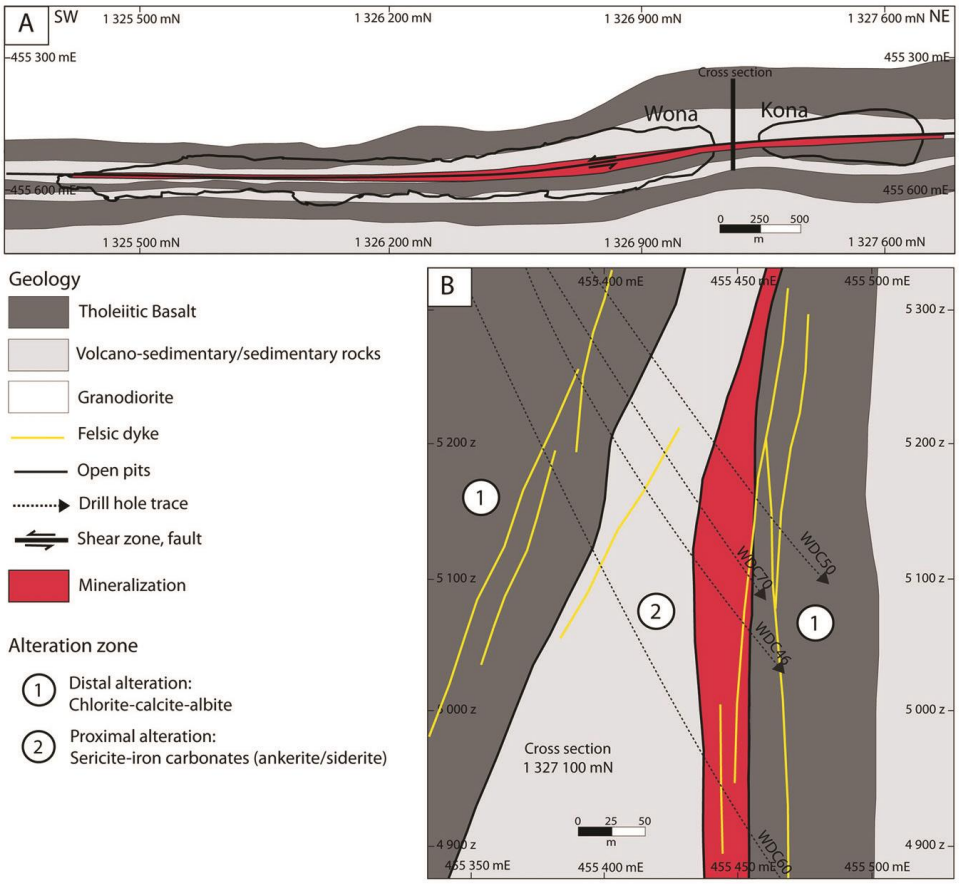

Fig. 2. (A) Simplified geological map of Wona-Kona gold deposit. (B) Cross section of the Wona deposit, looking toward the north.

rocks like black shales due to their difference in competence and resulting in a strongly deformed unit compared to the rest of the series. Later events, including D3 folding, intense crenulation and quartz veining are suggestive of sinistral shear zones reactivation and are associated with the gold mineralizing processes at the district-scale (Augustin, 2011; Sinaré, 2012). The D2–D3 events locally observed in the Mana district are ascribed to the regional D2 event in western Burkina Faso, described by Baratoux et al. (2011) and Metelka et al. (2011).

The orebody is recognized along 5 km of strike and is surrounded by a large hydrothermal alteration halo, extending up to 50 m symmetrically in the host rocks (Fig. 2B). The distal alteration is characterized by a pervasive chlorite, albite and calcite assemblage. The proximal alteration zone, which can extend up to 20 m away from the orebody, is composed of sericite, iron carbonates (ankerite/siderite) and disseminated magnetite. In the NW part, sericitic schist hosted in volcanic rocks and felsic dykes are developed and associated with pegmatitic veins. These are highly anisotropic yellowish unit defining metric-thick deformation corridors with microfolds, crenulation cleavages and strong transposition. However, these corridors are not gold-mineralized.

The presence of this assemblage indicates greenschist metamorphic facies conditions during gold mineralization. Nevertheless, contact-related amphibolite facies grades are locally recorded in the basaltic rocks surrounding the Wona intrusion.

4. Mineralization

The gold mineralization within the Wona-Kona deposit occurs within highly strained rocks, within a 200 m wide sheared zone of regional extent. The same type of mineralization is observed in Wona and Kona pits and is associated with the shearing. The orebody is continuous longitudinally, being unaffected by significant displacing crosscutting faults. In the northeast part, the thickening of the black shale units interbedded with volcanoclastic rocks coincides with enhance gold mineralization that can reach up to 40 m wide (Fig. 3A). In the southern part, as the main zone gets thinner, additional parallel zones appears to the east of the main zone. Those satellite zones are generally just a few meters thick and hosted in volcanoclastics and black shale units. These units are also intruded by felsic porphyry dyke swarms. In some parts of the deposit, felsic dykes are parallel to the volcano-sedimentary rocks and

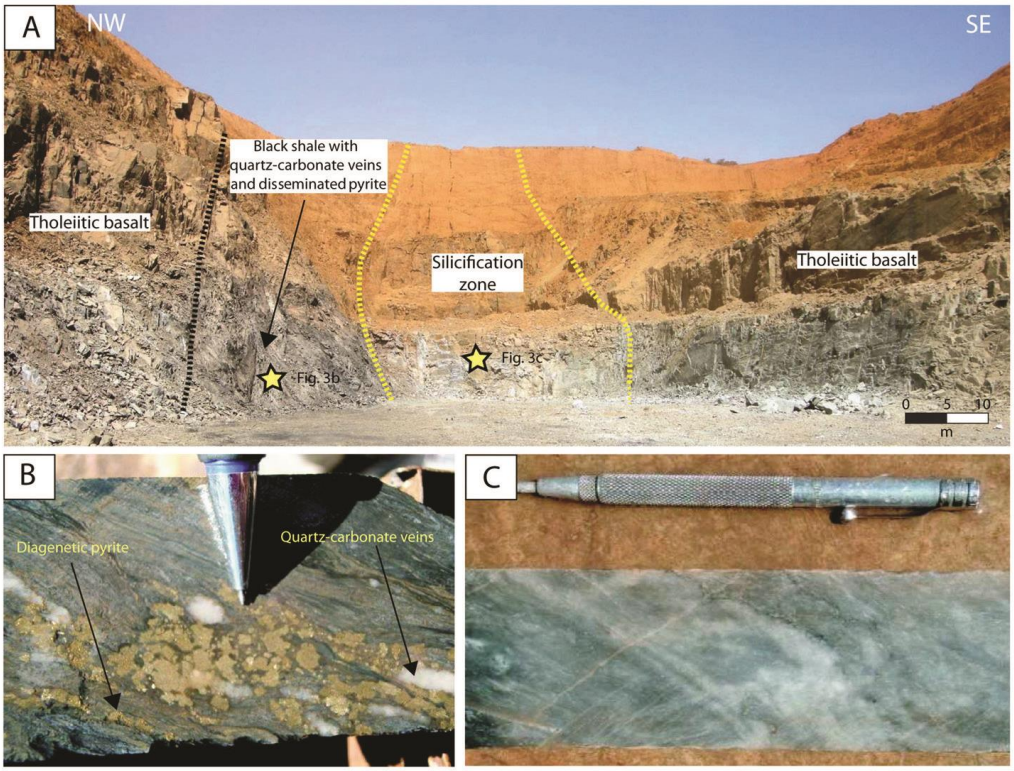

Fig. 3. Photography of the silicified orebody and host rocks of Wona-Kona deposit. (A) Mineralized cross section in the Wona pit, view to North. (B) Diagenetic pyrite, late pyrite and quartz–carbonate vein occurrences as seen in drill core. (C) Silicified main zone in drill core.

are also strongly silicified, sericitized and mineralized. It is suggested that these dykes provided favorable rheological contrasts during shearing for channeling the hydrothermal fluids.

4.1. Ore mineralogy/accessory minerals

Three styles of mineralization were identified based on sulfides textures, occurrences and gold grades. The first style is disseminated pyrite occurring in the black shales around the orebody (Fig. 3A, B). Gold concentrations in these rocks are low <0.2 g/t and are not of economic interest. The second style consists of pyrite and arsenopyrite occurring in small quartz–carbonate veins (centimeter in width) parallel to the shear zone (Fig. 3B). These veins also contain minor chalcopyrite and sphalerite. In these rocks, Au grades range from 0.7 to 1.0 g/t in the proximal alteration zone that extent up to 20 m away from the orebody. This mineralization is locally mined when occurring together with the main mineralization style. The third and main mineralization style corresponds to pyrite and arsenopyrite occurring within a large silicified zone in the shear zone. Pyrite and arsenopyrite are associated with traces of chalcopyrite and sphalerite. In addition, fine grains of free gold were identified in late fractures (Fig. 3A, C). This mineralization forms the major part of the orebody and Au grades range from 2.4 to 5 g/t.

Three generations of pyrites and two of arsenopyrites were discriminated in relation to ore styles. They show distinct textural features (Fig. 4) and have different metal contents as determined by LA-ICP-MS at UQAC (Table 2). The first generation of pyrite (py1) occurs as disseminated, porous and fine-grained nodular aggregates that are oriented parallel to bedding in the black shale (Fig. 4A). This observation suggests a syn-diagenetic origin for the pyrite as proposed by Large et al. (2007) and Thomas et al. (2011) for similar textures. These pyrites have the highest metal contents (Table 2). The second generation of pyrite (py2) and first generation of arsenopyrite (asp1) occur as euhedral grains (Fig. 4B, C) within the quartz–carbonate veins associated with the D2 deformation event and related greenschist metamorphic conditions. These pyrites and arsenopyrites have the lowest metal contents and are thought to be of metamorphic origin. The third generation of pyrite (py3) and second generation of arsenopyrite (asp2) are intimately associated with the strong silicification which defines the orebody. Py3 forms external rims around py1 (Fig. 4D) and asp2 occurs as euhedral to anhedral grains that are finely disseminated in the rock (Fig. 4E). Asp2 is richer in all metals relative to asp1 (Table 2). Py3 is richer in all metals than py2 but not as enriched as py1 (Table 2). It is proposed that py3 and asp2 precipitated from hydrothermal fluids that promoted the silicification in the shear zone. Free gold that is spatially associated with late fractures in the pervasive silicification zones is interpreted as the last mineralization event. We suggest that Au was extracted from py3 by progressive fluid interaction. In addition to sulfides, disseminated magnetite occurs close to the orebody. There is a symmetric transition from external magnetite in the proximal alteration zone to pyrite

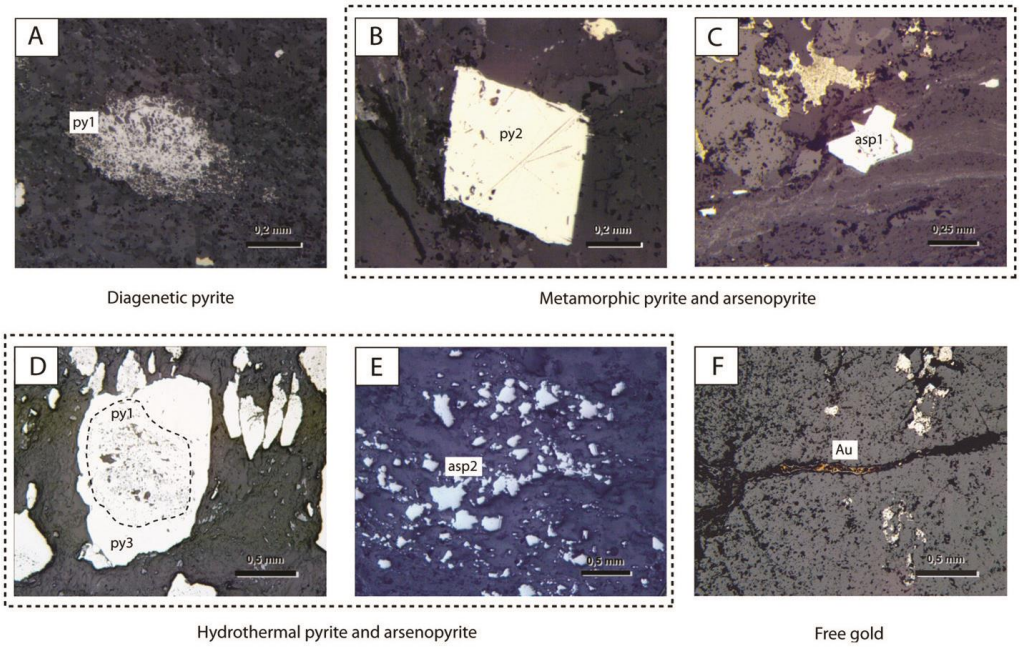

Fig. 4. Photomicrographs of the different generations of pyrite and arsenopyrite at Wona-Kona deposit. (A) Diagenetic pyrite in black shale (py1). (B) Metamorphic pyrite in quartz–carbonate veins. (C) Metamorphic arsenopyrite (asp2) in quartz–carbonate veins. (D) Hydrothermal pyrite (py3) overgrowth diagenetic pyrite (py1) in main silicification zone. (E) Hydrothermal arsenopyrite (asp2) in main silicification zone. (F) Late free gold (Au) in a fracture crosscutting the pervasive silicification.

in the silicified orebody, without clear replacement of magnetite by pyrite. This transition reflects a significant change in the oxygen fugacity (reduction) of the fluids which is probably related to gold precipitation.

4.2. Wona-Kona orebody genesis

The Wona-Kona gold deposit is described as an orogenic gold deposit formed during the polycyclic ductile–brittle deformation events resulting in multiple mineralization episodes (Augustin, 2011; Gaboury, 2013). The link between orebody formation and the deformation is obvious and some features clearly supporting a long-lasting and polyphase formation. For example, the quartz–carbonate veins are folded and boudinaged following increments of D2 deformation. The progressive silicification and later veining and fracturing manifest a progressive change in the rheological behavior of the orebody as a response to alteration and deformation. Such an evolution also influenced the gold precipitating mechanisms from gold-bearing sulfide to free gold in late fractures associated with the last event D3. From a genetic point of view, hydrothermal fluids of the Wona-Kona deposit are identified as orogenic, being CO_2 rich and H_2O poor, with traces of N_2, C_2H_6 and CH_4 (Gaboury, 2013). Finally, the presence of C_2H_6 indicates a fluid sourced from gold-enriched carbonaceous sedimentary rocks such as the pyritic black shale (Gaboury, 2013), which is common in the assemblage pile at the district-scale.

Table 2
Mean trace element values for each pyrite and arsenopyrite type determined by LA-ICP-MS.

	Diagenetic pyrite	Metamorphic pyrite	Hydrothermal pyrite	Metamorphic arsenopyrite	Hydrothermal arsenopyrite
No. of analyses (ppm)	22	129	37	95	52
Au	0.75	0.13	0.18	2.86	30.76
V	3.92	0.39	0.35	0.94	19.67
Co	388.11	56.07	170.14	185.27	309.70
Ni	528.36	241.23	332.57	189.51	376.50
Cu	951.20	0.93	1.07	6.12	2.56
Zn	10.07	1.01	2.33	1.66	5.12
As	4399.32	1846.00	2027.75	n.d.	n.d.
Se	38.75	14.63	28.59	45.02	99.20
Ag	7.74	0.75	0.46	0.99	8.09
Sb	49.82	5.21	5.44	204.63	351.90
Te	2.67	2.99	3.72	10.98	350.10
Pb	83.67	18.19	12.52	5.78	27.75
Bi	0.21	0.12	0.18	0.14	0.27

n.d. = not determined.

Acknowledgments

This project is part of a larger research program on the Mana District supervised by D. Gaboury (UQAC) since 2007 in collaboration with SEMAFO Inc. We thank SEMAFO Inc. for their financial support, granting access to their technical data, permitting field work and for the authorization to diffuse these results. We are grateful of the support from the Mana Minéral SARL team. We would like to thank L. Baratoux and K. Hein for insightful reviews of the early drafts. Finally, Laurence Robb and an anonymous reviewer are gratefully acknowledged for thorough revision and improvement of this manuscript.

References

Augustin, J., 2011. Facteurs de contrôle et processus métallogéniques des minéralisations aurifères du gisement de Wona, mine Mana, Burkina Faso. Mémoire de Maîtrise. Université du Québec à Chicoutimi, pp. 1–220.

Baratoux, L., Metelka, V., Naba, S., Jessell, M.W., Grégoire, M., Ganne, J., 2011. Juvenile Paleoproterozoic crust evolution during the Eburnean orogeny (2.2–2.0 Ga), western Burkina Faso. Precambrian Res. 191, 18–45.

Bertrand-Sarfati, J., Moussine-Pouchkine, A., Affaton, P., Trompette, R., Bellion, Y., 1990. Cover sequences of the West African Craton. In: Dallmeyer, R.D., Lecorche, J.P. (Eds.), The West African Orogens and Circum-Atlantic Correlatives. Springer-Verlag, pp. 65–82.

Bonkoungou, L., 1994. Le Tarkwaïen du sillon de Houndé (Burkina-Faso): un ensemble volcano-détritique acide calco-alcalin a 2.15 Ga. Etude Pétrologique, Métamorphique et Structurale. University of Nantes, p. 419.

Bossière, G., Bonkoungou, I., Peucat, J.J., Pupin, J.P., 1996. Origin and age of Paleoproterozoic conglomerates and sandstones of the Tarkwaian Group in Burkina Faso, West Africa. Precambrian Res. 80, 153–172.

Deynoux, M., 1983. Les Formations de Plate-Forme d'Age Precambrien Superieur et Paleozoique Dans l'Ouest Africain Correlation Avec les Zones Mobiles. Pergamon Press. Oxford, United Kingdom.

Gaboury, D., 2013. Does gold in orogenic deposits come from pyrite in deeply buried carbon-rich sediments?: insight from volatiles in fluid inclusions. Geology 41, 1207–1210.

Hottin, G., Ouedraogo, O.F., 1992. Carte géologique du Burkina Faso échelle 1/1,000,000, 2ème édition. Ouagadougou: Bureau des Mines et de la Géologie du Burkina (BUMIGEB).

Large, R.R., Maslennikov, V., Robert, F., Danyushevsky, L.V., Chang, Z.S., 2007. Multistage sedimentary and metamorphic origin of pyrite and gold in the giant Sukhoi Log Deposit, Lena Gold Province, Russia. Econ. Geol. 102, 1232–1267.

Metelka, V., Baratoux, L., Naba, S., Jessell, M.W., 2011. A geophysically constrained lithostructural analysis of the Eburnean greenstone belts and associated granitoid domains, Burkina Faso, West Africa. Precambrian Res. 190, 48–69.

SGS, 2008. Technical Report on the Resources and Reserves of the Mana Gold Deposits. Burkina Faso. pp. 1–83.

Sinaré, M., 2012. Métallogénie du gisement aurifère de Yaho, ceinture birimienne de Houndé. Burkina Faso. Mémoire de Maîtrise. Université du Québec à Chicoutimi, pp. 1–266.

Thomas, H.V., Large, R.R., Bull, S.W., Maslennikov, V., Berry, R.F., Fraser, R., Froud, S., Moye, R., 2011. Pyrite and pyrrhotite textures and composition in sediments, laminated quartz veins, and reefs at Bendigo gold mine, Australia: insights for ore genesis. Econ. Geol. 106, 1–31.